Università degli studi di Padova

Dipartimento di Fisica e Astronomia
"G. Galilei"

Scuola di Dottorato di Ricerca in Astronomia
Ciclo XXVII

# Optical design study, testing and qualification of a Schwarzschild-Couder telescope for CTA

## and an assessment on the Intensity Interferometry capabilities with CTA

**Direttore della Scuola:** Ch.mo Prof. Giampaolo Piotto

**Relatore:** Ch.mo Prof. Alberto Franceschini

**Co-relatore:** Dott. Enrico Giro

**Co-relatore:** Dott. Claudio Pernechele

**Dottorando:** Gabriele Rodeghiero

2015

*A Riccardo e Valentina*
*compagni di viaggio di ieri*
*e di oggi*

# Contents

# List of Tables

# Acronyms

**AGN** Active Galactic Nuclei

**AMC** Active Mirror Control

**ALPs** Axion Like Particle

**ASTRI** Astrofisica con Specchi a Tecnologia Replicante Italiana

**BFL** Back Focal Length

**CGH** Computer Generated Hologram

**CHARA** Center for High Angular Resolution Astronomy

**CMB** Cosmic Microwave Background

**CRs** Cosmic Rays

**CTA** Cherenkov Telescope Array

**CTAO** Cherenkov Telescope Array Observatory

**CTE** Coefficient of Thermal Expansion

**DC** Davies-Cotton

**DM** Dark Matter

**DOF** Degree of Freedom

**EBL** Extragalactic Background Light

**EE** Ensquared or encircled Energy

**EFL** Effective Focal Length

**EPD** Entrance Pupil Diameter

**ESO** European Southern Observatory

**EXPD** Exit Pupil Diameter

**FEA** Finite Element Analysis

**FoV** Field of View

**GC** Galactic Center

**GEC** Galbiati Eie Group

**GLAST** Gamma-ray Large Area Space Telescope

**GRB** Gamma Ray Burst

**IACT** Imaging Atmospheric Cherenkov Telescope

**IC** Inverse Compton

**II** Intensity Interferometry

**INAF** Italian National Institute of Astrophysics

**IP** Interferometric Parallax

**LAT** Large Area Telescope

**LHAASO** Large High Altitude Air Shower Observatory

**LST** Large Size Telescope

**M1** Primary Mirror

**M2** Secondary Mirror

**MACE** Major Atmospheric Cherenkov Experiment

**MC** Monte Carlo

**MIUR** Italian Ministry of Education, University and Research

**MQs** Microquasars

**MPPC** The Multi Pixel Photon Counter

**MST** Medium Size Telescope

**NAOJ** National Astronomical Observatory of Japan

**NLR** Narrow Line Region

**NRAO** National Radio Astronomy Observatory

**NSB** Night Sky Background

**PMDs** Photo Detection Modules

**PMMA** Poly Methyl Methacrylate

**PSD** Power Spectral Density

**PWN** Pulsar Wind Nebulae

**QG** Quantum Gravity

**SC** Schwarzschild-Couder

**SED** Spectral Energy Distribution

**SFH** Star Formation History

**SM** Standard Model

**SMBH** Super Massive Black Hole

**SNR** Signal to Noise Ratio

**SnRs** Supernova Remnants

**SiPM** Silicon Photo Multipliers

**SST** Small Size Telescope

**UDA** User Defined Aperture

**VCZ** Van Cittert-Zernike

**VHE** Very High Energy

**VLBA** Very Long Baseline Array

**VLBI** Very Long Baseline Interferometry

**VLTI** Very Large Telescope Interferometer

**WIMPs** Weakly Interacting Massive Particles

# Introduction

There is a growing common effort in the very high energy community towards the development of new research infrastructures to answer the fundamental questions of modern high-energy astrophysics and astroparticle physics. The Cherenkov Telescope Array Observatory (CTAO) is an international project aiming to deploy two separate arrays to observe the whole VHE sky between E = 20 GeV up to E $\sim$ 300 TeV in a long term plan of about 30 years of operations. CTA is designed to increase the sensitivity by a factor 10 at 1 TeV, to enlarge the detection area, the angular resolution and the field of view over the facilities operating today. The observatory will be characterized by high flexibility, enhanced monitoring and deep survey capabilities, short time scale and simultaneous observations in multiple fields.
This PhD thesis addresses the optical design study and testing of dual mirror Imaging Atmospheric Cherenkov Telescopes (IACTs) for the incoming CTAO. All of the IACTs facilities currently operating rely on single mirror solutions, which are mostly parabolic or Davies-Cotton optical designs, however there is a novel interest in the development of dual mirror configurations following the Schwarzschild-Couder optical design. This peculiar design, based on two highly aspherical mirrors promises wide-field, aplanatic telescopes characterized by small f-numbers and more compact structures. Dual mirror solutions allow use smaller camera pixels ($\sim$3-6 mm) based on Silicon Photo Multiplier technology in substitution of the larger Photo Multiplier Tubes ($\sim$1 inch) currently in use. The increased complexity in terms of optics manufacturing, replication and alignment is motivated from the attractive new capabilities of such configuration. In this context the Italian National Institute for Astrophysics (INAF) supported by the Italian Ministry of Education, University and Research (MIUR), is developing a small sized telescope prototype for CTA, named ASTRI, which is based upon the Schwarzschild-Couder optical design. The present work deals with the challenging realization of this optical configuration that has never been applied to IACTs. After two introductory chapters on the gamma-ray astronomy and the ASTRI optical design and its main subsystems (chapters 1 and 2), the performances of this system are compared with those of the other common wide-field telescopes in use for Cherenkov observations and for other applications in astrophysics (chapter 3). This comparative study is based on a commercial ray tracing software into which the optical designs of the envisaged telescopes are reproduced. Subsequently in chapter 4, an extended study of the ASTRI capabilities in relation to the performance and environmental requirements issued by CTA is presented in a detailed analysis of compliance supported by ray tracing simulations, finite element analysis and tolerance studies. In chapter 5 the work on the qualification tests of the secondary mirror gives an insight into the complexity of the Schwarzschild-Couder optics. The realization of this optical element is challenging in relation to currently available technologies, in particular concerning the cost requirements imposed by the CTA project. These constraints and the large sagitta of the mirror ($\sim$190 mm) requires the use of the hot slumping technique in substitution of the cold slumping and diamond milling approaches usually used in the manufacturing of mirrors for Cherenkov applications. The results of a careful and extended test campaign on a mirror prototype have indicated that this manufacturing technique can provide a reliable engineering process of production for such large, highly aspherical optics.

With a perspective on the science with future large telescopes as those provided by CTA, an assessment study upon the potentialities of the Intensity Interferometry (II) technique is carried out in chapter 6. In particular, a new kind of observation based on II is explored; the method aims to estimate the direct distance of the celestial objects. The order of magnitudes of the problem parameters space and the sensitivity that CTA and other future large observatories should achieve is estimated by means of numerical simulations. A short-term concept of experiment to assess the reliability of this new method is also discussed in relation to a pilot measurement that could be pursued with the state of the art technology.

# Riassunto

Vi é un crescente interesse nella cominutá dell'astrofisica delle alte energie verso lo sviluppo di nuove infrastrutture di ricerca per rispondere alle questioni fondamentali della moderna astrofisica delle alte energie e della fisica delle astroparticelle. Il Cherenkov Telescope Array é un progetto internazionale che ha lo scopo di costruire due array separati per osservare l'intero cielo alle altissime energie tra 20 GeV e 300 TeV lungo un periodo di attivitá di almeno 30 anni. CTA é pensato per aumentare la sensibilitá di un fattore 10 ad 1 TeV, per allargare l'area di detection, la risoluzione angolare e il campo di vista rispetto ai telescopi attualmente operanti. L'osservatorio sará caratterizzato da un'elevata flessibilitá, potenziate capacitá di monitoraggio e survey profonde, osservazioni a piccole scale temporali e osservazioni simultanee in campi multipli. Questa tesi dottorato si concentra sullo studio del disegno ottico e dei test di un telescopio Cherenkov a due specchi per l'osservatorio CTA. Sebbene tutti i telescopi Cherenkov operanti oggigiorno, si basino su uno specchio singolo, perlopiú secondo disegni parabolici o Davies-Cotton, c'é un nuovo interesse nello sviluppo di configurazioni a due specchi secondo la configurazione Schwarzschild-Couder. Questo disegno peculiare, basato su due specchi altamente asferici definisce dei telescopi aplanatici con ampi campi di vista caratterizzati da f/# molto piccoli (sistemi molto veloci) e strutture piú compatte. Soluzioni a due specchi consentono l'uso di pixels piú piccoli ($\sim$ 3-6 mm) basati sulla tecnologia dei foto-moltiplicatori al silicio in sostituzione ai piú grandi tubi foto-moltiplicatori ($\sim$ 1 pollice) attualmente in uso. L'aumento di complessitá in termini di lavorazione delle ottiche, replica ed allineamento é motivato dalle promettenti, nuove, performance di questa configurazione. In questo contesto l'Istituto Nazionale per l'Astrofisica (INAF) supportato dal Ministero Italiano per l'Educazione, l'Universitá e la Ricerca (MIUR), sta sviluppando un telescopio di piccola taglia per CTA, chiamato ASTRI, e basato su un disegno ottico Schwarzschild-Couder. Il presente lavoro si confronta con la difficile realizzazione di questa configurazione ottica che non é mai stata applicata ai telescopi Cherenkov.
Dopo un capitolo introduttivo sull'astronomia gamma e sul disegno ottico di ASTRI (capitoli 1 e 2), le performance di questo sistema ottico sono comparate con quelle dei comuni telescopi a grande campo in uso per osservazioni Cherenkov e per altre applicazioni in astrofisica (capitolo 3). Successivamente nel capitolo 4, un'esteso studio delle caratteristiche e delle performance di ASTRI in relazione ai requisiti di performance e ambientali richiesti da CTA é presentato in una dettagliata analisi di compatibilitá supportata da simulazioni di ray tracing, analisi agli elementi finiti e studi di tolleranza. Nel capitolo 5 i test di qualifica dello specchio secondario danno una visione della complessitá delle ottiche Schwarzschild-Couder. La realizzazione di questo elemento ottico é difficile in relazione alle tecnologie esistenti e in particolare agli stretti vincoli di costo imposti dal progetto CTA. Questi vincoli e la grande sagitta dello specchio ($\sim$ 190 mm) richiedono l'uso della tecnica dello slumping a caldo in sostituzione dello slumping a freddo o della fresatura a diamante generalmente usati per la produzione di ottiche Cherenkov. I risultati di un'estesa campagna di test su alcuni prototipi di specchio ha accertato che questa tecnica di produzione puó supportare un affidabile processo di ingegnerizzazione per grandi specchi altamente asferici. Con uno sguardo alla scienza con i futuri grandi telescopi come CTA, é stato effettuato anche uno studio di valutazione sulle potenzialitá della tecnica dell'interferometria di

intensitá (riportato nel capitolo 6). In particolare, é stato investigato un nuovo tipo di osservazione basato sull'interferometria di intensitá; questo metodo si propone di stimare la distanza geometrica degli oggetti celesti. Gli ordini di grandezza dello spazio dei parametri del problema e la sensibilitá che CTA e altre grandi osservatori del futuro dovrebbero raggiungere sono stimati a mezzo di simulazioni numeriche. In questa cornice é anche discusso un possibile esperimento per testare la precisione del metodo con le attuali tecnologie a disposizione.

# Chapter 1

# The gamma-ray astronomy

Very high-energy photons are the most powerful probe for the astrophysics and fundamental physics in the non-thermal and extreme Universe. These messengers bring us information about the conditions undergoing in many extreme phenomena that cannot be reproduced in the laboratory. This branch of physics is a young and continuously developing field that in the past two decades has undergone a huge growth. Thanks to the advent of cornerstone space missions as the Fermi and AGILE satellites and the construction of ground-based Cherenkov telescopes, the gamma-ray astronomy has unlocked a completely new, unprobed window on the high-energy Universe. This chapter reviews the major milestones of this exciting field from the early beginnings until the current and future large infrastructures under development.

## 1.1 A multi messenger Universe

Until 1945, astronomy meant optical astronomy [90], that corresponds to a narrow band of the electromagnetic spectrum between 1 $\mu$m$\geq \lambda \geq$ 300 nm. In this waveband, that entirely contains the band where our eyes are sensitive (400-700 nm), most of the baryonic matter present in the Universe emits electromagnetic signals. The starlight in fact has a thermal distribution described by the black body model at temperatures between 3000 and 10000 K with an emission peak in the optical band. However a lot of astrophysical phenomena take place in other windows of the electromagnetic spectrum spanning the radio, infrared, ultraviolet, x-ray and $\gamma$ ray bands. A purely conventional quantitative definition of the different electromagnetic windows are reported in Table 1.1 below:

| **Waveband** | **Spectral extension** |
|---|---|
| **Radio** | 100 m $\geq \lambda \geq$ 1 cm |
| **Microwave** | 10 mm $\geq \lambda \geq$ 0.1 mm |
| **Infrared** | 100 $\mu$m $\geq \lambda \geq 1\mu$m |
| **Optical** | 1 $\mu$m $\geq \lambda \geq$ 300 nm |
| **Ultraviolet** | 4300 nm $\geq \lambda \geq$ 10 nm |
| **x-ray** | 10 nm $\geq \lambda \geq$ 0.01 nm, 0.1 keV $\leq E \leq$ 100 keV |
| $\gamma$ **ray** | $\lambda \geq$ 0.01 nm, $E \geq$ 100 keV |

Table 1.1: A standard subdivision of the electromagnetic spectrum [90].

The overall content of wavelengths of the Universe is dominated by the so called Comic Microwave Background (CMB) radiation, that originated from the Big Bang and its emission peaks at about $\lambda$ = 1.875 mm as shown in Figure 1.1a. This isotropic and diffuse radiation

plays an important role also in the detection of high-energy photons in the gamma domain as discussed in section 1.3.8.

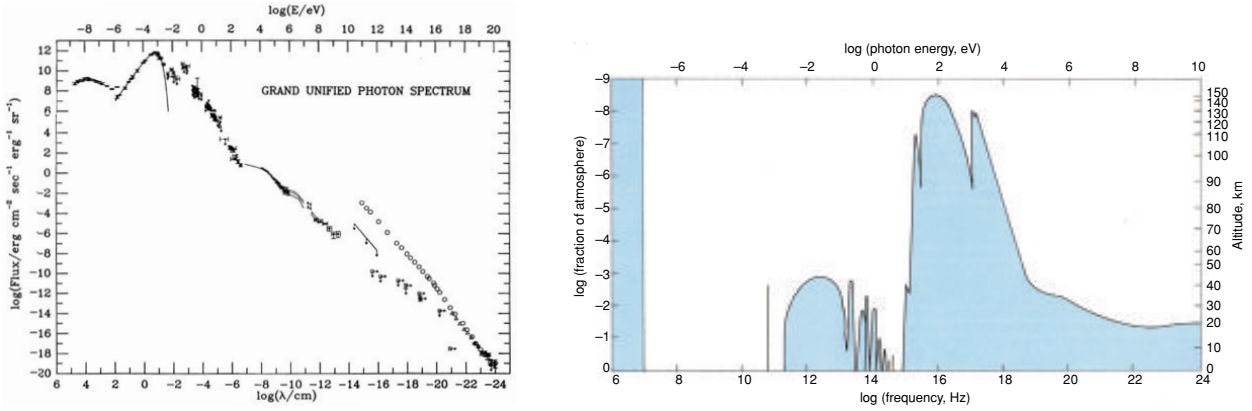


(a) (b)

Figure 1.1: (a) Average flux of diffuse extragalactic photons taken from M.T. Ressell & M.S. Turner [113], the maximum of the measured profile corresponds to the CMB emission peak. There is a double sequence of points beyond $10^{10}$ eV: the squares represent the $\gamma$ ray photons that reach the same energies of the particles cosmic rays indicted with the circles. (b) Atmospheric opacity: the sky-blue regions are opaque to radiation, while the solid line shows the altitude at which the atmosphere becomes transparent (attenuation factor 1/e) for different wavelengths. The high energy portion of the electromagnetic spectrum is completely unaccessible from ground-based observations. Picture from M. S. Longair [90].

Except for some sharp bands in the near infrared and a large window in the radio band the Earth's atmosphere is opaque to most of the infrared radiation and all the wavelengths beyond 320 nm as shown in Figure 1.1b. The source of opacity for the infrared radiation comes mainly from the absorption by molecules of water vapor and OH present in the atmospheric mixture, while the ultraviolet radiation is absorbed by ozone ($O_3$) molecules in the stratosphere. x-rays and low energy $\gamma$ rays are blocked by photoelectric processes with the molecules of the Earth's atmosphere while the Very High Energy (VHE) $\gamma$ rays undergo Compton scattering processes and electron-positron pair production (see section 1.3 for details). To observe the infrared, x-ray and $\gamma$ ray emission from the celestial bodies, balloons, sounding rockets and satellite are hence fundamental. The development of sounding rockets capable of carrying instruments outside the absorbing layers of the Earth's atmosphere made possible the discovery of the x-ray emission from sources outside the Solar System. In the 1962, R. Giacconi and his team were planning an experiment to study fluorescence x rays produced on the lunar surface by x-rays from the Sun and to explore the sky for other possible sources. The Aerobee rocket carried on-board a payload consisting of three large area Geiger counters (Figure 1.2a) that revealed considerable flux of radiation that was identified as consisting of soft x rays coming from a region of the sky where two peculiar objects - Cassiopeia A and Cygnus A - are located (Figure 1.2b) (Giacconi [50]). This important discovery, subsequently awarded with the Nobel prize (2002), and contemporary developments of ground-based experiments to detect $\gamma$ rays marked the birth of the high-energy astrophysics.

The nineteenth century saw the discovery of other cosmic messengers that are not electromagnetic signals. In the 1900 scientists noted that an electroscope isolated from any radioactive and ionizing source discharged progressively with time. The phenomenon was attributed to a sort of background radiation of unknown origin. About ten years later Victor Hess and Domenico Pacini independently carried out two revolutionary experiments on the nature of such radiation bringing to the discovery of the so called *cosmic rays*. Pacini performed a series of measurements to estimate the variation of the discharge velocity of an electroscope (and so the intensity of the radiation) when the instrument was immersed below the sea surface (see Figure 1.3a). He observed a progressively diminishing of the level of radiation and so a slower process of discharge

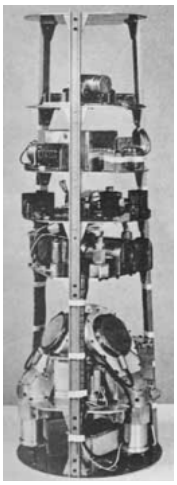

(a)

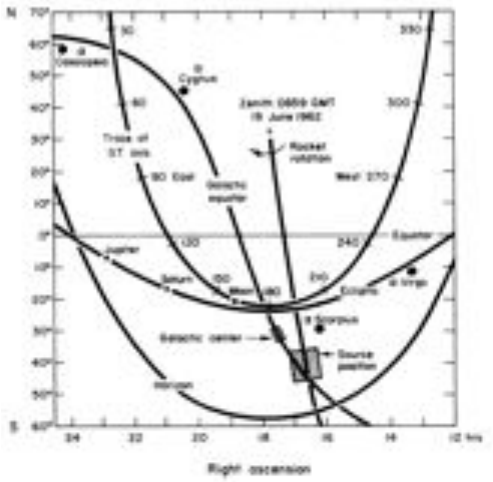

(b)

Figure 1.2: (a) The payload of the Aerobee rocket that flew on June 12, 1962, picture from Nobel prize lecture R. Giacconi, December 8, 2002. (b) Sky chart showing the portion of sky explored by the Aerobee counters that detected x-ray emission from Cassiopeia A and Cygnus A, from (Giacconi [50]).

of the electroscope (Pacini, D. 1912 [105]). Contemporary, Hess flew himself on board a balloon with a similar experimental apparatus up to an altitude of about 9 km (Figure 1.3b). He observed an increase of the average ionization (see Figure 1.4a) of the air that manifested as a quick discharge of the electroscope while the balloon was rising up into the atmosphere (Hess, V. 1913 [63]).

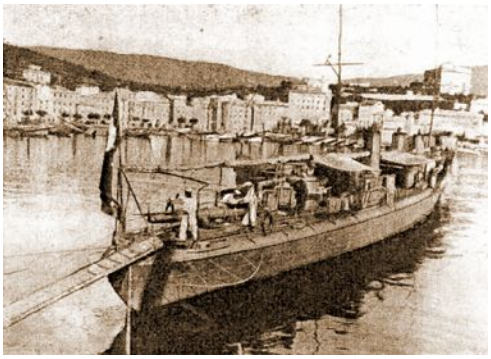

(a)

(b)

Figure 1.3: (a) The Fulmine boat that Pacini used to carry out the experiments with the electroscope by means of a box immersed in the water in front of the Livorno's harbor. (b) Hess's balloon used to expose the electroscope to the upper parts of the troposphere.

Both the experiment results proved the extraterrestrial origin of the the radiation that after subsequent observations with the cloud chamber was called cosmic rays. Today we know that cosmic rays are made of charged particles, protons ($\sim$90%), $\alpha$ particles ($<$ 10%), heavier elements and electrons ($<$ 1%) and photons with energy $>$ 1 MeV ($0.1-1$%) that for historical reasons are called $\gamma$ rays (A. De Angelis et al. 2008 [29]). The energy distribution of the cosmic rays spans more than 10 orders of magnitudes (see Figure 1.4b) and it is described by a power law with a spectral index slightly evolving with energy, in the range 2.5 - 3. Of particular importance is the presence of a *knee* at about $10^{15.5}$ eV in the energy distribution, that separates two different populations with different origins, galactic and extragalactic, respectively before and beyond this point [29].

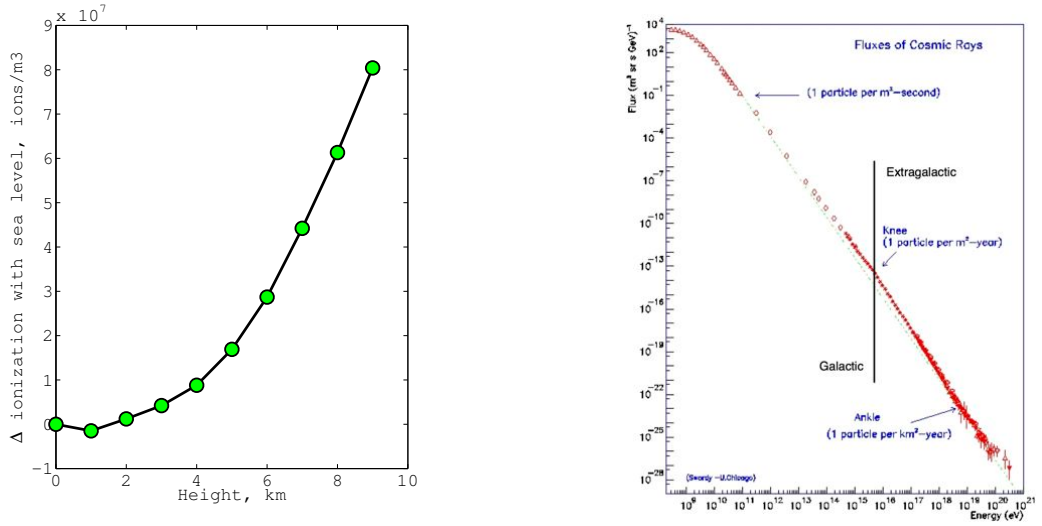


(a) (b)

Figure 1.4: (a) Measurements of the ionization level with respect to the sea level during balloon flights in 1913 (Kolhörster, [78]). (b) The energy distribution of the cosmic rays reaching the Earth covers more than 10 orders of magnitude. Cosmic rays above the knee ($10^{15.5}$ eV) are thought to be of extragalactic origin.

This interpretation is based on estimations of the strength of the magnetic field of our galaxy that shouldn't be able to trap particles of energies greater than the knee. The cosmic rays that invest the Earth (primary particle) enter the upper layers of the atmosphere and impact one of its atoms developing a cascade process, also labelled extensive air shower, of ionized particles and photons (secondary and tertiary particles) that reach the ground. Cosmic rays as well as VHE photons, are messenger of the violent Universe and their origin seems to be related to the acceleration processes inside shock fronts of the supernova remnants and of the others astrophysical sources where extreme processes develop. For more details on the production mechanism refer to section 1.5.

Among the most elusive particles permeating the Universe there are neutrinos. A large quantity of neutrinos (0.1<E<10 MeV) originates from nuclear fusion reactions inside the Sun and other stars. Neutrinos of solar origin were detected by Ray Davis and John Bahcall by a large tank filled of perchloroethylen in the Homestake mine (Bahcall 1989 [14]). Upon collision with a neutrino, a chlorine atom transforms into a radioactive isotope of argon, which can be detected by a Geiger counter. Also the core-collapse of a supernova releases a huge quantity of neutrinos ($\sim 10^{53}$) during the formation of the neutron star via the reaction $e^- + p \rightarrow \nu_e + n$. A total of 20 neutrinos from the SN 1987A were successfully detected by the Kamiokande and IMB observatories in about 10 s confirming the theoretical scenario (Hirata et al., 1987 [67]). In the Universe there should be also neutrinos of cosmogenic origin created via the interaction of a cosmic ray with a CMB photon by the reaction $p + \gamma \rightarrow n + \pi^+$, the cosmic ray disappears (pion decay) and a neutrino at $10^{18}$ eV and a muon appear: $\pi \rightarrow \mu + \nu_\mu \rightarrow (e + \nu_\mu + \nu_e) + \nu_\mu$. The first bunch of high-energy cosmic neutrinos (28 events between 2010-2012) was isolated by the IceCube Observatory (Halzen [55]) as shown in Figure 1.5b.

Although the cross-section of these particles is extremely small, neutrinos reach us from the edge of the Universe without absorption and with no deflection by magnetic fields and for this reason they are precious information carriers. After this short insight on the main characters of the high-energy and astroparticle physics, the next section (1.2) is entirely devoted to the pioneering experiments that led to the born of the $\gamma$ ray astronomy.

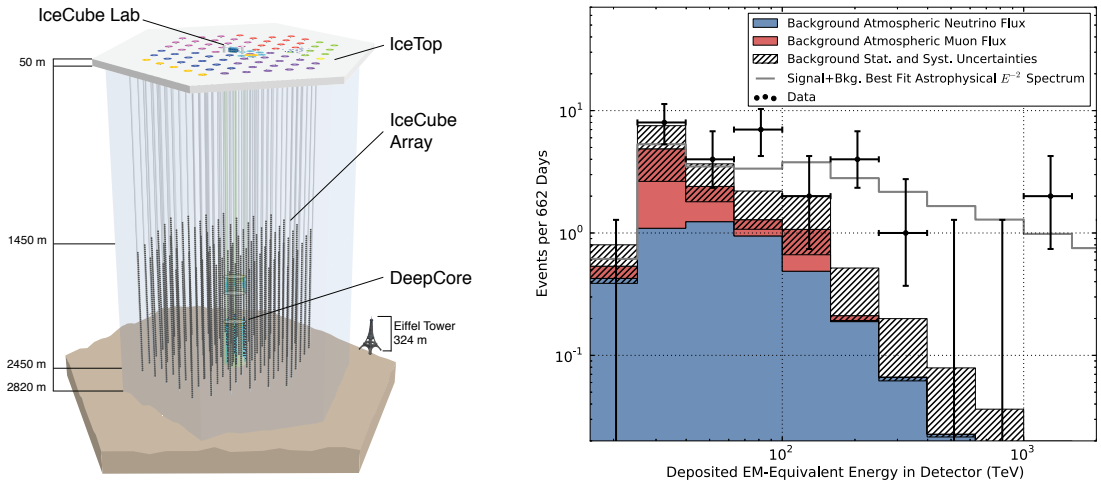


(a) (b)

Figure 1.5: (a) IceCube observatory exploits a cubic kilometer of Antarctic glacial ice that is extremely transparent to the Cherenkov light created by secondary charged particles produced in neutrino-nucleon interactions. The light bumps are detected by an array of 5160 digital optical modules. (b) Distribution of the deposited energies of suspected cosmogenic neutrinos, the energy associated to these events is too high to be produced by atmospheric neutrinos or muons [55].

## 1.2 The beginning of the gamma-ray astronomy

In 1900, the French chemist and physicist Paul Villard, discovered very high-energy radiation (E $>$ 100 keV), while studying radiation emitted from radium atoms. The name *gamma rays* was given by Ernest Rutherford soon after. The birth of gamma-ray astronomy cannot be conceived within a single episode, rather it is related to a series of revolutionary observations by many scientists that spent decades of their life in studying $\gamma$ ray related phenomena. Two different paths that proceeded independently, but almost contemporary and complementary, have led to the modern gamma ray astronomy: ground-based telescopes and satellites researches. Following the review of R. Mirzoyan [97] we will survey the main milestones of the gamma ray observations from the ground and subsequently the advances in VHE space science.
Of particular importance for the development of $\gamma$ ray ground-based observations is the discovery of the *Cherenkov* radiation. Marie Curie firstly noted, in 1910, a bluish faint light emitted by the bottles containing a solution of liquids and some radioactive compounds. She didn't give much importance to the phenomenon attributing the effect to a luminescence process. The phenomenon was then studied by Mallet that discovered the continuum spectrum of this radiation and excluded it from being a result of some luminescence processes. The task of studying this *new* light was given to Pavel Cherenkov by his supervisor Sergei Vavilov in 1932. Cherenkov carried out a series of crucial experiments by means of a very simple setup (shown in Figure 1.6a).

A cylindrical glass vessel was filled with different liquids (having different refractive indices). A collimated $\gamma$ ray beam from a radium sample was spatially filtered by lead shield with a 3 mm hole and traversed the glass vessel; the light emitted by the liquid was reflected by a conical mirror in an upward direction to the object glass of a photographic camera during a long exposure time (72 h) (Cherenkov [25]). Cherenkov discovered that $\beta$-particles and more generally electrons liberated into the liquid during scattering processes of the $\gamma$ ray created a bluish radiation that propagated mainly in the onward direction of the primary beam. On the photographic film a pattern with two diffuse maxima, symmetrical with respect to the primary beam was imprinted. Already Heaviside in 1889 pointed out that charged particles exceeding the speed of light in a medium could exist and he foresaw that this phenomenon should have been accompanied by a radiation pattern of conical shape. At the time of the Cherenkov's studies,

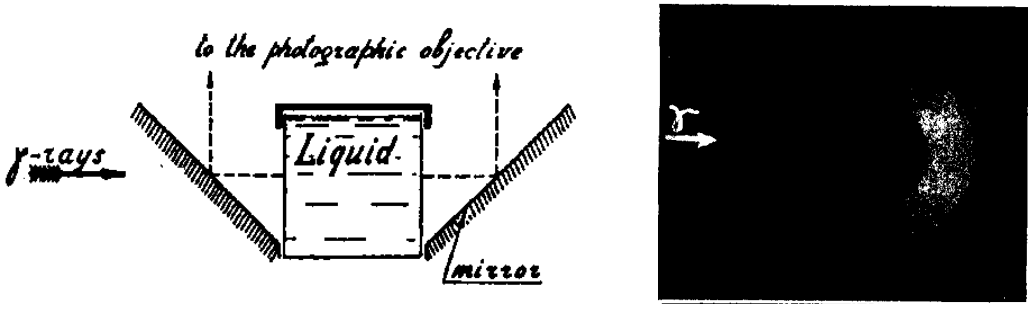


(a) (b)

Figure 1.6: (a) The $\gamma$ ray beam was shaped by a small hole in a lead shield and passed throughout the first mirror and the glass vessel containing the liquid. The superluminal electrons inside the liquid stimulated the emission of Cherenkov radiation that was reflected by the two mirrors toward a photographic camera. (b) The original footprint of the Cherenkov radiation recorded with the setup [25].

two theoreticians, Tamm and Frank, gave a quantitative explanation of the measurements by Cherenkov, proving that a charged particle moving in a medium with velocities exceeding that of the light perturbed and polarized the matter that subsequently was stimulated to emit a beamed radiation in the forward direction of the transiting particle (see section 1.4.3 for details). For this discovery Cherenkov, Tamm and Frank received the Nobel prize in 1956 and kicked-off a new technique of observation of the $\gamma$ rays. The physicist Patrick Blackett suggested to search for the possibility of detecting Cherenkov radiation induced by cosmic rays impinging the upper layers of the Earth's atmosphere. A few years later, in 1952, Jelley and Galbraith following this idea performed a simple but genial experiment by observing the sky simultaneously with a small optical telescope (10 inches in diameter) and an array of Geiger counters. The body of the telescope was a rubbish can (see Figure 1.7a) with a photo-multiplier tube (PMT) at the focus of the parabolic mirror. The basic idea of the experiment was that of observing simultaneous light pulses with the telescope and particle counts with the Geiger counters to prove the Blackett's theory. After having adjusted the trigger level of the PMT above the noise threshold of the sky background the experiment detected many light pulses directly correlated to the cosmic rays detection (see Figure 1.7b). They also estimated an average duration of the light pulses of about 0.2 $\mu s$ (Jelley and Galbraith [45]): the era of the IACTs was begun.

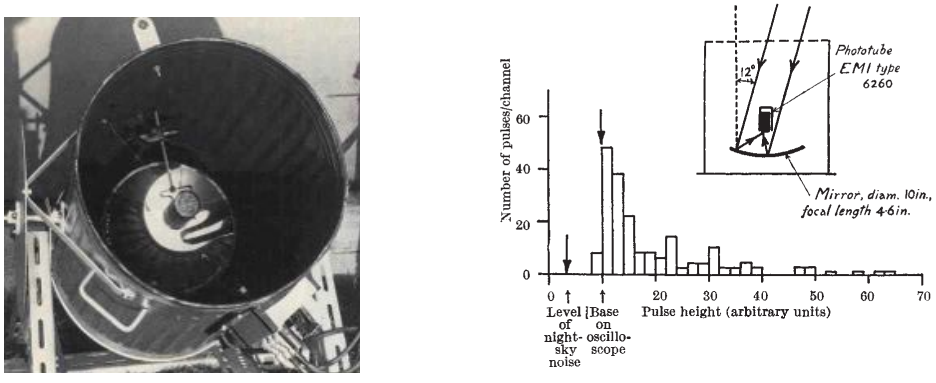


(a) (b)

Figure 1.7: (a) The optical telescope derived from a can was equipped with a PMT at its focus. (b) Light pulses recorded by the PMT with a correlated cosmic ray recorded by the Geiger counter.

In the decade of sixties Chudakov built up the first array of Cherenkov telescopes in Crimea by means of dismantled technology from the Second World War. The array was composed by 12 telescopes (1.55 m in diameter) equipped with PMTs and mounted on gunmounts dismissed

by the Army. The team observed a lot of suspected high-energy sources like the Crab nebula, Cygnus A and some other galaxies. The observations didn't retrieve any clear signal of detection but they contributed to point out some lower and upper limit in the threshold of detectability of these sources. The first photographic image of a Cherenkov air shower came in 1960 thanks to the work of HiIl and Porter. A great advantage came from the use of a wide-field, high-resolution Schmidt telescope coupled with an image intensifier. The system (shown in Figure 1.8a) had an image intensifier at the focus of the Schmidt telescope that was triggered by an auxiliary telescope + PMT. With this setup Hill and Porter were able to image for the first time a Cherenkov air shower as reported in their first photograph (Figure 1.8b) (Jelley and Porter [71]).

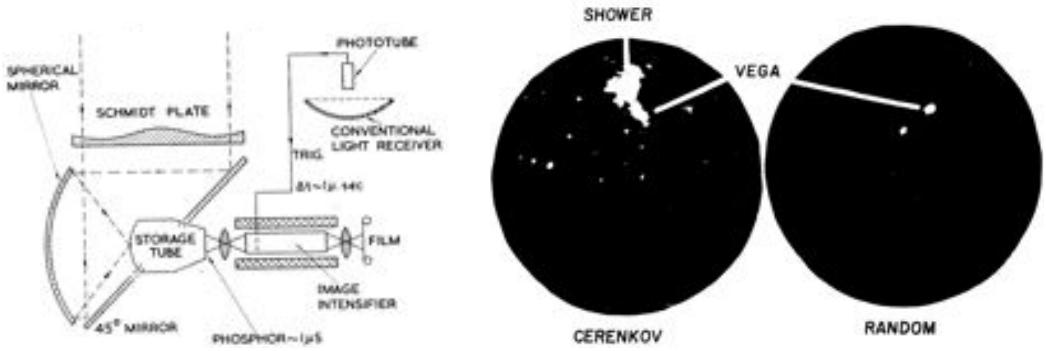


(a) (b)

Figure 1.8: (a) A conventional light receiver (spherical mirror + PMT) triggered an image intensifier at the focus of the Schmidt telescope. (b) Photographs taken with the image intensifier of a Cherenkov air shower and a random trigger of the sky within the same field. Images from (Jelley and Porter [71]).

With reference to Figure 1.8b, (left) a photograph from the image intensifier of a triggered Cherenkov air shower, the event has a comparable brightness with Vega, (right) image of the same field with a random trigger where only Vega is visible. With this system Hill and Porter were able to detect about 7 events/hour. Thanks to the advent of the first computers Victor Zatsepin understood that the maximum intensity of the light from a shower did not coincide with the direction of the primary particle and he pointed out the importance of observing the Cherenkov air showers from different points of view in a stereoscopic modality. In 1967, Giovanni Fazio and Trevor Weekes began the construction of a 10 m F/0.7 telescope at the Whipple Observatory [41]. The project underwent many upgrades until the final configuration with a 37-pixel imaging camera covering a field of view of 3.5°. The signal detection was optimized also thanks to a parametrization of the topology of the Cherenkov showers images elaborated by M. Hillas [65]. After about 20 years of attempts they succeeded in the observation of the Crab Nebula with a significance of $9\sigma$ in the TeV band (Weekes, T. C. et al. 1989 [138]). Considering the excellent agreement between theory and data (see Figure 1.9), the observation proved that the measured flux came from the hard Compton synchrotron spectrum of the nebula. This cornerstone experimental achievement is commonly assumed to be the birth of the ground-based VHE gamma astronomy.

Parallel to the ground-based observations a series of advances in the space satellite-based researches were going on. Explorer XI was an American satellite launched on April 27, 1961 that carried the first space-borne gamma-ray telescope detecting photons with energies $E > 100$ MeV. The mission duration was about seven-month and it detected twenty two events from $\gamma$ rays of extraterrestrial origin and thousands of events from $\gamma$ ray produced by the collision of cosmic rays with Earth's atmosphere. The detections were distributed isotropically in the sky with no evident anisotropies with the galactic latitude (Kraushaar et al. [83]). The first observations with

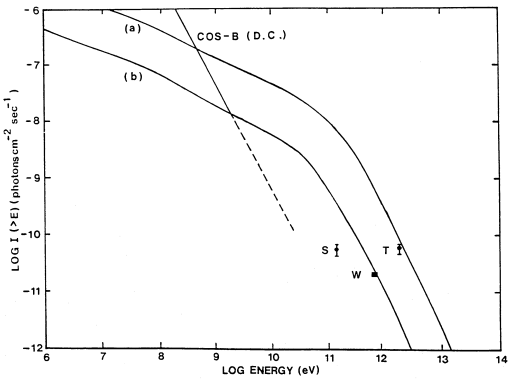


Figure 1.9: Solid lines: simulated Compton-scattered spectrum of the Crab Nebula for different values of the magnetic field $10^{-4}$ (a), $3 \times 10^{-4}$ G (b), measured points S (Fazio et al. 1972 [41]), T (Mukanov 1983 [99]), W (Weekes et al. [138]).

good directivity and sufficient angular resolution were carried out by the satellite OSO-3 during the years 1967-1968. The mission demonstrated the existence of a galactic component which is concentrated in a band around the galactic equator with a broad maximum toward the galactic center. It also showed the existence of an isotropic component with a softer energy spectrum probably of extragalactic origin (Kraushaar et al. [84]) (see Figure 1.10a). In the late 1960s the U.S. deployed the Vela constellation of satellites to detect possible gamma radiation pulses emitted by nuclear weapon tests in space by the URSS. On July 2, 1967, the satellites detected a flash of gamma radiation that was unlike any known nuclear weapon signature for time duration and shape profile. The pulse instead showed two distinct peaks in the light curve. The initial suspected sources for the production of the event, solar flares and new supernovas, didn't find any confirmation for that date. In years following (1969-1972), the Vela satellites detected about sixteen short bursts of photons in the energy range 0.2-1.5 MeV of duration between 0.1-30 s with a directional information that excludes the Earth and the Sun as sources (Klebesadel et al. [75]). Also scientists from the URSS, by means of the series of COSMOS satellites observed many of the gamma-ray events detected by the Vela constellation and in the end both countries agreed about the discovery of a class of new natural sources that was called gamma ray burst (GRB).

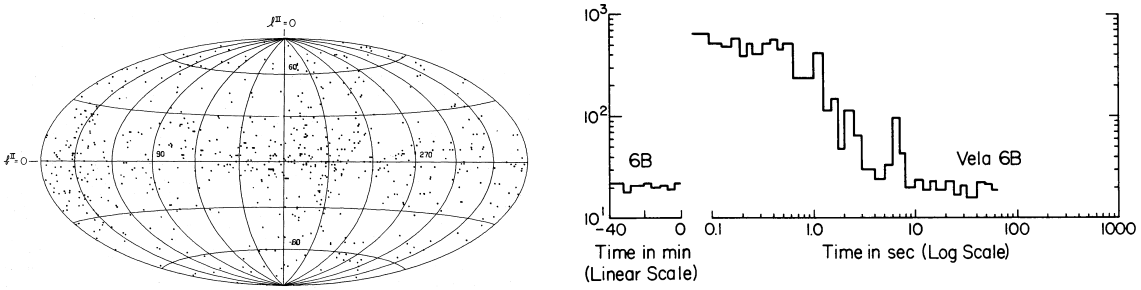


(a) (b)

Figure 1.10: (a) Celestial distribution of all gamma-ray events detected by OSO-3 satellite, picture from Kraushaar et al. [84]. (b) Count rate as a function of time for the gamma-ray burst of 1970 August 22; background counts are visible before and after the event, Picture from Klebesadel et al. [75] .

The number of satellites launched to study gamma ray emission from celestial bodies by all the countries is impressive: 22 missions in 1960s, 31 in 1970s, 11 in 1980s, 16 in 1990s and 4 in 2000s [149]. The cornerstone mission in this field that marked also the beginning of the modern era of such studies is the Compton Gamma Ray Observatory (CGRO) that operated for about

ten years since 1991. The satellite covered more than 6 order of magnitude in energy from 30 keV to 30 GeV and amongst its primary discoveries it proved the isotropic distribution of the GRBs, it mapped the entire Milky Way using the $^{26}Al$ gamma-ray line (Figure 1.11) and it discovered in the *blazar* AGNs the primary source of the highest energy cosmic $\gamma$ rays.

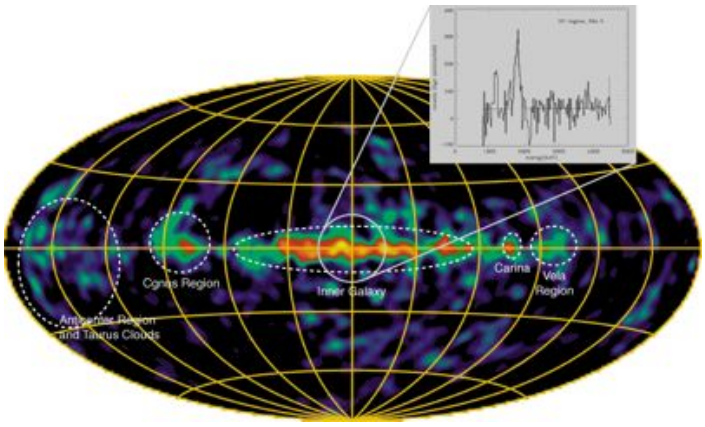


Figure 1.11: $^{26}Al$ CGRO/Comptel map of the Milky Way at an energy of 1.8 MeV that is the characteristic energy of the radioactive decay of aluminum isotope. This radioactive isotope is thought to originate primarily from nucleosynthesis in supernovae. Because gamma rays at these energies traverse the interstellar medium with negligible absorption, COMPTEL maps at 1.8 MeV provide an efficient way to trace sites of nucleosynthesis in the Galaxy [152]. Image courtesy from the COMPTEL Collaboration.

## 1.3 Processes of production and absorption for $\gamma$ rays

Differently from the other electromagnetic bands where a certain phenomenon can be explained by means of one or at least two different mechanisms, the gamma-ray window is characterized by many possible radiation mechanisms. So far, there are mechanisms of production of $\gamma$ rays like the Bremsstrahlung, the Synchrotron radiation, the inverse Compton scattering, the curvature radiation and the pion decay. The processes of absorption are the photoelectric effect, the Compton scattering and the pair production. The study of the cosmic $\gamma$ rays is extremely important because they are primary messengers of the non-thermal and violent Universe, they allow to infer the mechanisms of their production and acceleration and they also keep the signature of the physical properties of the environment they have traversed from the source to the observer. In the following subsections each of these processes is briefly discussed individually.

### 1.3.1 Bremsstrahlung

The Bremsstrahlung is a 'radiation breaking' that occurs whenever a fast-moving electron undergoes a Coulomb collision with an ion. This process is also called *free-free* because it is a transition between an unbound state of the electron to another unbound state (at different energy). If we consider a hot, completely ionized and optically thin plasma made of hydrogen at temperatures $10^7 - 10^8$K in thermodynamic equilibrium and moving at non-relativistic speed. In this condition the number density of the electrons is the same of the ions (protons, Z = 1) $n_e = n_i$. When an electron collides with an ion it is decelerated by the positive charge and part of its kinetic energy is converted into radiation (see Figure 1.12a). This fixes a maximum limit to the energy of the emitted photon, that cannot be greater than the kinetic energy of the electron, i.e. $\nu_{max} = \frac{mv^2}{2h}$. When an ensemble of electrons inside the plasma cloud is considered, the emission is integrated on the Maxwellian distribution of the particles velocities and it leads to an emissivity of the gas for Bremsstrahlung in the form of eq. 1.1.

$$j(\nu)d\nu \propto g(\nu, T, Z)Z^2 n_e n_i \frac{e^{-h\nu/kT}}{T^{1/2}} d\nu \tag{1.1}$$

The radiation spectrum derived is continuous, as shown in Figure 1.12b, and it is proportional to the number density of the particles and decreases exponentially towards high frequencies.

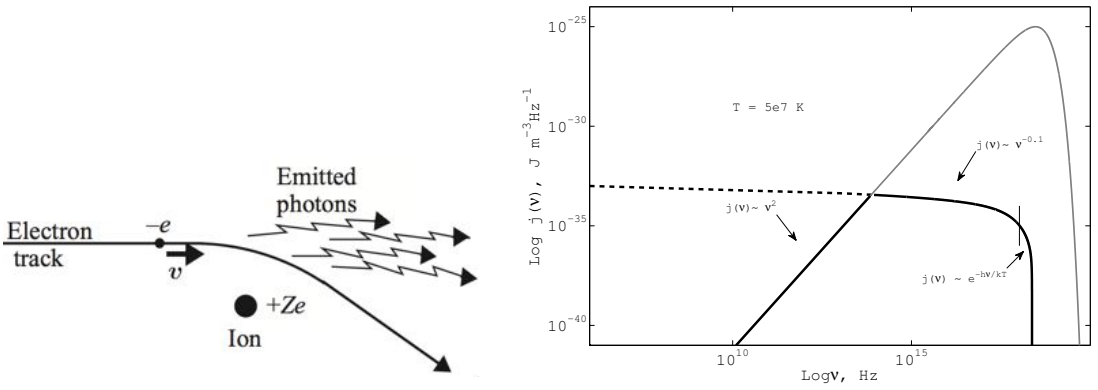


(a) (b)

Figure 1.12: (a) Free-free collision between an electron and an heavier ion that creates a deceleration responsible of the photon emission. Image taken from H. Bradt [18]. (b) Log-log plot of the emissivity of the plasma as a function of the frequency; the free-free spectrum is marked by the black solid line. The grey solid line refers to the black body model for the same temperature of the plasma cloud that describes the emission spectrum in the optically thick regime (Plot done with Matlab).

The term $g(\nu, T, Z)$ is the so called Gaunt factor that accounts for quantum mechanical corrections slowly varying with $\nu$. The Bremsstrahlung spectrum can be subdivided into three segments (from low to high frequencies): a Rayleigh-Jeans region ($j_\nu \propto \nu^2$) where the plasma is optically thick and it is described by the black body model, a rather flat ($j_\nu \propto \nu^{-0.1}$) intermediate region and an exponential decrease ($e^{-h\nu/kT}$) with a cut-off in correspondence of $h\nu = kT$. For increasing temperatures the cut-off moves towards higher frequencies while for increasing particles number densities the spectrum moves towards larger emissivity. This mechanism can explain the emission from hot cosmic plasmas up to the x rays. When the electrons are relativistic or ultra-relativistic ($v \sim c$), they obey to a power law (see section 1.3.2) instead of the Maxwell-Boltzmann distribution and they the collisions with the ions give origin to $\gamma$ ray.

### 1.3.2 Synchrotron radiation

One of the most important mechanism that can give origin to high-energy photons is the so called synchrotron radiation (e.g. in GRB prompt emission according to some models). The radiation emission is stimulated by an acceleration process like in the Bremsstrahlung scenario, but in this case the force is related to the magnetic field instead of the electric field. In the synchrotron scenario an electron spirally orbits around a magnetic field line and being accelerated by the Lorentz's force it emits photons. In the case of a non-relativistic electron the emission of radiation has a classical toroidal shape centered on the particle and the photons emitted have a monochromatic frequency equal to the gyration frequency of the electron around the magnetic field line. If conversely the electron is relativistic ($v \sim c$), the power spectrum of the radiation is polychromatic and it is increasingly broader as the electron is highly relativistic. Also the shape of the radiation pattern changes by a relativistic aberration effect that creates a head-on beaming of the radiation in a cone in the direction of the particle motion (see Figure 1.13a). The synchrotron radiation is also highly polarized. The spectrum of the radiation is directly related

to the energy spectrum of the electrons that are governed by a non-thermal distribution that can be expressed by power law as in equation 1.2.

$$N(E)dE = CE^P dE \tag{1.2}$$

$P$ is the spectral index of the particles that usually is in the range $-3 \leq P \leq -2.5$ and it depends on the environment where the particles have been produced. In a *log-log* plot the power law of the particles energy distribution is decreasing for increasing energies and consequently the power law describing the photons energy spectrum has the form:

$$j_\nu(\nu)d\nu \propto B^{1-\alpha}\nu^\alpha d\nu \qquad\qquad \alpha = \frac{P+1}{2} \tag{1.3}$$

with $B$, magnitude of the magnetic field accelerating the electrons. The spectral index $\alpha$ controls the steepness of the photons power law and in Figure 1.13b two distributions of electrons coming from two different environments (the Crab nebula and the intergalactic space) with different spectral indices are shown.

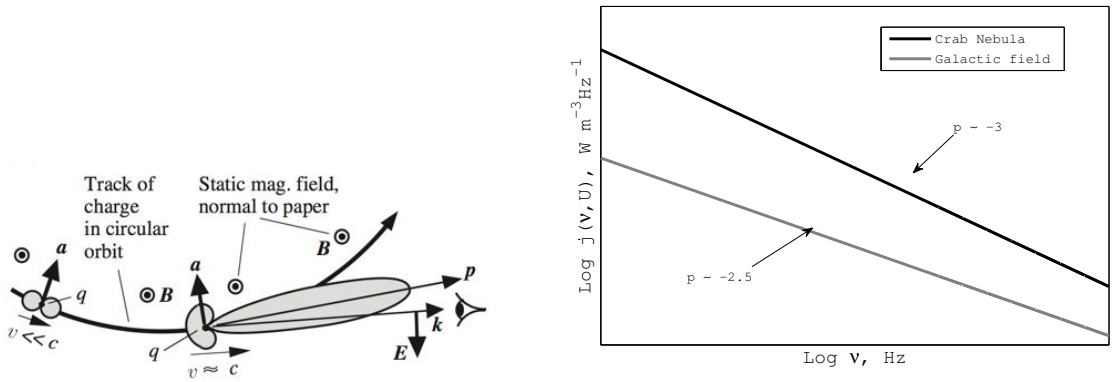


(a) (b)

Figure 1.13: (a) Schematics of the synchrotron radiation production for a non-relativistic particle ($v << c$) that orbits around a magnetic field exiting the paper and it shows the ordinary dipole radiation pattern and for a relativistic particle emitting a strongly beamed light cone in the direction of its motion ($v \sim c$). Image taken from H. Bradt [18]. (b) Log-log plot of the emissivity of a non-thermal ensemble of relativistic electrons as a function of the frequency; the black solid line is the spectrum for the electrons populating the Crab having a steep spectral index (P= -3) and being immersed in a magnetic field $B \sim 5e-8T$. The grey solid line refers to the electrons orbiting the galactic field (P = -2.5 and $B = 6e-10T$) that are less energetic than the previous and they produce a faint and less steeper radiation spectrum (Plot done with Matlab).

The radiation energy emitted by the orbiting electrons gradually depletes the kinetic energy of the particles. This phenomenon is much more pronounced as more the particle energy is high, but once the electron has lost part of its energy the rate of decay slows down. For instance the electrons at PeV scales in the Crab environment that produce VHE $\gamma$ ray photons have a lifetime of just 9 days [18].

### 1.3.3 Curvature radiation

The synchrotron radiation is emitted whenever a charged particle orbits a magnetic field line. The velocity vector of the particle ($\vec{v}$) can have any angle with respect to the magnetic field line ($\vec{B}$). If this angle is sufficiently close to zero, in the presence of a strong magnetic field (B = $10^4$-$10^5$ T) the particle follows the field line and orbits the compact source (originating the field) and it is stimulated to radiate photons. This phenomenon is called curvature radiation and it takes place mainly around a spinning neutron star. Since these objects have a physical size of about R = 10 km, the energy radiated by a single electron is smaller than in the synchrotron

scenario. However if the electrons are moving in clumps of particles grouped in a spatial cloud smaller than the emitted wavelength, the power of the coherent radiation outcoming can be boosted significantly and the emission falls in the GeV window.

### 1.3.4 Inverse Compton

The classical Compton scattering takes place whenever there is a collision process between a photon and a stationary electron. In this interaction the photon exchanges part of its energy with the electron that is accelerated and exits the collision with a certain angle of scattering (see Figure 1.14a.). The outcoming photon has a longer wavelength and the dependence of the wavelength shift with the scattering angle is given by equation 1.4:

$$\lambda_s - \lambda = \frac{h}{m_e c}(1 - \cos\theta) \tag{1.4}$$

the term $h/m_e c = 2.42 \times 10^{-12}$ m is called Compton wavelength. For an head-on collision the wavelength shift is null while it is maximum for $\theta = \pi$ as shown in Figure 1.14b.

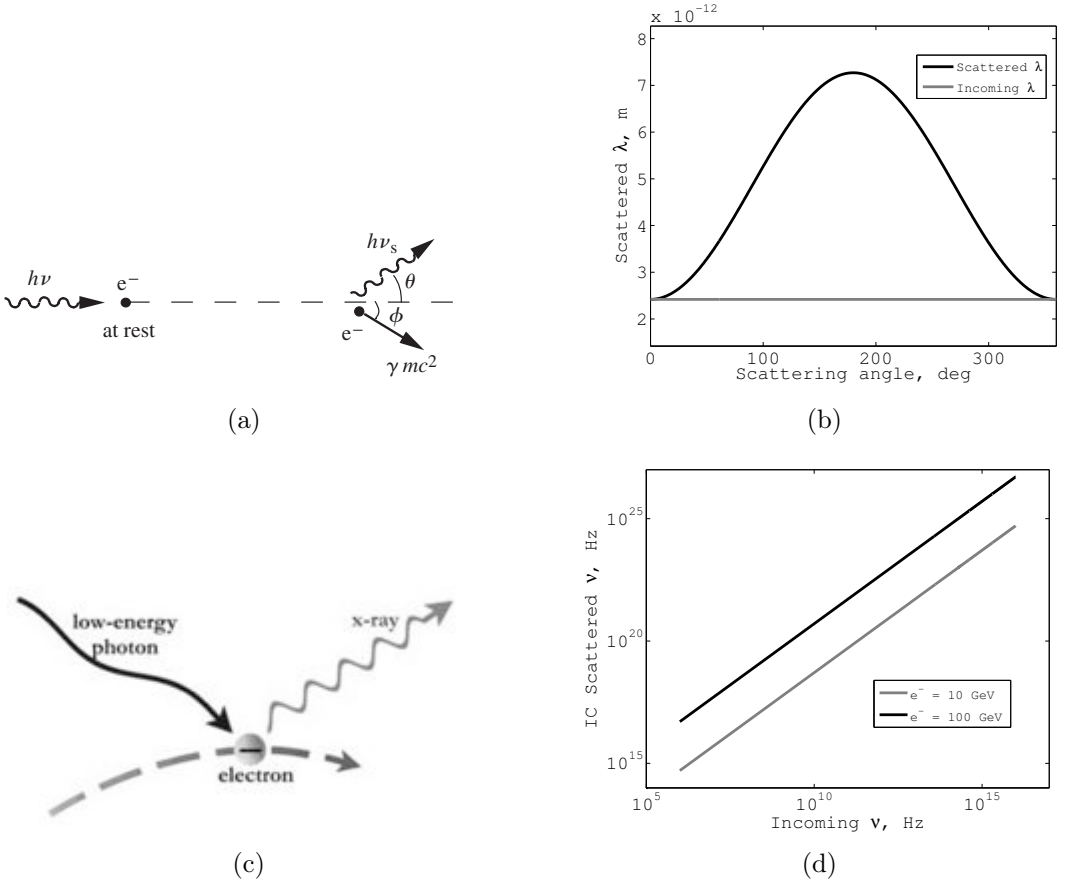


Figure 1.14: (a) Classical Compton scattering: a photon travels towards an electron at rest, collides and then delivers part of its energy to the particle that is scattered out under a certain angle, image taken from Bradt [18]. (b) Incoming (grey) and scattered wavelength shifted towards longer values, the maximum shift is for $\theta = \pi$. (c) Inverse Compton schematics: a relativistic electron collides with a photon and propels it towards VHE regime, image courtesy [150]. (d) Energy boost of the photons by means of IC effect induced by electrons of different energies; the higher the electron energy the higher the outcoming photon energy. Plots (b) and (d) done with Matlab.

If the electron instead of being at rest is moving at relativistic speed the Compton interaction is reversed and we get the so called Inverse Compton (IC). The IC effect occurs when a population of relativistic electrons collides with a photon gas (such as, for instance, the one originated by the

synchrotron mechanism). When the radio, infrared or optical photons have energies lower than the electrons energy distribution ($h\nu << m_e c^2$), in the collision with these relativistic particles they are boosted towards GeV-TeV scale (see Figure 1.14c). For an isotropic distribution of photons the modification in their frequencies after IC scattering is described by the relation:

$$\nu_s = \frac{4}{3}\gamma^2 \nu \tag{1.5}$$

The frequency boosting is caused by the term $\gamma^2$ ( $\gamma = U/m_e c^2$, kinetic over rest energy) of the electrons. A quantitative example of IC scattering is given in Figure 1.14d: electrons at GeV scales can transform radio photons at GHz to VHE at TeV. Provided that the plasma cloud is optically thin, the IC photons can leave the source and account for the observed GeV-TeV fluxes in the Spectral Energy Distributions (SEDs) of the VHE sources. The overall emissivity of a plasma cloud by IC scattering is given by equation 1.5 weighted on the photons and electron number density and electrons cross-section.

### 1.3.5 Pion decay

Another important source of $\gamma$ ray photons is provided by the pion decay. Pions are the lightest and unstable mesons and they are the carrier of the strong nuclear force. They are usually produced in the collision between hadrons. The process of interest for this context is the collision between cosmic rays and the hadrons in the cosmic matter (mainly gas). There are three types of pions: charged positive and negative $\pi^{\pm}$, and neutral $\pi^0$. The charged pions, with masses $m_{\pi^{\pm}} \sim 139.6 MeV/c^2$, have a short lifetime ($\sim$ 26 ns) and they decay by the following leptonic reactions : $\pi^{\pm} \rightarrow \mu^{\pm} + \bar{\nu_{\mu}}$ and $\pi^{\pm} \rightarrow e^{\pm} + \bar{\nu_e}$. The neutral pions, that have masses $m_{\pi^0} \sim 135$ MeV and a lifetime of $8 \times 10^{-17}$ s, undergo electromagnetic decay by the emission of high-energy $\gamma$ rays:

$$\pi^0 \rightarrow \gamma + \gamma \tag{1.6}$$

$$\pi^0 \rightarrow e^+ + e^- + \gamma \tag{1.7}$$

Decay 1.6 is the preferred channel (99%). Pion decay together with the IC scattering is among the most efficient mechanisms of production for the $\gamma$ ray radiation. In the next sections the main mechanisms of absorption of $\gamma$ ray radiation are presented.

### 1.3.6 Compton scattering

The Compton scattering is the process by which an incoming high-energy photon collides with an electron at rest and transfers part of its energy and momentum to the electron. See the first part of section 1.3.4 for details.

### 1.3.7 Photoelectric effect

One of the main mechanism of absorption of high-energy photons by the atoms of the matter is the photoelectric effect. In 1905 Albert Einstein explained the photoelectric effect using the Planck's hypothesis which states that the energy of light is quantized into the photons. At relatively low energies ($h\nu << m_e c^2$), if the photon energy is greater than the binding energy $E_b$ of an electron into a certain atomic shell the particle is freed from the attractive force of the nucleus and it is ejected with a kinetic energy, ($h\nu - E_b$). This process dominates the photons absorption interactions for energies below 100 keV (x ray).

### 1.3.8 Pair production

The most important absorption mechanism for the VHE radiation in the Universe is given by the photon-photon ($\gamma\gamma$) interactions (Nikishov [102]) that leads to the pair production of matter and anti-matter particles via the interaction:

$$\gamma + \gamma \rightarrow e^+ + e^- \tag{1.8}$$

The $\gamma$ ray photons interact with the galactic and extragalactic cosmic background photons that permeate the space-time of the Universe. This background radiation is called extragalactic background light (EBL) and it is the integrated mean surface brightness of the sky due to resolved and unresolved by galactic and extragalactic sources in all the wavebands of the electromagnetic spectrum from all the cosmic epochs. The cosmic radio background radiation accounts for a small contribution to the EBL and it is described by a power law; the cosmic microwave background (CMB), that is the fossil radiation from the cosmological last scattering surface is the predominant source of the EBL ($\sim$ 400 photons/cm$^{-3}$) and it is a perfect black body at 2.725 K. The infrared background is mainly due to re-emitted starlight by dust grains, galactic cirrus, cold stars and zodiacal light, while the optical and UV backgrounds are directly related to stellar and AGNs emission. The x-ray background is well resolved into discrete sources while the $\gamma$ ray background detected by the Fermi-LAT is mainly diffuse and probably associated to the interactions of the cosmic rays with the interstellar medium [3]. The cumulative emission from the EBL is shown in Figure 1.15.

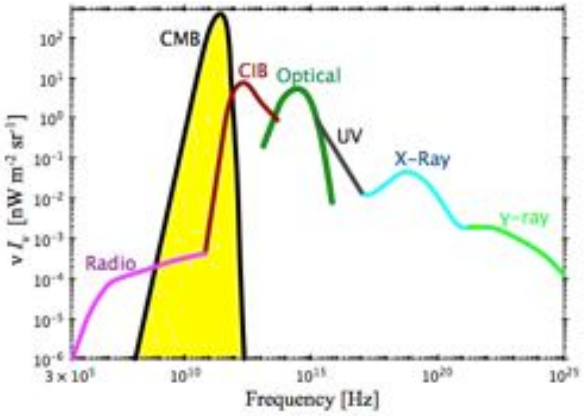


Figure 1.15: Extra galactic background light, with the predominant CMB contribution put on evidence, photo courtesy Dole and Bethermin.

Depending on the energy of the $\gamma$ ray there are different resonant target photons for the pair production process (see Table 1.2). The Universe has so far different opacity to the VHE photons directly related to their energy and to the photons number density of the EBL. For instance the VHE photons suffering strong absorption by the abundant CMB photons are those at E $>$ 160 TeV. The optical depth that defines the cosmic opacity for photons at a certain energy emitted by an extragalactic source at redshift $z_e$ is given by the equation:

$$\tau(E_\gamma, z) = c \int_0^{z_e} dz \frac{dt}{dz} \int_0^2 dx \frac{x}{2} \int_{\frac{2m_e c^4}{E_\gamma e x(1+z)}}^{\infty} d\epsilon \frac{dn_\gamma(\epsilon, z^*)}{d\epsilon} \sigma_{\gamma\gamma}(\beta) \tag{1.9}$$

with $n_\gamma(\epsilon, z^*)$ number density of EBL photons at a given redshift and energy and $\sigma_{\gamma\gamma}(\beta)$ cross-section of the opacity for pair production $\gamma\gamma$.

| $E_\gamma$ | $\lambda_{EBL}$ | Waveband |
|---|---|---|
| $<$ 8 GeV | $<$ 10 nm | X rays |
| 8-300 GeV | 10-390 nm | UV |
| 300-600 GeV | 390-750 nm | Optical |
| 600 GeV-1TeV | 750 nm-1.2 $\mu m$ | NIR |
| 1-20 TeV | 1.2-25 $\mu m$ | MIR |
| 20-160 TeV | 25 $\mu m$-1 mm | FIR |
| $>$160 TeV | $>$1 mm | Microwaves |

Table 1.2: Maximum absorption of GeV and TeV photons by different EBL components. Table taken from C. Schultz [118]

The behavior of the optical depth for different energies of the incoming photons for different redshifts has been estimated many authors, here the work by A. Franceschini et al. [44] is shown in Figure 1.16a. It is common to define a $\gamma$ ray horizon in correspondence of $\tau = 1$, i.e. when the flux from the source is attenuated by a factor 1/e. The $\gamma\gamma$ opacity heavily depletes photon flux above 100 TeV while it is moderate in the range between GeV and 100 TeV because of the less abundance of targeting photons in UV-optical-IR. This depletion leaves a clear signature on the spectra of the TeV sources that are progressively eroded as their redshift increases (see Figure 1.16b). The $\gamma\gamma$ opacity is strongly dependent on the estimation of the EBL number density that is very difficult to assess in some wavebands.

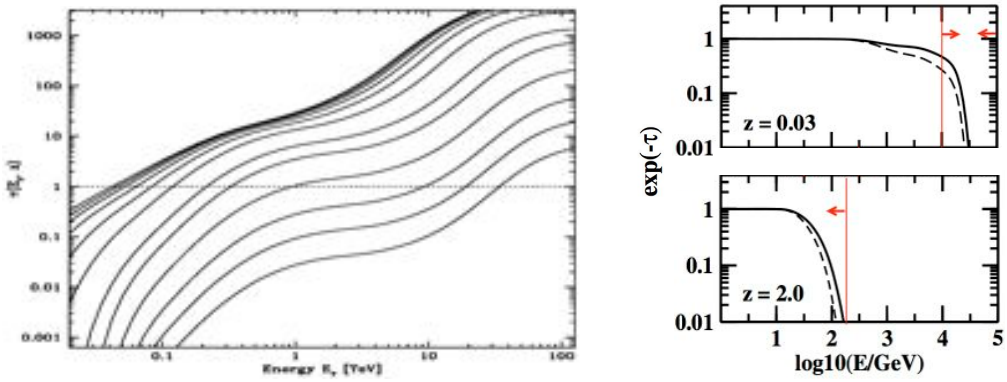


(a) (b)

Figure 1.16: (a) Optical depth for $\gamma\gamma$ absorption for different photons energies at z = 0.003, 0.01, 0.03, 0.1, 0.3, 0.5, 1, 1.5, 2, 2.5, 3,4 from bottom to top; sources above 100 TeV are almost entirely absorbed for every z. Image taken from Franceschini et al. [44]. (b) Simulated extinctions factors for TeV AGNs at different redshifts. The TeV band for a source at z = 2 is completely unaccessible to observation, image taken from Kneiske and Dole [77].

Several models foresee that TeV photons are severely absorbed by the EBL, even if a strong experimental evidence in favor of an anomalous transparency in excess of expectations of the Universe recently came up [127]. Observations of the source 3C 279 (z = 0.536) from 80 to $>$300 GeV, by MAGIC telescope imply a low amount of EBL at higher redshift, supporting the conclusion drawn from earlier measurements by the Hubble Space Telescope and Spitzer that correctly estimate most of the light sources in the Universe. The observations of this distant source in VHE gamma rays demonstrate that a large fraction of the Universe is accessible to VHE astronomy (The MAGIC Collaboration [127]).

### 1.3.9 SSC model

Particularly important for the interpretation of the the VHE sources SED is the Synchrotron-Self-Compton (SSC) mechanism. As discussed in section 1.3.2, relativistic electrons immersed in a magnetic field emit synchrotron radiation. If the photons number density is sufficiently high, the radiation can be up-scattered to higher energies via IC process by the same population of relativistic electrons. The SSC mechanism is responsible for the presence of two well defined peaks in the SED of many galactic and extragalactic VHE sources. The first peak, that can extend up to 40 MeV (see Crab nebula in Figure 1.21a) is rather robustly associated to the synchrotron mechanism, while the second peak that can reach the TeV domain is widely believed to be produced by IC scattering of the synchrotron photons even if different interpretations involving hadrons are not ruled out by observations yet. Following the textbook by Bradt [18], to produce $\gamma$ rays up to 40 MeV electrons with energies $\sim 10^{15}$ eV are required. With a Lorentz factor of $\gamma = U/m_e c^2 = 2 \times 10^9$ and $\gamma^2 = 4 \times 10^{18}$ eV, the electrons can IC scatter the radio photons of $10^9$ Hz up to $\sim 10^{27}$ Hz. The combination of the two processes give rise to a quick loss of energy into radiation, where contributions of syncrothron and IC to the cooling are regulated by the ratio $\frac{u_{ph}}{u_B}$ of the magnetic and radiation energy densities within the emitting region.

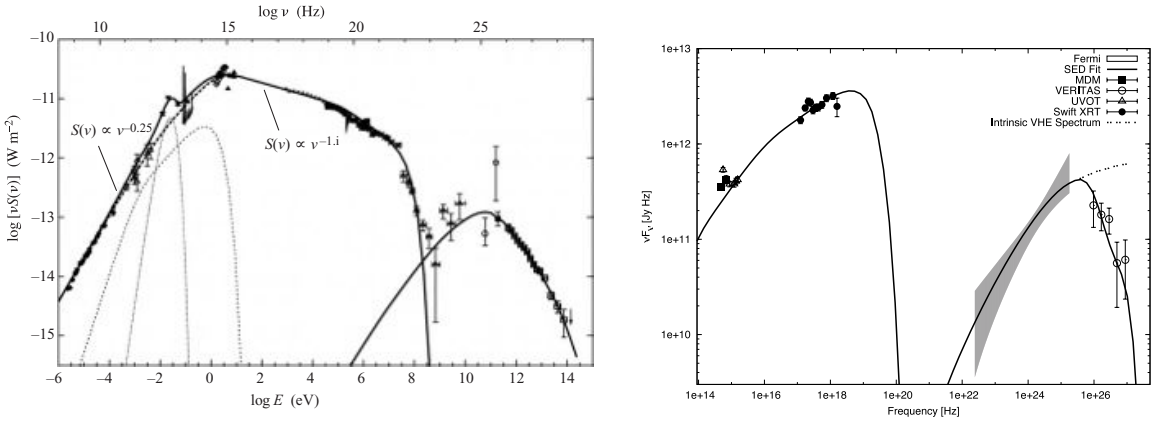


(a) (b)

Figure 1.17: (a) SED of the Crab nebula over 19 decades of frequency reaching from the radio to TeV gamma rays. The solid lines are a fit to the data for SSC model for a nebular magnetic field of 16 nT. Image taken from Aharonian et al. [5]. (b) Broadband SED of RGB J0710+591. The closed squares are R- and B-band data from the MDM 1.3 m telescope; the open triangles are from the Swift UVOT; closed circles are from the Swift XRT; the shaded area is the Fermi LAT measurement; the open circles are the measured VERITAS data. The broadband spectral model is the equilibrium SSC version. Note that the optical measurements (MDM and Swift u, b and v bands) are contaminated by emission from the host galaxy and are thus not used in the SED fit. The SED model curve includes EBL absorption using the model of Franceschini et al. (2008) [44], and the dashed line is the de-absorbed VHE spectrum. From the work of Acciari et al. (2010) [2].

These objects show intrinsic variability at hours-days and shorter timescales, as demonstrated by the observation of objects like Mrk421 by Gaidos et al. (1996) [46] and IC310 by the MAGIC Collaboration (2014) [128]. This extremely rapid variability requires repeated quasi-simultaneous observation in multi-bands from radio to TeV. Usually an enhancement of synchrotron radiation is followed by an increase in the IC peak flux. Concerning the AGNs, and in the specific Blazars (see section 1.5 for details), there can be two different SSC spectra depending on the overall energy content of these objects: low energy blazars (LBL) with emission extending from radio to gamma ray ($\sim$ GeV) and high energy blazars (HBL), as RGB J0710+591 (Figure 1.21b), that show emission at TeV, but are quiet in the radio. The best-fit SSC model allows to estimate also the magnetic field in which the source is immersed.

## 1.4 Methods of detection

The detectors observing the gamma ray sky operate in a photon-starved regime. The statistics of gamma ray photons is very poor and it is impossible to concentrate the photons, which leads to telescopes radically different from the ones dedicated to observations of larger wavelengths [29]. The detection techniques can be subdivided into two main categories: satellites or ground-based detectors (see Figure 1.18).

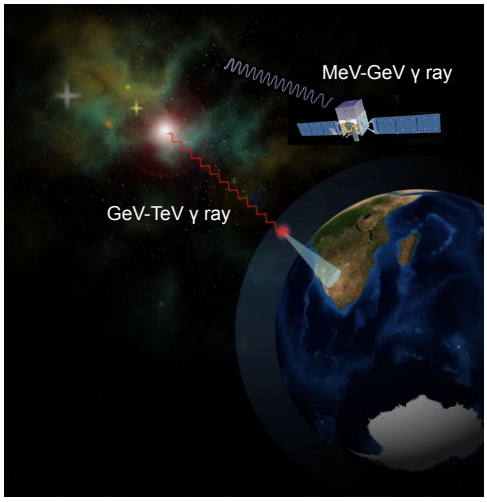


Figure 1.18: Gamma-ray photons can be observed from space by satellite-based detectors observing in the MeV-GeV domain or by ground-based detectors observing the GeV-TeV spectral window. Image adapted from [148].

There are cons and pros between the two methods as summarized in Table 1.3. The satellite observatories have a very limited effective area ($A_{EFF}$) and a low sensitivity, but they have a large duty cycle and a low background. Conversely ground-based detectors have large effective area and consequently a high sensitivity, but they have also a low duty cycle and they suffer a high background. Space observatories are characterized by extremely high costs while those of ground-based detectors are orders of magnitude lower. There is however a most important difference between the two approaches which is represented by the energy window they can observe: satellites observe in the MeV-GeV range, while ground-based detectors can detect photons with energies between GeV to TeV. Best results can be achieved if the two techniques are operated in synergy to provide a huge spectral energy coverage. An example of this important synergy comes from the cross calibration between IACTs and HE satellites through the observation of the Crab Nebula [94].

| **Satellites** | **Ground-based** |
|---|---|
| Small $A_{EFF} \sim 10$ m$^2$ | Huge $A_{EFF} \sim 100 - 600$ m$^2$ |
| Low sensitivity | High sensitivity |
| Large duty cycle | Low duty cycle |
| Low background | High background |
| High cost | Low cost |
| MeV-GeV | GeV-TeV |
| Large FoV | Small FoV (IACTs), Large FoV (EAS) |

Table 1.3: Gamma-ray Universe can be observed by means of satellites observatories or ground-based detectors. The approaches have different relative advantages/disadvantages.

In the following sections 1.4.1 and 1.4.2 the two techniques are discussed more in detail separately.

### 1.4.1 (V)HE satellites

From the legacy of the past gamma-ray satellites (section 1.2), a family of HE and VHE observatories is operating today under the direction of many space agencies. Following a chronological order, Swift is certainly one of the most important NASA space multi-wavelength observatories (gamma-ray, X-ray, UV and optical) with about 100 GRBs discovered per year since its launch in 2004. Swift is able to recognize the position of the GRB with 0.5-5 arcsec precision, providing also spectroscopic observations from 180-600 nm and 0.3-150 keV and especially triggering ground-based IACTs for the observation of prompt or afterglow phases of these events. A small, but successful Italian mission is AGILE, which is a space borne observatory sensitive to the energy range between 30 MeV and 50 GeV. It was launched in April 2007 and it discovered temporal flux variability in many sources and about a dozen of pulsar emitting at the GeV scale. The design of AGILE was inherited from the experience of the EGRET instrument on board of the CGRO. The state of the art of gamma-ray satellites is represented by Fermi (originally Gamma-ray Large Area Space Telescope, GLAST), which is the result of a common effort by many countries under the leadership of NASA. The mission began operations in the June 2008 and its spacecraft bus hosts the most sensitive instrument ever built in the range 20 MeV-300 GeV, the Large Area Telescope (LAT). The detection scheme of $\gamma$ rays inside the LAT is based on the conversion of the photon to an $e^+e^-$ pair into a series foils of Tungsten. Subsequently, the charged particles are tracked by planes of Silicon, that reconstruct the direction of the photon, until they are absorbed by a calorimeter and their energy is measured. Above 1 MeV, the dominant absorption mechanism of $\gamma$ rays is the pair production as shown in Figure 1.19. The effective area of the LAT is $\sim$1 m$^2$, which improved of about two orders of magnitude the area of EGRET, while its field of view is $\sim$2 sr.

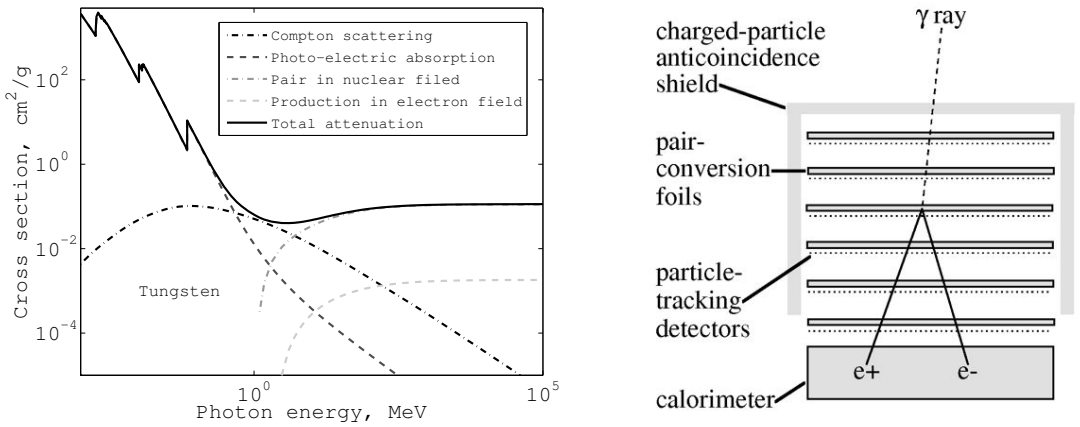


(a) (b)

Figure 1.19: (a) Gamma-ray cross-section inside the Tungsten for different absorption and scattering phenomena, the overall contribution is traced by the black solid line. Plot done with Matlab based on the cross-section database provided by the XCOM software [153]. (b) Working principle of the LAT onboard of the Fermi satellite, image from [147].

Despite the high duty cycle and the privileged view on the Universe of the space observatories, the high costs and the relatively short lifetime motivate the construction of also ground-based detectors. Moreover, to probe the VHE scale ($\sim$TeV domain) satellite are rather inefficient in terms of effective area and $\gamma$ stopping power[1]. For this reason a series of ground-based detectors

[1]This drawback should be mitigated in the future satellite mission Gamma-400 [129]

that observe the products of the interaction of the primary $\gamma$ ray with the Earth atmosphere have been recently developed as discussed in section 1.4.2.

### 1.4.2 Ground-based detectors

Ground-based detectors are divided into two main categories: Imaging Air Cherenkov Telescopes (IACTs) and Extensive Air Shower (EAS) detectors. Both the techniques rely on the observation of particles and photons from the interaction of the primary $\gamma$ ray with the upper layers of the troposphere. In the $\gamma$ ray ground-based observations, the atmosphere is a part of the detection system and the processes of interaction of HE and VHE photons with the atmospheric air mixture are shown in Figure 1.20.

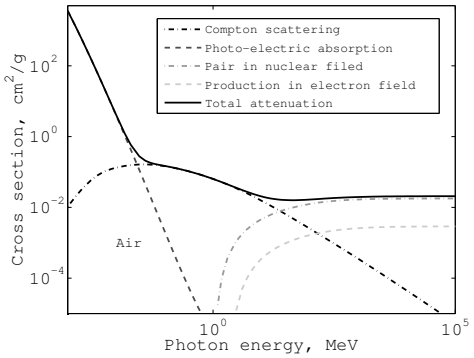


Figure 1.20: Gamma ray cross-section inside the air mixture for different absorption and scattering phenomena, the overall contribution is traced by the black solid line. Plot done with Matlab based on the cross-section database provided by the XCOM software [153].

Above E ∼50 GeV the production of atmospheric electromagnetic showers by primary $\gamma$ rays is dominated by the pair production and bremsstrahlung mechanisms that alternate consecutively as shown in Figure 1.21 (a, left). The showers originated from hadronic primary particles are in general wider and subjected to larger fluctuations with respect to the electromagnetic showers, Figure 1.21, (a, right).

### 1.4.3 Cherenkov radiation

While the history of the Cherenkov radiation discovery has been discussed in section 1.2, here we concentrate on the physics of the phenomenon and the main characteristics of the Cherenkov air showers in relation to the observation with the IACTs.
In a quantum mechanical picture, when a charged particle moves inside a polarizable medium, it excites the molecules to the higher levels. Upon returning back to their ground state, the molecules re-emit some photons in the form of electromagnetic radiation. According to the Huygens principle, the emitted waves move out spherically at the phase velocity of the medium. If the particle motion is slow, the radiated waves bunch up slightly in the direction of motion, but they do not cross. However if the particle moves faster than the phase speed of light in the medium, it sets up an electromagnetic shock and the emitted waves add up constructively leading to a coherent radiation at angle $\theta$ with respect to the particle direction, known as Cherenkov radiation (see Figure 1.22). The effect is analogous of the sonic boom in the air caused by the pass of a supersonic aircraft or missile. The signature of the effect is a cone of emission in the direction of particle motion [154].

With reference to the geometry in Figure 1.23a, calling $\beta = v/c$ the ratio between the particle and the light speed, $\Delta t$ the time of flight of the particle and $n$ the refractive index of the medium,

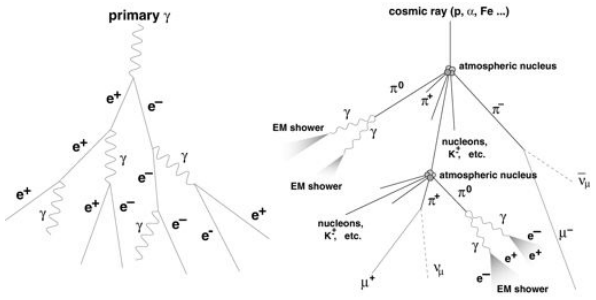


(a)

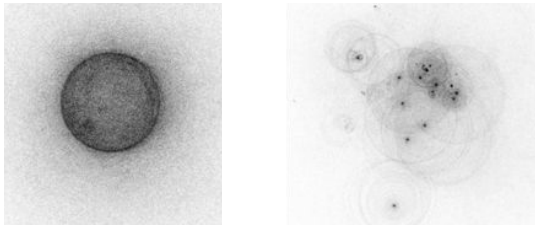

(b)

Figure 1.21: (a) Illustration of the propagation scheme of an atmospheric shower initiated by a $\gamma$ ray (left) and a cosmic ray (right). Image from [137]. (b) Simulation of the light pool on the ground for an electromagnetic shower (left) and a cosmic ray shower (right), image from [68].

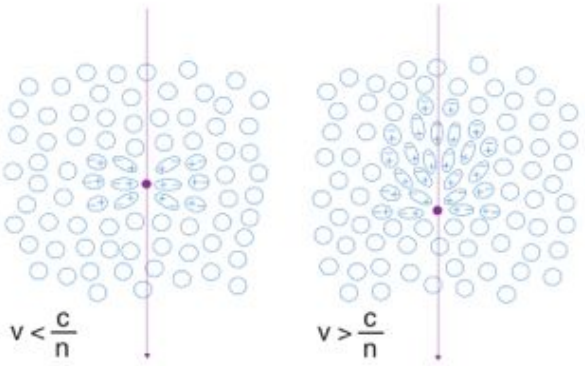


Figure 1.22: Left: polarization of a dielectric, refractive medium by a slowly moving charged particle (purple arrow), no anisotropies are observed in the pattern. Right: polarization effect of a fast moving charged particle, superluminal in the medium, that causes the emission of a coherent radiation called Cherenkov radiation. Image from C. Schultz [118].

the Huygens principle can be applied to retrieve the angle for which the wavefronts are added coherently to create Cherenkov radiation.

$$\frac{c}{n}\Delta t = \beta c \Delta t \cos\theta \qquad \rightarrow \qquad \cos\theta = \frac{1}{\beta n(\lambda)} \tag{1.10}$$

For a medium of a given refractive index $n$, there is a threshold velocity $\beta_{min} = \frac{1}{n}$, below which there is no emission of radiation. At this critical velocity the direction of radiation coincides with that of the particle. On the other hand, for an ultra-relativistic particle, ($\beta = 1$), there is a maximum angle of emission, given by $\cos\theta = \dfrac{1}{n}$. A real medium is always dispersive ($n > 1$), so actually radiation is restricted to those wavelengths for which $n(\lambda) > \frac{1}{\beta}$. Conversely in the X-ray domain $n(\lambda)$ is always $< 1$ and radiation is forbidden. The cone angle of the Cherenkov radiation depends on the speed of the particle and the refractive index of the medium: in air at

standard temperature and pressure eq. 1.10 gives $\theta \sim 1°$. The cone angles in water and ice are wider, about $\theta \sim 40°$ as shown in Figure 1.23b.

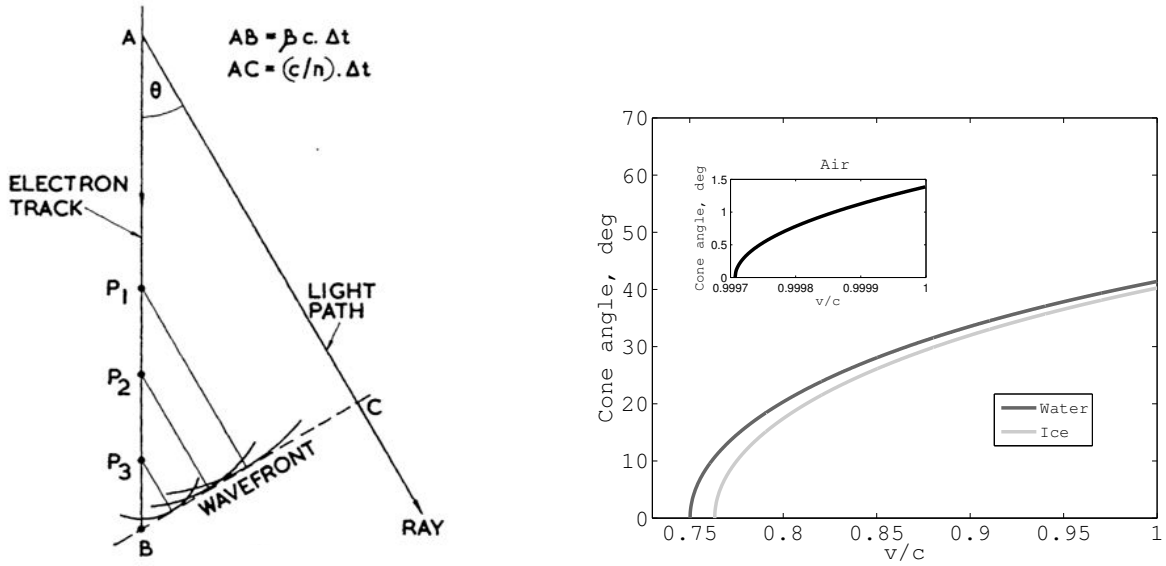


(a) (b)

Figure 1.23: (a) Geometry of the Cherenkov emission: the wavefronts from the polarized molecules combine coherently for a well defined angle $\theta$. The overall envelope results in a cone of radiation pointing in the direction of the particle motion. Image taken from Jelley and Galbraith [45]. (b) Cone angle of the Cherenkov radiation as a function of $\beta$ for a particle propagation in air (plot in the inner box), water and ice (Plot done with Matlab).

To achieve coherence of the emission the length of the particle track in the medium should be large compared with the wavelength of the radiation itself, otherwise diffraction effects will become dominant. Moreover, the velocity of the particle must be constant during its passage through the medium, i.e. the differences in the times for particle to traverse successive distances $\lambda$ should be small compared with the period $\frac{\lambda}{c}$ of the emitted light. The number of photons emitted by a charged particle of charge $ze$ per unit path length $x$ and per unit $\lambda$, is equal to:

$$\frac{dN^2}{dxd\lambda} = \frac{2\pi\alpha z^2}{\lambda^2} \cdot \left(1 - \frac{1}{\beta^2 \cdot n^2(\lambda)}\right) \tag{1.11}$$

where $\alpha = \frac{1}{137}$ is the fine structure constant and $n(\lambda)$ is the refraction index of the medium that is a function of the photon energy. Great part of the Cherenkov photons are emitted in the ultraviolet range, because $\frac{dN^2}{dxd\lambda} \propto \frac{1}{\lambda^2}$. For the specific case of an electron moving along a track of length $l$ within a spectral region defined by wavelengths $\lambda_1$ and $\lambda_2$ we will have:

$$\int_l^0 \int_{\lambda_1}^{\lambda_2} \frac{dN^2}{dxd\lambda} \qquad \rightarrow \qquad N = 2\pi\alpha z^2 l \left(\frac{1}{\lambda_2} - \frac{1}{\lambda_1}\right) \cdot \left(1 - \frac{1}{\beta^2 \cdot n^2(\lambda)}\right) \tag{1.12}$$

The Cherenkov radiation spectrum produced an ultra-relativistic electron ($\beta = 0.9997$) traversing a layer $l \sim 10$ km of air and $\sim 100$ m in water or ice, is plotted in Figure 1.24. The photons flux is enhanced in the UV-blue region of the spectrum. Equation 1.12 does not take into account the intrinsic absorption and scattering of radiation occurring into the medium.

### 1.4.4 Extensive Air Shower detectors

EAS detectors are generally constituted by array of scintillators or water Cherenkov detectors with no moving parts and no pointing capabilities. They have high duty cycle and large FoV, but

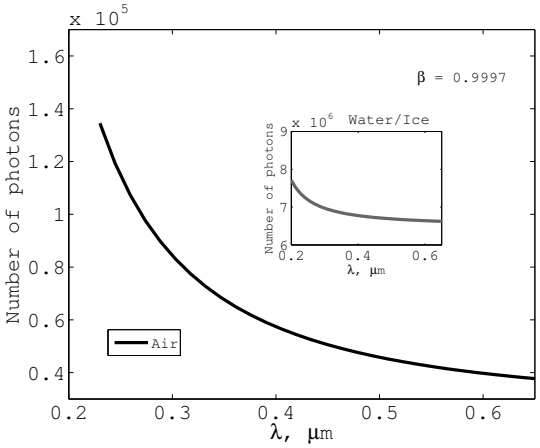


Figure 1.24: Simulated Cherenkov spectrum (eq. 1.12) produced by an ultra-relativistic electron. The emission has been integrated over 10 km in air and 100 m in water and ice. Absorption and scattering phenomena are not taken into account. (Plot done with Matlab).

a low sensitivity and they are mostly sensitive to TeV photons as they need a shower extending through the atmosphere for many radiation lengths so that the detectors are reached by the cascade products. The data recorded from the sensitive elements of the arrays are used to determine the energy and direction of the cosmic ray or $\gamma$ ray. In the past years two EAS detectors have been built: MILAGRO and ARGO-YBJ. The MILAGRO experiment (Los Alamos) used 700 photomultipliers submerged in water plus another 200 detectors around the pond. This system, now dismantled, detected the Crab with a significance of $5\sigma$ in 100 days of observation. The ARGO-YBJ was an experiment born from the collaboration between Italy and China at the Yangbajing Laboratory (Tibet). The observatory was constituted by an array of resistive plate counters with an energy threshold in the range 0.5-1 TeV. The ARGO-YBJ sensitivity lead to detect the Crab with a significance of $5\sigma$ within 50 days of observation. In the same site of ARGO-YBJ China is now going to deploy LHAASO, a new generation EAS, see section 1.4.6 for details.
A new project currently under construction, but already operating, is the High-Altitude Water Cherenkov Observatory (HAWC) at the Sierra Negra Volcano (Mexico). This facility is designed to observe TeV gamma rays and cosmic rays with an instantaneous aperture that covers more than 15% of the sky. With this large field of view, the detector will be exposed to two-thirds of the sky during a 24-hour period [146]. HAWC will perform a high-sensitivity synoptic survey of the sky at wavelengths between 100 GeV and 100 TeV by means of 300 close packed water tanks, 7.3 m in diameter and 4.5 m deep, each containing 200 $m^3$ of water. Each of these tanks is equipped with four photomultiplier tubes at the bottom facing upward. A sky map based on the first three months of data taking is shown in Figure 1.25.

Once the installation will be completed, HAWC aims to detect the Crab in one day of observation at $5\sigma$ and to achieve a sensitivity of 30 mCrab (mCrab $= 10^{-3}$ the Crab flux) in two years of observation.

### 1.4.5 Imaging Air Cherenkov Telescopes

A more sensitive, even if more complex technique to detect VHE $\gamma$ ray photons is based on the IACTs. As discussed in section 1.2, this experimental technique is very young (first TeV detection by IACT in 1989), though still capable of significant improvements. The advantages with respect to EAS detectors are the higher sensitivity and the low energy threshold, while the

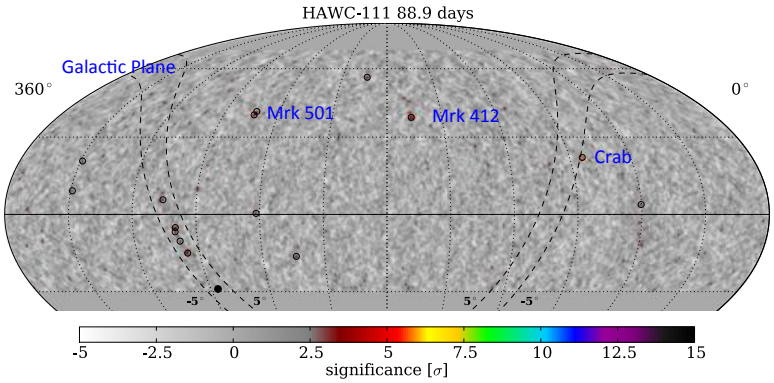


Figure 1.25: Preliminary results of of three months of observation with HAWC, the brightest VHE sources as the Crab, Mrk 421 (in the image wrongly Mrk 412) and Mrk 501 are detected with high significance [114].

drawbacks are the low duty cycle and the small FoV. The IACTs operating today are arranged in arrays of 2 to 5 telescopes and they are grouped in three different observatories: MAGIC and VERITAS for the Northern sky, H.E.S.S. for the Southern sky.
The MAGIC telescopes are two twin reflectors, 17 m in diameter and 85 m apart, located in the Canary Island of La Palma. The project is a common effort between Germany, Italy, Spain, Finland, Switzerland, Japan, Poland and Croatia. The MAGIC telescopes have been designed to reach the low energy threshold of 50 GeV and to perform a stereoscopic vision that allows a better background rejection and an angular resolution of about 0.07 degrees. The array can slew in $\sim$ 20 s towards any pointing position in sky to chase a GRB event.
The VERITAS array is made of four 12 m telescopes and it is located at the Fred Lawrence Whipple Observatory, Arizona. The telescopes are deployed such that they have the highest sensitivity in the VHE energy band (50 GeV - 50 TeV), with maximum sensitivity from 100 GeV to 10 TeV. This VHE observatory effectively complements the Fermi satellite.
The H.E.S.S. array is made of four 12 m telescopes and a central 28 m reflector that are sensitive to the energy range from 10 s of GeV to 10s of TeV. H.E.S.S. is located in Namibia, near the Gamsberg mountain and it is operated by a consortium of many countries with major contributions from Germany and France. The worldwide distribution of the IACTs operating nowadays is shown in Figure 1.26.


Figure 1.26: Distribution of the IACTs in the world; the CANGAROO III array has been dismantled. Image from C. Schultz [118].

The IACTs detect the Cherenkov radiation emitted by superluminal particles inside air showers ignited by a primary $\gamma$-ray photon. The mechanisms of production of Cherenkov radiation

were described in section 1.4.3, while here we concentrate on the phenomenology of the Cherenkov observation from the IACTs detection perspective. The Cherenkov light cone that propagates into the atmosphere has an angle of about 1°, resulting in a *light pool*, the footprint of the air shower on the ground, of about 120 m in radius (Figure 1.28a). The higher is the energy of the primary $\gamma$ ray, the larger the number of Cherenkov photons released. The light intensity radial profile of the light pool is almost constant until r $\sim$ 120 m and then it progressively decreases for larger radii (see Figure 1.27).

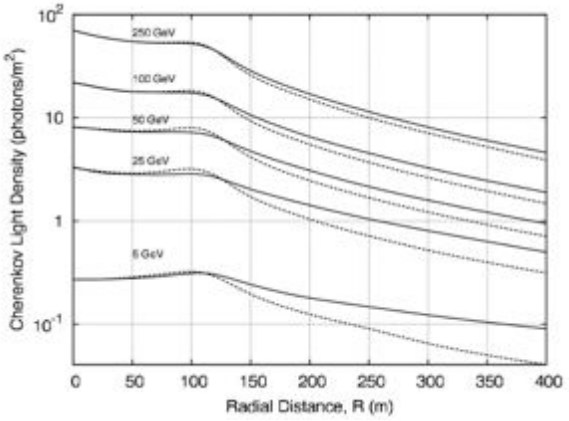


Figure 1.27: Simulation of the density profile of the Cherenkov radiation light pool. Starting from the core center, the density slowly decreases until a radial distance of ∼120 m followed by a steeper decrease in the outer, halo region. The solid and dashed lines represent the showers developing along the Earth magnetic field and perpendicular to it. Plot from Aharonian et al. [6].

Though produced across many radiation lengths in atmosphere, and therefore in a time of microseconds, the air shower has an *observed* duration compressed in few ns (increasing with the core distance). This is because the particles causing the flash travel slightly ahead of the photons they generate. Thus, as a rule of thumb, the observed time span is the relative delay between photons produced at various heights. The air shower has a duration between 2-3 ns at the ground level and IACTs reflectors are used to collect and concentrate the Cherenkov photons onto the focal plane of an extremely fast camera capable of GHz sampling. This time compactness of the signal is crucial for the observations as Night Sky Background (NSB) is more easily dominated on such short time scales. The $\gamma$ ray from a point-like source produces on the focal plane a light pattern of elliptical shape with the semi major axis pointing in the direction of the camera centre (Figure 1.28b). If the $\gamma$ ray is observed simultaneously with two different telescopes, the intersection between the two semi major axes identifies the impact point of the photon from which one can derive the direction of the source in sky. As the distance of the $\gamma$ ray impact point from the telescope increases the ellipse on the focal plane moves towards the edge of the FoV becoming more elongated.

As discussed in section 1.2, the study of the patterns topology is particularly important, mainly in relation to the Hillas parameters [65], to discriminate between the electromagnetic shower of interest and the background hadronic events. The hadronic showers are widened events with random direction. Also the temporal structure of the electromagnetic and hadronic shower is different, being the latter more spread out over time. These discrimination studies are extremely important at the GeV-TeV energy scale because the hadronic showers are about $10^3$ more abundant than the electromagnetic events [29]. The showers ignited by electrons have the same topology of those created by a $\gamma$ ray, but they have a limited impact on the observations. Monte Carlo (MC) simulations are required to discriminate between $\gamma$ ray and hadronic events and to estimate the energy of the primary photon. MC analysis makes use of CORSIKA program

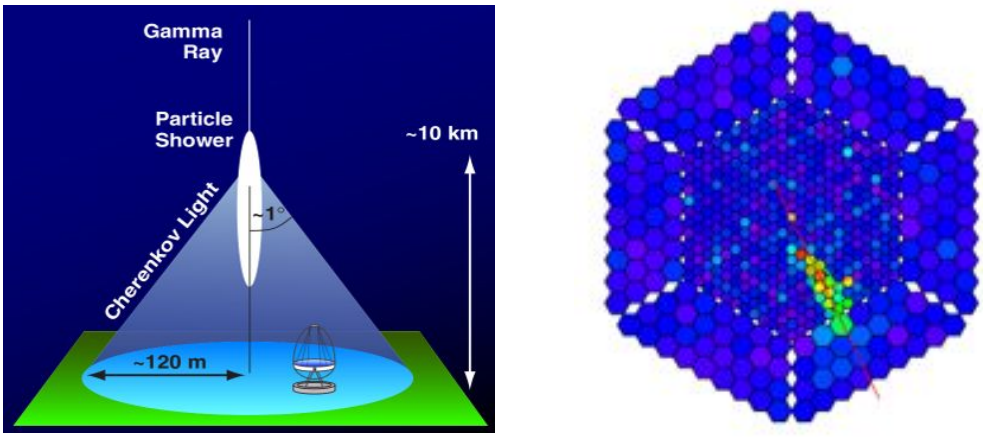


(a) (b)

Figure 1.28: (a) Geometry of the Cherenkov air shower: the primary $\gamma$ ray initiates an electromagnetic air shower at about 10 km with a Cherenkov radiation cone angle of about 1 deg that reaches the ground creating a light pool 120 m in radius. (b) The shape of the pattern from an electromagnetic shower is an ellipse that for point-like sources has the semi-major axis pointing to the center of the camera FoV.

[61] to model the development of the extensive air showers that are given in input to a program (sim_telarray [4]) that traces the ray tracing of the Cherenkov photons until the focal plane, accounting for all the effects of the detection system (optics and electronics). This software simulates the raw images obtained with the IACT technique and the Hillas parametrization is applied to estimate the hadroness of the event and its energy. There are two pointing modes for the IACTs observations that allow the detection of the source of interest and the estimate of the background [29]:

- **on-off mode**: the telescope pointing switches between the source and a background region with no sources.
- **wobble mode**: the telescope points in a slightly off-source direction and the background is extracted simultaneously in the anti-source region.

All the photons detected by the camera at ns scale are analogically transmitted to a trigger system set on a given threshold; the signals above this level are sampled by the acquisition system. As shown in Figure 1.27 the number density of Cherenkov photons is extremely small even for the highest $\gamma$ ray energies and the IACTs having detection systems based on photomultiplier tubes can work only during moonless time or at a halved voltage in the presence of moonlight. Consequently IACTs have typically a total observation time per year of about 1500 hours. To summarize the different characteristics of the detection techniques discussed in these sections Table 1.29 from De Angelis et al. [29] is reported below.

The future of VHE astrophysics see a series of new generation instruments to be built in the next ten years that are briefly presented in the next section 1.4.6.

### 1.4.6 The next generation of IACTs and EAS detectors

The future of the ground-based gamma-ray astronomy foresees important improvements in the performances with respect to the current facilities described in section 1.4.2. The scenario of the next 20 years will see the construction and the operation of the new generation instrument for IACTs, the Cherenkov Telescope Array Observatory (CTAO). This project supported by an international consortium of 29[2] member states aims to deploy two different arrays with many

[2]Countries involved at July 2014

| Quantity | GLAST | IACTs | EAS |
|---|---|---|---|
| Energy range | 20 MeV – 200 GeV | 100 GeV – 50 TeV | 400 GeV – 100 TeV |
| Energy resolution | 5-10% | 15-25% (*) | $\sim$ 50% |
| Duty Cycle | 80% | 15% | $>$ 90% |
| FoV | $4\pi/5$ | 5 deg $\times$ 5 deg | $4\pi/6$ |
| Resolution(PSF) | 0.1 deg | 0.07 deg | 0.5 deg |
| Sensitivity(**) | 1% Crab (1 GeV) | 1% Crab (0.5 TeV) | 0.5 Crab (5 TeV) |

Figure 1.29: A comparison of the characteristics of Fermi-GLAST, the IACTs and of the EAS particle detectors arrays, table from De Angelis et al. [29].
(*) Decreases to 15% after cross-calibration with Fermi-GLAST.
(**) Computed over 1 year for Fermi-GLAST and the EAS (ARGO), and over 50 hours for the IACTs.

tens of telescopes in both the sky hemispheres. The goal is to observe the whole sky over about 4 orders of magnitude in energy, from $\sim$20 GeV to $\sim$300 TeV. A comprehensive description of CTA can be found in the first paragraphs of chapter 4. Besides this major facility other nations are deploying their own observatories for gamma-ray observations from ground. India is constructing the Major Atmospheric Cherenkov Experiment (MACE), a 21 m diameter IACT in the Hanle high altitude astronomical site (4200 m). The F/1 telescope will have an imaging camera with 1088 PMTs giving a PSF on sky of 0.125° and a trigger threshold of about 20 GeV [82].
A new, large experiment of the EAS type that will be deployed by China is the Large High Altitude Air Shower Observatory (LHAASO) and it will be constructed at the Yangbajing site in Tibet. The goal of LHAASO is to investigate the origin of high energy cosmic rays, and the evolution of the Universe and high energy celestial bodies. The detector consists of three parts: 1 km$^2$ array (LHAASO-KM2A), including 5100 scintillation detectors and 40 km$^2$ distributed muon detectors, 24 air fluorescence/Cherenkov detectors (LHAASO-WFCTA) and 100 m$^2$ burst detectors array (LHAASO-SCDA), and 90 km$^2$ water Cherenkov detector (LHAASO-WCDA). In a second phase, with the contribution of international partners, advanced detection technology will be introduced such as full coverage track detection technology, and two MAGIC-like telescopes to improve the spatial resolution and lower the threshold energy [155]. The sensitivity of LHAASO compared to the other VHE observatories is shown in Figure 1.30.

Even if EAS experiments suffer lower sensitivity for a given exposure time with respect to IACTs, LHAASO will be more sensitive than CTA above 10 TeV over exposure times in the order of 1 year. This enhanced sensitivity coupled with the wide instantaneous sky coverage ($\sim$18°) makes LHAASO suitable for extended sky surveys and long term monitoring programs. LHAASO will also complement the observations of the existing Northern facilities as MAGIC and VERITAS and the incoming CTA North.

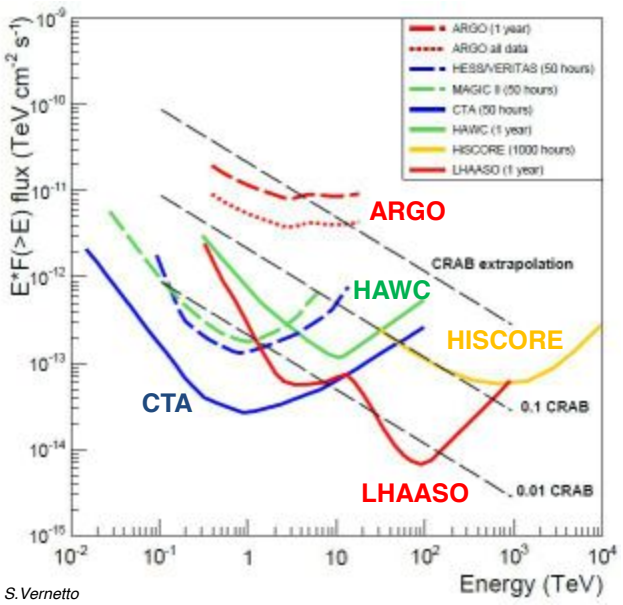


Figure 1.30: Sensitivity integral for an observing time T = 50 h for IACTs and T = 1 year for EAS arrays. T = 1 year with EAS means 1500-2200 hours of observation for each source in the visible declination band (about 4-6 hours per day) Image from S. Vernetto [136].

## 1.5 Galactic and extragalactic VHE sources with CTA

In this section we review the main science topics that CTA will investigate once operative. The discussion is organized in many paragraphs, each devoted to different single class of objects.

### Pulsar and pulsar wind nebulae

A pulsar is a rotating, magnetized neutron star that originates from the collapse of a super-massive star after the supernova explosion. Due to conservation of the angular momentum during the gravitational collapse, as the moment of inertia decreases, the neutron star initiates a fast rotation. The pulsar emits radiation energy that originates from its rotational energy, which generates an electrical field from the movement of the very strong magnetic field and accelerates protons and electrons [106]. Because of the pulsar intense magnetic field ($10^{14}$-$10^{15}$ g [151]), the emission is collimated along the magnetic moment, precessing around the rotation axis and it is visible from Earth only when the axis points towards the observer. This configuration creates a pulsed signal emission with frequencies between $\sim 30$ and $\sim 10^{-9}$ Hz. The spectrum of emission is described by a power law. In the case of the Crab pulsar the pulsed $\gamma$ ray emission has been detected and extensively studied (Aliu et al. 2008 [11]) as shown in Figure 1.31. New[3] measurements obtained by the MAGIC collaboration, with more than 300 hours of observations, extend the energy spectrum of the Crab pulsar to $\sim 2$ TeV with no evidence of energy cut off [145].

Another parent family of the pulsars class are the pulsar wind nebulae (PWN). A PWN or Plerion, is an object consisting of a neutron star and a surrounding nebula. In these systems, that are the most populated class of galactic VHE sources, the nebula is powered by the pulsar wind of the pulsar. The most important PWN known is the Crab Nebula, that is also the brightest VHE source in the sky and it is used as a standard candle for calibrations. There are also experimental evidences of observable extragalactic PWNe located in the Large Magellanic

[3] 2014

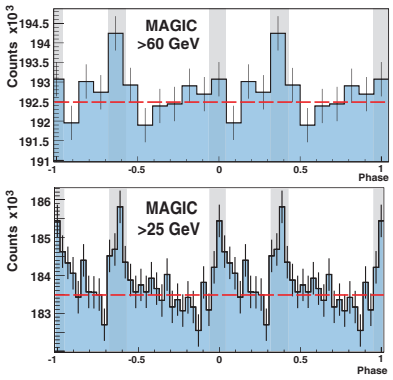


Figure 1.31: Pulsed emission in different energy bands. Top: evidence of an emission (3.4 $\sigma$) greater than 60 GeV measured by MAGIC. Bottom: emission $\geq$ 25 GeV, measured by MAGIC. Image and label from Aliu et al. [11].

Cloud [79]. Observations with CTA will allow a homogeneous sampling of the PWNe of the Galaxy. If the estimated lifetime of TeV-emitting leptons in such nebulae is $\sim$ 40 kyr (for B = 3 $\mu$G, similar to what has been found in several PWNe such as Vela X), between 300 and 600 PWNe will be detected [156]. Such an unprecedented number of TeV objects of the same class will enable detailed population studies. It is expected that the improved angular resolution of CTA observations will both constrain the interaction between the host supernova remnant (SnR) and its PWN, estimating how much gamma-ray emission is associated to each component.

**Supernova remnants**

A supernova remnant (SnR) is the structure resulting from the explosion of a star in a supernova. The supernova remnant is bounded by an expanding shock wave, and consists of ejected material expanding from the explosion, and the interstellar material it sweeps up and shocks along the way. There are indications that cosmic rays are accelerated by SnRs. The main argument supporting this scenario is the fact that SnRs alone would be able to maintain the CRs population at the observed level, if some fraction ($\sim$10%) of their kinetic energy were somehow converted into CRs [156]. Very tight connections exist between CRs studies and gamma-ray astronomy, due to the fact that CRs protons can undergo hadronic interactions with the interstellar medium producing neutral pions that in turn decay into gamma-rays following the mechanism described in section 1.3.5. Hadronic models are commonly favored (e.g. Stecker 1971 [125], Dermer 1986 [32]). The theoretical and experimental indications on the potential of generating TeV photons by young SnRs (mainly with Type Ia supernova progenitors), suggest that these objects are the main producers of galactic CRs of energies up to the knee. The detection of photons with E $\sim$ 100 TeV from RX J1713.7-3946 is a proof of the acceleration of primary particles in supernova shocks to energies well above $10^{14}$ eV (De Angelis [29]). A definitive proof of this scenario is however not yet achieved and it justifies the construction of CTA. The cut-off energy of the CRs distribution should depend on the age of the supernova and the magnetic field that the particles were shocked in. If enough different cut-off energies are measured, this acceleration scenario could be tested and the strength of the magnetic fields estimated [157].
Since the energy of a supernova explosion is remarkably constant, $\sim 10^{51}$ erg, a rough estimate of the expected gamma-ray flux from a given SnR can be obtained if one knows the density of the ambient medium, and the SnR distance. If a SnR is bright in TeV gamma rays for $\sim$ 3000 yr (approximately the age of Vela Jr), and $\sim$ 2.8 supernovae are expected to explode each century in the Milky Way, the number of SnRs currently emitting TeV gamma rays and potentially detectable with CTA is $\sim$ 80 [156]. An interesting perspective with CTA is the possibility to

resolve the shell and some filaments of the SnRs. If a goal PSF of about 1 arcmin at ∼10 TeV is achieved, CTA could probe these filaments in the VHE gamma-ray domain for objects up to distances of several kpc. Conversely in the case of unresolved sources, a follow-up at other wavelengths is mandatory.

**Cosmic rays and pevatrons**

As discussed in the previous section, galactic cosmic rays (CRs) have long been suspected to be produced at supernova shock fronts via diffusive acceleration (Fermi acceleration). Except for localized excesses around CRs sources, the CRs intensity is expected to be, both spatially and temporally, quite homogeneous throughout the Milky Way. The interaction between CRs and the interstellar gas makes the galactic disk a prominent source of diffuse gamma-rays at energies as observed by the LAT instrument at energies between 100 MeV and 10 GeV at galactic latitudes $10^\circ \leq b \leq 20^\circ$ (Abdo et al. 2009 [1]). CTA should provide detailed observations both for galactic sources and for the closer starbursts Luminous/Ultra-Luminous Infrared Galaxies LIRGs/ULIRGs, investigating possible differences in the acceleration of CRs in galaxies different from our own and their transport mechanisms. CTA will also possibly infer the link between star formation and CRs population [156]. An important quest regards the production of extremely high energy particles by the so-called Pevatrons. At the highest energies, PeV ($10^{15}$ eV) particles are accelerated at the beginning of the Sedov phase of a supernova (∼ 200 yrs), when the shock speed is high; the Sedov-Taylor phase, also known as the *blast wave* phase, is an adiabatic expansion phase in the life cycle of supernova. The particles released quickly escape as the shock slows down. The highest energy particles are released first, and particles with lower energy are progressively released later (Ptuskin & Zirakashvili 2003 [110]). A SnR is a Pevatron for a very short time. About 10 such objects are expected to be active in the Galaxy within the range of CTA sensitivity [156].
In addition there is an experimental evidence for a gap between TeV and PeV scales in the CRs spectrum, that should be successfully filled with CTA thanks to its better mass resolution with respect to ground-based particle arrays [161]. With CTA will be also possible to measure the CRs electrons spectrum at TeV scale through different techniques from conventional gamma-ray analysis, but whose robustness has been already proved by H.E.S.S. [7].

**The galactic centre and galactic plane**

The Galactic Center (GC) is a sky region of $\sim 4^\circ \times 2^\circ$ in galactic longitude and latitude respectively, surrounding the center of our Galaxy, and corresponding to about 600 pc x 300 pc size at the estimated distance of 8 kpc. It is a prominent source in X rays and gamma rays and the study of its high-energy emission is crucial for understanding the physical phenomena taking place in its dense and extreme environment, phenomena that are possibly common to other galactic nuclei. However this emission is very complex and consists of both thermal and non thermal radiation produced by compact and extended sources, surrounded by more diffuse components (Figure 1.32) (Goldwurm 2010 [52]).

One of the major motivations to perform a survey of this region is for measuring the energetic radiation from the GC super-massive black hole (SMBH) that is now firmly detected (with an estimated mass of 4 x $10^6$ $M_\odot$) and associated to the compact radio source Sgr A*. The increased angular resolution of CTA should resolve part of the unresolved sources around the GC helping in disentangling the different contributions. Of great interest is also the possibility of indirect dark matter detection through its annihilation or decay into the GC region.
Another important research concerns the dense galactic plane of the Milky Way. Between 2004 and 2007 H.E.S.S. carried out a survey of a large fraction of the galactic plane, in the longitude

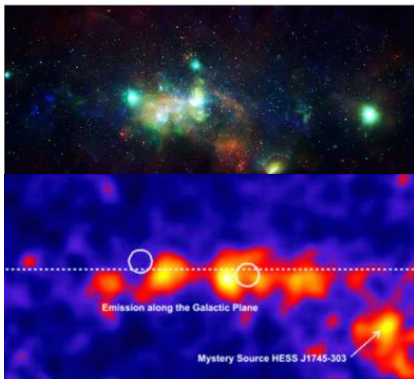


Figure 1.32: Top: X-ray image of the galactic center obtained with the deep survey of the Chandra observatory in the 1-8 keV range (for the color figure: red is for 1-3 keV, green for 3-5 keV and blue for 5-8 keV) (Muno et al. 2009 [100]). Bottom: H.E.S.S. image of the GC, after subtraction of the emission from the two point sources in the white cirlces, a band of gamma ray emission emerges, tracing the Galactic Plane [8].

range of l = 250 to 65 degrees and latitude |b| < 3.5 degrees, detecting 60 TeV sources (Carrigan et al. 2013 [22]) as shown in the pie chart 1.33a and in the diagram 1.33b.

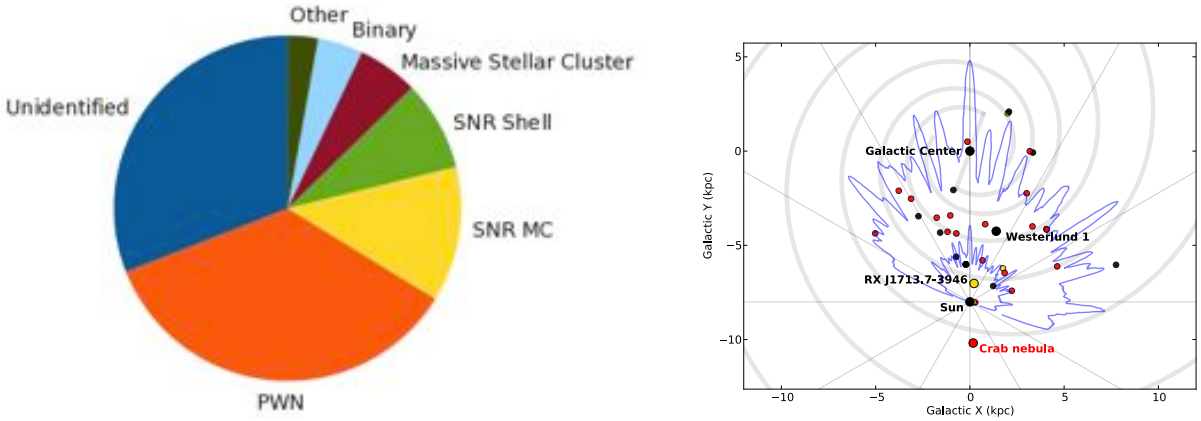


(a) (b)

Figure 1.33: (a) Galactic sources seen H.E.S.S. until February 2013 (classifications taken from TeVCat). Pulsar wind nebulae (PWN, orange) are the most common sources (35% of the total), followed by supernova remnants, either interacting with a molecular cloud (SnR molecular clouds, yellow, ∼13%) or exhibiting emission from their shell (SnR Shell, light green, ∼ 8%). Besides a few massive stellar clusters (dark red, ∼ 6%) and some binary systems (light blue, ∼ 4%) a large part of the H.E.S.S. source population remains unidentified (dark blue, ∼ 31%). 'Other' (dark green) comprises the globular cluster Terzan 5 and the high-frequency peaked BL Lac object HESS J1943+213. (b) Face-on view of our Galaxy, with the spiral arms (solid grey lines). The H.E.S.S. horizons for 1% and 10% of the Crab Nebula luminosity above 1 TeV (ph $s^{-1}$), for a $5\sigma$ point-like source, are depicted by the blue curves. Superimposed are the H.E.S.S. galactic sources with known distances, as listed in TeVCat. Images and labels taken from Carrigan et al. 2013 [22].

CTA will likely increase the number of detected VHE sources and it will help the classification of the unidentified sources.

### Microquasars

Microquasars (MQs) are a subclass of X-ray binaries displaying non-thermal continuum emission in all wavebands. They consist of a compact object that can be a neutron star or a black hole and a companion star: the former accretes with the matter ejected or/and poured from the latter. If the compact object is a black hole the system behaves like a microquasar that is the analogue of an AGN, but at much smaller spatial scale. The interesting aspect of MQs are

the emission mechanisms that are the same of the AGNs. However, due to the much smaller mass of the galactic compact objects, the phenomena are associated to timescales orders of magnitude shorter than those in extragalactic jets (e.g. Mirabel & Rodriguez 1999 [95]). Because of the relative proximity and shorter timescales found in MQs, it is possible to better study the physics of accretion flows and jet formation near the horizon of a black hole. Despite this, the accretion-ejection connection, the formation of jets, the way the jets couple to the BH spin, their interaction with the ambient environment remain unclear and motivate their observation with the third generation of IACTs [156]. In the CTA-Galactic plane survey runs, each location could be visited at least 8 times in runs of 0.5 hours, giving a sensitivity to variability with amplitudes larger than 20 mCrab, relevant for instance for the discovery of new gamma-ray binaries. Population synthesis models for binaries show that there should be $\sim 30$ binaries in our Galaxy where the pulsar is young, and thus are candidates to emit gamma rays [156].

**Active galactic nuclei and radiogalaxies**

An active galactic nucleus (AGN) is a compact region at the centre of a galaxy that hosts a SMBH and shows an extremely high luminosity with respect to the remaining host galaxy. This luminosity extends over the radio, microwaves, infrared, optical, ultra-violet, X-ray and gamma ray wavebands. The radiation from AGN is believed to be a result of accretion of mass by a supermassive black hole at the centre of its host galaxy. AGNs produce powerful outflows that offer excellent conditions for efficient particle acceleration in internal and external shocks, turbulence, and magnetic reconnection events. The jets, as well as particle accelerating regions close to the SMBH at the intersection of plasma inflows and outflows, can produce readily detectable VHE gamma-ray emission [156]. Up to now[4], more than 45 AGNs including 41 blazars and 4 radiogalaxies have been detected by the present IACTs, which represent more than one third of the cosmic sources detected [156]. With the expected sensitivity of CTA, the sample of observed AGNs is expected to increase at VHE by an order of magnitude, leading to population studies and contributing to a unification scheme. The capability of CTA for the exploration of the shortest timescales will provide insights also on the geometry and location of the emitting zone.
The observation of the AGNs population will be among the main goals of CTA Northern array.

**Starburst galaxies and star formation history**

A starburst galaxy is a system undergoing an exceptionally high rate of star formation, as compared to the long-term average rate of star formation in the galaxy or the star formation rate observed in most other galaxies. In a starburst galaxy, the rate of star formation is so large that the galaxy will consume all of its gas reservoir, from which the stars are forming, on a timescale much shorter than the age of the galaxy. This boost of star formation rate is generally attributed to a merger or close encounter with another galaxy. Starburst galaxies show a high rate of supernova explosions in the central region due to the intense star formation and therefore they are preferred sites of CRs acceleration and VHE $\gamma$ ray production by pion decay originated via collision between CRs and the interstellar medium.

The star formation history (SFH) in a more general view will be one of the science topics on which CTA could be a cornerstone project. The study of the interaction of VHE photons with the EBL is of crucial importance to assess the radiation content of the Universe at different cosmic epochs. A large sample of AGNs at approximately the same redshift observed with CTA should determine a reliable value for EBL removing the effect of AGN self-absorption. The

[4] August 2013

EBL attenuation should be a cosmological phenomenon affecting the spectra of all sources in a consistent way showing the same attenuation imprint from the EBL. Thus, in order to measure an unattenuated part of the spectrum for sources at a redshift of at least z = 1.0 (which corresponds to about 50% of the universe), an energy threshold of 30 GeV or lower is required [156].

### Gamma Ray Bursts

Gamma ray bursts (GRBs) manifest as a sudden, very intense $\gamma$-ray emission of extragalactic origin, and they are associated to distinct types of progenitors. The long GRBs ($t_{90}$[5] $< 2$ s) are associated to the merger of binary neutron stars (Woosley & Bloom 2006 [144]). Usually, the initial VHE emission is accompanied by a subsequent afterglow emission in X rays and $\gamma$ rays. The afterglow emission can potentially be detected for hundreds or even thousands of seconds, but the telescopes must be repointed in a few tens of seconds in order to try to catch the prompt. CTA as a whole must be able to change to a new target (i.e. transition from data-taking on one target to data-taking on another target) anywhere within the observable sky within 90 s [93].
Due to the very short life time of GRBs, the observation is extremely challenging. For instance MAGIC is triggered by Fermi and Swift satellites and it can repoint the telescopes in about 20 s subsequently to a GRB alert. Despite many successful follow-up observations of a GRB alerts, no clear detection could be claimed by MAGIC (Albert et al. 2007 [9], Aleksić et al. 2013 [10]). Detection of distant GRBs (z $> 2$) would provide beacons to probe the SFH of the early Universe. Simulations show that these GRBs can be observed by CTA if it features a 30 GeV threshold and $\sim 30\%$ energy resolution below 100 GeV [156].

### Dark matter and fundamental physics

Despite the fact that a cosmological model has been built around the dark matter (DM) paradigm, there are still no clues of the nature of the DM. In the cosmological standard model $\Lambda CDM$ the DM represent the $\sim 27$ % of the entire content of the Universe (Hinshaw, G. et al., 2013 [66]). One of the most popular scenarios for cold DM (CDM) is that of weakly interacting massive particles (WIMPs), that includes a large class of non-baryonic candidates with a mass typically between few tens of GeV and few TeV and an annihilation cross section of the order of the weak interaction. The sources best candidates for hosting large amounts of DM, in principle detectable throughout VHE $\gamma$ ray emission, are spheroidal dwarf galaxies, characterized by high mass-to-luminosity ratio, clusters of galaxies exhibiting gravitational lensing and the galactic centre. Up to now no clear evidence of VHE emission has been detected yet from any potential DM source. CTA will host about 24-28 medium sized telescopes from the U.S. institutes with an enhanced sensitivity at 10 TeV with the goal of increasing the search in the DM parameter space [143]. Any detection or non-detection by CTA will be nevertheless significant for supporting or discarding the DM models.
In addition to DM search, CTA will also be capable to probe other fundamental physics topics such as possible Quantum Gravity models (QG) and the exotic Axion-Like Particles (ALPs). QG effects should manifest with variations of the propagation velocity of VHE photons with different energies emitted by AGNs at cosmological distances. On the other hand, ALPs, are also valid candidates to constitute a part or all of CDM. They are expected to convert into photons (and vice versa) in the presence of magnetic fields. In the case of a very distant AGN, the ALP/photon can cause either attenuation or enhancement of the photon flux or even induce anomalous transparency at tens of TeV (in competition with the EBL absorption, see e.g. Fairbairn et al. 2014 [40]), depending on the ALP mass [156].

[5] $T_{90} > 2$ s) are associated to the core collapse of massive stars, whereas short GRBs ($t_{90}$ is defined as the time interval over which 90% of the total background-subtracted counts are observed, with the interval starting when 5% of the total counts have been observed [81].

# Chapter 2

# The ASTRI Prototype

ASTRI (Astrofisica con Specchi a Tecnologia Replicante Italiana) is a flagship project of the Italian Ministry of Education, University and Research related to the next generation IACT, within the framework of the CTA International Observatory. In this context, INAF is currently developing a scientific and technological breakthrough to allow the study of the uppermost end of the VHE domain. The ASTRI project timeframe is of about 3 years, and foresees the full development, the realization, operation and calibration of a 4-m class, Small Sized Telescope (SST) prototype compliant with the requirements of the High Energy array of CTA. The ASTRI SST-2M prototype will adopt an aplanatic, wide field, double reflection optical layout in a Schwarzschild-Couder design. The dual-mirror end-to-end prototype will observe a wide energy range, from a few TeV up to $>$ 100 TeV. The aspherical primary and secondary mirrors designs present challenging aspects with respect to currently available technologies, in particular concerning the tight cost requirements imposed by the CTA project. Moreover, the focal plane instrument explores small pixelated detector sensors such as multi-anode PMTs or Silicon Photo Multipliers. Among the number of technological challenges, this telescope will be the first instrument implementing both the Schwarzschild-Couder optical configuration and the double reflection for imaging air Cherenkov telescopes.

## 2.1 Schwarzschild-Couder telescope

In 1905, Karl Schwarzschild gave the complete theory of imagery in the field for any reflecting telescope with a single axis [140]. Karl Schwarzschild described an aspherical mirror or surface in general by the following sagitta expression:

$$z = \frac{1}{2r} \cdot y^2 + \frac{1}{8r^3}(1 + b_s) \cdot y^4 + \frac{1}{16r^5}(1 + b_s)^2 \cdot y^6 + \cdots \tag{2.1}$$

with $2y$ aperture of the mirror, $r$ vertex radius of curvature and $b_s$ the Schwarzschild conic constant. Different values of the conic constant can describe different types of surfaces:

- $b_s = 0 \rightarrow$ sphere
- $b_s = -1 \rightarrow$ parabola
- $-1 < b_s < 0 \rightarrow$ ellipse
- $b_s < -1 \rightarrow$ hyperbola
- $b_s > 0 \rightarrow$ oblate spheroid

The most important consequence of Schwarzschild work is stated by the theorem that carry his name:

*For any geometry (with sufficient spacing between the mirrors), two aspheric mirrors allow the correction of two Seidel conditions, i.e. $S_I$ and $S_{II}$, to give an aplanatic telescope.*

Schwarzschild tried to realize an optical system able to correct the first four Seidel aberrations (spherical aberration, coma, astigmatism and curvature field) but the solution gave a convex primary with a secondary larger than the primary and consequently the system had no practical interest as astronomical telescope. He concentrated therefore on a more feasible two mirror *aplanatic* system with non-zero values of $S_{III}$ and $S_{IV}$. An aplanatic telescope is a system free from spherical aberration and coma. The original optical configuration, reported in Figure 2.1 ,was a fast f/3 system (revolutionary for the time) with a FoV of $\pm 1.4°$. The main drawbacks of such configuration were the large obscuration ratio, $R_A = 0.5$, and the position of the focus that was between M1 and M2, disfavoring his accessibility with respect to the Cassegrain configuration. In addition, the conic constants of the two surfaces were $b_{s1} = -13.5$ and $b_{s2} = +1.96297$, respectively an hyperbolic and an oblate spheroid difficult to manufacture and test.

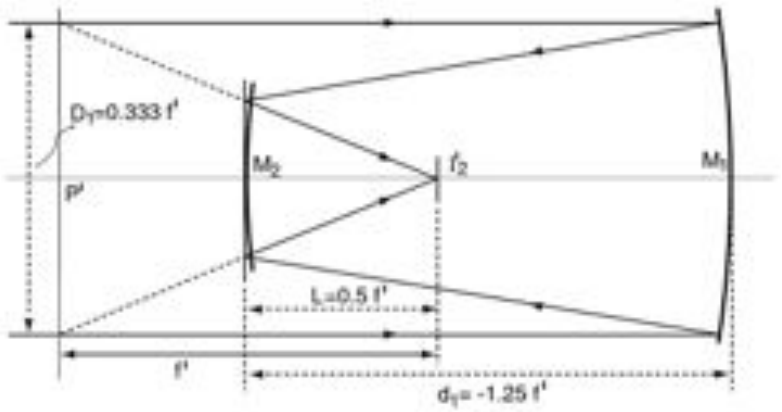


Figure 2.1: Schwarzschild's original aplanatic telescope (1905), photo courtesy R.N. Wilson [141]

In 1926 Couder developed a configuration that was a Schwarzschild modified telescope, which foresaw the correction of the $S_{III}$ aberration rendering the telescope an anastigmatic system by setting the M1-to-M2 distance exactly twice the Effective Focal Length (EFL) of the system. This scheme resulted in a less compact design (Schwarzschild telescope had $d_1 = 1.25 * EFL$), even the obscuration ratio was lower given the higher mirrors separation. Historically, the difficulties related to the realization of a concave secondary and the poor baffling characteristics of such a configuration addressed the astronomers toward more effective solutions like the Schmidt configuration, even if the Schwarzschild-Couder (SC) design was the best two-mirrors solution correcting all the aberrations described by the first three Seidel coefficients. Today the SC configuration is finding a new application in a research field that was not known at the epoch of Karl Schwarzschild, but that benefits of the large FoV and fast F/# offered by such telescope.

## 2.2 The ASTRI Schwarzschild-Couder configuration

The first work that proposed the use of SC aplanatic telescopes for application in $\gamma$ ray astronomy with IACTs was developed by V. Vassiliev et al. [134]. The ASTRI project follows the approach proposed by V. Vassiliev by means of a SC configuration to create a wide-field and compact SST

prototype. The optical design allows a significant reduction of the plate scale with respect to single-mirror solutions, making it compatible with finely-pixilated cameras. The starting point for the telescope design is the detector. Once the requirement on the telescope resolution is fixed, the plate scale for a given pixel size comes from it automatically and consequently the focal length of the system is derived. The pixel size is fixed by the technology to be used and all the large Cherenkov telescopes operating today (before the CTA generation instruments) work with the PMTs and the Winston cones that have dimensions in the order of centimeters. The only exception is the FACT telescope developed by the ETH of Zurich that was the first prototype to explore the potentialities of the SiPMs (A. Biland [17]). The ASTRI project explores this new technology based on SiPMs, with pixels having a physical size of 3.1 × 3.1 mm. As discussed in section 4.4.4, the angular resolution for required for CTA SSTs is fixed at $\Delta\theta < 0.25°$ over the 80% of the FoV. The plate scale of a telescope depends only on the focal length and it is defined as:

$$Platescale = \frac{206265''}{f} \tag{2.2}$$

substituting the ASTRI focal length (also labelled EFL) value (f = 2141.1 mm), the derived plate scale is $PS$ = 96"/mm. Considering the size of the SiPMs the telescope has an angular resolution in sky of $\Delta\theta \sim 0.166°$.
To get the same resolution with the PMTs detectors (size ∼ 30 mm), the required focal length would be $f$ = 10401 mm, resulting in a largely bigger system. The SC configuration is able to address the requirements for CTA SSTs and at the same time it results in a more compact configuration with respect to the single-mirror telescopes. An extended discussion about the characteristic of the different wide-field telescopes is presented in chapter 3.

| **Surface** | **Aperture** | **Curvature radius** | **Distance to** |
|---|---|---|---|
| **M1** | 4306 mm | -8223.8 mm | M2: 3108 mm |
| **M2** | 1800 mm | 2180 mm | DET: 520 mm |
| **DET** | 360 mm | 1060 mm | - |

Table 2.1: Geometry of the three main optical system components.

| **Telescope parameters** | **Size** |
|---|---|
| **EFL** | 2141.1 mm |
| **BFL** | 7130.8 mm |
| **Total track** | 3500 mm |
| **Working F/#** | 0.51 |
| **EPD** | 4200 mm |
| **EXPD** | 2268.1 mm |
| **FoV** | 9.6° |
| **Obscuration ratio*** | ∼40% |
| **Plate scale** | 96"/mm |
| **Angular magnification** | -1.85 |

Table 2.2: Main telescope design parameters retrieved by the optical design developed by a commercial ray tracing software.* Obscuration ratio ($D_{M2}/D_{M1}$).

A picture of the SC optical system envisaged for the ASTRI SST-2M prototype described by the parameters reported in Tables 2.1 and 2.2 is shown in Figure 2.2.

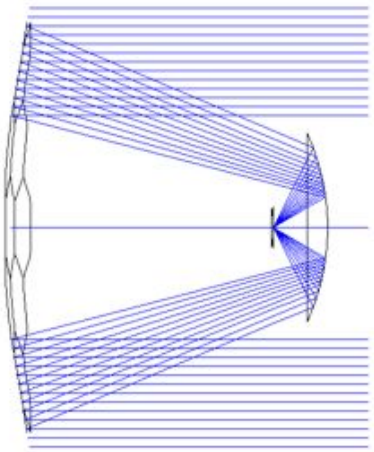

Figure 2.2: The ASTRI Schwarzschild-Couder configuration and the rays optical path for an on-axis source at infinity.

The drawbacks of this system are the presence of M2 that introduces a double reflection and consequently a loss in system effective area, a large obscuration ratio, the intra-focus position of the focal plane and a more complex alignment procedure.

## 2.3 The ASTRI mirrors

The mirror surfaces of M1 and M2 are aspherical and can be described with the classical polynomial equation 2.3 used in optics:

$$z(r) = \frac{cr^2}{1 + \sqrt{1 - (1+k)c^2r^2}} + \sum_{i=2}^{N} \alpha_{2i} r^{2i} \tag{2.3}$$

with $c$ paraxial curvature of the surface and $k$ conic constant. The $\alpha_i$ terms are the aspherical coefficients that parametrize how much the surface differ from the spherical profile. In the next two paragraphs we describe extensively and separately the M1 and M2 surfaces.

### 2.3.1 M1

The surface describing M1 obeys to equation 2.3 with a paraxial curvature $c$ = - 1/8223.8 mm$^{-1}$ and $k = 0$ as it was a spherical mirror, and a series of aspherical coefficients that describe the deviations from a canonical sphere. For manufacturing reasons the primary mirror is segmented in a mosaic of 18 hexagons subdivided into three different rings, each having different surface curvatures that change continuously from the paraxial to the marginal region. This design comes from the optimization process in order to preserve the required PSF sizes along the entire FoV. Each hexagon has an aperture of 849 mm edge-to-edge. In relation to Figure 2.3 the 18 hexagons are subdivided as follows:

1. First ring, hexagons: 1,2,3,4,5,6
2. Second ring, hexagons: 7,8,9,10,11,12
3. Third ring, hexagons: 13,14,15,16,17,18

The surface asphericity increases from the inner ring (the first) to the outer (the third) as plotted in Figure 2.4. The ASTRI M1 therefore has a progressively flattened aspherical profile

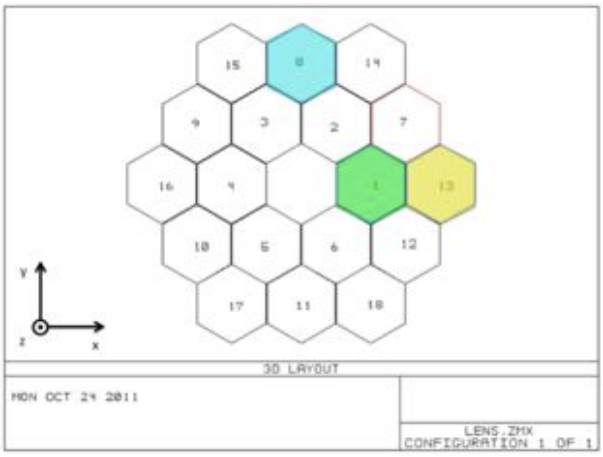


Figure 2.3: The surface of M1 is tessellated with 18 hexagons, one hexagon per each ring is put in evidence by the colors. The central hexagon being completely obscured by M2 is not implemented.

moving toward the outer rings: the nominal radius of curvature of the inner ring is $R_1 = -8223.8$ mm while that of the outer is $R_3 = -12738$ mm. The aspherical coefficients that appear in equation 2.3 are listed in Table 2.3.

| **Aspherical coefficients** | **Value** |
|---|---|
| $\alpha_4$ | 9.6106e-13 |
| $\alpha_6$ | -5.65501e-20 |
| $\alpha_8$ | 6.77984e-27 |
| $\alpha_{10}$ | 3.89558e-33 |
| $\alpha_{12}$ | 5.28038e-40 |
| $\alpha_{14}$ | -2.99107e-47 |
| $\alpha_{16}$ | -4.39153e-53 |
| $\alpha_{18}$ | -6.17433e-60 |
| $\alpha_{20}$ | 2.73586e-66 |

Table 2.3: Aspherical coefficients for M1.

The values of the main parameters describing M1 are collected in Table 2.4.

| **Parameter** | **Value** |
|---|---|
| **Diameter** | 4350 mm |
| **Radius of curvature*** | 8223 ± 6 mm |
| **Focal length** | 4111.5 ± 3 mm |
| **Sag** | 0 to 268.4 mm |

Table 2.4: Main M1 optical parameters. *Paraxial value.

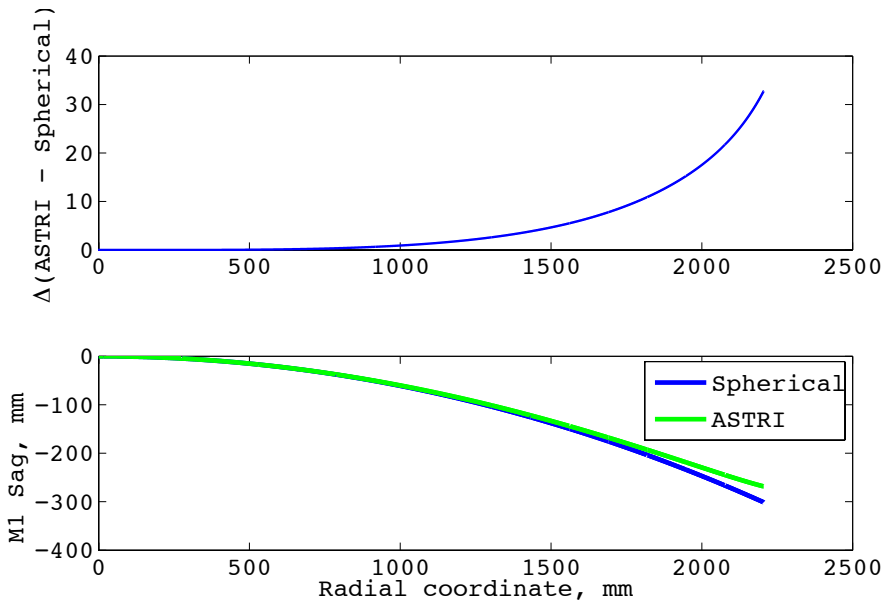


Figure 2.4: Bottom, green curve: M1 profile as a function of the radial aperture, the blue curve refers to a spherical surface with the same aperture and paraxial radius of curvature. Top: difference (in mm) between the M1 ASTRI profile and the equivalent spherical mirror.

### 2.3.2 M1 segmentation

Once the parameters describing the primary mirror surface have been derived, the next step consists on a study of the segmentation of M1. This process has to take into account the optimization of the surface coverage to avoid light losses among segments, while guaranteeing a feasible manufacturing process. The approach followed to calculate the (x,y,z) coordinates of the hexagons centers and vertices is described in a work for the Thirty Meter Telescope by Baffes et al [12]. The starting point consists on an planar array of hexagons with the edges overlapped and without any space between them. The initial coordinates are those of a regular hexagon with an edge-to-edge distance equal to 849 mm; then their cartesian coordinates are converted to a polar reference and given in input to a scaling law that returns the scaled vertices coordinates (eq. 2.4).

$$R' = R_0 \frac{1 + \alpha(\frac{R_{max}}{k})^2}{1 + \alpha(\frac{R_0}{k})^2} \tag{2.4}$$

with $R_{max}$ radial coordinates of the outer vertex belonging to the third ring, $k = 8223.8$ mm paraxial radius of curvature and $\alpha = 0.1525$ scale parameter tuned on the data of the document Error Budget Tree for the ASTRI prototype (ASTRI internal report [159]).

Once the $R'$ planar radial coordinates are retrieved their are loaded in the Zemax optical design of the telescope. Zemax is licensed software for the development and the study of complex optical designs [158]. The coordinates of the hexagons are then listed in a *User Defined Aperture* (UDA) file that allows to describe polygonal shape by simply listing a series of (x,y) coordinates automatically connected by a line. The final configuration of M1 is shown in Figures 2.6. The central hexagon of M1 is not implemented because fully obstructed by the secondary mirror, and also the inner ring is partially shielded by M2 as shown in Figure 2.6b. There is a gap of 9 mm between adjacent hexagonal segments for mounting and alignment purposes.

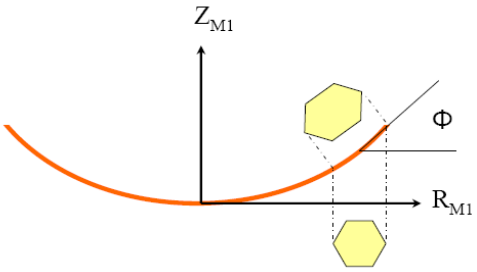


Figure 2.5: Scaling and elongation of an hexagon from a planar to a curved surface. Photo courtesy Baffes et al [12].

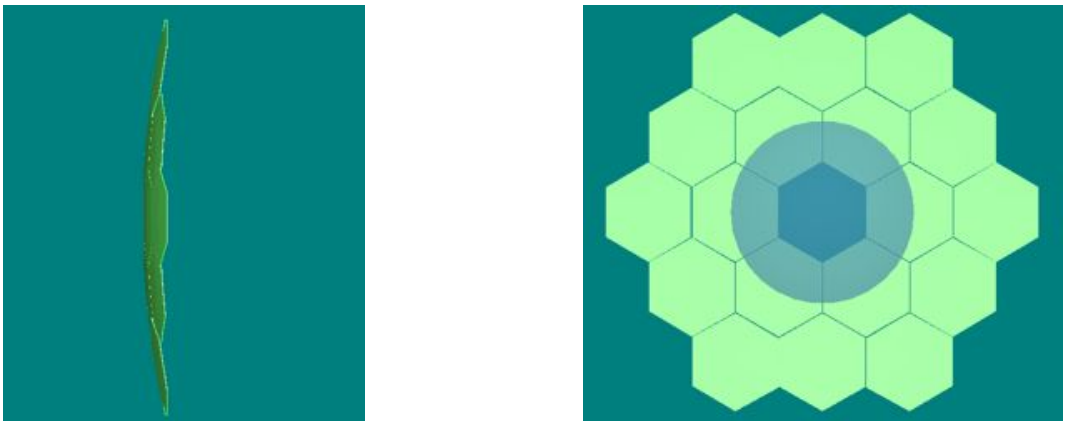

(a) (b)

Figure 2.6: (a) M1 profile in the xz-plane (b) Face-on view of M1 with the M2 obstruction; the central hexagon is completely shaded by M2 and all the segments belonging to the first ring are partially shielded for a on-axis source.

### 2.3.3 M1 Segments support system

Each M1 segment is supported in an isostatic way by one fixed support (axial fixed point), two active supports (axial actuators) and a tangential rod (controller rod) to stabilize the entire segment. The actuator, attached to the rear of the mirror by means of a pad glued on the glass, applies a vertical movement to the mirror segment by an eccentric mechanism that moves a piston rod acting on the rear surface of the mirror segment (see Figure 2.7b). The linear range of a sample of actuators has been measured by means of an lvdt device and it is estimated around 9-10 mm as shown in Figure 2.7c. The axial movement of the two actuators allows the rotations around the x and y axes of each mirror segment for correcting the orientation of the whole mirror surface. The base of the three supports of each segment is fixed on a light structure that is connected to the mirror cell; this configuration allows to mount and unmount each segment together with its support structure without involving the others.

This segment support system is part of the Active Mirror Control mechanism (AMC) that compensates the loads and the misalignments induced by environmental factors and that is described in section 2.6.

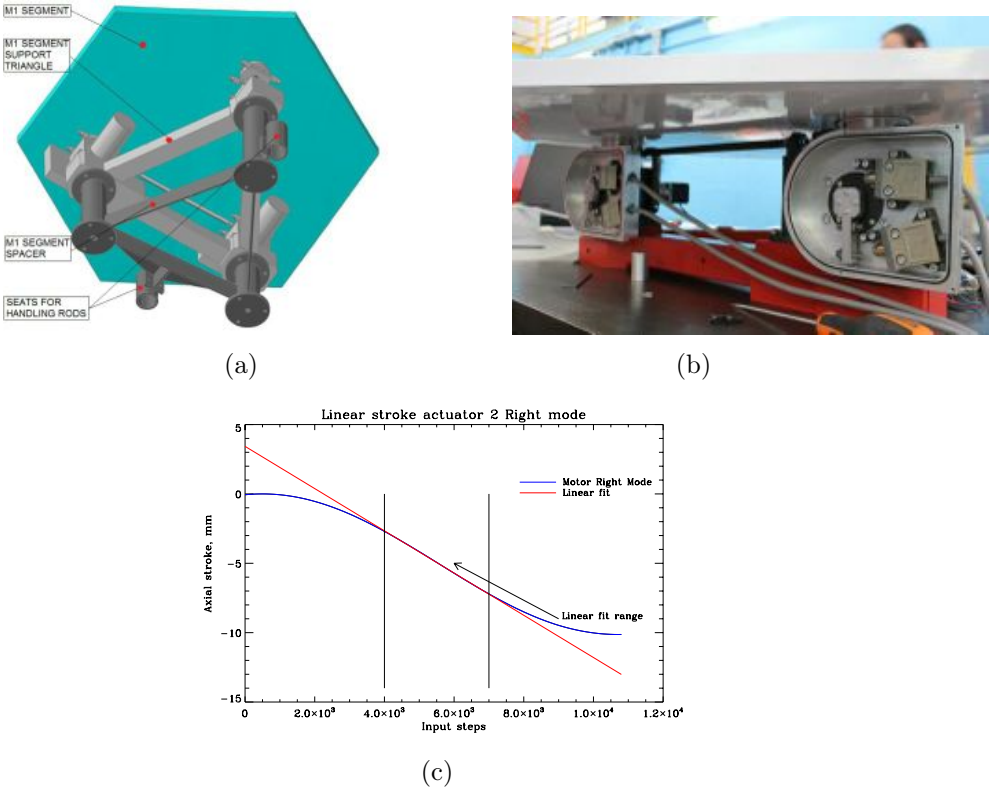


(a) (b)

(c)

Figure 2.7: (a) M1 segment support system with the three supports, one axially fixed and two active actuators to tilt the segment around x and y axes. (b) The two actuators controlling the orientation of the M1 panels. (c) Overall actuator range measured by an lvdt, the linear range is about 9 mm.

### 2.3.4 M2

The ASTRI secondary mirror (M2) has a diameter $D_2 = 1800$ mm and a radius of curvature $R_2 = 2180$ mm as reported in Table 2.6. The surface is described by the usual conic equation referenced to its vertex:

$$z(r) = \frac{cr^2}{1 + \sqrt{1 - (1+k)c^2r^2}} + \sum_{i=2}^{10} \alpha_{2i} r^{2i} \tag{2.5}$$

with the aspherical coefficients $\alpha_{2i}$ collected in Table 2.5.

The surface is highly curved: the sag of the mirror profile at vertex is about 194 mm. The values of the main parameters describing M2 are collected in Table 2.6.

The images in Figures 2.8a and 2.8b report a front and lateral projection of ASTRI M2, and in Figure 2.9 the plot of M2 radial profile together with the departures from a spherical mirror is shown.

### 2.3.5 M2 support system

The support and driving system of the secondary mirror is realized by three axial actuators, connected to the mirror through three whiffletrees to better share the mirror weight and loads (see Figure 2.10a) [131]. These three axial actuators have a linear range of about 7.5 mm and they allow the mirror positioning both in focus along the optical axis and in the tilt around the two orthogonal axes. The lateral torque components induced by gravity and other loads as wind and ice, are contained by three lateral constraints realized by three tie rods. These rods have a

| Aspherical coefficients | Value |
|---|---|
| $\alpha_4$ | 1.62076e-11 |
| $\alpha_6$ | -2.89584e-17 |
| $\alpha_8$ | 8.63372e-24 |
| $\alpha_{10}$ | 3.34856e-30 |
| $\alpha_{12}$ | -1.03361e-36 |
| $\alpha_{14}$ | -6.73524e-43 |
| $\alpha_{16}$ | -3.06547e-49 |
| $\alpha_{18}$ | 3.17161e-55 |
| $\alpha_{20}$ | -3.71183e-62 |

Table 2.5: Aspherical coefficients for M2.

| Parameter | Value |
|---|---|
| **Diameter** | 1800 mm |
| **Radius of curvature** | 2180 ± 6 mm |
| **Focal length** | 1090 ± 3 mm |
| **Sag** | 0 to 194 mm |

Table 2.6: Main M2 optical parameters.

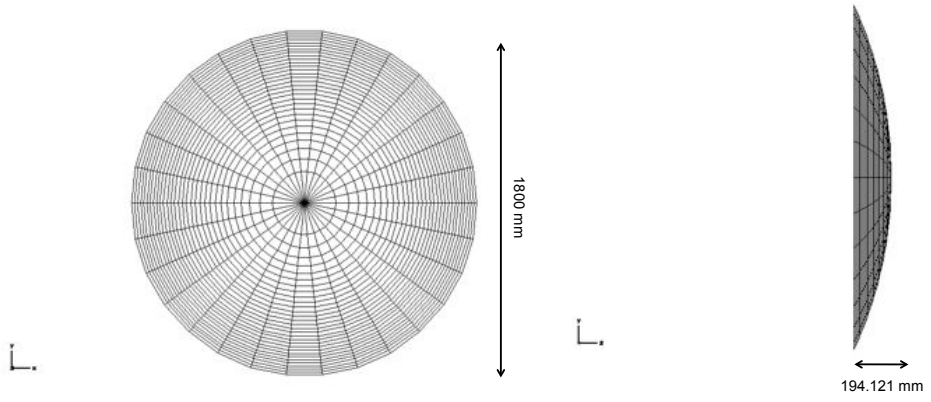


(a) (b)

Figure 2.8: (a) Front view of M2 and (b) lateral view of M2, the sag is ∼194 mm.

high axial stiffness but are endowed by flexures at the two ends (see Figure 2.10c). The movement of the axial actuator of the M2 mirror is obtained by a rotating nut driven by a stepper motor through an irreversible gearbox that is fixed to the backup structure of the secondary mirror. The nut is preloaded against the triangle, that shares the load among the three rods applied to the mirror pads (see Figure 2.10a). To limit the movement of the mirror in case of failure, and also to limit the maximum load on its lateral surface, suitable adjustable safety devices have been foreseen, that leave about 5 mm backlash all around the mirror in all directions.

The gluing of the pads onto the rear surface of the mirror has been done at the conclusion of all the qualifications test described in chapter 5. The pads are glued all contemporary by means of a mechanical dummy of the Mirror Support System (MSS) that mimics the unit integrated on the telescope (see Figure 2.10b). The dummy MSS is centered on the mirror by a laser beam that

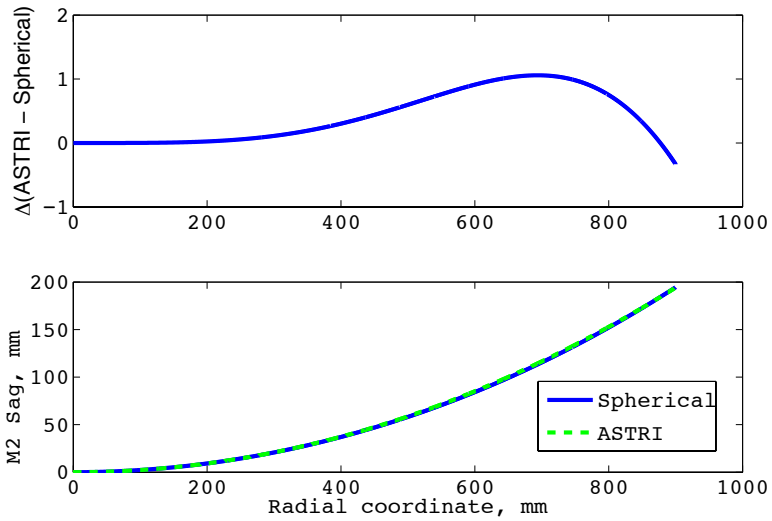


Figure 2.9: Top: residuals between ASTRI M2 and a spherical surface of equal diameter and paraxial radius of curvature. Bottom: radial profile of M2.

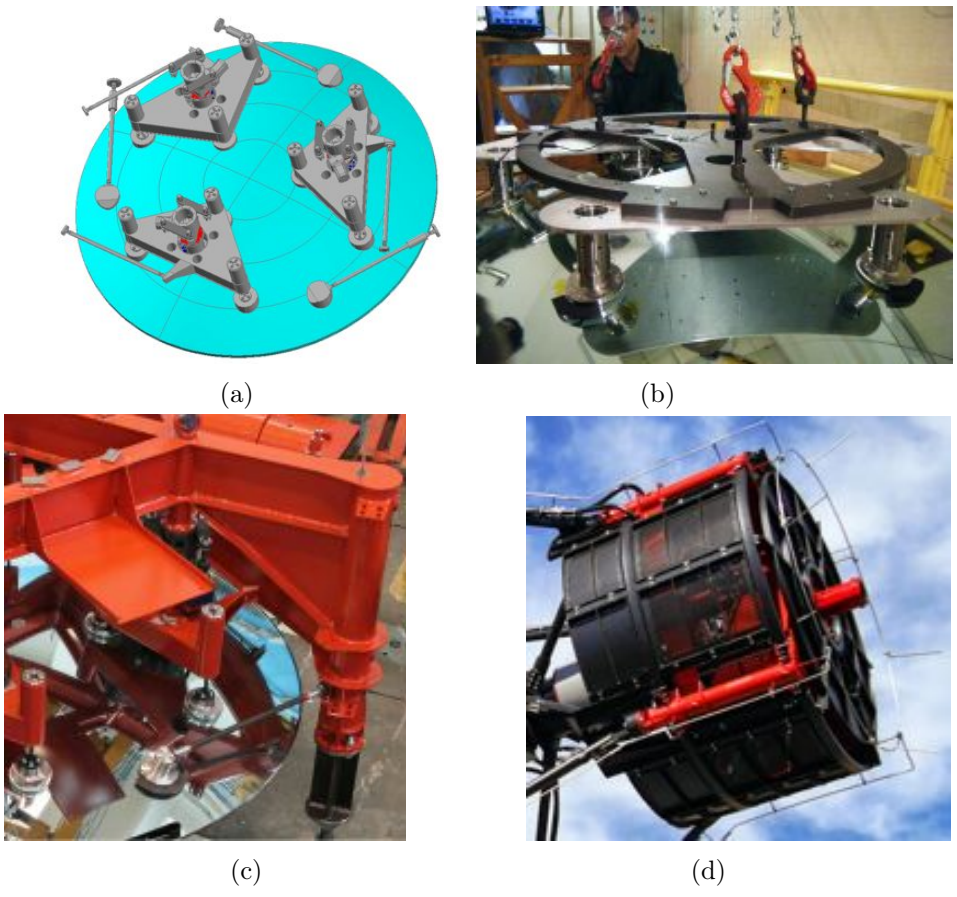


Figure 2.10: (a) Design model of the M2 MSS with the three whiffletrees in evidence. (b) Mechanical dummy of the MSS used for the operations of pads gluing. (c) M2 mounted on its MSS, in evidence one of the three tie rods that limits lateral shifts of the mirror. (d) Complete M2 subsystem integrated at the telescope.

points at the mechanical centre of the mirror recognized by centering tests discussed in section 5.6. After about 3 weeks of rest the mirror is ready be me handled and it can be integrated onto

its real MSS (Figure 2.10c) and mounted at the telescope (Figure 2.10d).

## 2.4 ASTRI PSF

As discussed in the previous sections, the ASTRI SST-2M prototype has a rather high obscuration ratio ($D_{M2}/D_{M1}$) $\sim 0.4$, a segmented aspherical primary mirror and an highly aspherical secondary mirror. Every single ring of hexagons as described in section 2.3.2 has different, continuously changing, radius of curvature and it contributes to the overall PSF as reported in Figure 2.11.

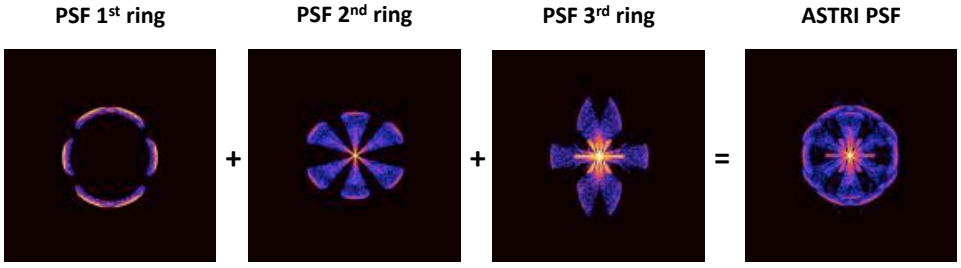


Figure 2.11: Simulated PSFs on the telescope focal plane subdivided by the three M1 rings for an on-axis source. When added together the nominal ASTRI PSF is obtained.

As plotted in Figures 2.12a and 2.12b the size of the PSF (80% of its light) is comparable with that of the Cherenkov pixel (black square in image 2.12a). The telescope design fits the requirement of having the 80% of the spot light inside the Cherenkov pixel along the entire FoV as can be observed in the PSF photometric profiles in Figure 2.13.

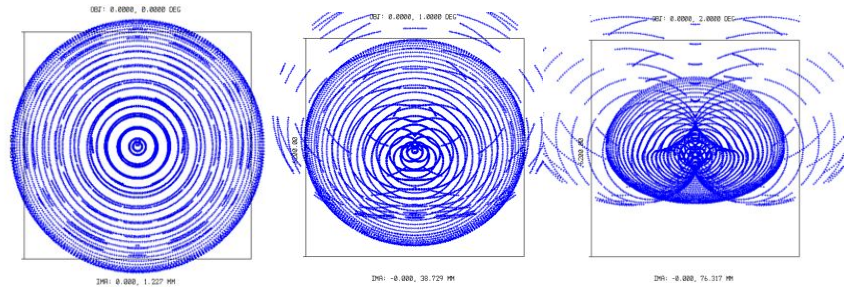

(a)

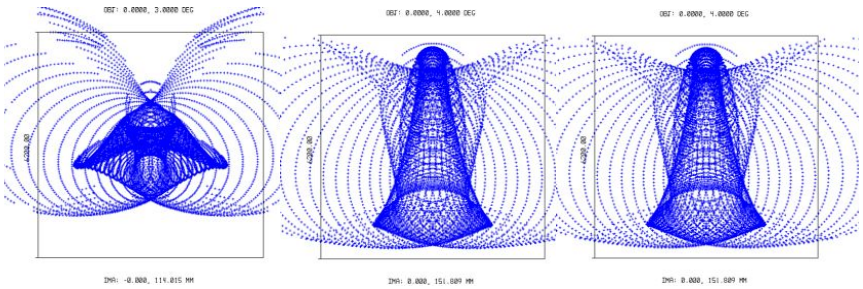

(b)

Figure 2.12: (a) ASTRI PSF evolution along the FoV, for 0° (on-axis), 1°, and 2° (b) PSF for 3°, 4°, 4.8° out of axis source at 10 km of distance. The PSFs are enclosed inside a box with the same size of the Cherenkov pixel (6.2 x 6.2 mm).

The telescope is designed to have a wide FoV ($\sim 9.6°$) and it is optimized to achieve the best angular resolution between fields 1° to 4° as shown in Figures 2.13 and 2.25. For this reason the on-axis field shows a worse performance than the off-axis fields.

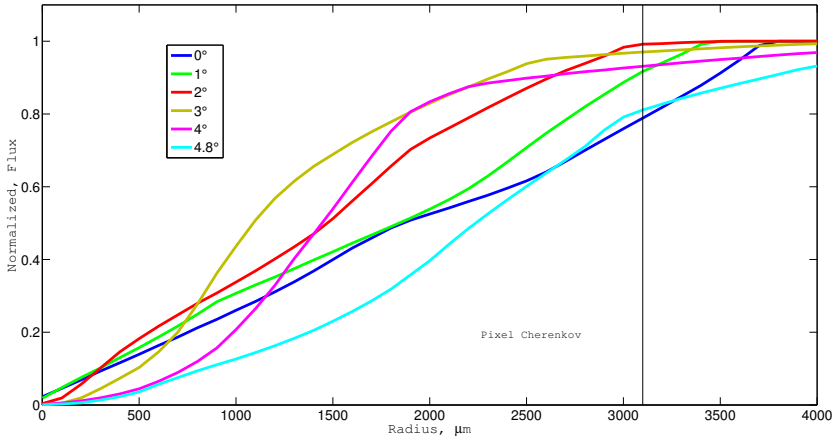


Figure 2.13: Normalized ensquared energy of the telescope PSFs for different fields inside the FoV, the edge of the Cherenkov pixel (3.1 mm) is reported as reference. The pixel should collect at least the 80% of the light of the entire PSF.

## 2.5 ASTRI camera

The ASTRI SST-2M prototype camera is part of the challenging synergy of the novel optical design, camera sensors, front-end electronics and telescope structure design. The shower images on the camera last from few ns ($10^{-9}$ s) to tens of ns and must be promptly identified against the unavoidable NSB light and detector dark noise. As mentioned in the previous sections, the SC configuration produces a curved focal plane and consequently the camera surface is convex with a radius of curvature $R_{FP} = 1060$ mm and a diameter $D = 500$ mm. To cover the focal plane the pixels are arranged in a modular configuration: the physical pixels (3.1 mm $\times$ 3.1 mm) of each sensor unit are grouped in a 2 x 2 logical pixel (6.2 mm $\times$ 6.2 mm) having a sky-projected angular size of $\sim 0.17°$. The Multi Pixel Photon Counters (MPPCs) are Silicon Avalanche Photo Diodes working in Geiger mode (G-APD) by setting a bias voltage greater than the Breakdown Voltage. An MPPC array is composed by 3600 SPADs of 50 $\times$ 50 $\mu$m, and it is produced by Hamamatsu, model $S11828 - 3344M$, further information can be found in the work of G. Sottile et al. [122]. There are many advantages in using MPPCs, such as excellent single photon resolution, high quantum efficiency, low operating voltage, and no damage when exposed to ambient light.There are however also some drawbacks like the very high dark counts, afterpulses, optical crosstalk and gain strongly dependent on temperature.

The aggregation of 4 $\times$ 4 sensor units (8 $\times$ 8 logical pixels) forms the Photon Detection Module (PDM). The PDM module is the mechanical unit containing MPPCs, Front End Electronics, FEE, and PDM-FPGA Printed Circuit Boards (PCBs). The focal plane is covered by a mosaic of 37 PDMs, 57 $\times$ 57 mm each, that fits the curved surface of the camera. The PDMs in the outermost regions of the focal plane are not entirely populated by physical pixels because they are vignetted by the mechanical structure of the camera as shown in Figure 2.14. A view of the focal plane backbone structure hosting the PDM units is given in figure 2.15 and a picture of a single PDM is shown in Figure 2.16.

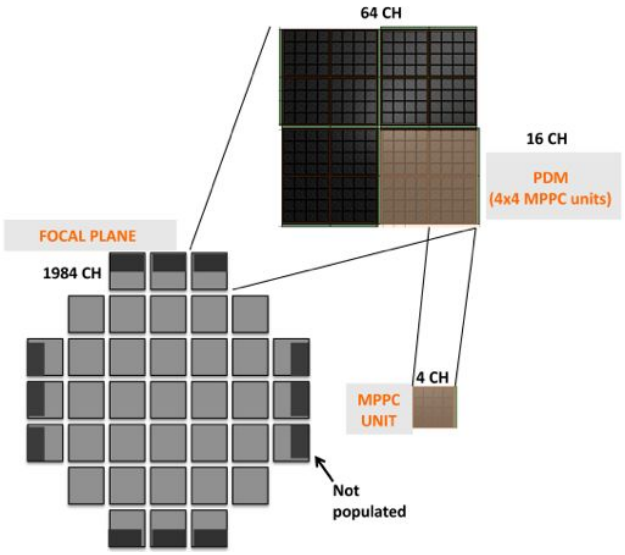


Figure 2.14: The pixels arrangement scheme is constituted by a hierarchical assembly of MPPCs units to create the PDMs. The focal plane is a curved mosaic of 37 plane PDMs (light grey blocks), 64 channels each. Nevertheless, the PDMs allocated at the borders of the focal plane have only half of their area populated by MPPCs (dark grey); this consequently diminishes to 1984 the total number of channels.

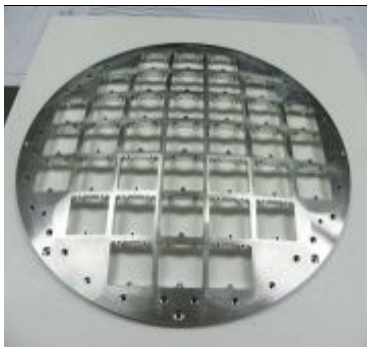

Figure 2.15: Front and side view of the ASTRI SST-2M focal plane backbone. The PDMs are arranged to cover the focal plane by a mosaic of units.

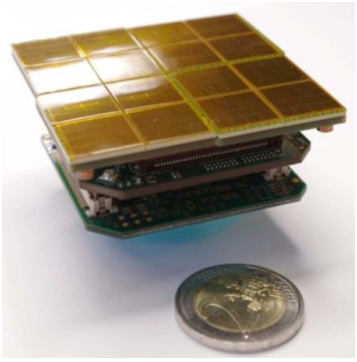

Figure 2.16: A prototype of Photo Detection Module, PDM, Front End and FPGA PCBs. The volume of a PDM is 57 × 57 × 30 mm (two euro coin for reference scale).

The camera can be subdivided into four main subsystems: mechanics, power supply, electronics, thermal. A detailed model of the ASTRI SST-2M camera is reported in Figure 2.17: the focal plane is covered by a Poly Methyl Methacrylate (PMMA) window and a light-tight lid. The PMMA window prevents sand, dust, water and all the other environmental agents from depositing over the PDMs and keeps a thermalized environment around the focal plane avoiding breakdown voltage variation and then gain variations of the MPPCs. The lid is composed by two petals that are opened during the observation runs while are closed during camera relative calibration procedures and when the telescope is not observing.

The electronics assembly comprises MPPCs, Front-End Electronics (FEE) that converts the analog MPPC signals in digital signals while the Back-End Electronics (BEE) controls and manages the overall system, including data management formats, lid mechanisms and fiber-optic calibration. The thermal system controls and keeps the camera temperature at a constant value during telescope observations to impede any possible gain variation of the MPPCs. For more information the reader should refer to the work of O. Catalano and collaborators [24].

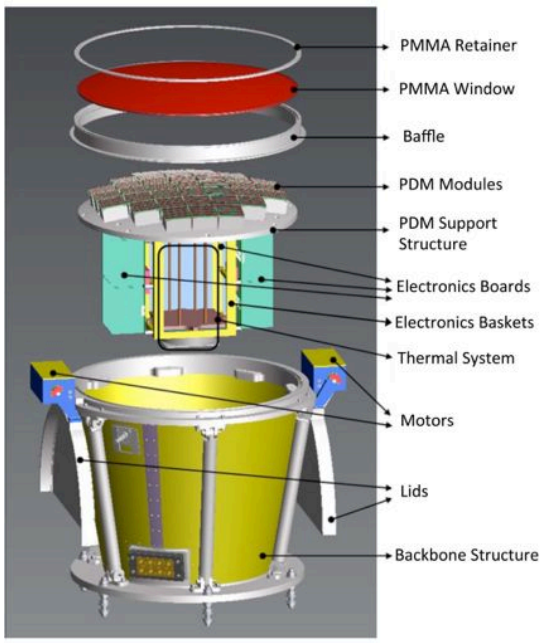


Figure 2.17: The ASTRI SST-2M camera subsystem with the main units (top to bottom): the PMMA window (red) above the PDMs mosaic and the lateral baffle (grey). Below the PDMs, there is the electronics assembly to process the analog signals from MPPCs, the thermal enclosure for thermal control of the camera, the backbone structure, the mechanical interface with the telescope and camera lids (open).

## 2.6 ASTRI active mirror control system

The active optics systems are usually implemented in the so called 4-meters class and higher. An active optics mechanism is used to control the optical shape of the telescope and to maintain proper focus and optical alignment in spite of thermal and gravitational perturbations. In addition, for the optical telescopes, the active optics can correct the deformations in shape of the mirror segments, thus permitting the use of thinner, hence lighter, mirrors and mechanical mounts [15]. In the optical telescopes, the active control consists in the automatic compensation of the optics deformations and misalignments in a closed loop, by monitoring the respective positions of the individual optical elements or measuring errors in the final wavefront. As discussed in section 4.4.2, the active optics has to deal with a wide range of temporal frequencies between the thermal and gravity effects, wind and atmospheric turbulence. For the optical telescopes the working principle is shown in Figure 2.18: the wavefront errors are measured using a bright star off-axis and then compensated by adjusting the position of the secondary mirror and deforming the primary mirror in a closed loop.

The Cherenkov telescopes conversely, do not require an optical phasing at fractions of wavelength of the mirror segments and the active optics mechanism is greatly simplified. These telescopes rely on an system of Active Mirror Control (AMC) that regulates only the orientation of the mirror with respect to the mechanical structure and it does not act on the shape of the mirror surface. The AMC unit is used only for alignment purposes of the mirror segments. Moreover, the AMC system is operated in an open loop, i.e. the mechanism is activated only when the mirror segments require to be aligned. An optical feedback on the alignment status of the telescope optics is provided by a laser mounted on each M1 segment by means of a mechanism that allows all the rotational degrees of freedom (DOF). The laser is hanged by a stiff support to M1 panels and two possible solutions are currently considered: the laser points to M1, it is reflected toward M2 and then imaged on the focal plane (see Figure 2.19a) or it points directly

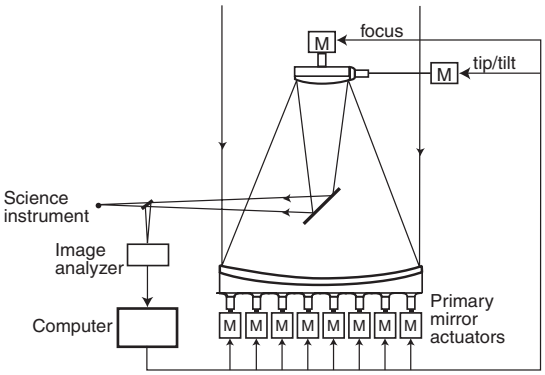


Figure 2.18: Active optics system for NTT and VLT optical telescopes. Photo courtesy Bely [15].

towards M2 and it is then reflected down to the focal plane (see Figure 2.19b).

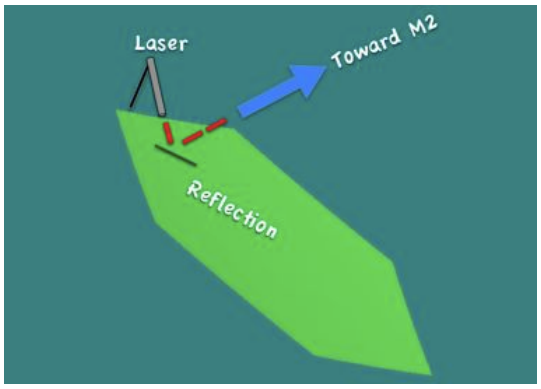


(a)

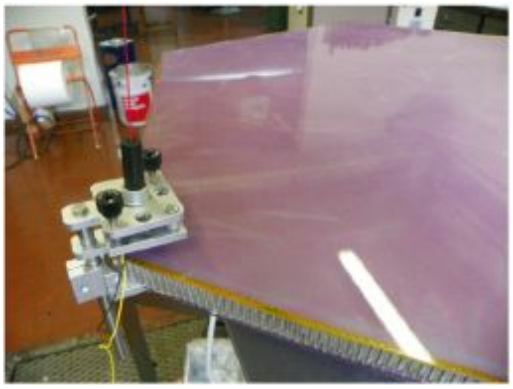

(b)

Figure 2.19: (a) Conceptual scheme of the AMC mechanism with a reflection on M1 and M2 (b) Prototype of the AMC mechanism with a single reflection on M2.

The laser spots should hit the detector plane in a dedicated area where an optical-NIR CCD is positioned. Two CCD cameras should gather the light spots from all the segments of M1. The laser spots coming from the three different rings have well distinguishable shapes: the point-like spots come from the inner ring, the medium elongated spots from the medium ring and most elongated and aberrated spots come from the outer ring (Figure 2.23). The CCD cameras have a sensitive area of 7.06 $\times$ 8.44 mm (Figure 2.22) and are integrated at the corners of the focal plane in some free slots as displayed in Figures 2.20 and 2.21. This avoid the interference of the active optics with the Cherenkov camera.

The lasers spots on the two CCD cameras are used to map any tilt induced on M1 and M2 surface during telescope operations. During telescope operations a software controls the centroids position inside the CCD cameras FoV and measures any possible departure from the nominal aligned pattern that can introduce a pointing error. The centroids shifts are recorded in a database and subsequently used for the data reduction procedure. This tracking flexures system will be used also for possible seasonal re-alignment of the mirror segments.

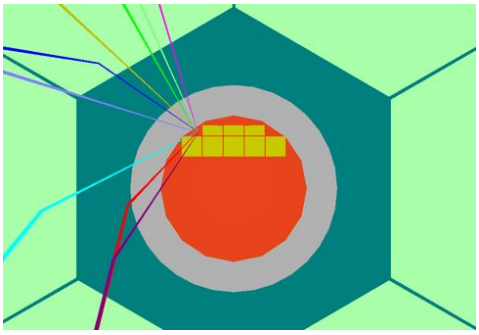

Figure 2.20: The focal plane (red circle) is tessellated by a mosaic of PDMs (yellow squares) and the CCD camera at the corner of the focal plane collects the laser beams coming from M2.

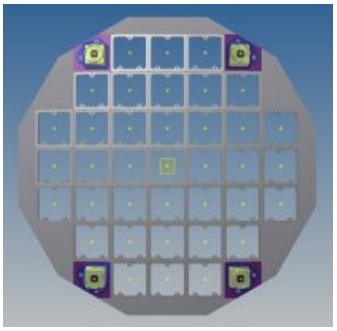

Figure 2.21: Four free slots at the corners of the Cherenkov camera focal plane for the integration of the CCD cameras.

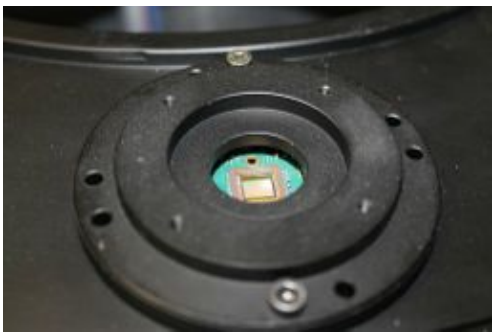

Figure 2.22: CCD camera sensor integrated on the focal plane of the telescope camera.

Figure 2.23: Simulated laser spots pattern as seen from the CCD camera.

## 2.7 ASTRI expected sensitivity

The ASTRI SST-2M prototype is a pathfinder telescope that will assess the performance of S-C design applied to IATCs of the SST class. The main physical tasks of the ASTRI project are the detection and observation of the three brightest VHE sources in the Northern sky: the Crab Nebula and the two AGNs, Mrk 421 and Mrk 501. The estimated energy threshold is defined as the peak of the Crab Nebula differential rate and it is obtained from the convolution of the telescope effective area and the energy spectrum of the Crab Nebula. For the ASTRI SST-2M prototype the energy threshold for a suitable, complete $\gamma$ ray event reconstruction is about 800 GeV [16] as shown in Figure 2.24a (grey line). If an array of multiple telescopes is considered, e.g. 7 elements spaced of 300 m, the energy threshold for a complete analysis is about 5 TeV (Figure 2.24a, black line).
After the commissioning and the operation of the ASTRI SST-2M prototype, INAF is planning to deploy an array of many ASTRI telescopes, namely ASTRI mini-array [135], at the site of CTA South. This array will take part in the early science phase of CTA and the expected sensitivity in comparison with an ASTRI single telescope is shown in Figure 2.24b.

As discussed in section 3.3, IACTs require a suitable angular resolution for a reliable image discrimination between gamma and hadronic events. The differences in shape parameters of gamma and hadron images are in the range $\sim 0.1^\circ - 0.2^\circ$ for the 10-100 TeV energy range where ASTRI operates. The determination of the event hadroness (Figure 2.26) becomes progressively easier for increasing energies. In Figure 2.25 the ASTRI PSF size in degrees for different fields in the FoV is traced.

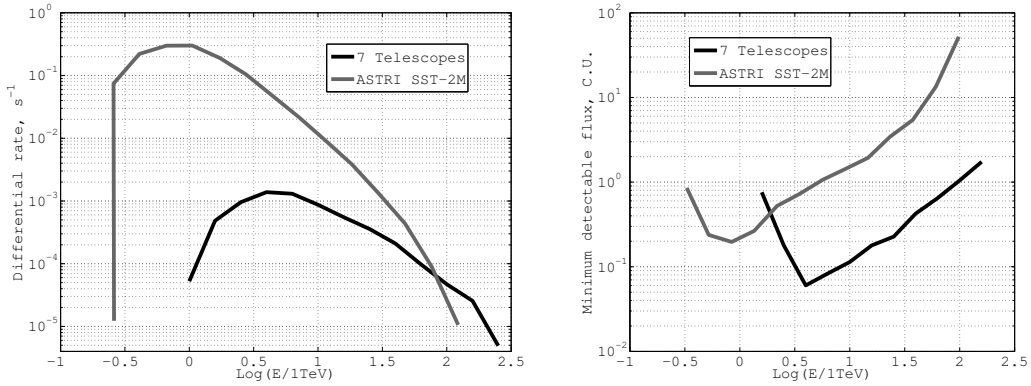


(a) (b)

Figure 2.24: (a) Estimated energy threshold defined as the peak of the Crab Nebula differential rate of photons for the ASTRI prototype (grey line) and the ASTRI mini-array of 7 telescopes (black line). (b) Sensitivity in Crab Units (C.U.) for the ASTRI prototype (grey line) and the ASTRI mini-array made of 7 telescopes (black line) at different energies.

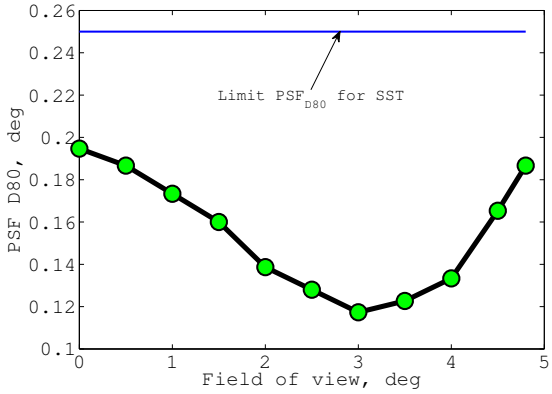


Figure 2.25: Simulated ASTRI PSF ($D_{80}$ values) in the FoV, for all the angles the telescope performs better than the required specifications for SST. The $D_{80}$ value is the reference diameter of the circle containing the 80% of the PSF energy.

MC simulations for different pixel sizes (0.15, 0.2, 0.25, 0.3°) indicate that the best trade-off is 0.2°, assuming the 50% of the total cost of the telescope is from the structure and the 50% from the camera, and hypothesizing that the cost of the latter scales linearly with the number of channels. A pixel size in sky of 0.17-0.2° corresponds to a pixel size on the focal plane of about 6.2 mm. A telescope with a pixel size of a few mm leads to use SiPMs detectors (typically 3 mm pixel) in substitution to larger PMTs of about 1 inch. The advantages of the use of the former detectors are discussed in the next chapter 3.

The limited sensitivity of the ASTRI prototype (0.2 C.U. at 800 GeV, Figure 2.24b) will not allow any competition with respect to the existing arrays and only the detection of the Crab Nebula and of the brightest AGNs (Mrk 421 and 501) is foreseen. The Crab Nebula can be detected at a 5 sigma level in about 2 hours, while Mrk 421 and Mrk 501 in low state (0.30 C.U. and 0.25 C.U.) in 22 and 32 hours respectively [16]. The mini-array sensitivity will be significantly higher than the protype's one (Figure 2.24b) and above 10 TeV it will be even better than the sensitivity of current generation of IACTs. In the future perspective of 50-70 SSTs in the final CTA Southern array the sensitivity will be enhanced by another order of magnitude opening a completely new window on the VHE Universe.

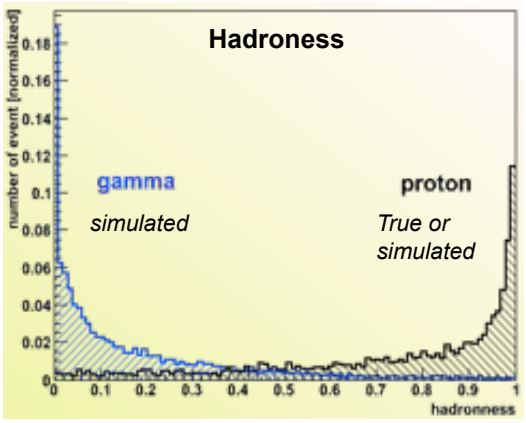


Figure 2.26: The hadroness parameter is a probability associated to the detected/simulated event of being a real $\gamma$ ray or a hadron. The parameter is dependent on the energy of the cosmic ray, and the distribution of $\gamma$ rays and hadroness have always a certain overlap for a given hadron degree. Image from [124]

# Chapter 3

# Comparative study of wide-field Cherenkov telescopes

This chapter collects a brief comparative study about the different optical solutions proposed for the development of wide-field Cherenkov telescopes. In particular, the discussion summarizes a trade-off between well known prime-focus designs and novel dual configurations proposed for $\gamma$ ray astronomy. The comparison is based on a study of the aberrations, the angular resolution, the isochronicity and obscuration factors of these systems. The analysis points out how the dual configurations even if more complex, perform better than prime-focus solutions and lead to use more compact design and finer pixelated cameras.

## 3.1 Prime-focus vs dual configuration

As discussed in section 1.2, the first observation of a $\gamma$ ray signal at TeV energy from the Crab Nebula took place in the 1989 by the Whipple telescope [138]. The Whipple telescope was the pioneer instrument of the current generation of imaging air Cherenkov telescopes operating today (see section 1.4.2 for details): MAGIC, H.E.S.S., VERITAS. All these telescopes have a prime focus optical design and they are very fast systems, F/# $\sim$1. The reflecting surfaces of the IACTs are tessellated by a mosaic of mirror tiles (square, hexagon or round) to form a uniform shape that can be parabolic, spherical or having a Davies-Cotton (DC) design [28]. Spherical and parabolic mirrors are described by eq. 2.3 with the conic constants respectively $k = 0$ and $k = -1$ and all the aspherical terms in the summation null. The DC configuration foresees an array of spherical facet mirrors which are all identical and mounted on a spherical structure with a radius of curvature $R$ equal to the focal length of the telescope. Each facet has the same radius of curvature, $2R$, facilitating fabrication at a reasonable cost and making alignment easy. The normals to the mirror facets point in the direction of the point $(x, y, z) = (0, 0, 2f)$. The $z_m$-coordinate and the tilt angle $\theta_m$ that each mirror has to keep are given by the following relations:

$$z_m = \rho_m - \sqrt{\rho_m^2 - x_m^2 - y_m^2} \tag{3.1}$$

$$\theta_m = \arctan \frac{R_i}{\rho_m - z_m} \tag{3.2}$$

with $\rho_m$ denoting the radius of curvature of the mirror, $x_m$, $y_m$ mirror facets coordinates and $R_i$ radial coordinate of the mirror facet inside the supporting spherical structure. The Schmidt telescope has still a single spherical mirror, but coupled with a refracting corrector plate positioned in the radius of curvature of the reflector. The resulting focal plane is curved with the

radius of curvature halved with respect to that of the primary mirror and it is located between the corrector plate and the reflector. The refracting corrector plate has an aspherical surface that compensates in advance for the spherical aberration induced by the primary mirror and its sag is described by eq. 2.3 with non-null aspherical terms inside the summation. The general baseline for the development of Cherenkov telescopes is driven by the need for fast systems (F/# $\sim$ 1), large collecting power, wide field observations and limited aberrations for off-axis sources. The need of wide-field imagers is extremely important for the SSTs that must guarantee a corrected FoV of $\sim 8^\circ$ with the possible goal of $\sim 9^\circ$. For this reason is worthwhile to discuss the main optical performances of prime-focus vs dual mirror configurations. The optical configurations envisaged in this study are prime-focus spherical, parabolic, DC, Schmidt and dual mirror SC. The main optical specifications of the telescope models assumed are collected in Table 3.1.

| **Surface** | **Diameter (mm)** | **Curvature radius (mm)** | **Total track (mm)** | **F/#** |
|---|---|---|---|---|
| **Prime-focus** | **Spherical** | | | |
| M1 | 4300 | -20800 | 10360 | 2.42 |
| Camera | 1780 | 0 | | |
| **Prime-focus** | **Parabolic** | | | |
| M1 | 4300 | -20800 | 10400 | 2.42 |
| Camera | 1780 | 0 | | |
| **DC** | | | | |
| M1 | 5000 | -20000 | 10000 | 2 |
| Camera | 1600 | 0 | | |
| **Schmidt** | | | | |
| M1 | 4200 | -4300 | 4310 | 0.53 |
| Corrector | 3772 | -6.07e-12* | | |
| Camera | 360 | -2150 | | |
| **SC** | | | | |
| M1 | 4306 | -8223.8 | 3215 | 0.51 |
| M2 | 1800 | 2180 | | |
| Camera | 360 | 1060 | | |

Table 3.1: Main optical parameters of the telescopes considered in the comparative study. $*4^{th}$ term of the even asphere describing the shape of the corrector plate.

## 3.2 Aberrations

In the results presented here the most important and frequent aberrations (Seidel aberrations) affecting the optical systems such as the spherical aberration, the coma, the astigmatism, the field curvature and the distortion are taken into account. All the telescopes are considered observing a source at 10 km height. With reference to Figure 3.1, the spherical mirror suffers important limitations due to all the main aberrations except for the distortion. The predominant contribution comes from the spherical aberration. The parabolic mirror performs better than the spherical for on-axis sources because it is free from spherical aberration even if it suffers of large comatic effects when observing off-axis sources. The DC configuration shows smaller off-axis aberrations than a parabolic and spherical reflector so that it has constant and good image quality out to a few degrees from the optical axis. The predominant aberration for the DC model is the distortion. If an additional optical element is added to the primary mirror of the telescope, the system can reach better performances over the entire FoV and having a more compact layout. In the Schmidt telescope the position of the corrector plate in the radius of curvature of the mirror eliminates the coma and astigmatism aberrations. As shown in Figure 3.1, the Schmidt telescope performs better than all the other optical solutions considered. A study by R. Mirzoyan and M. I. Andersen [96] proposes the use of a Schmidt configuration for

the Cherenkov telescopes to increase the corrected FoV. The final design described by the authors results in a F/0.8 system with a FoV of 15°. The main technical drawback of the proposed design is related to the corrector plate that has a diameter of 7 meters and it must be segmented because a monolithic lens of such diameter cannot be built. Also the corrector of the Schmidt telescope considered in the present comparative study (see Table 3.1) has a diameter of 3.7 m that is practically hard to implement.

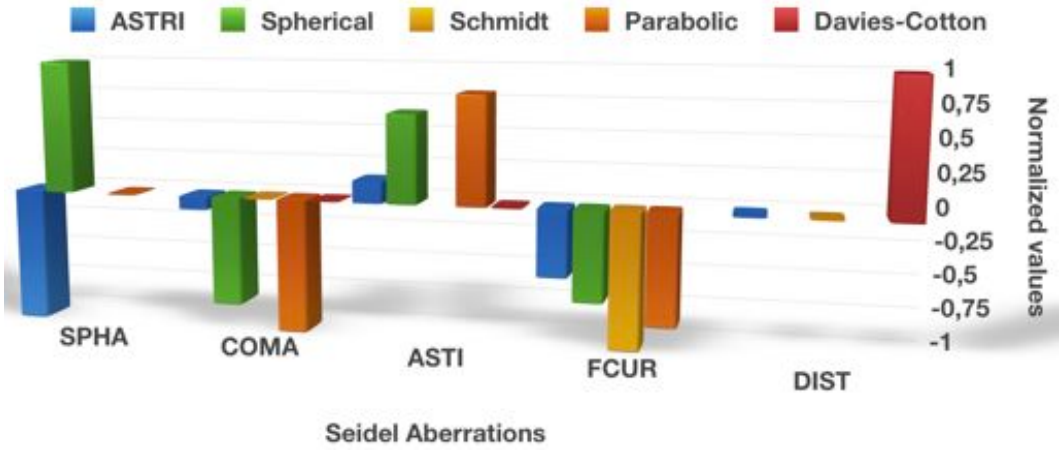


Figure 3.1: Main aberrations affecting the optical systems considered in the simulations. The values are normalized for each single optical configuration to permit a reliable comparison between the different telescopes. SPHA = spherical aberration, COMA = coma, ASTI = astigmatism, FCUR = curvature of field, DIST = distortion.

A more practical solution to contain the aberrations over a wide-field comes from the use of a secondary mirror by means of a SC telescope. As shown in Figure 3.1 the coma and the astigmatism are contained over the entire FoV; as for the Schmidt telescope the focal plane is curved. These improved performances over prime-focus telescopes are gained by the use of a secondary mirror that creates also a more compact system as discussed below in section 3.3.

## 3.3 Resolution

As discussed by R. Mirzoyan and M. I. Andersen [96], to distinguish between gamma and hadron showers the resolution required is about $\sim 0.1° - 0.2°$ for the TeV energy range and a few time less for the 100 GeV energy range. This requires an adequate angular resolution of the telescopes to disentangle between the two sources of the air showers. Usually the starting point for the design of a telescope is the detector that is intended to be used and the requirement of resolution in sky. All the large Cherenkov telescopes currently operating use the PMTs that have $\sim$ 1 inch size. A great novelty has been introduced in the last years by the First G-APD Cherenkov Telescope (FACT), that is the first in-operation test of the performance of silicon photo detectors in Cherenkov Astronomy [17]. As explained in section 2.5, SiPMs have much smaller size ($\sim$ one order of magnitude) in comparison to PMTs and can lead to a new design approach of the Cherenkov telescopes.
For instance, the plate scale for ASTRI is 96"/mm. Considering the pixel size of SiPMs (3.1 x 3.1 mm) binned in a matrix 2 $\times$ 2 to create a logical pixel in the camera of 6.2 $\times$ 6.2 mm gives an angular resolution of the system in sky of $\Delta\theta \sim 0.166°$. To get the same angular resolution with the PMTs, the required focal length would be f $\sim$ 10400 mm, resulting in a large system of about 10 m for a prime-focus telescope. In comparison, the separation of ASTRI M1-M2 is only $\sim$ 3.2 m. A dual mirror SC design allows to get the same angular resolution of a single mirror telescope with a more compact system. This compactness leads to smaller supporting mechanics

and a lighter camera envelope. The PSFs in arcmin and in mm (on the focal plane) for all the telescopes simulated are plotted in Figures 3.2a and 3.2b.

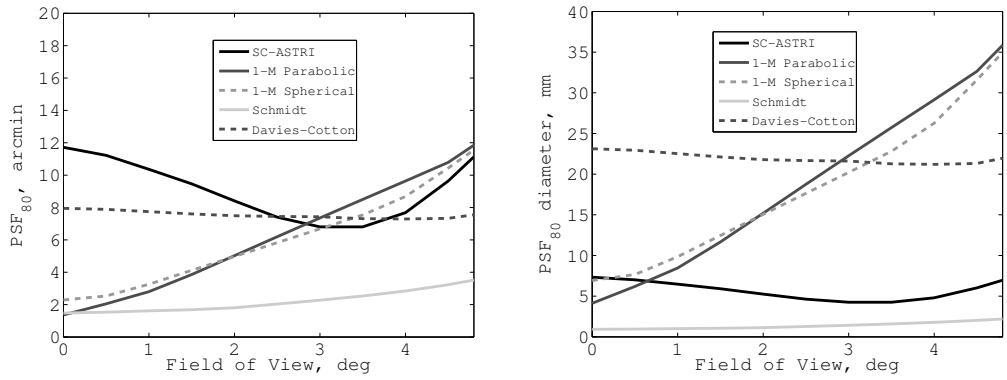


(a) (b)

Figure 3.2: (a) Angular size of the telescopes PSF in sky over a FoV $\sim 9.6°$. (b) Linear size (diameter) of the PSFs on the focal plane of the telescopes: single mirror designs require the use of PMTs while dual elements design can exploit much more compact pixel solutions.

A graphical representation of the telescope PSFs is given in Figure 3.3. Each PSF has a scale bar expressed in micron. As the reader can note the PSFs from prime-focus telescopes have physical sizes in the order of 20-30 mm and require the use of PMTs, while the PSFs from Schmidt and SC telescopes are about 6 mm and lead to the use of SiPMs.

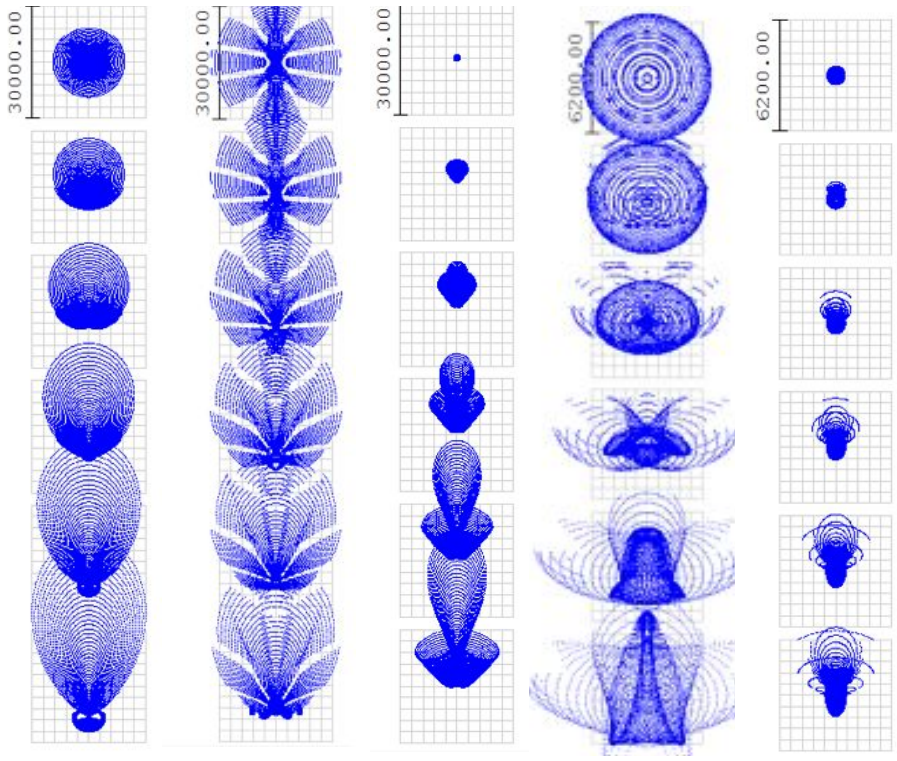


Figure 3.3: From left to right: PSFs of a spherical, Davies-Cotton, parabolic, ASTRI and Schmidt telescope. From top to bottom: PSFs evolution at the same points inside the FoV (0,1,2,3,4,4.8°). The scale bar is in micron.

## 3.4 Wavefronts time spread

An important aspect that has to be taken into account in the design of the Cherenkov telescopes is the optical path difference of the rays that enter the telescope pupil in different points. These optical path differences have to be minimized and the telescopes must be as much isochronous as possible in order to get an effective suppression of the background. As for the angular resolution, the requirement on isochronicity is more stringent for energies below 100 GeV. The prime-focus telescopes (Figures 3.4 and 3.6) are less isochronous than the Schmidt design (Figures 3.7). DC performs better than the spherical and parabolic solutions while SC (Figure 3.8) constitutes an intermediary case. DC design have important deviations from isochronicity as the diameter of the reflector increases; for the present model no significant deviations from the average time spreads of the other telescopes are observed. As expected the outer fields of the FoV suffer from greater un-isochronicity for all the telescopes considered. In the following, the plots of the tangential and sagittal time spreads computed at $\lambda = 0.55$ $\mu$m for the different telescopes studied are shown in Figures 3.4, 3.5, 3.6, 3.7 and 3.8.

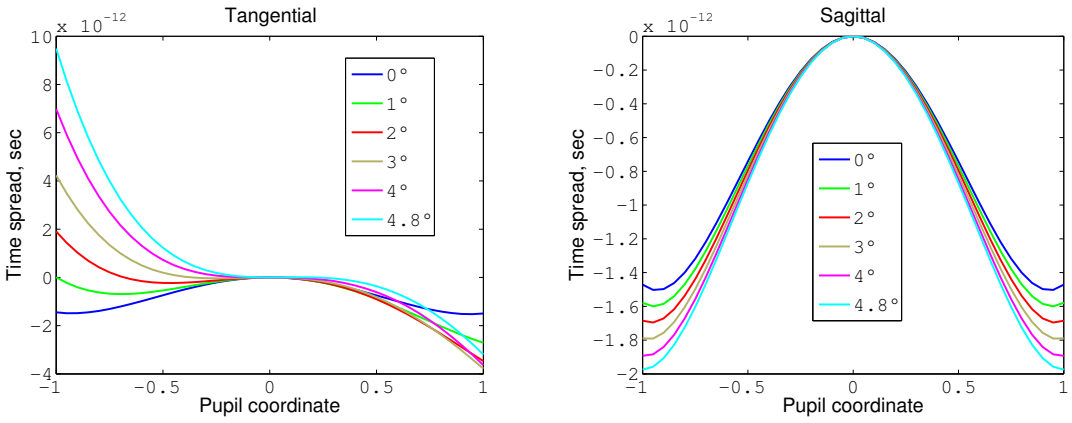


(a) (b)

Figure 3.4: (a) Tangential and (b) sagittal time spread of the photons at $\lambda = 0.55$ $\mu$m after the reflection on a spherical mirror (normalized pupil coordinates).

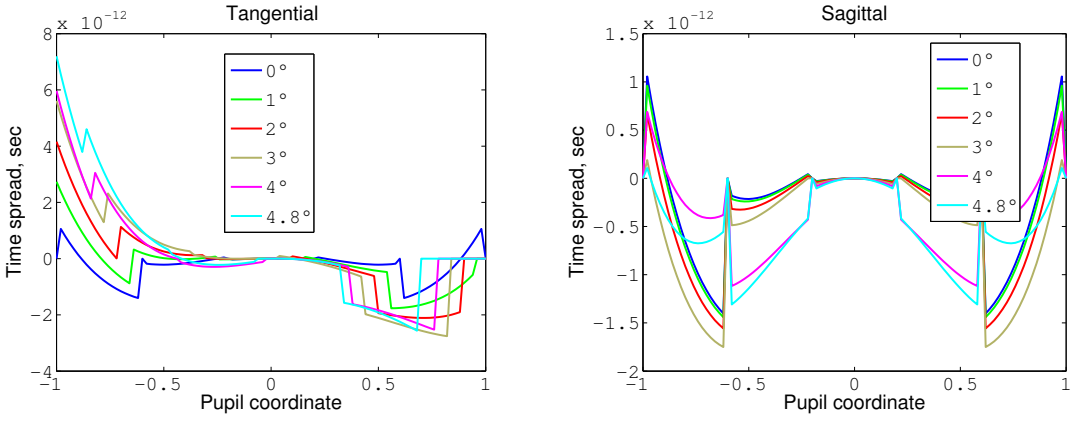


(a) (b)

Figure 3.5: (a) Tangential and (b) sagittal time spread of the photons at $\lambda = 0.55$ $\mu$m for a Davies-Cotton telescope (normalized pupil coordinates).

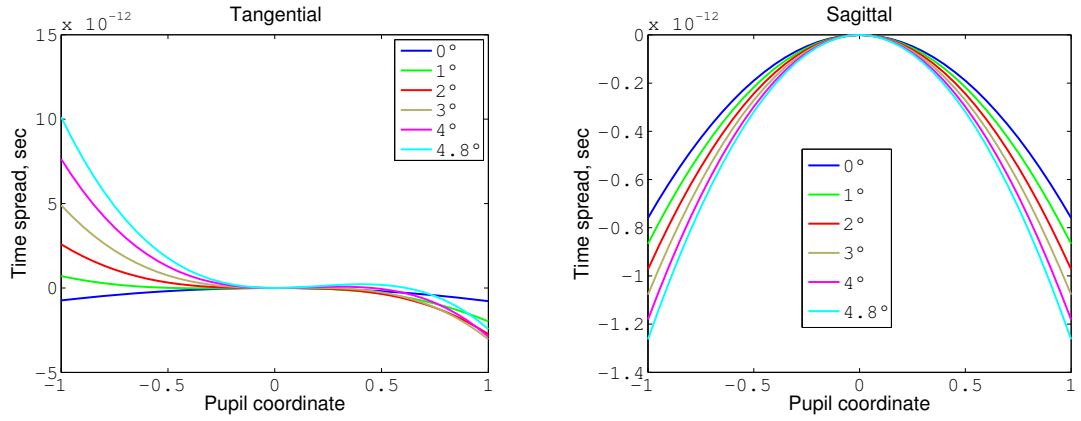


(a) (b)

Figure 3.6: (a) Tangential and (b) sagittal time spread of the photons at $\lambda = 0.55$ $\mu$m after the reflection on a parabolic mirror (normalized pupil coordinates).

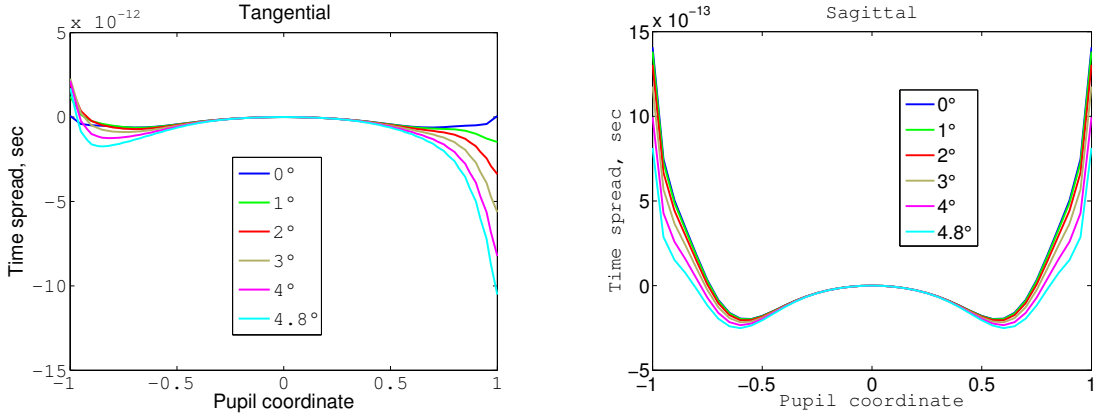


(a) (b)

Figure 3.7: (a) Tangential and (b) sagittal time spread of the photons at $\lambda = 0.55$ $\mu$m for a Schmidt telescope (normalized pupil coordinates). This optical configuration preserves the best isochronicity among all the telescope solutions.

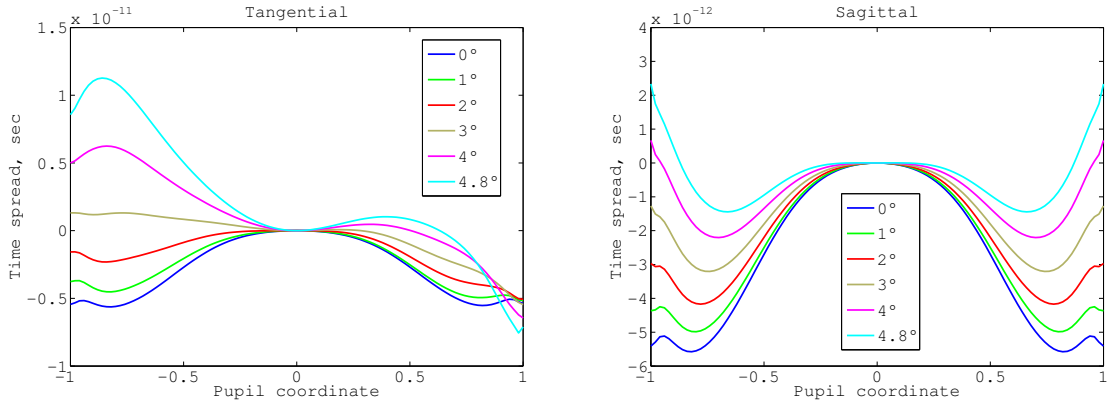


(a) (b)

Figure 3.8: Tangential and (b) sagittal time spread of the photons at $\lambda = 0.55$ $\mu$m for a SC telescope like ASTRI (normalized pupil coordinates). This optical configuration preserves a good isochronicity and performs better than the prime-focus solutions along the sagittal axis.

## 3.5 Obscuration ratio

There is a conceptual difference between the central obscuration ratio in an on-axis reflecting telescope, that is the part of the aperture blocked by the secondary mirror and baffle and the vignetting, which is the gradual fading near the edge of the field of an optical system due to partial obscuration by intermediate optical components [15]. The vignetting is a function of the field coordinates on the focal plane and depends on an asymmetrical obstruction of the rays. The obscuration ratio instead limits the entrance pupil by the presence of an absorbing element that can be a mirror, a camera or a baffle. When dealing with prime-focus telescopes, it is interesting to note that although fast systems (small F/#) limit the obscuration ratio in comparison to a slower system, fast telescopes can exploit smaller pixel size and consequently have a more compact and smaller camera. Moreover the overall structure is more compact and the supporting mechanics can be lighter and hence creating less vignetting of the rays. The introduction of a secondary optical element, a mirror or a corrector plate, improves the telescope performances at the expenses of the overall obstruction ratio $\epsilon$.

$$\epsilon = \frac{D_{M2}}{D_{M1}}$$

with $D$ diameter of the mirrors. In the case of Schmidt telescopes the corrector plate and the camera position decreases the fraction of unobscured rays as shown in Figure 3.9. Also the presence of a large secondary mirror in the SC configuration develops significant obscuration of the primary mirror. The percentages of rays incident upon the entrance pupil which pass all obscurations and apertures in the system and survive to the image surface, normalized to relative pupil area are shown in Figure 3.9.

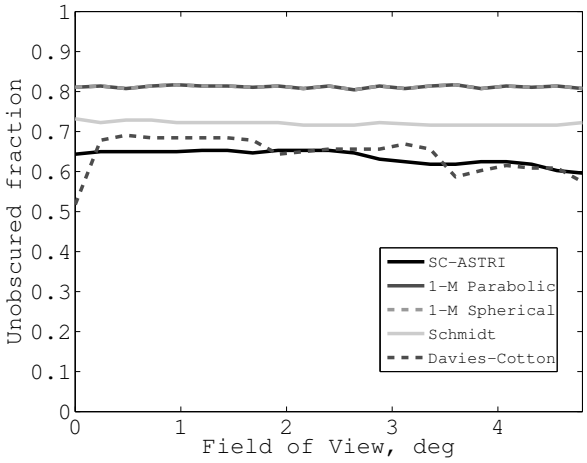


Figure 3.9: Fraction of unobscured rays for the simulated telescopes. Two elements systems suffer greater obscuration ratios.

## 3.6 Concluding remarks

The problematics of the wide fields with prime-focus reflector have been long studied by many authors as J.M. Davies, E.S. Cotton [28], A. Schliesser and R. Mirzoyan [115] and T. C. Weekes et al. [139]. For the development of new IACTs optical designs even more complex telescopes have been assessed by V. Vassiliev et al. [134] and R. Mirzoyan and M. I. Andersen [96]. The work by A. Schliesser and R. Mirzoyan [115] proves that by using a F/2 design is possible to build prime-focus telescopes with a full FoV of 10° at 0.1° resolution. The paper by R. Mirzoyan and M. I. Andersen [96] instead, proposes the use of a Schmidt configuration to improve the corrected FoV and resulting in a F/0.8 system with a FoV of 15°. The comparative study presented here is addressed to the recognition of an equivalent angular resolution by means of different optical design configurations. As pointed out by the authors above mentioned and verified by the simulations here presented, the use of a dual element system (Schmidt or SC telescopes) allows better performances to be achieved over a wide FoV at the expenses of a greater complexity of the system and a certain obscuration ratio of the primary mirror. The advantages coming from the use of a dual elements design are however important in terms of reduction of the camera dimensions and a reduced size of the telescope overall mechanical structure.

# Chapter 4

# ASTRI compliance analysis with the science and performance requirements of CTA

In this chapter a detailed discussion is deserved to the ASTRI design in relation to the performance and environmental requirements for SST. All the requirements mentioned and discussed in the following sections are collected in the documents CTA Observatory MAN-PO/121011, Science Requirements for CTA SCI-LINK/121120, Performance Requirements for CTA MAN-PO/121004, Environmental Requirements for CTA MAN-PO/120918, SST Requirements MAN-PO/120808 that can be found at the CTA Indico webpage [160]. The scheme of this chapter follows the hierarchy of the CTA high-level documentation: from the CTA concept (section 4.1) the science requirements are listed (section 4.2). Then, from the science requirements the performance and environmental requirements (Level A) which apply across all components of the CTA Observatory are derived (section 4.3). Finally the SST requirements (Level B) are discussed in detail in separate paragraphs collected in section 4.4.

## 4.1 The CTA concept

The Cherenkov Telescope Array (CTA) is an observatory for very-high-energy gamma-ray astronomy which will provide observers with data on astrophysical objects over a very wide range of gamma-ray energies. The CTA Observatory is intended to provide a service to a wide scientific community, beyond those institutes currently involved in the design of the instrument and in the preparation of its construction (the CTA Consortium). CTA will be a targeted instrument following a standard model for observatory operations. Observation proposals from scientists will be reviewed and selected based on scientific merit, and CTA observation time may be allocated, observations performed, and data reduced and delivered to the proposer (The CTA Observatory [161]). Detailed Monte-Carlo (MC) simulations have been performed to establish the performance of a range of CTA candidate arrays assuming demonstrated techniques and technologies. In parallel, scientific requirements have been developed to assess the possible scientific impact of the Observatory. In the next section the science requirements are briefly introduced given the extended discussion already stated in section 1.5. A wide discussion instead is deserved to the performance requirements in relation to ASTRI/SST design to achieve the scientific goals.

## 4.2 CTA science requirements

The Cherenkov Telescope Array, CTA, project is an initiative to build the next generation ground-based very high energy gamma-ray instrument. It will serve as an open observatory to a wide astrophysics community and will provide a deep insight into the non-thermal high-energy Universe [161]. CTA will perform investigations on three main science branches:

- Cosmic particle acceleration, propagation and impact: investigate the site of production of cosmic rays, the mechanism of acceleration and transport and the feedback on star formation and galaxy evolution.
- Probing extreme environments: the physical processes occurring in the neutron stars, black hole, relativistic jets, AGNs and galaxies clusters.
- Physics frontiers: the nature of the dark matter, the speed of light for VHE photons and axion like particles.

With respect to its precursors MAGIC, HESS and VERITAS, CTA is designed to increase the sensitivity by a factor 10 at 1 TeV, to increase the detection area, angular resolution and FoV. CTA will cover a wide range of energy spanning from 20 GeV to 300 TeV and it will be characterized by high flexibility, enhanced monitoring and deep survey capabilities. CTA will also perform short time scale observations and simultaneous observations in multiple fields. CTA will provide full-sky coverage by deploying two different arrays: CTA South, the largest observatory, to address the observations of galactic objects and the galactic black hole and CTA North mainly devoted to the extragalactic sources. To achieve this ambitious goal the observing facility has to fulfill a series of performance requirements that are presented in the next section.

## 4.3 CTA performance requirements

An array of many tens of telescopes will allow the detection of gamma-ray induced cascades over a large area on the ground, increasing the number of detected gamma rays dramatically. This results in both improved angular resolution and better suppression of cosmic-ray background events. To achieve the science requirements the CTA Observatory has to be compliant with a series of performance requirements that can be subdivided into a series of classes:

- Sky coverage
- Energy range
- Sensitivity / minimum detectable flux for point-like sources
- Energy resolution
- Effective collection area
- Field of view
- Angular resolution
- Flexibility of operation

The CTA Observatory will cover the entire VHE sky by deploying two arrays, one in the Northern and the other in the Southern hemisphere. The CTA South energy coverage extends for approximately five orders of magnitude and it is subdivided into three main segments: low

energy < 100 GeV, medium energy 100 GeV - 10 TeV and high energy > 10 TeV. The Northern hemisphere array will have a smaller number of elements and a narrower energy coverage, about 20 GeV - 20 TeV. The uncertainty in the photons energy reconstruction must be < 15 %. CTA will consist of three types of telescopes with different sizes in order to cover the full energy range as listed below.

- The low energy instrumentation, 20-100 GeV, will consist of 4 Large Sized Telescopes (LST) 24-metres-class telescopes, FoV ∼4-5 deg.
- The medium energy range, from 100 GeV to 10 TeV, will be covered by ∼ 25 Medium Sized Telescopes (MST) of the 10-12 metres class, FoV ∼ 6-8 degrees.
- The high energy instruments, operating between 1 and 300 TeV, will consist in 35 to 70 Small Sized Telescopes (SST) 4-6 metres diameter telescopes, FoV ∼ 10 degrees.
- To improve coverage of the Dark Matter parameter space, an additional array of medium-sized telescopes ($D_{M1} = 9.66$ m), Schwarzschild-Couder type [134], will be deployed.

The required differential sensitivity in the energy range of interest is subdivided between the three telescope sizes and shown in Figure 4.1. The overall optical efficiency of the telescope to signal photons must be >15 %.

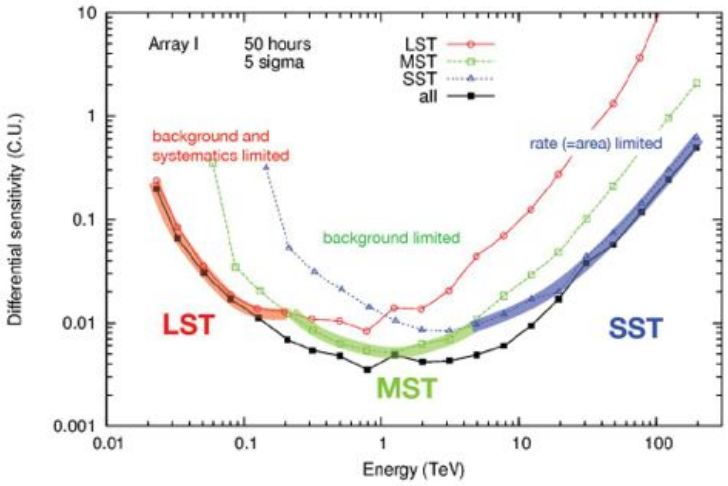


Figure 4.1: Energy coverage and differential sensitivity of CTA for the three different telescopes size, image taken from G. Lamanna [87].

In contrast to other telescopes, where the collection area is related to the dimension of the primary dish, here it is connected to the maximum core distance at which showers can be detected, which is of the order of a few hundreds of meters which is greater than the physical dimensions of the telescope itself. The detectability limit for a shower is related to a minimum number of Cherenkov photons that should be collected in order to have a fairly good imaging of the shower (e.g. 100 photons). Thus increasing the optical collection area of the telescope, e.g. increasing the dimension of the primary mirror, allows to reconstruct images for increasingly dim showers, preferentially produced by low energy gamma ray primaries; thus extending downwards the observed energy band rather than increasing the collection area for gamma rays. The collection area for CTA South will have to meet the profile shown in Figure 4.2.

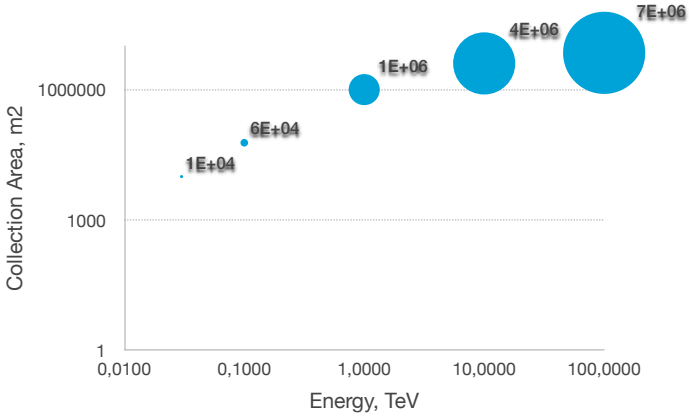


Figure 4.2: Collection area for CTA South in the energy range 30 GeV-100 TeV (logarithmic scale).

The field of view of CTA in the range 30 to 100 GeV will have to be greater than 1 degree while it will have a FoV $> 3$ degrees between 0.1-300 TeV. The LST, MST and SST telescopes will have different angular resolutions as shown in Figure 4.3.

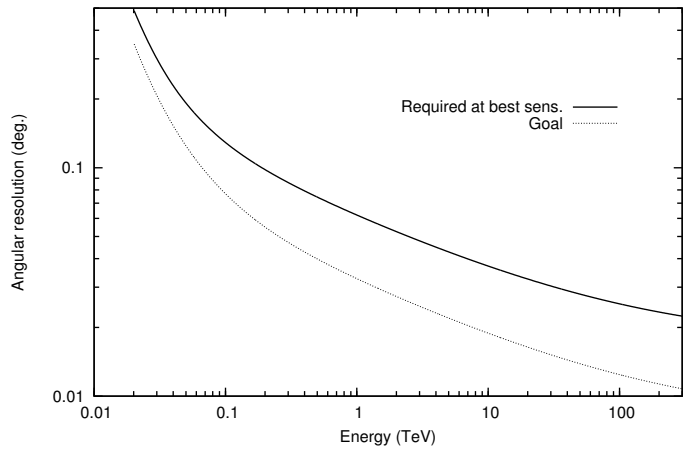


Figure 4.3: Required and goal angular resolution for the CTA Southern array as a function of energy, showing the 68 % containment radius of the $\gamma$ ray point-spread-function. The corresponding curves for the CTA Northern array are identical below 20 TeV and not specified above that threshold. Plot taken from CTA MAN-PO/121004 [161].

CTA will provide high flexibility of operation and scheduling, ranging from all telescopes targeting the same object, to subdivision into a number of independent subarrays targeting different objects and/or energy ranges. Great potentialities will come from the modular design of CTA that allows extensions and upgrades of the array layout. Extensions will increase the CTA performance envelope by adding new instrumentation with new capabilities to the CTA baseline configuration. In the next section the performance requirements of SSTs are discussed in relation to the ASTRI solutions designed to fulfill each of them.

## 4.4 SST Requirements

The SST requirements belong to Level B requirements and they concern the specifications of the telescope performances and the environmental conditions which they have to survive. We

first introduce the environmental parameters of impact for the operations and subsequently the system performances that an SST has to fulfill and the related estimations for the ASTRI prototype. The order of this compliance analysis is subdivided as: performances on positioning and pointing, optics, thermal analysis and camera calibration.

### 4.4.1 Environmental factors

The Cherenkov telescopes have no protective enclosures or domes therefore they are continuously exposed to the atmospheric environment during day and night-time for their entire lifetime. This 'exposed' condition has important implications on the telescope design and maintenance in order to guarantee the observational and operational requirements and instrumentation reliability during the entire lifetime of the project (30 years). The telescope prototype is conceived to withstand the most severe expected loading conditions among the candidate sites of the final telescope array, as well as the site of the prototype itself. Concerning earthquakes, CTA requirements state that the telescope structure has to survive a peak horizontal ground acceleration $<$ 0.26g and a peak vertical ground acceleration $<$ 0.3g with 10% probability of exceeding these figures within 10 years. The simulation of the ASTRI SST-2M response to earthquake-induced accelerations is shown in Figure 4.4 taken from Galbiati EiE Consortium (GEC), (Internal report [163]).

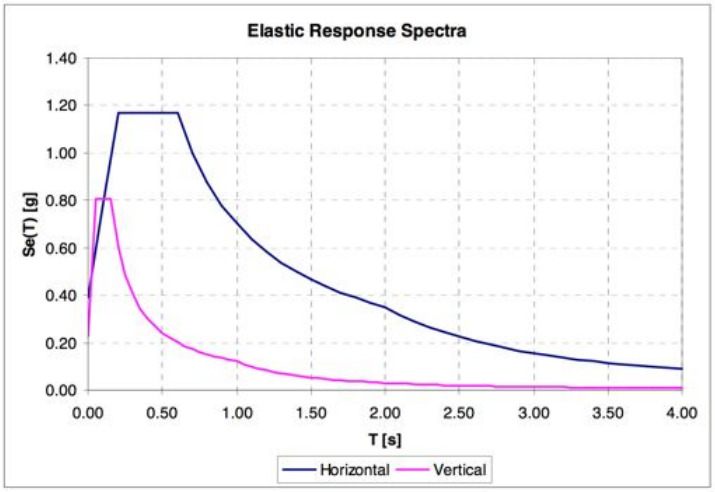


Figure 4.4: Response spectra of the ASTRI SST-2M structure for strong seismic level (Argentina site).

Regarding precipitation, no equipment must incur damage (survival condition) for precipitation in the form of rain, snow and hail for wind speeds $<$90 km/h. To prevent damage from snow ASTRI SST-2M is equipped with snow mechanical shields that protect the primary mirror segments and also M2 is protected from precipitations by the MSS (see Figure 2.10d). The telescope is designed to survive for 1-s wind gusts of $<$200 km/h or 10-minute average wind speeds $<$120 km/h, to survive in a temperature range -25 °C +60 °C and to operate between -10 °C +30 °C. A strong wind can induce vibrations on the mechanical structure of the telescope and in the most unlucky scenario it can excite its mechanical resonances. In this scenario the telescope can undergo loss of pointing and tracking accuracy with negative effects on the quality and reliability of the observations, the order of magnitude of the winds effect is discussed in section 4.4.2.

### 4.4.2 Positioning and pointing

Concerning the positioning and pointing capabilities, SSTs must be able to rotate to any point in the sky above 30 degrees in elevation in at most 90 s. The telescopes must be able to track any target for elevation angles smaller than 89.2 degrees in the positioning range for observations with a precision in each axis of <0.1 degrees. The rms space-angle (post-calibration) pointing precision by which a physical position in the camera can be mapped to a celestial coordinate at a given time, must be <7 arcsecs during favorable observation conditions. In relation to these requirements an error budget tree (Internal report [159]) for the ASTRI SST-2M prototype has been created for the three main components of the ASTRI prototype: M1, M2 and the camera detectors. The reference system is as follows (see also Picture 4.5):

- X parallel to the telescope elevation axis
- Y parallel to the cross-elevation axis
- Z parallel to the optical axis.

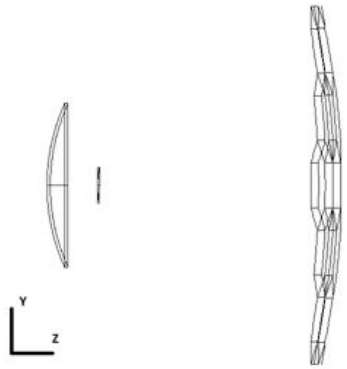


Figure 4.5: Reference frame assumed for the tolerance study on the opto-mechanical flexures. The x axis is entering the paper.

The maximum tolerable errors on the alignment of M1, M2 and camera are collected in Tables 4.1, 4.2 and 4.3 respectively.

| Parameter | Value |
|---|---|
| **M1 segments in plane alignment errors X** | ± 2 mm |
| **M1 segments in plane alignment errors Y** | ± 2 mm |
| **M1 segments alignment axial alignment errors Z** | ± 4 mm |
| **M1 segment tilt around X** | ± 30 arcsec |
| **M1 segment tilt around Y** | ± 30 arcsec |
| **M1 segment tilt around local Z** | ± 4 arcmin |

Table 4.1: Alignment constraints for M1 panels.

#### Errors contribution to telescope pointing

The errors affecting the telescope pointing performance can be divided into four main components:

| Parameter | Value |
|---|---|
| **M2 displacement respect to M1 X** | ± 3 mm |
| **M2 displacement respect to M1 Y** | ± 3 mm |
| **M2 displacement respect to M1 Z** | ± 4 mm |
| **M2 tilt around X respect to M1** | ± 10 arcmin |
| **M2 tilt around Y respect to M1** | ± 10 arcmin |
| **M2 displacement respect to the detector** | ± 10 arcmin |

Table 4.2: Alignment constraints for M2.

| Parameter | Value |
|---|---|
| **Detector displacement respect to M2 X** | ± 5.5 mm |
| **Detector displacement respect to M2 Y** | ± 5.5 mm |
| **Detector tilt around X respect to M2** | ± 20 arcsec |
| **Detector tilt around Y respect to M2** | ± 20 arcsec |

Table 4.3: Alignment constraints for the PDMs in the camera focal plane.

- Encoders errors: off-set positioning errors of the mechanics of the telescope along azimuth and elevation axes that are directly retrieved by the electronics and easily subtracted.
- Gravity flexures errors: reproducible contribution to the error budget of the telescope constant with time and depending on the pointing direction of the telescope. The gravity flexures can create an opto-mechanical mismatch that acts differently for different elevation values but it can be mapped by the use of the CCD cameras at the corners of the focal plane (see section 2.6) and lookup tables once a kinematic model of the telescope will be derived from the commissioning phase.
- Wind flexures errors: for limit wind speed in operational conditions (0 to 50km/h) two different scenarios are envisaged; for a telescope frequency below 3 Hz the wind, that can be constant and/or turbulent-gusty, leads to a measurable contribution with the CCD cameras. Above the threshold of 3 Hz the perturbations induced by the wind, independently of their nature, cannot be measured and corrected.
- Thermal flexures errors: assumed as deterministic if a reliable model of the temperature and gradients affecting the telescope is applied. Thermal effects act in different ways along the night and they are stronger during the twilight. Static thermal induced errors are expected during the seasonal cycle. A mapping of the thermal behavior of the ASTRI prototype will be performed by means of a set of temperature sensors distributed in different parts of the telescope structure.

GEC Consortium that has studied and realized the design of the telescope, has assessed the structural performances by means of a Finite Element Analysis (FEA) (Internal report [163]). This analysis allows estimation of the error budget of the pointing model of the telescope induced by the four environmental factors discussed above. For conservative reasons, the degradation of the telescope performances is assessed by considering a worst and unlikely scenario characterized by a strong thermal gradient (7 °C) perpendicular to the telescope elevation axis, a constant wind of 50 km/h and a pointing elevation of 30° where the torques on M2 and the camera are maximized. As show in Figures 4.6 the greatest contribution to the misalignment and tilt of

the optics comes from gravity. To map these flexures an AMC unit has been implemented as described in section 2.6.

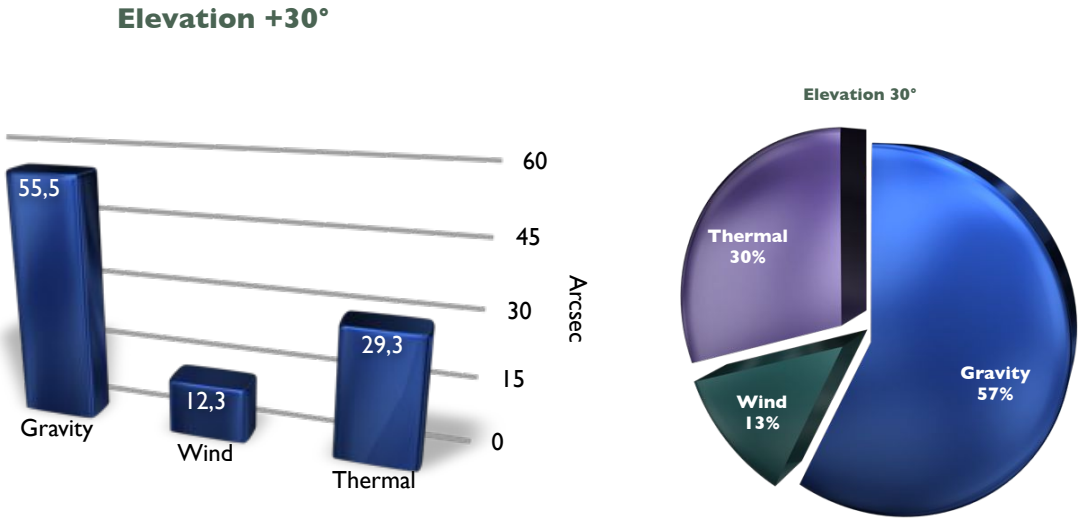


(a) (b)

Figure 4.6: (a) Flexure errors in arcsecs along X (elevation axis) from gravity, wind and thermal gradients for a telescope elevation of 30°. (b) Pie chart of the percentage contributions from the same environmental errors.

By introducing these flexures in the optical design it has been verified that the optical performances of the telescope remain inside the specifications. The translations and the tilts from FEA are introduced in the non-sequential Zemax optical design that allows to model each telescope component as a single, independent element. The PSF size on-axis changes from 9.6 to 9.65 arcmin and the centroid relative displacement is about 1 arcmin on the focal plane. In Figure 4.7 the PSF for an on-axis source for the the nominal design and for a 30° telescope elevation are compared.

(a) (b)

Figure 4.7: (a) ASTRI nominal PSF for an on-axis source. (b) ASTRI PSF for a 30° elevation of the telescope uncorrected by AMC.

Taking into account all the environmental factors and their induced flexures on the opto-mechanical structure of the telescope the pointing error is $< 35$ arcsec and the tracking error $< 6$ arcmin. To be compliant with the CTA requirement of the rms post-calibration pointing precision $< 7$ arcsec, a T-point strategy must be considered. T-point is an interactive software tool which uses observations of star positions to create a pointing model of the telescope concerned [164].

The software accepts lists of pointing observations specifying (i) where the star really was and (ii) where the telescope readouts said the star was. It fits a user-specified pointing model (the desired list of parameters to be estimated) to the observations, so that the coefficient values give the best possible match between the star positions and the corrected telescope readouts. The effective reliability of this tool, currently used by many large optical observatories, allows to recover a pointing accuracy of ∼1-1.2 arcsec starting from an overall telescope pointing accuracy of ∼35 arcsec [164]. In this way the mechanics provides a pointing accuracy of ∼35 arcsec and T-points lowers this limit at a few arcsec.

### 4.4.3 Tolerance study on optics alignment

A complementary analysis to FEA is the tolerance study of the telescope optics alignment. Tolerances on decentering (X,Y,Z) and tilts (X,Y,Z) for M1, M2 and camera PDMs, collected in Tables 4.1, 4.2 and 4.3, have been put together into a series of MC simulations to assess the evolution of the RMS radius and centroid of the telescope PSFs. The RMS spot radius is the root-mean-square radial size. The distance between each ray and the reference point is squared, and averaged over all the rays, and then the square root is taken, giving a rough idea of the spread of the rays. A shift of the PSF centroid translates in an error of the pointing of the telescope. The effects of the flexures are evaluated for different angles into the FoV (0°,1°,2°,3°,4°,4.8°). For each angle in the FoV 200 MC simulations have been run randomly combining the flexures on M1 panels, M2 and the camera PDMs. The final output is a series of 200 different, realizations of the telescope based on random combinations of the flexures inside the specified range. The graphical results for field 2° are plotted into histograms and scatter plots in Figure 4.9. The 75% quartile of the MC distribution is taken as reference value and the results for all the fields in the FoV are shown in Figure 4.10. A a direct view of the flexures effects on the PSFs can be observed in Figure 4.8.

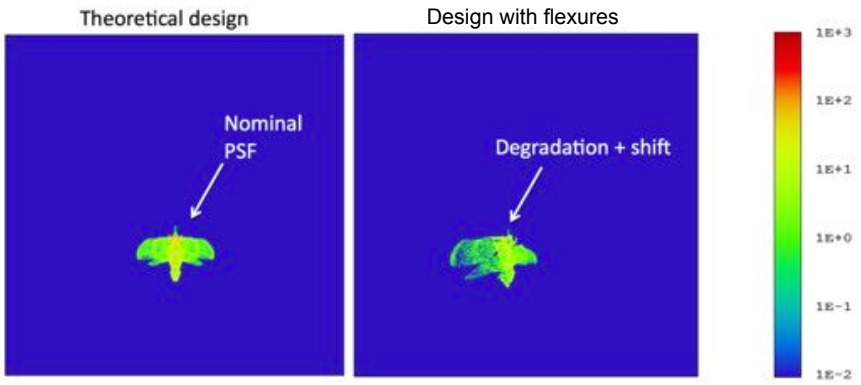


Figure 4.8: Degradation and centroid shift of the PSF after the introduction of the flexures from MC analysis in the nominal telescope model.

### 4.4.4 Optics and effective area

The estimation of the effective area of the telescope is of crucial importance for the MC simulations and the Cherenkov observations reconstruction. The decreasing of the effective area for the off-axis sources is due to a combination of a vignetting of the camera volume, obscuration from M2 MSS, changes in the reflection and transmission properties of the coating and pixelization of the focal plane. The lifetime of individual CTA mirror facets, allowing for multiple recoatings, must be $>$ 15 years, while mirror recoating to comply with performance (reflectivity and PSF)

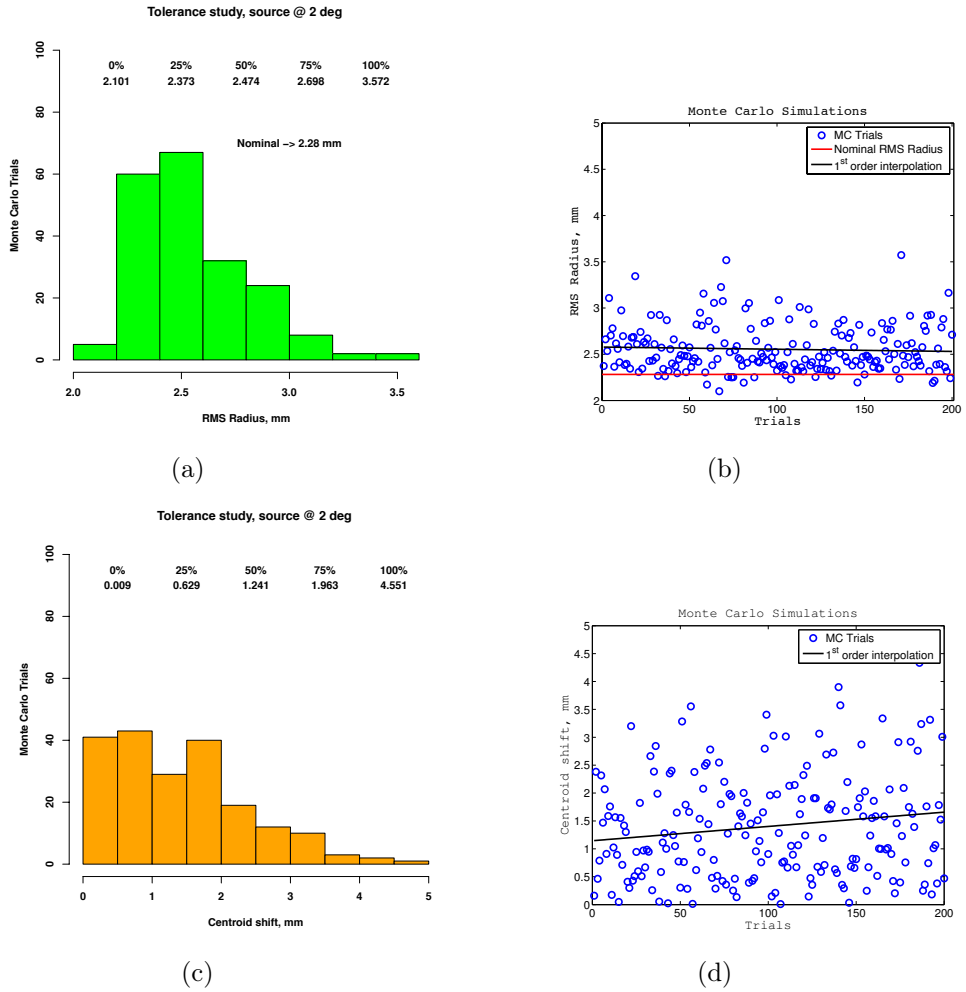


Figure 4.9: (a) PSF RMS radius in MC trials. (b) Scatter plot of the PSF RMS radius from MC simulations compared the nominal value. (c) Histogram of the centroid shifts from MC and relative scatter plot (d).

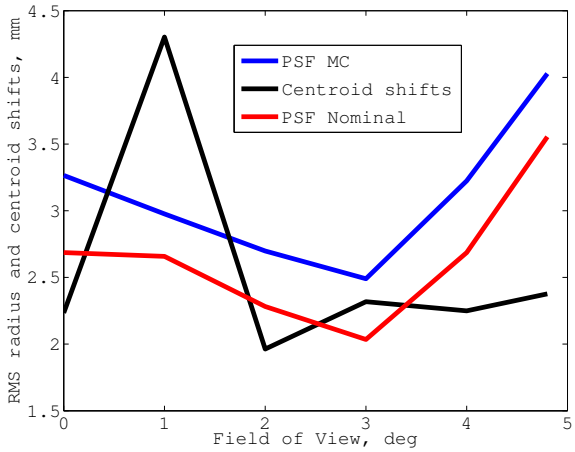


Figure 4.10: The PSF RMS radii at different of angles in the FoV from MC simulations (blue) is systematically higher than the nominal profile (red). (Black) Centroid shifts after the introduction of the tolerances in the optical design.

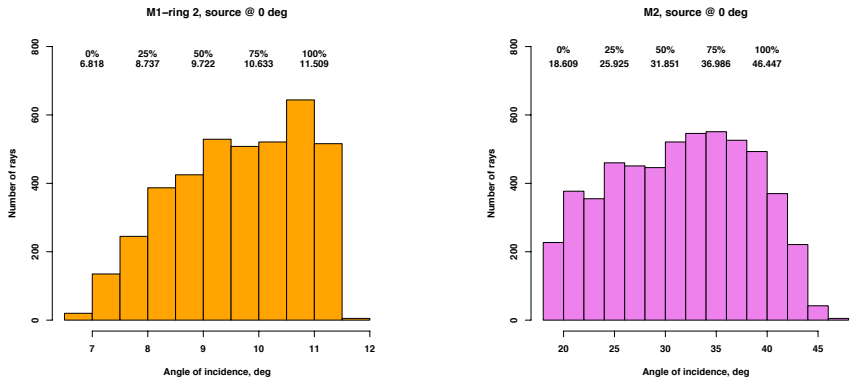


(a)




(b)

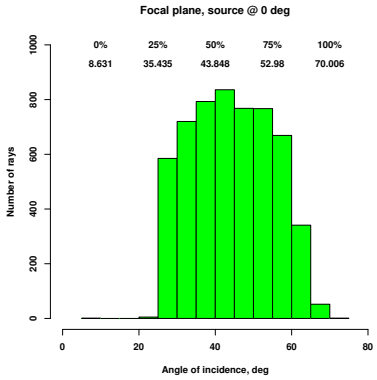


(c)

Figure 4.11: (a) Top: left, photons angles of incidence on M1 (intermediary radial segment) and on M2 (right) for an on-axis source. Bottom: AoI distribution on the telescope focal plane. M2 and the focal plane must accept photons with large AoI. The numerical values above the histogram correspond to the quartiles of the AoI distribution.

requirements must be required less than once every 6 years. The initial average specular reflectivity of a SST reflector, at all wavelengths from 300-550 nm, must be >85 % and must be always >65 % during operations. In relation to these requirements, the reflectivity and transmission properties of the coating have been optimized in order to maximize the effective area of the entire system. Reflectivity and transmission of the optics have been measured on some optical samples by a spectrophotometer and given in input to Zemax software. For M1 two solutions have been investigated:

- Baseline coating solution: an Aluminum coating (150 nm) with a protective layer of $SiO_2$ (100 nm thick)
- Enhanced coating solution: a multi-layer dielectric coating (approx. 40 layers): $SiO_2$, and a mixture based on $Ta_2O_5$

M2 is coated with a single Aluminum layer (200 nm thick) covered with a protective layer (150 nm) of $SiO_2$. The PMMA window (face toward M2 and face toward the focal plane) is coated with a dielectric multi-layers (9 layers) based on $SiO_2$ and $ZrO_2$. The mirror coatings have been optimized based on the angles of incidence (AoI) of the photons on the optical surfaces that have been derived from Zemax and are shown in the histograms in Figure 4.11.

In addition to mirror reflectance there are other geometrical factors to be taken into account for the estimation of the telescope effective area: M1 obstruction by M2, M2 obstruction by camera body, vignetting from the telescope mechanical structure and intra-pixel dead space.

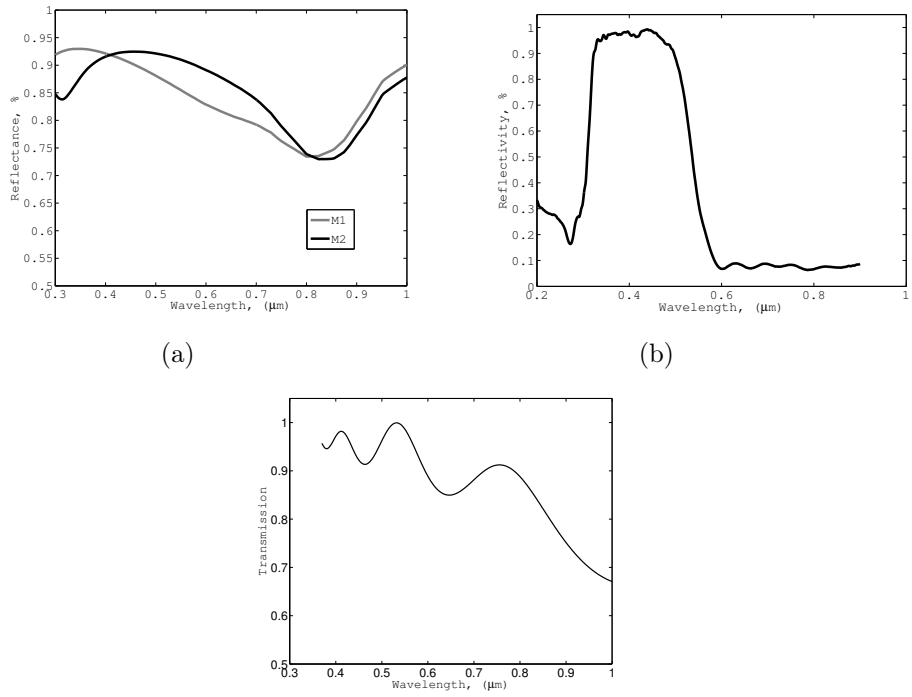


(a) (b)

(c)

Figure 4.12: (a) Reflectance of M1 and M2 coatings based on Al + $SiO_2$. (b) Reflectance of M1 dielectric coating based on a mixture of $SiO_2$ and $Ta_2O_5$. (c) Transmission of the PMMA window that covers the focal plane.

Recalling section 3.5, the obscuration ratio is the portion of the aperture blocked by the secondary mirror and baffle while the vignetting is the gradual fading near the edge of the field of an optical system due to partial obscuration by intermediate optical components (e.g. truss of MSS). Both M1 segmentation and M2 obstruction create a sensible decrease of the effective area of the telescope. The geometric area of the primary mirror is $A_{M1} = 11.177$ m$^2$ and by adding the M2 obstruction this value reduces to $A_{M1M2} = 9.9275$ m$^2$. Adding the mirror reflectance to the bare assembly M1 + M2 the effective area profile obtained is shown in Figure 4.13a.

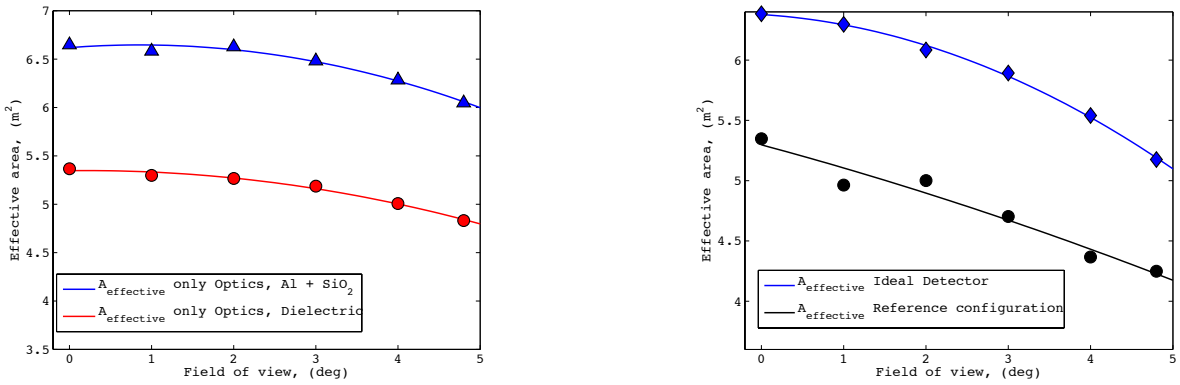


(a) (b)

Figure 4.13: (a) Effective area estimation for M1 + M2 assembly for the two different coating solutions of M1; Al+$SiO_2$ outperforms the dielectric solution. (b) Effective area for a focal plane with and without intra-pixel dead spaces and an Aluminum coating.

Another important contribution to the decrease of the effective area comes from the light losses caused by the dead space between adjacent MPPC units. Figure 4.14 shows the final design of a PDM quarter (4x4 MPPC units) and the PSF footprint on the pixels array. In Figure 4.13b the effective area profiles along the FoV for an ideal continuos detector and the real based on a mosaic of MPPCs are compared.

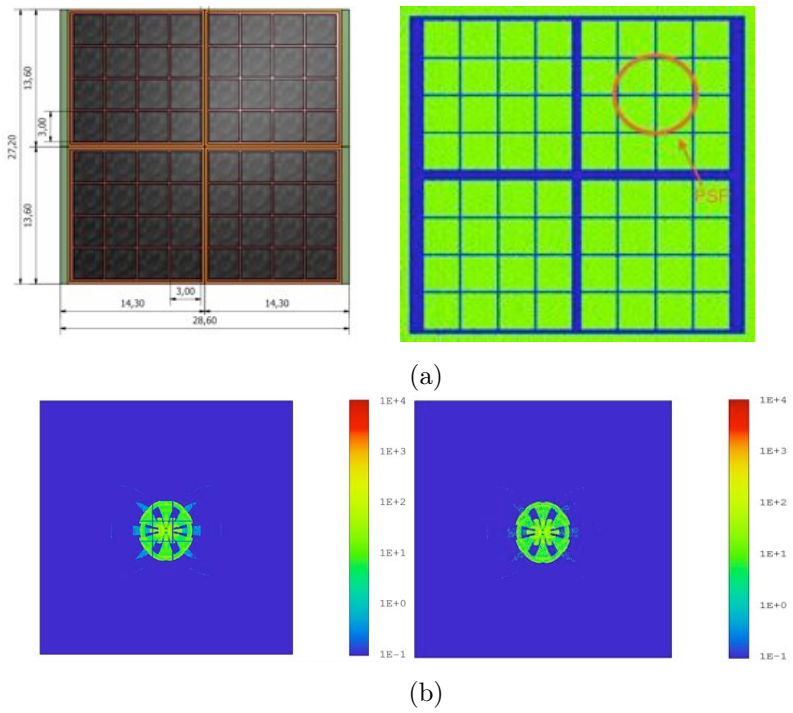


(a)

(b)

Figure 4.14: (a) Light projection above the MPPC units simulated by Zemax; significant light losses occur in the dead spaces among adjacent MPPC units while losses are contained between adjacent pixels. (b) **Left** ASTRI PSF on the MPCC pixels of the focal plane with the dead space wasting part of the PSF light. **Right** ASTRI PSF for an ideal detector.

Finally, the vignetting from the truss of telescope mechanical structure sustaining M2 MSS, the obscuration caused by M2 and the camera accounts for an important effective area reduction of the whole telescope. Two simulations, for an on-axis and off-axis source, have been performed introducing the mechanical structure of the telescope (Figures 4.15b and 4.15c). The final overall budget (accounting for all the factors above mentioned) of the effective area is shown in Figure 4.16a. These estimations confirm that the ASTRI prototype is compliant with the SST requirement on effective mirror area to be always >3.5 $m^2$ for all angles within the required FoV. The effective area is optimized for observations between 350 and 450 nm.

Assuming a quantum efficiency for the detectors in the order of 40%, the overall optical efficiency of the system is about 18% that is compliant with the requirement of being > 15%. As required from SST requirements, the telescope shall focus light (over 80% of the required camera FoV) with an optical $PSF_{D80}$ <0.25 degrees in sky.

The PSF describes the response of the telescope to a point source or point object. The D80 parameter refers to the diameter containing the 80% of the encircled energy. In the CTA requirements documentation it is conventionally assumed the D80 parameter as representative value for the size of the PSF. As shown in Figure 4.17 the ASTRI SST-2M prototype is fully in specification and performs even better than the requirements. Another requirement concerning the optical performances of the telescope is about the time spread introduced by the optics in the incoming Cherenkov wavefront. The telescope must focus light (over 80% of the required camera FoV) with an RMS optical time spread of <1.5 ns and as discussed in section 3.4 the ASTRI SST-2M prototype is fully in specifications.

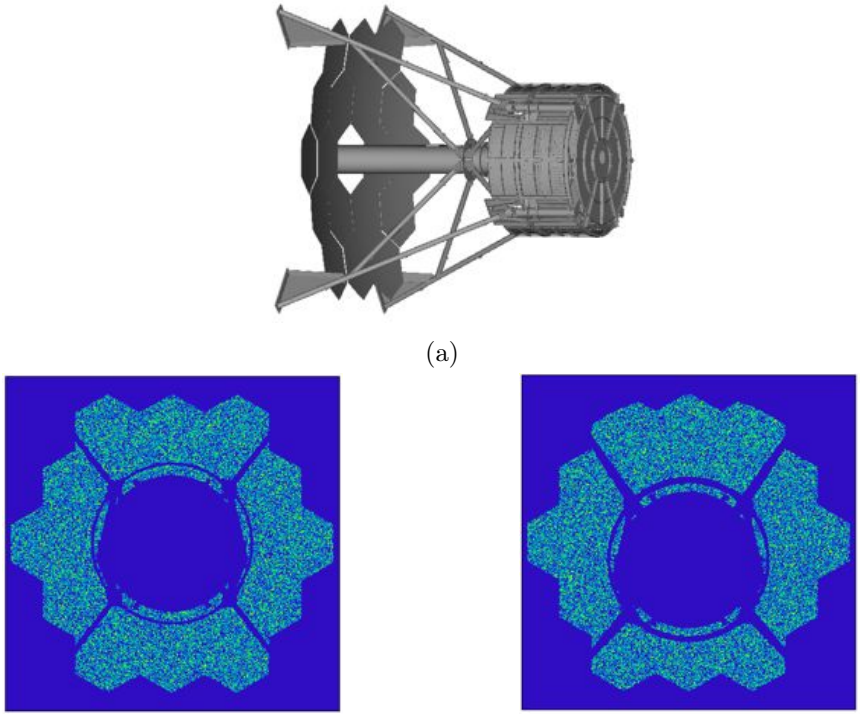

(a) (b) (c)

Figure 4.15: (a) Shaded model of the mechanical structure surrounding M2 and the camera. (b) Simulation of the shadowing of the M2 MSS on the primary surface for an on-axis source, blue regions are the obscured-vignetted areas. (c) Obscured-vignetted areas for an off-axis source at 4.8°.

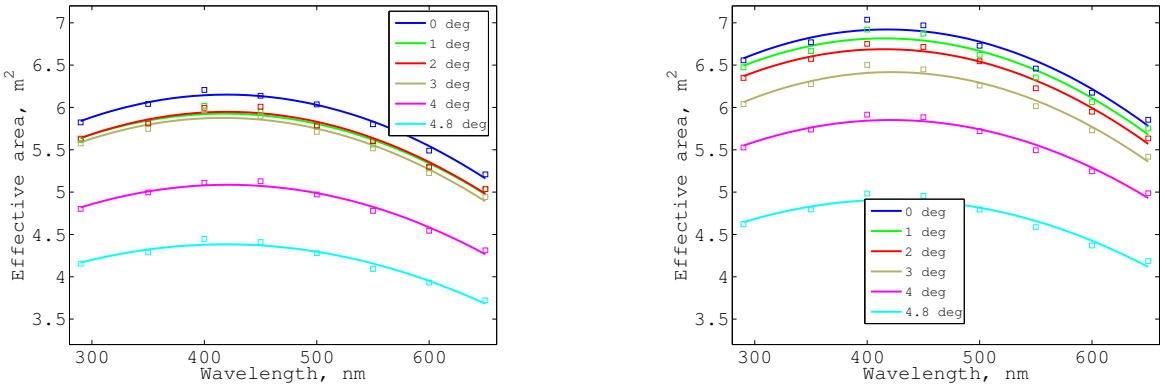


(a) (b)

Figure 4.16: (a) Effective area estimation taking into account coating reflectance, obstruction factors, focal plane segmentation and the vignetting from the telescope mechanical structure. The curves remain all above 3.5 m$^2$ in effective area fulfilling the CTA-SST performance requirements. The largest effective area is achieved between 350 and 450 nm. (b) Effective area estimation of the entire telescope without the effect of focal plane segmentation,i.e. the effective area from the overall telescope independently from any kind of camera.

### 4.4.5 Tolerance study on optics manufacturing

Since the manufacturing process of the optics is based on cold (M1) and hot (M2) slumping technique without any subsequent polishing refinement, it is rather important to estimate the maximum errors on the paraxial radius of curvature and local profile errors that the mirrors can tolerate. A series of simulations have been performed varying the paraxial radius of curvature of

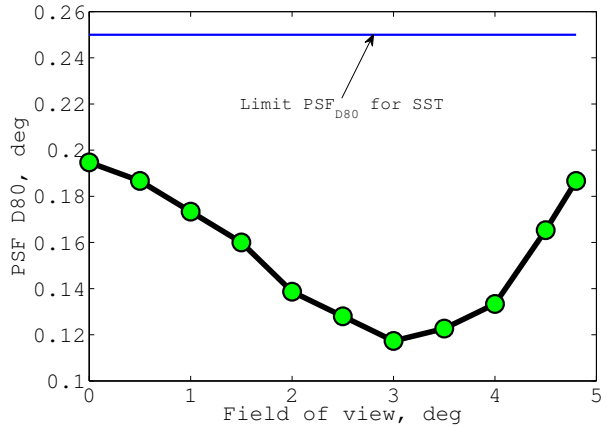


Figure 4.17: Simulated ASTRI PSF ($D_{80}$ values) in the FoV, for all the angles the telescope performs better than the required specifications for SST. The $D_{80}$ value is the reference diameter of the circle containing the 80% of the PSF energy.

M1 and M2 by steps of 3 mm around the nominal values (refer to Tables 2.4 and 2.6) to study the evolution of the PSF size. The results show that a gross error of ± 6 mm can be tolerated both on M1 and M2 radius of curvature profiles as shown in Figure 4.18.

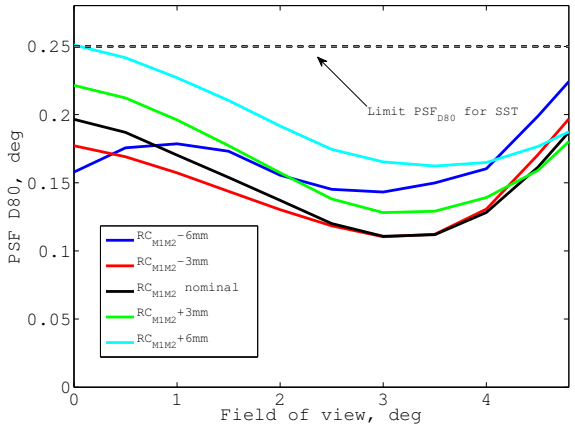


Figure 4.18: Simulated ASTRI PSF ($D_{80}$ values) in the FoV, for different radii of curvature of M1 and M2. The plots refer to deviations of ± 3 and ± 6 mm from the nominal value. For deviations ≤ ± 6 mm the telescope performances are still inside the specifications.

In relation to local surface profile errors, estimations of the tolerable profile errors due to the mold and the replication process are in the order of 60 $\mu m$ peak to valley (PV) and 220 $\mu m$ PV for M1 and M2 respectively (Internal report [159]).

### 4.4.6 Thermal analysis

The temperature plays an important role in the thermal balance of the telescope that is continuously exposed to the sunlight during the day. During daytime the telescope is constantly pointed in the North direction to avoid any damage of the camera by solar light reflected accidentally from the mirrors. Consequently the dish supporting the primary mirror tiles absorbs a large quantity of heat. After the sunset the telescope undergoes a transitory phase and eliminates

the heat stored during the day by radiative processes. It can be expected that the linear and volumetric deformation of the optics and the telescope structure induced by the heat, leads to a changing of the mirrors focal lengths. If the analysis is restricted to the bare optics (no mechanical support systems), the effect is however very small. As the temperature rises the glass expands and both radius of curvature and glass thickness linearly expand. The change in size of these quantities is described by equation:

$$L = L_0(1 + \alpha\Delta T) \tag{4.1}$$

with $L_0$ nominal length (radius of curvature) at a certain temperature (assumed room temperature), $\Delta T$ change of temperature and $\alpha$ coefficient of thermal expansion (CTE) of the glass. M1 and M2 mirrors are made of borofloat glass, from which $\alpha \sim 3.25 \times 10^{-6}/K$. Considering the operative range inside which the telescope has to work -15C°+25C°, the maximum deviation $\Delta R_{M2}$ that the radius of curvature undergoes is $\sim$ 0.3 mm, which corresponds to 0.014% of its nominal values. The M1 segment are constituted by a sandwich of two thin glasses (2 mm) and an aluminum honeycomb (10 mm). In this case, the segments are composed of different material with different CTEs so equation 4.1 is not a good approximation. By FEA simulations it is derived a maximum deviation $\Delta R_{M1} \sim 1$ mm in the entire temperature working range. These results show that the thermal expansion of the optics has no influence on the telescope performances even for an extreme variation of temperature inside the working range. Conversely the deformations of the mechanical structure supporting the mirrors and the telescope units are important. By a series of FEA simulations developed by BCV Progetti s.r.l. (Internal report [108]), three different thermal scenarios (see Figure 4.19) are assessed and the deviations and tilts of the M1 segments, M2 and the camera are estimated.

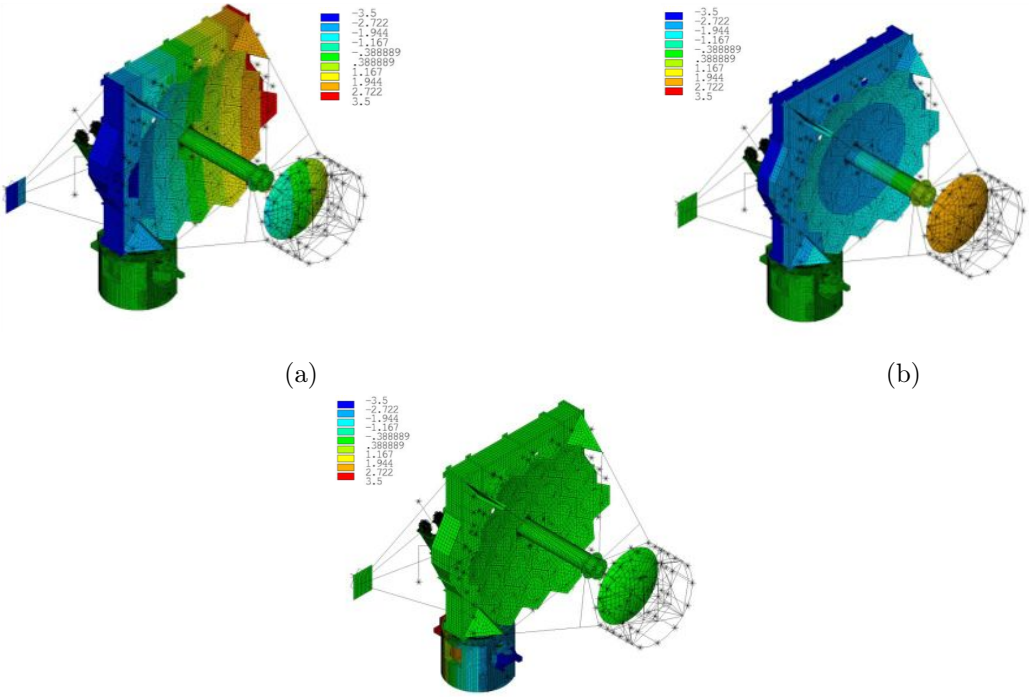


Figure 4.19: (a) Linear distribution ± 3.5°C along elevation axis (X) applied to all structures and subsystems rotating around elevation axis.(b) Linear distribution ± 3.5°C along optical axis (Z) applied to all structures and subsystems rotating rotating around elevation axis. (c) Linear distribution ± 3.5°C in a direction orthogonal to elevation axis applied to base and column structures.

In the first case a gradient of ± 3.5°C is developed along the elevation axis, in the second

the same gradient affects the z-optical axis and in the third it affects the supporting tower of the telescope. The thermal gradients given to the structure are very high and unlikely in a real situation, but they represent a very conservative upper limit for this analysis. Based on the estimates derived from FEA simulations a range of variation for shifts and tilts of the optical elements is introduced in the telescope optical design. For a tilt or shift along a certain axis, the worst value among the three models have been chosen; then following the same procedure described in section 4.4.3 a series of MC simulations are performed randomly combining the shifts and tilts induced by the thermal gradients. The effects on the PSFs size and centroids are plotted in Figure 4.20.

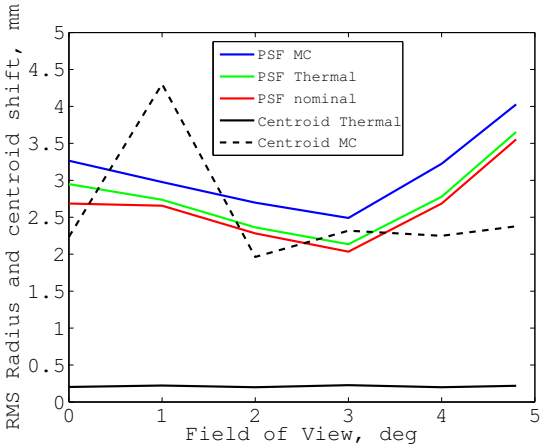


Figure 4.20: Degradation and centroid shift of the PSFs after the introduction of the tolerances from the thermal FEA analysis in the nominal telescope model. For comparison the overall maximum tolerances (MC) discussed in section 4.4.3 are over plotted from Figure 4.10.

The perturbations induced by the temperature on the mechanics supporting the optics cause a limited degradation of the PSFs size and contained shift centroids. To get a term of comparison with the error budget analysis carried out in section 4.4.2 the curves referring to the overall tolerances are over plotted in Figure 4.20 (labelled with MC).

### 4.4.7 Camera Calibration

To fulfill the requirement for camera calibration for which each telescope must include a flat-fielding device which provides pulsed illumination of all camera pixels with an intensity between 25 and 100 photoelectrons per pulse and a time duration in the range 1-10 ns FWHM, a dedicated optical study has been carried out. The camera illumination is achieved by means of an optical fiber that diffuses the light inside the protective PMMA window above the focal plane. The optical fiber is illuminated through a laser when the camera lids are closed. A series of development tests on a prototype window have been carried out supported also by a series of ray tracing simulations for different scattering models of the window. The results of this investigation are summarized in a refereed publication that is reported in Appendix 6.6.3.

### 4.4.8 Assessment study on instrumental polarization

Even if not requested from the SST performance requirements, we report below an assessment study on the instrumental polarization introduced by the telescope optics with the aim of estimating whether this phenomenon can affect significantly the level of natural polarization of the Cherenkov radiation. Cherenkov radiation is naturally 100% linearly polarized [34]. The polarization vector is perpendicular to the Cherenkov cone, pointing away from the particle's path as shown in Figure 4.21b. Multiple scattering in the shower causes an angular distribution of secondaries relative to the shower axis, resulting in a dilution of the net polarization observed on the ground as shown from the measurements of HEGRA in Figure 4.21a (Döring et al. 2001 [34]).

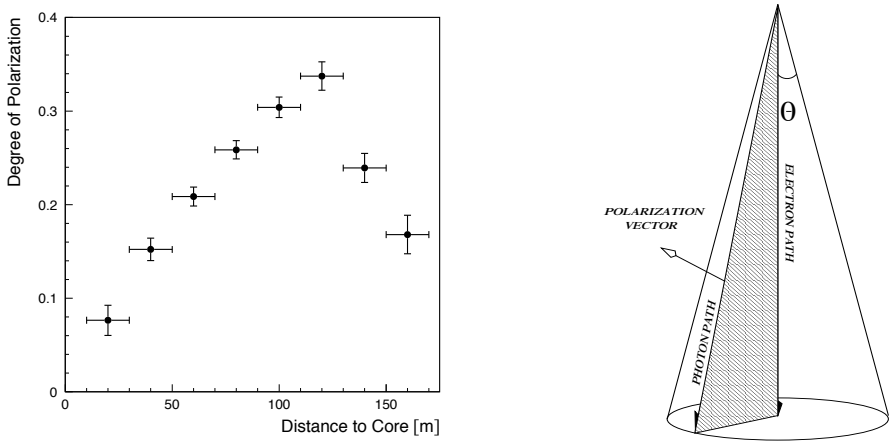


(a) (b)

Figure 4.21: (a) The measurements from HEGRA show that the degree of polarization exhibits a maximum near the Cherenkov radius of about 120 m, where radiation from the well-collimated upper part of the shower is collected, and decreases both for smaller core distances (for symmetry reasons, light observed on the shower axis has to be unpolarized) and for larger core distances, where heavily scattered particles contribute [34]. (b) The Cherenkov light is linearly polarized along the radial direction of the shower and the plane of polarization is recognized by electron and the photon optical path (Image from Contreras et al. [27]).

Telescopes are design to minimize the introduction of spurious instrumental polarization that alters the state of polarization of the incoming radiation. However particular optical configurations with wide angle of incidence or asymmetric design (e.g. the Nasmyth focus of a Cassegrain telescope) can introduce significant residual polarization (Giro et al. [51]). In general any reflection on a metallic surface other than at normal and grazing angle produces polarization in the reflected beam. Oblique incidence on a mirror produces both diattenuation (polarizing action) and phase retardation. These effects are minimal at near-normal and at grazing incidence; the largest effects occur at intermediate angles of incidence [130]. Rotationally symmetric telescopes of large focal ratio show very little instrumental polarization while in the off-axis configurations the symmetry is broken and the residual polarizing action occur. This effect is larger as the optical system becomes faster. ASTRI falls in this latter case, where a very fast optical system (f/0.5), causes ray reflections at large AoI over a wide FoV. As discussed in section 4.4.4 the median angles of incidence (AoI) on M1 and M2 are $\theta_1 = 10^\circ$ and $\theta_2 = 32^\circ$ respectively, and their distribution on M1 and M2 surfaces is shown in Figures 4.22a and 4.22b.

The slight azimuthal asymmetry in the configuration of the primary mirror panels (Figure 4.23a) and the asymmetric light footprint on M1 and M2 surfaces (Figures 4.23a and 4.23b) could contribute to a certain degree of instrumental polarization.

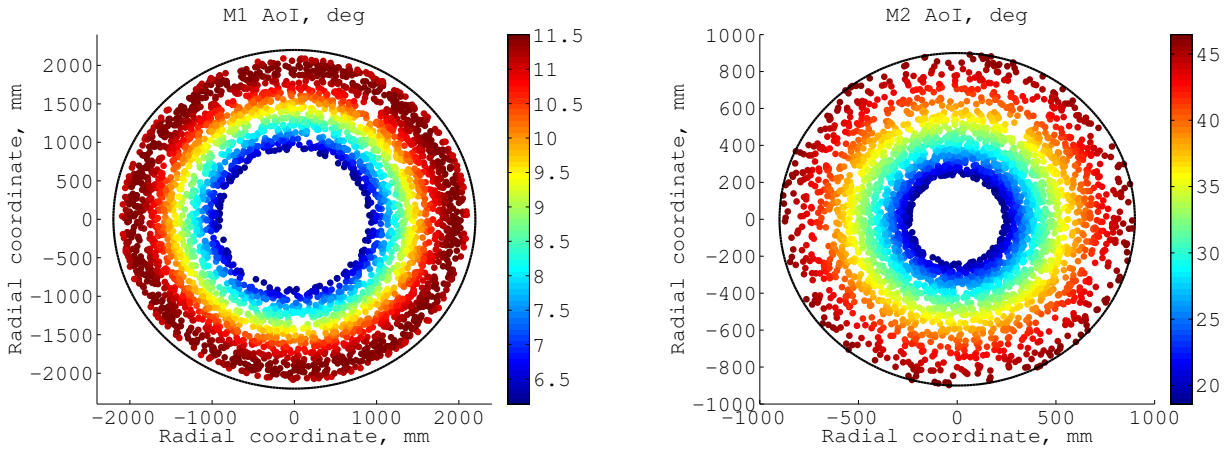


(a) (b)

Figure 4.22: (a) AoI distribution on M1. The AoI are relatively small and the central hole is due to the obscuration by M2; in this simulation M1 is monolithic. (b) AoI distribution on M2: the distribution is wide and a significant fraction of angles is above 30°.

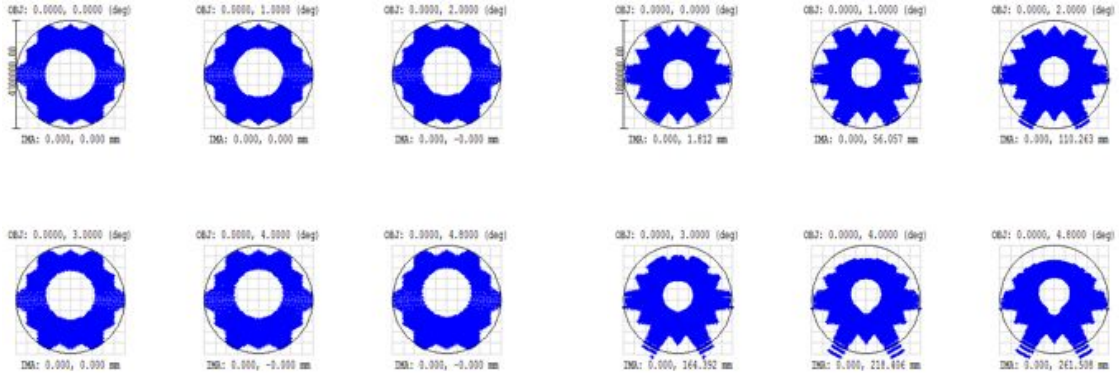

(a) (b)

Figure 4.23: (a) Light footprint on M1 and shadowing of M1 by M2 for different fields inside the FoV between 0° and 4.8°, the black circle recognizes the osculating circular profile for M1. (b) Light footprint on M2 and the shadowing of M2 by the camera, the black circle recognizes the profile of M2.

To quantify the possible presence and level of instrumental polarization an adequate mathematical formalism is introduced. The polarization state of the incoming light can be described through a Stokes vector (see, e.g., Chandrasekhar [23]):

$$S = \begin{pmatrix} S_1 \\ S_2 \\ S_3 \\ S_4 \end{pmatrix} = \begin{pmatrix} I \\ Q \\ U \\ V \end{pmatrix} = \begin{pmatrix} I \\ I_0 - I_{90} \\ I_{45} - I_{135} \\ I_l - I_r \end{pmatrix} \tag{4.2}$$

The Stokes vector components parametrize different polarization states of light: $I$ represents the total intensity of the light beam, $Q$ the difference between the intensity of horizontal and vertical linearly polarized light, $U$ the difference between the intensity along 45° and 135° planes of polarization and $V$ describes the difference between left and right circular polarization. The Stokes vectors can describe unpolarized, partially polarized and fully polarized light, and when coupled with the Mueller matrices (array of $4 \times 4$ elements) they track the evolution of the polarization state of the photons as they travel inside the telescope. The ray tracing software (Zemax) used to assess the level of instrumental polarization however, uses the Jones matrices

formalism (Jones 1941 [72]) to describe the state of polarization of the light. These matrices, although simpler (array 2 × 2 elements) can only describe fully polarized light states and they cannot accept the unpolarized state vector of interest for the current analysis. The Jones vectors components $E_x$ and $E_y$ are related to the Stokes vector by the following relations:

$$\begin{aligned} I &= E_x E_x^* + E_y E_y^* \\ Q &= E_x E_x^* - E_y E_y^* \\ U &= 2E_x E_y^* \cos\delta \\ V &= 2E_x E_y^* \sin\delta \end{aligned} \tag{4.3}$$

with $E_x$ and $E_y$ amplitudes of the field along orthogonal directions and $\delta$ relative phase retardation between the two fields components. Unpolarized light can be described by an electric vector that, at any instant in time, corresponds to a well defined polarization state, but fluctuates randomly between different polarization forms on a time scale that is large compared with the period of the light, but small with respect to the time interval over which the measurement is performed. Therefore, over a relatively extended period of time, all polarization biases are averaged out and the beam appears to be unpolarized [123]. The unpolarized light is simulated in the ray tracing software by means of a macro that makes varying the radiation plane of polarization between 0° and 180° with 1° step; the ray is parametrized by the Jones components $E_x^{in}$ and $E_y^{in}$ and traced inside the telescope. The values $E_x^{out}$ and $E_y^{out}$ of the ray at the focal plane are recorded and converted by relations 4.3 into the corresponding Stokes vector. The sample of Stokes vectors (180 elements) following the same optical path are then averaged in a unique vector, $S_{out}$. This last operation is possible because the Stokes vectors are additive quantities. The procedure is then applied to an array of equally spaced points that sample the telescope pupil. The radiation incident on a reflecting surface can be split in two components, one parallel to the plane of incidence (*p-component*, $R_{\|}$ ) and the other perpendicular to it (*s-component,* $R_{\perp}$). By means of the Fresnel equations that describe the behavior of the two orthogonal field components as a function of the AoI, the reflectance of the mirror to the radiation can be traced from normal to grazing incidence. The $s$ and $p$ components are reflected in a different percentage except for two limit angles, $\theta_{0°}$ and $\theta_{90°}$, as shown in Figure 4.24a. The reflection on the metallic surface introduces also a phase retardation $\delta$ among the two field components (Figure 4.24b).

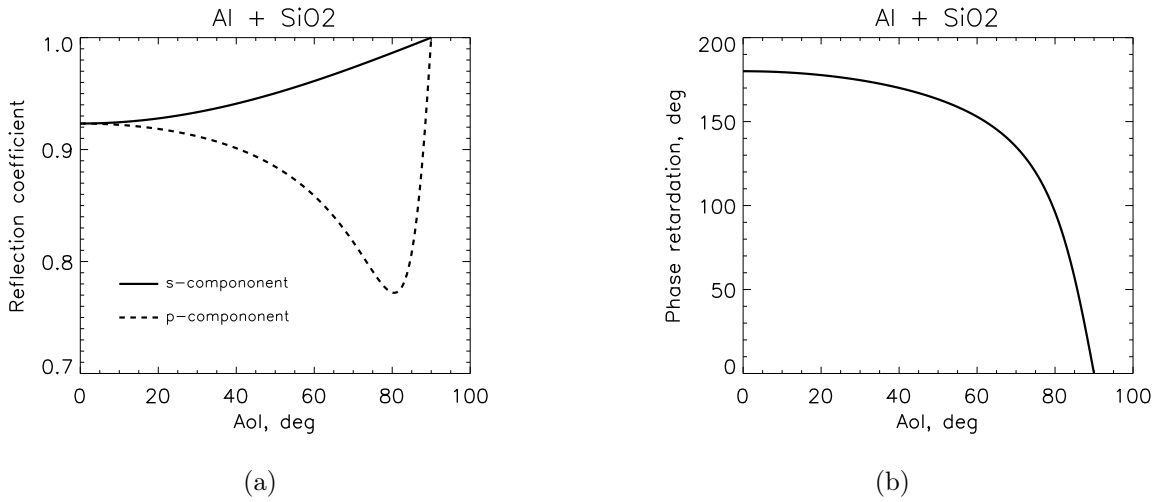


Figure 4.24: Reflection coefficients and (b) phase retardation as function of the angle of incidence for light at 500 nm of wavelength. The curves have been calculated for the coating of M1 and M2, aluminum plus a quartz protective layer, using the Zemax materials coating database.

Assembling together all these ingredients the instrumental polarization of the ASTRI prototype is assessed for two peculiar configurations: a source observed on-axis and another at the limit of the FoV. The magnitude of the normalized Stokes vector components derived from the procedure described above are shown in Figures 4.25a (on-axis) and 4.25b (off-axis). The normalization is achieved by dividing the Stokes vector components by the intensity of the field $I$. The pupil maps refer to the Stokes vector resulting from the cumulative effects of M1 and M2 observed at the focal plane of the telescope for an unpolarized radiation input.

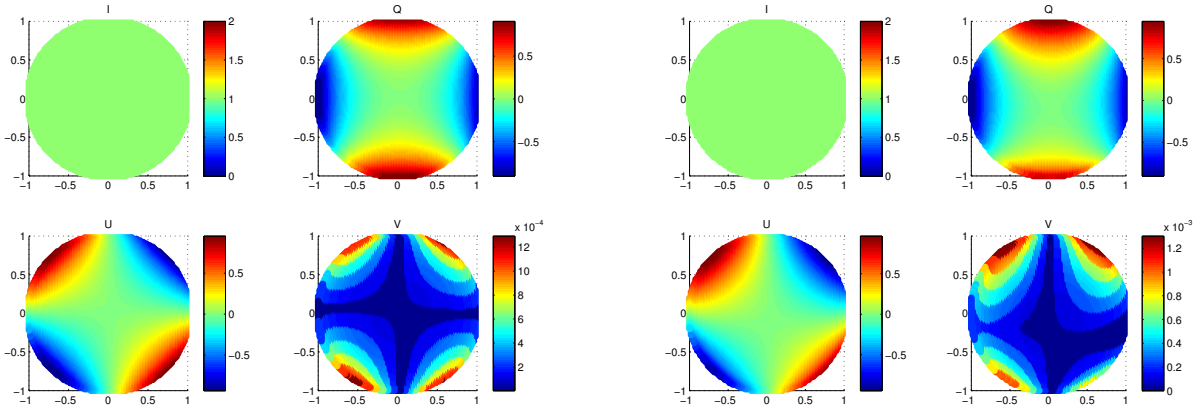


(a) (b)

Figure 4.25: (a) Polarization pupil map at the focal plane of ASTRI for a source on-axis. The Stokes parameters Q,U,V have symmetric distribution with respect to the centre of the pupil and their average over the aperture is close to zero. (b) Polarization pupil map at the focal plane of ASTRI for a source at 4.8°. The Stokes parameters Q,U,V show a slight asymmetric distribution with respect to the centre of the pupil as expected from off-axis fields. This symmetry gives origin to a residual instrumental polarization. The Stokes parameters of both the maps are normalized to the I component.

For unpolarized light the parameters Q, U, and V are zero, S = (1,0,0,0) and the degree of polarization, defined as:

$$p = \frac{\sqrt{Q^2 + U^2 + V^2}}{I}$$

is zero. Partially polarized light constitutes an hybrid state with $0 < (Q^2 + U^2 + V^2)/I^2 < 1$. The average Stokes vector over the pupil map of Figure 4.25a is $S_{0^\circ} = (1, 0.0000, 0.0020, 0.0002)$. The Q, U, V have a distribution symmetric with respect to the centre of the map with a very small polarization residual: maximum component U $\sim$ 0.2 %. The off-axis field show an asymmetric pupil map for the Q, U, V components and the average Stokes vector gives $S_{4.8^\circ} = (1, -0.0006, 0.0023, 0.0003)$. The residual polarization is still contained even if slightly larger for all the Stokes components and maximum at U $\sim$ 0.24 %. A complementary view of the Stokes parameters for the on-axis case is given in Figure 4.26: the amplitude of Stokes Q and V components is broad, but the average combines to nearly zero; V has an asymmetric profile but it is three orders of magnitude lower than the former.

This first assessment analysis has led to establish an order of magnitude for the instrumental polarization of the ASTRI optics. As discussed above, the values of the residual polarization are very small and likely drowned into noise in any practical scenario of observation. A further step would be an independent analysis carried out by means of an analytical procedure based on the Mueller formalism to confirm/complement the approach based on ray tracing. Additional polarization residuals are expected from shape discontinuities and surface scattering of M1 and M2 and from possible inhomogeneities of the coating on the secondary mirror and between different panels of M1. For this particular aspect the measurement of the Stokes parameters

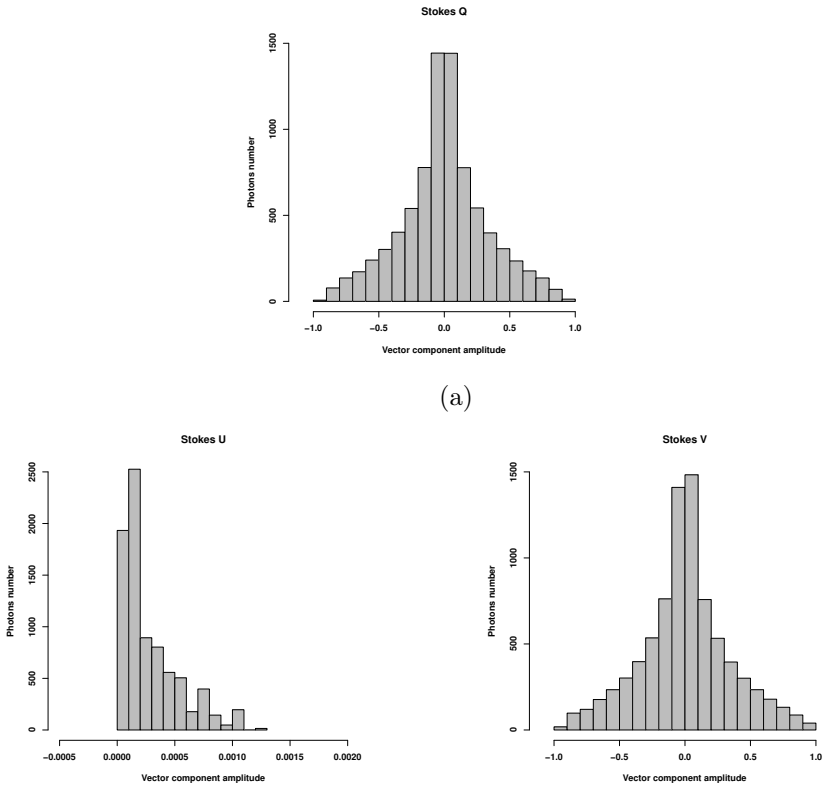


Figure 4.26: (a) Histograms of the Stokes Q (a), U (b) and V (c) parameters for the ensemble of rays simulated and traced at different points in the telescope pupil. Q and V have a symmetric distribution with mean centered on 0.002 and 0.0002 respectively. U is asymmetric, but extremely small.

of the telescope during its commissioning phase and consecutive operational phases is highly recommended.

# Chapter 5

# M2 Optical qualification tests

In this chapter the results on the measurements of the M2 prototypes manufactured by the FLABEG company are discussed. Three mirrors 19 mm thick, named Teil0, Teil1 and Teil2 have been delivered as reported in section 5.2. A detailed test campaign has been performed on the prototype Teil1. The results are encouraging and demonstrate the feasibility of the manufacturing of large and highly aspherical mirrors for Cherenkov astronomy using the hot slumping technique.

## 5.1 The hot slumping technique

For the manufacturing and replication of large and lightweight reflecting surfaces at a reasonable cost the classical lapping techniques are not adequate. In the recents years, for the manufacturing of the mirrors for the IACTs other techniques like the diamond milling (Bastieri et al. [13]) and the cold glass slumping (Pareschi et al. [107]) have been successfully implemented.
For the production of highly curved surfaces the hot slumping is mandatory over the cold slumping. In general with the hot slumping technique a thin and flat glass sheet is placed above a master mould previously optically figured and polished at the desired shape; then a suitable thermal cycle is applied. When sufficiently heated the glass will soften enough to slump onto the mould surface and adapts to the mould's shape. When the system is cooled down to room temperature, the slumped glass shell is released from the mould and coated with the proper reflecting layer [48]. Different slumping processes exist: almost all share the basic idea of forming a thin glass mirror by shaping it over a mould through the application of a suitable thermal cycle. The thermal cycle changes the viscosity properties of the glass allowing it to deform in order to assume a desired shape. Depending on the side of the forming mirror that comes in contact with the mould (Figure 5.1), two approaches are distinguished: the direct approach, in which the optical surface of the mirror comes in contact with the mould during the process, or the indirect approach, in which the contact happens on the back side (Winter et al. [142]).


Figure 5.1: Two possible setups for the hot slumping of a glass: direct, with the optical surface in direct contact with the mould and indirect, with the optical surface not in contact with the mould. Photo taken from Ghigo et al. [49].

Figure 5.2 schematizes the process of glass bending. The direct hot slumping requires the mould has a surface micro-roughness very low to avoid changes on the glass. All the process has to be executed in a clean room where dust particles are removed from the mould, since a dust grain trapped between the mould and glass surfaces during the slumping process prevents

a correct copy of the mould's shape in an area some $cm^2$ wide [48]. The maximum temperature that can be reached is 650 °C, and to reduce thermal gradients above the mould the entire system is kept under vacuum. To prevent errors of shape of the glass, especially during the cooling phase, a pressure is applied.

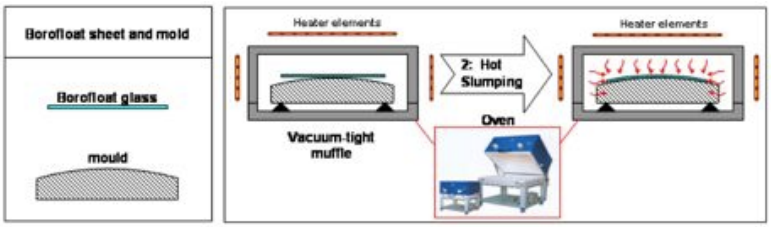


Figure 5.2: Hot slumping process: a thin flat glass shell is bended upon a mould in a hot thermalized, vacuum and clean environment. Photo courtesy Ghigo et al. [48]

M2 prototypes have been produced via indirect hot slumping which foresees the following steps (Ghigo et al. [49]): (i) the concave mould is ground and figured with the required shape, (ii) the glass segment is covered with a substrate of detaching material to avoid sticking with the mould, (iii) the glass sheet is placed above the concave mould, (iv) the thermal cycle is started, and at temperatures between the annealing point and the softening point the glass slumps under its own weight into the mould copying its shape, (v) after the cooling of the oven the glass is released from the mould. The indirect approach has to obey to a series of constraints:

- High uniformity in the thickness of the glass
- Full contact of the glass foil with the mould only by gravity is feasible
- Very high thickness constancy of the glass required
- Reflecting layer to be deposited after the slumping (possible stresses)

but it has the great advantage (with respect to direct approach) of not requiring highly polished mould surfaces. A further discussion on the effects of the hot slumping on the mirror PSFs can be found in section 5.9.

## 5.2 M2 Prototypes

Using the hot, indirect slumping technique, three different types of mirror have been manufactured and delivered by FLABEG:

- Three thick mirrors of 19 mm
- An intermediary mirror of 15 mm
- Two thin shell mirrors of 6 mm

The mirrors of 19 and 15 mm thick have a sufficient stiffness to support their weight autonomously and the pads of the mirror support system are directly glued on the back of the glass. Conversely the thin shells 6 mm thick need to be glued to a supporting honeycomb structure to create a mirror sandwich (glass shell | honeycomb | glass shell). In this thesis work only the prototypes 19 mm thick have been considered for two main reasons: i) one 19 mm prototype was chosen to be integrated on the ASTRI SST-2M prototype in summer 2014, ii) the 19 mm prototype ensures a better mechanical and thermal stability in comparison to the thinner prototypes.

## 5.3 Residuals map of the M2 prototypes

The thick M2 prototypes (19 mm) have been the first mirrors to be produced. The mirror has to be compliant with the requirements of shape given in paragraph 2.3.4 in Table 2.6. The tolerances on the manufacturing process of M2 are listed in Table 5.1.

| **Manufacturing** | **Value** |
|---|---|
| **Mould** | 120 $\mu$m PV$^{\dagger}$ |
| **Replication process** | 200 $\mu$m PV |
| **Total** | 217 $\mu$m PV, quadratic propagation |
| **Total** | 54 $\mu$m PV, account for M2 demagnification factor m = 4 |

Table 5.1: Tolerances in the manufacturing process of M2 from the ASTRI Error budget tree [159], † Peak to Valley.

The glass used to produce M2 prototype is BOROFLOAT. The total weight of the mirror is $\sim$ 130 kg. A picture of the uncoated mirror before shipment is reported in Figure 5.3

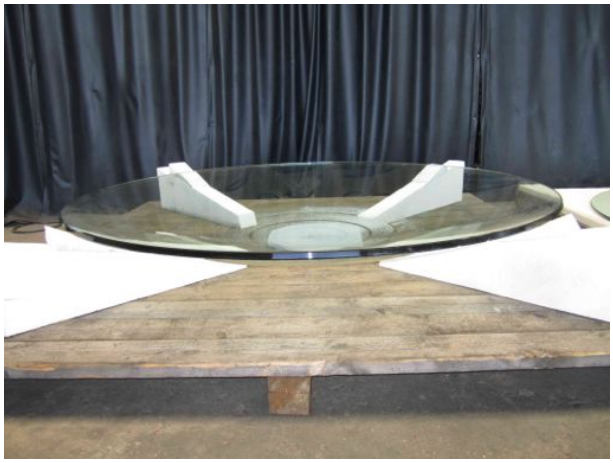

Figure 5.3: A picture of an uncoated M2 prototype (19 mm thick) taken at FLABEG before shipment.

A first evaluation of the mirror quality has been carried out by FLABEG before mirror delivery. The machine used to measure the mirror profile is a ZEISS 3-D coordinate measuring machine. FLABEG released two datasets, one for Teil1 and the other for Teil2, of the residuals map from the nominal sag of M2 as shown in Figures 5.4 and 5.5. Most of the points are inside the tolerances range (deviations $<$ 0.2 mm, PV), the outer regions undergo more pronounced deviations from the nominal sag. Some regions at the edge of the mirror are missing, the map surface has a completeness of about 90 %.

To get a cross-check with the data released by FLABEG an optical simulation with the measured mirror profile is performed to verify that the telescope performances remain inside the specifications. To introduce the 3-D residuals map, a first attempt consists in parametrizing the measured surface following the Delaunay triangulation method [31] (see Figure 5.6). The triangles coordinates are collected in a text file and imported in Zemax as a *Polygon Object*.

The smaller the Delaunay triangles are, the better is the surface representation. However, triangles excessively small produce files unreasonably large; the best trade-off recognized for the present situation is for triangles with a 4 mm edge. The triangulation of the mirror surface although produces a convolution of the nominal surface with a mesh of 4 mm triangles, resulting in a broader and smeared out PSF as shown in Figures 5.7b and 5.7c. This is not a real physical effect, rather an artifact introduced by the surface representation, but it creates important biases

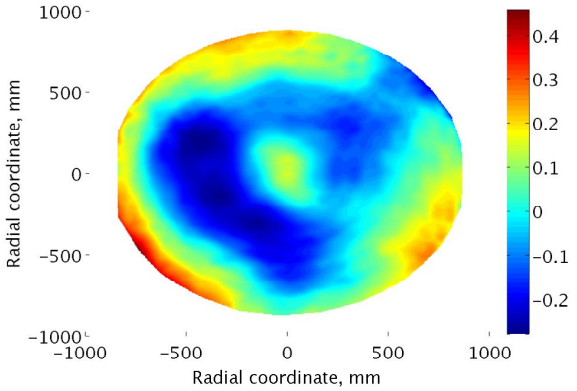


Figure 5.4: 3-D colormap of the residuals from nominal sag for Teil1 prototype retrieved by ZEISS 3-D coordinates measuring machine, units are in mm.

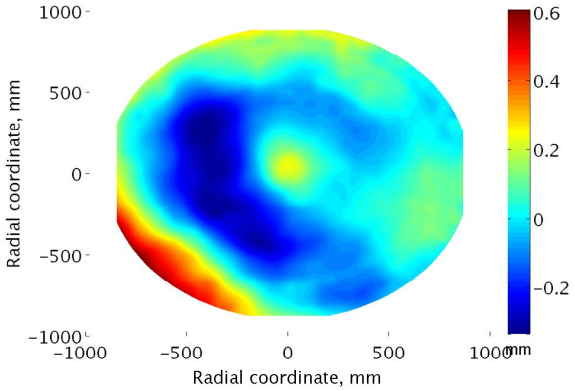


Figure 5.5: 3-D colormap of the residuals from nominal sag for Teil2 prototype retrieved by ZEISS 3-D coordinates measuring machine, units are in mm.

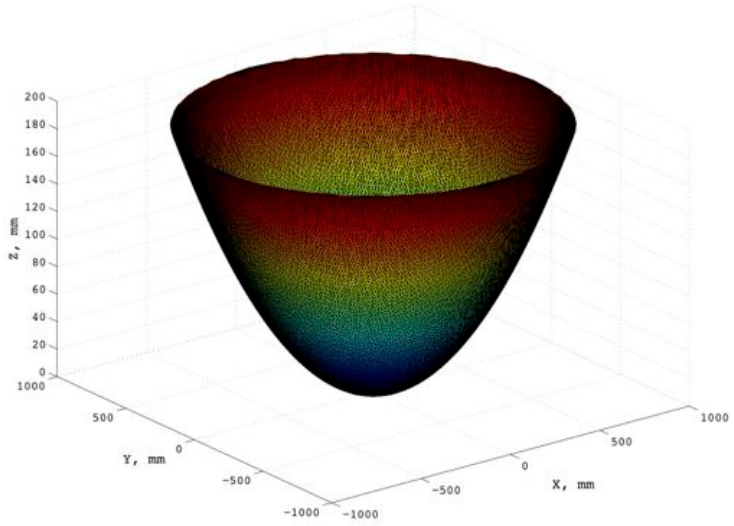


Figure 5.6: View of the 3-D representation of M2-19 with the surface mesh built with a Delaunay triangulation (triangles 4mm edge). This object constitutes the input model to Zemax software.

in the photometric estimations of the PSFs sizes. For this reason an alternative surface representation of the surface based on the Zernike Polynomials has been implemented as described in section 5.4.

## 5.4 Surface mirror representation with the Zernike polynomials

The use of the Zernike polynomials for describing the classical aberrations of an optical system is well known (R. J. Noll [103]), but they can describe aberrated surfaces more in general, like optical surfaces, i.e. lens and mirrors. In this paragraph we present the M2 surfaces representation by the use of the Zernike polynomials. These functions are particularly useful to represent the data coming from the optical testing of the mirrors into the ray tracing softwares.

The Zernike polynomials are a set of polynomials that are orthonormal on the unit circle. The best and convenient representation of the Zernike polynomials is achieved by the use of the polar

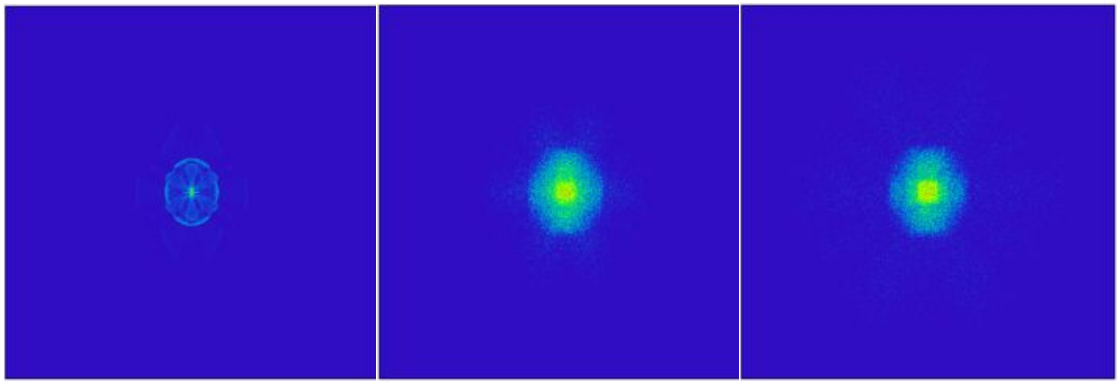

(a) (b) (c)

Figure 5.7: (a) ASTRI nominal PSF (b) ASTRI nominal PSF obtained with a triangulation of the nominal M2 reported for comparison, (c) ASTRI PSF obtained with a triangulation of the FLABEG prototype M2-19.

coordinates, so that the polynomials are a product of angular functions and radial polynomials. The Zernike polynomials are invariant in form with respect to a rotation of the axes about the origin. The even polynomials given by cosine function correspond to symmetric function while odd polynomials given by sine function correspond to antisymmetric function.

$$R_n^m(\rho)e^{im\theta} = \begin{cases} R_n^m(\rho)cos(m\theta) \\ R_n^m(\rho)sin(m\rho) \end{cases}$$

the radial term is:

$$R_n^m(\rho) = \sum_{s=0}^{(n-m)/2} \frac{(-1)^s(n-s)!}{s!(\frac{n+m}{2}-s)!(\frac{n-m}{2}-s)!}\rho^{n-2s}$$

The index $n$ represents the radial degree or the order of the polynomial since it is the highest power of $\rho$ in the polynomial, and $m$ may be called the azimuthal frequency. The wave aberration function $W(\rho,\theta)$ of the system can be expanded in terms of a complete set of Zernike circle polynomials which are orthogonal over a unit circle in the form:

$$W(\rho,\theta) = \sum_{n=0}^{\infty}\sum_{m=0}^{n}\left[\frac{2(n+1)}{1\delta_{m0}}\right]^{1/2} \cdot R_n^m(\rho)\cdot(c_{nm}cos(m\theta) + s_{nm}sin(m\theta))$$

that can be written in a more compact expression:

$$W(\rho,\theta) = \sum_{j=1}^{\infty} a_j Z_j(\rho,\theta)$$

where $a_j$ are the aberration coefficients, that splits into three equations:

$$Z_{evenj}(\rho,\theta) = \sqrt{2(n+1)}R_n^m(\rho)cos(m\theta) \rightarrow m \neq 0$$

$$Z_{oddj}(\rho,\theta) = \sqrt{2(n+1)}R_n^m(\rho)sin(m\theta) \rightarrow m \neq 0$$

$$Z_j(\rho,\theta) = \sqrt{2(n+1)}R_n^m(\rho) \rightarrow m = 0$$

Using this orthogonality, any function $f(\rho,\theta)$ defined on the circle can be expressed as a sum of Zernike modes, just as sine and cosine functions are used in familiar 1-D Fourier analysis:

$$f(\rho,\theta) = \sum_{n=0}^{\infty} \sum_{m=-n}^{n} a_{nm} Z_n^m(\rho,\theta)$$

By representing data in this way we can summarize a complicated structural deformation or aberration in terms of a small number of coefficients associated with the dominant Zernike modes. The magnitude of each term is the RMS contribution of the term. The coefficients are evaluated by inverting the previous equation:

$$a_{nm} = \int\int_{circle} f(\rho,\theta) Z_n^m(\rho,\theta) \rho d\rho d\theta \tag{5.1}$$

The $a_{nm}$ can be determined directly from the above equation if $f(\rho,\theta)$ is a known function, or computed numerically if $f(\rho,\theta)$ is a set of measured data. An optical surface can be represented by an infinite sum of Zernike polynomials of progressively increasing degree. In the next paragraph this surface representation is applied to the residuals map of the M2 prototypes and imported in the Zemax optical design of the telescope.

**Zernike surface in Zemax**

A Zernike surface in Zemax is defined by the following sag equation:

$$z(r) = \frac{cr^2}{1+\sqrt{1-(1+k)c^2r^2}} + \sum_i \alpha_i r^{2i} + \sum_{i=1}^{N} a_i Z_i(\rho,\phi) \tag{5.2}$$

Where $c$ is the curvature of the surface, $k$ is the conic constant, the $\alpha_i$ terms are the aspherical coefficients, $N$ is the number of Zernike coefficients in the series, $a_i$ is the coefficient of the $ith$ Zernike Standard polynomial, $r$ is the radial coordinate in lens units, $\rho$ is the normalized radial coordinate, and $\phi$ is the angular coordinate. The surface is described by the sum of three main terms:

- A spherical sag
- A summation of aspherical terms
- A summation of Zernike polynomials

The Zernike coefficients $Z_1 - Z_N$ are calculated with a Matlab script and imported with a dedicated macro into Zemax the optical design. The procedure followed to get the Zernike coefficients is reported in the flow chart below.

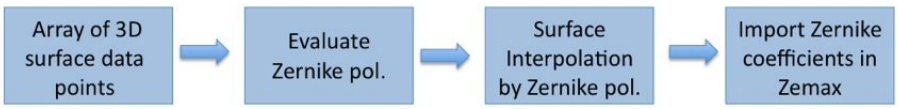


Figure 5.8: Conceptual procedure followed to compute the Zernike coefficients and importing them in the optical design.

To retrieve the Zernike coefficients $a_{nm}$ we have to evaluate the Zernike polynomials $Z_i f(\rho,\theta)$ in equation 5.1 for a given set of surface profile data points. We can consider a 3-D mesh points $(x_N, y_N, f(x_N, y_N))$ to be inserted in the matrix expression below:

$$\begin{pmatrix} Z_0^0(x_1,y_1) & Z_1^{-1}(x_1,y_1) & .. & Z_n^m(x_N,y_N) \\ Z_0^0(x_2,y_2) & Z_1^{-1}(x_2,y_2) & .. & Z_n^m(x_2,y_2) \\ .. & .. & .. & \\ Z_0^0(x_N,y_N) & Z_1^{-1}(x_N,y_N) & .. & Z_n^m(x_N,y_N) \end{pmatrix} \begin{pmatrix} a_{00} \\ a_{1-1} \\ .. \\ a_{nm} \end{pmatrix} = \begin{pmatrix} f(x_1,y_1) \\ f(x_2,y_2) \\ .. \\ f(x_N,y_N) \end{pmatrix}$$

This collection of linear equation can be schematized by the expression $ZA = F$, that can easily reversed to get the column vector of Zernike coefficients A:

$$A = (Z^T Z)^{-1} Z^T F$$

The A vector is then passed to Zemax for the surface representation.

### 5.4.1 Zernike representation for Teil1 and Teil2

The procedure described in the previous section to retrieve the Zernike Polynomials has been applied to the measured profiles of Teil1 and Teil2 for which a residuals map was available. As the reader can observe, the measured residuals map of Teil1 (Figure 5.9) is reproduced by the use of 231 Zernike terms (Figure 5.10). Although differences between the two patterns remain, this approach has the net advantage of providing a continuous, analytical representation of the mirror surface. This representation avoid the bias introduced by the previous method based on the surface triangulation. Once the Zernike terms are calculated by a Matlab dedicated script, they are loaded in the Zemax telescope optical design and the PSFs can be simulated as shown in Figures 5.11 and 5.12.

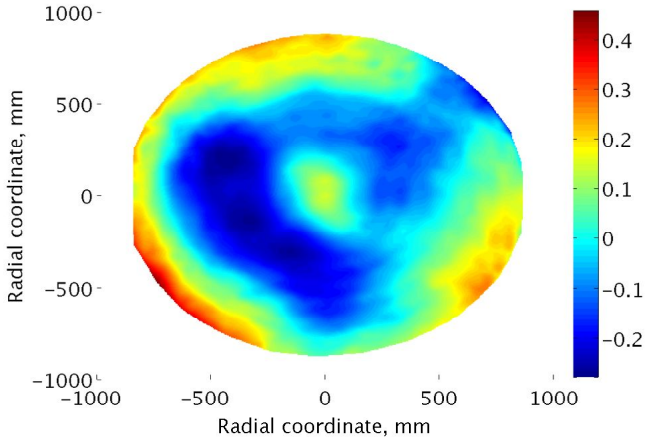


Figure 5.9: 3-D colormap of Teil1 provided by the manufacturer and retrieved by ZEISS 3-D coordinates measuring machine, units are in mm.

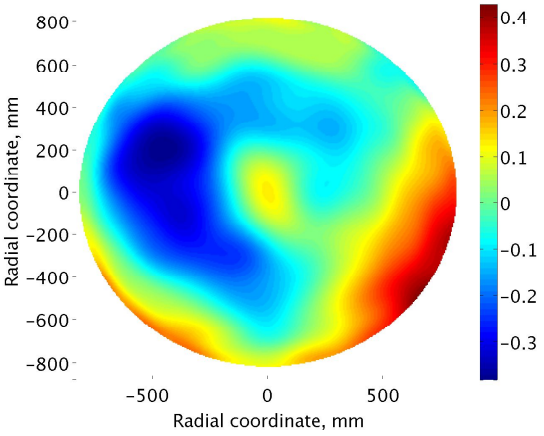


Figure 5.10: 3-D colormap of Teil1 reconstructed on the basis of the ZEISS 3-D dataset by a series of 231 Zernike Polynomials, units are in mm.

The simulated PSFs of the ASTRI prototype with the Zernike representation of M2 (Figure 5.12) show more irregular rims and distorted patterns with respect to the nominal series of Figure 5.11. However when the photometric properties of the PSFs are compared, the degradation of the spots introduced by the real M2 prototype turn out to be acceptable. Following a procedure described extensively in section 5.7, the photometry of the PSFs has been calculated by means of a series of circular apertures. The plot of the energy content as a function of the photometric aperture shows the so called normalized, Ensquared Energy, (EE), and gives a quantitative estimation of the PSFs size. The plots of the profile of the EE for the telescope PFSs with the nominal and measured M2 sag are traced in Figure 5.13 and 5.14 respectively.

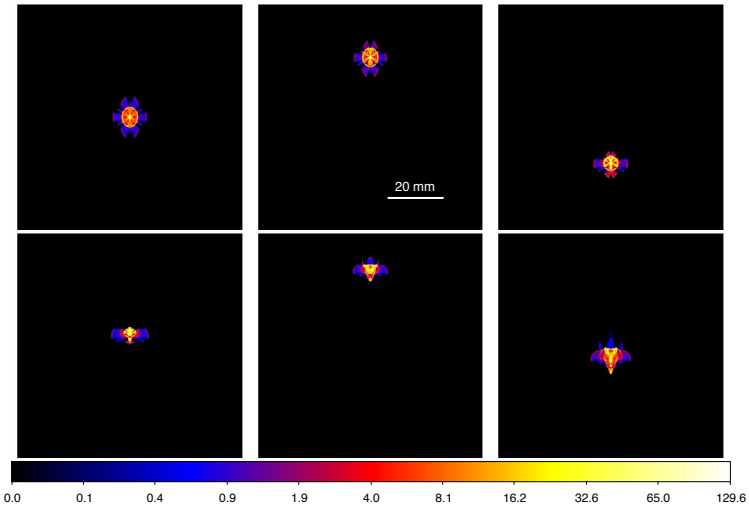


Figure 5.11: PSFs of the ASTRI prototype at different positions inside the FoV obtained with a nominal sag of M2. Top panels from top left 0,1,2°, bottom panels from top left 3,4,4.8°.

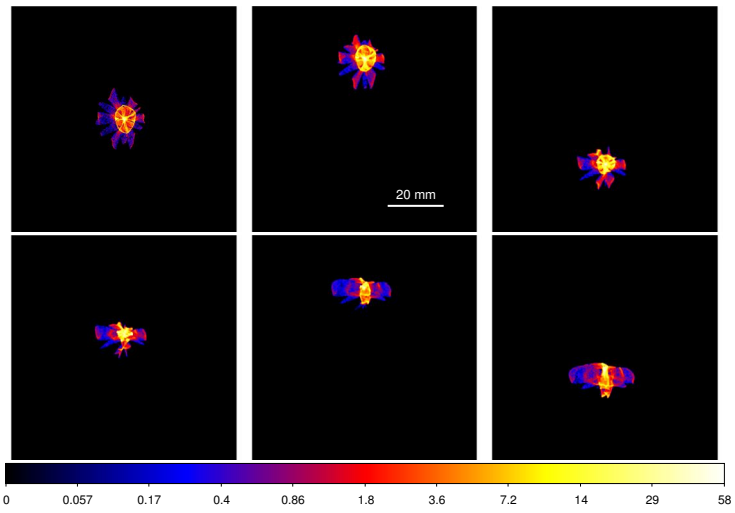


Figure 5.12: PSFs of the ASTRI telescope at different positions inside the FoV obtained with the measured sag of M2 represented by 231 Zernike terms. Top panels from top left 0,1,2°, bottom panels from top left 3,4,4.8°.

As a rule of thumb, the 80% of the EE should be contained in the pixel of the Cherenkov camera. As discussed in section 2.4 however, the ASTRI prototype is optimized to achieve best performances between 1 and 4° in the FoV. The curves describing the EE for the ASTRI prototype with the nominal M2 grow steeper than those obtained with the measured profile. This is a direct consequence of the deformations and the general broadening of the PSFs above mentioned. The introduction of this latter profile causes a general increase of the PSFs size for all the fields considered in the FoV ($\sim$ 30% of R80 in average).

Figure 5.15 shows the residuals between the photometric radii from the measured and nominal M2 prototype; the fact that the differences are negative means that for a certain photometric radius the EE of the nominal PSFs is greater than that recreated by the measured sag. The variations in percentage of the EE are in the order of 20 %, but it is important to note that, most of them are concentrated and contained inside the pixel size of the Cherenkov camera. This

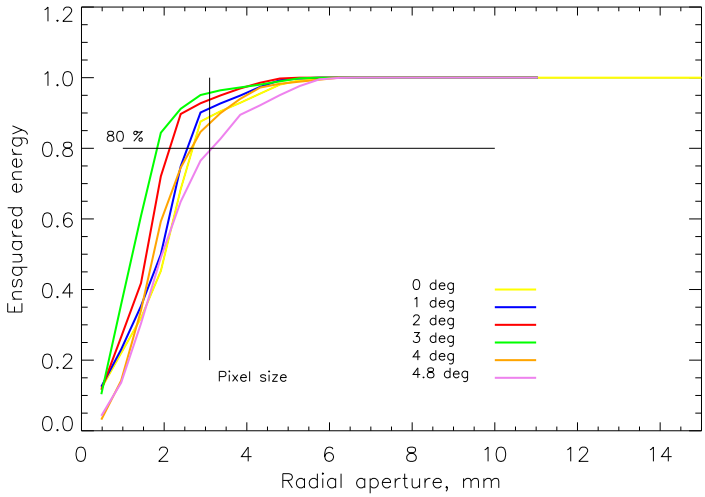


Figure 5.13: Normalized ensquared energy of the PSFs from the ASTRI prototype with the nominal M2 profile. The reference value for performance studies and PSF size estimation is the radius enclosing the 80% of the total energy. The size of Cherenkov camera pixel is reported for direct comparison.

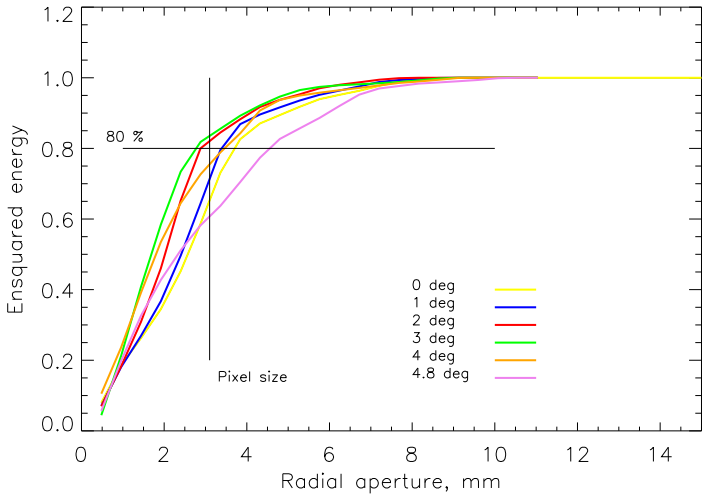


Figure 5.14: Normalized ensquared energy of the PSFs from the ASTRI prototype with the measured M2 profile. The reference value for performance studies and PSF size estimation is the radius enclosing the 80% of the total energy. The size of Cherenkov camera pixel is reported for direct comparison.

means that the general broadening of the spots affects only partially the resolution of the system and any variation that is inside the pixel of the camera does not affect the performance of the system. It is worthwhile to observe that the fields undergoing the most important deviations are those on-axis (0°) and and at the edge of the FoV (4,4.8°), while the intermediary regions of the FoV, where the telescope is optimized to operate, still preserve a compact spot size.

Despite this increase of the PSFs size, the telescope is fully compliant with the requirement for SSTs stating that the telescope must focus light (over 80% of the required camera FoV diameter) with an optical $\mathrm{PSF}_{D80}$ of $<$0.25 degrees as shown in Figure 5.16.

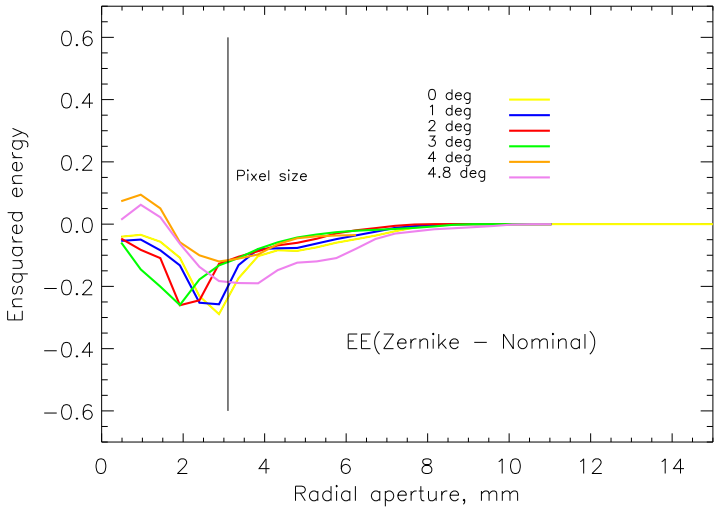


Figure 5.15: Normalized ensquared energy residuals between $EE_{Zernike}$ and $EE_{Nominal}$. The largest deviations occur inside the camera pixel. The size of Cherenkov camera pixel is reported for direct comparison.

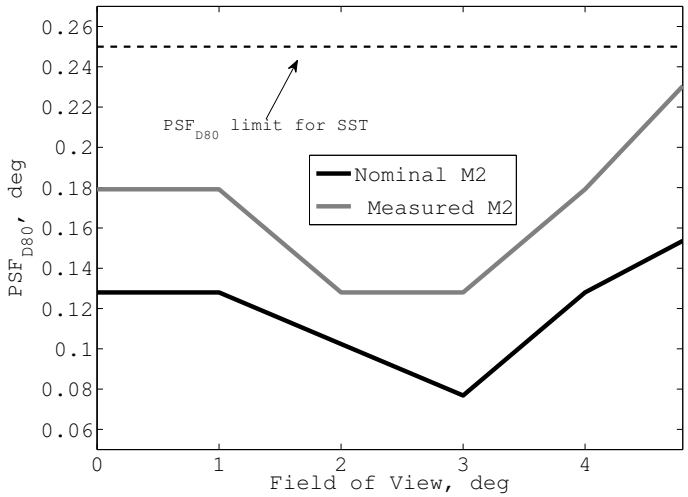


Figure 5.16: $\mathrm{PSF}_{D80}$ for the telescope with a nominal M2 design and for a measured M2 represented by 231 Zernike polynomials. All the fields are below the limit fixed for the SSTs.

A possible solution to increase the compactness of the PSFs relies on a slight off-set of M2 from its nominal position. As shown in Figure 5.17, a simple shift of M2 toward the focal plane of 1 mm leads to restore the field at 4.8° close to the size of the Cherenkov pixel. This operation is possible thanks to the actuators of M2 that provide a range of about 7.5 mm as discussed in section 2.3.5.

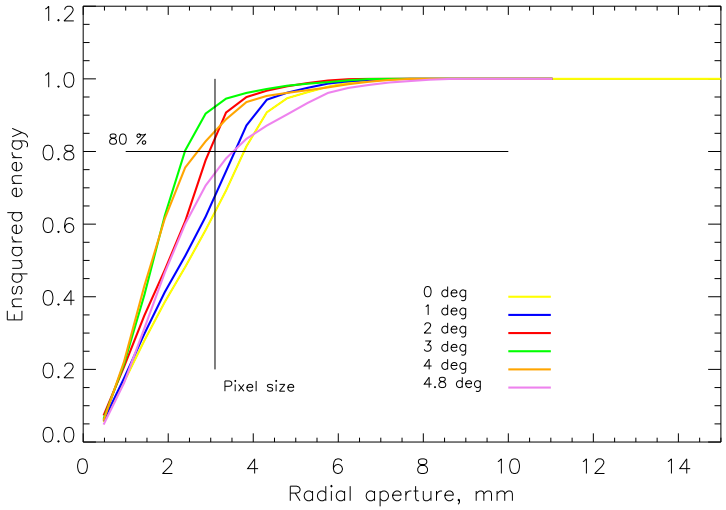


Figure 5.17: Normalized ensquared energy of the PSFs from the ASTRI prototype with the nominal M2 profile for 1 mm off-set of the secondary mirror with respect to its nominal position. This modification results in a series of PSFs more compact with respect to Figure 5.14.

## 5.5 M2 profile ellipticity

Due to the hot slumping process (previously discussed in section 5.1), the shape and the centre of the mirror figure can change from the regular circle requested by design. To ensure the mounting of the mirror at the telescope in the right position with a tolerance of ± 2mm, the profile ellipticity of the mirrors must be evaluated. The nominal shape of the mirror profile is a circle with a radius r = 925 mm, the measurements will estimate the ellipticity of the mirror profiles by an elliptical best curve fitting.

### Test procedure description

To perform the ellipticity measurement eight points equally distributed along the azimuth angle have been recorded using a graduated bar. A laser fixed to the graduated bar points to the mirror centre marked by the manufacturer. The bar is rotated along the profile in different azimuth position to gather different measurements of the mirror radius.

### Test result

In Figures 5.18, 5.20 and 5.22 the plot of these points and the elliptical profile retrieved by the least squares method is compared to the nominal profile. For the three mirrors prototypes (19 mm thick), Figures 5.19, 5.21 and 5.23 show the residuals of the prototype profiles from the nominal design. The requirement to be verified is that the profiles have departures from the nominal radius $< \pm$ 25 mm.

The best estimate of the semi-major and semi-minor axes, $a$ and $b$, of the elliptical profiles are given in Table 5.2 and in Figure 5.24.

All the three prototypes examined are inside the specifications stated above, $\Delta r_{nominal-measured} < |\pm 25| mm$.

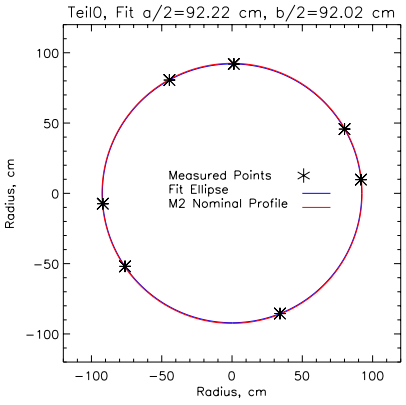


Figure 5.18: Nominal M2-Teil0 profile compared with the fitted profile based on the experimental data points.

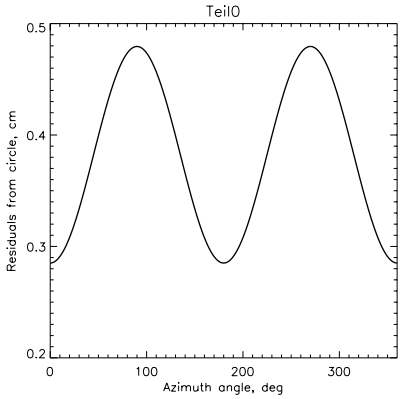


Figure 5.19: Residuals between circular nominal shape - measured, fitted profile.

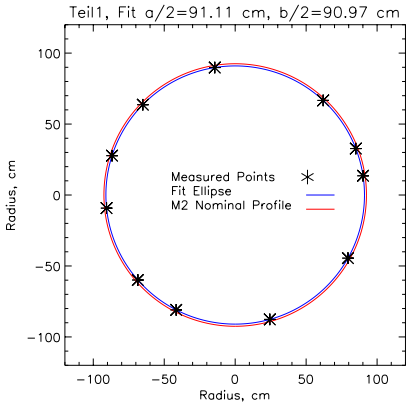


Figure 5.20: Nominal M2-Teil1 profile compared with the fitted profile based on the experimental data points.

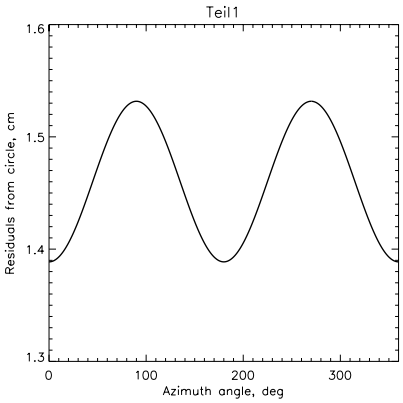


Figure 5.21: Residuals between circular nominal shape - measured, fitted profile.

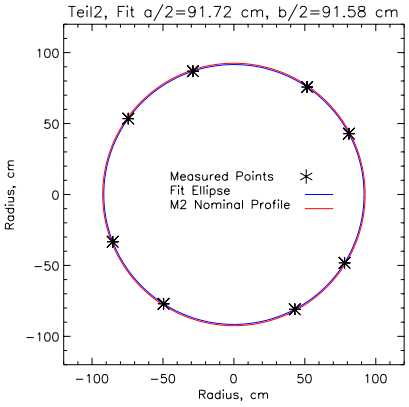


Figure 5.22: Nominal M2-Teil2 profile compared with the fitted profile based on the experimental data points.

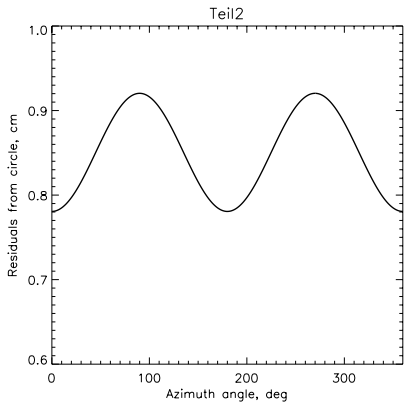


Figure 5.23: Residuals between circular nominal shape - measured, fitted profile.

| Prototype mirror | a | b |
|---|---|---|
| **Teil0** | 922.2 mm | 920.2 mm |
| **Teil1** | 911.1 mm | 909.7 mm |
| **Teil2** | 917.2 mm | 915.8 mm |

Table 5.2: Estimated values for the semi-minor and semi-major axes of the three M2 prototypes.

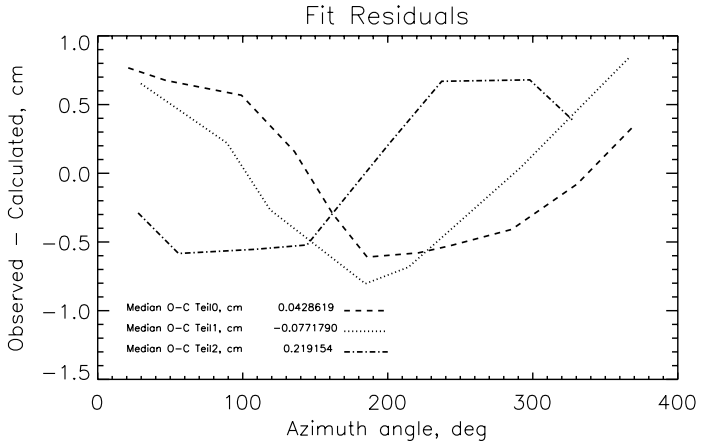


Figure 5.24: Summary of the residuals between measured and nominal profiles for the three mirror prototypes (Teil0, Teil1 and Teil2). All the profiles meet the specification and present deviations (in absolute value) from the nominal radius $< 25$ mm.

## 5.6 M2 centre estimation

The verification of the real position of the mirror optical vertex must be assessed before mirror coating deposition. During the hot slumping process, the glass is deformed by heat and pressure and some shifts can arise between the mechanical shape and the optical one. This must be taken into account in the alignment with the mirror support system, MSS. An estimation of this misalignment is then mandatory. The glass after bending shows a series of concentric circular arcs on the rear surface centered on the optical vertex defined by the mold (see Figure 5.25). The offset between the centres of these arcs and the optical centre marked by the manufacturer represents the estimation to be taken into account when the pads for the MSS are glued onto the rear of the mirror. The measurements have been performed only on Teil1 and Teil2.

### Test procedure description

A series of pictures of the entire glass is taken by a digital camera suspended above the glass at about 2 meters of height. The images are analyzed by visualization software (Ds9) and a series of sampling points on the arcs is retrieved for subsequent fitting and centre estimation (Figure 5.25, 5.27). This estimation for Teil1 and Teil2 mirrors shows a maximum displacement of 1.8 mm which is inside tolerances in alignment (2 mm, refer to section 4.4.2) estimated for M2 with respect to the telescope optical axis.

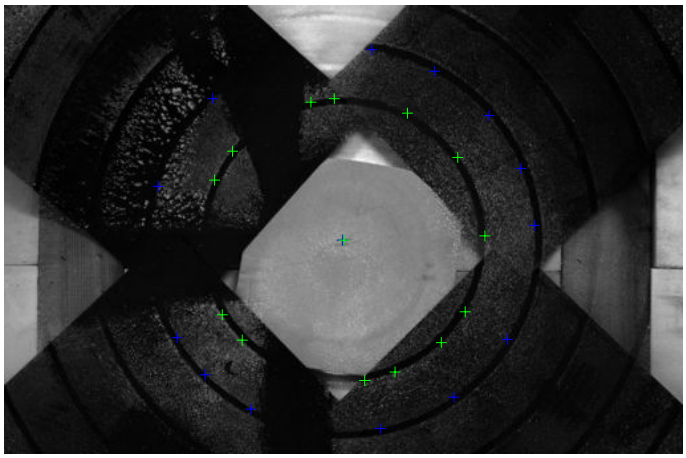

Figure 5.25: Sampling points (blue and green) along the mirror arcs used for the verification of the mirror centre marked by the manufacturer.

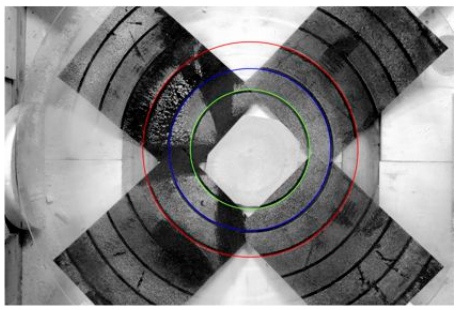

Figure 5.26: Fitted elliptical curves on mold arcs imprinted on the rear surface of the slumped glass.

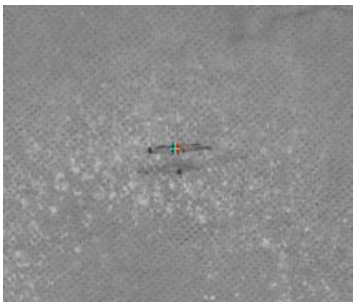

Figure 5.27: Estimated mirror centres retrieved from the fitting of the three arcs (green, blue and red). The black cross is provided by the manufacturer.

**Test result**

| Prototype mirror | Centre displacement |
|---|---|
| **Teil1** | $\Delta c = 1.48 \pm 0.05$ mm |
| **Teil2** | $\Delta c = 1.32 \pm 0.57$ mm |

Table 5.3: Estimated values of displacement between the mirror mechanical centers marked by the manufacturer and those retrieved by the mold footprints on the rear of the glass.

## 5.7 M2 PSF photometric study and focal length estimation

One of the most direct and valuable tests for the mirror qualification is the PSF measurement and the study of its photometric properties. This measurement, together with the measurement of the mirror focal length, that is directly linked with the former, is usually used for the acceptance and qualification of the Cherenkov mirrors. Although it gives a cumulative information on the overall optical surface that requires a careful interpretation, it constitutes one of the best compromises in terms of time vs information retrieved.

**Test procedure description**

The mirror is illuminated uniformly with a light source positioned at a distance approximately equal to the mirror radius of curvature; this set up is often labelled as $2f$ configuration and is shown in Figures 5.28 and 5.29. The light source, a LED working at $\lambda = 640$ nm, is kept at 63.5 mm off-axis with respect to the mirror optical axis. A large CCD camera retrieves the PSF images at the opposite side of the LED, specularly with respect to the mirror optical axis (Figure 5.28). We label $p$ as the separation between the light source and the mirror, and $q$ as the separation between the CCD camera and the mirror. The CCD camera and the light source have also an off-set along the direction of the optical axis i.e. $q = p + 35$ mm. These off-sets are due to the mechanical volume of the CCD camera and they are needed to avoid the vignetting of the light source. Both the light source and the CCD camera are mounted on the same platform that can be moved to find the mirror best focus position.

The CCD camera used for the test campaign of all the mirrors is a *Flicamera* CCD-PL0133411 by Fingerlake. The CCD camera has an array of 2048 x 2048 pixels with a pixel size of 24 $\mu$m and it is cooled by Peltier cells down to about $-25°C$. For further information refer to the datasheet of the camera available at [167]. For each PSF acquired, an image background is taken switching off the LED to get a frame accounting for the background contributions/disturbances. A subsequent analysis by an IDL routine that makes use of the Daophot utilities [126] allows extracting the PSF photometric properties of interest. The reference value used in the present research to estimate the mirror quality is the $R80$ parameter that corresponds to the photometric radius containing the 80% of the total PSF light. The size of the PSF in the 2f configuration is about twice the size of the PSF expected by moving the light source at infinity. Once the best focus position is recognized, the separation between the mirror and the light source gives an estimate of the radius of curvature, $R$, of the optical surface. Measuring this separation by a disto (distance) device (model Stanley Tru laser TML 130) provides an estimate of the focal length of the mirror which is half the radius of curvature value, $f = R/2$. In this test the images are taken moving the platform holding the CCD and the light source from a position of extra-focus towards the mirror at steps of 5 mm.

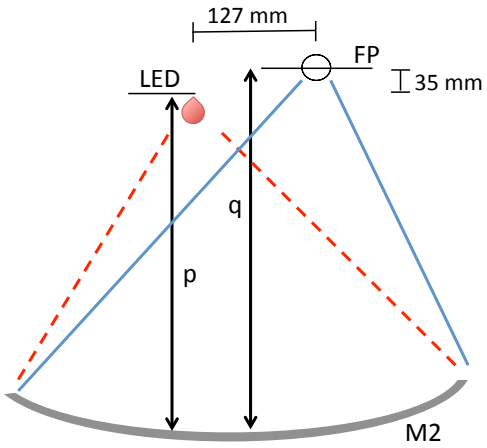


Figure 5.28: Schematics of the 2f-setup used for the study of the PSF and focal length estimation. FP = focal plane.

Figure 5.29: Real 2f-setup used for the study of the PSF and the determination of the focal length.

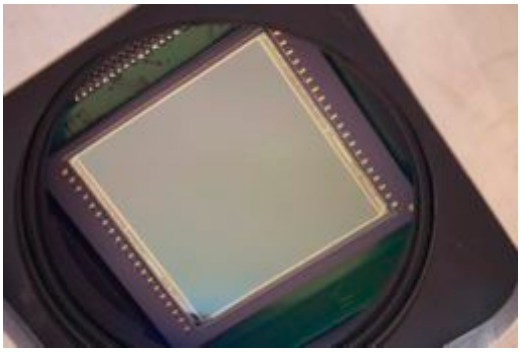

Figure 5.30: CCD sensor 2048 x 2048, 24 $\mu m$ pixel, Fingerlake FLICAMERA.

Figure 5.31: LED $\lambda = 640$ nm used for the illumination of M2 during the test campaign. The PSF of the mirror is visible on the CCD camera shutter.

### Data analysis

The first step of the image analysis process with IDL foresees the subtraction of the background that is taken with the light source switched off and it accounts for all the possible source of noise (spurious light source), dark current and bias. Then the centroid position of the PSF is estimated by a dedicated IDL routine for the spots sufficiently regular i.e. for point-like spots. However dealing with an aspherical surface means that the intra-focus spots have not a point-like shape, rather they show a donut-like pattern as shown on the right of Figures 5.32 and 5.33.

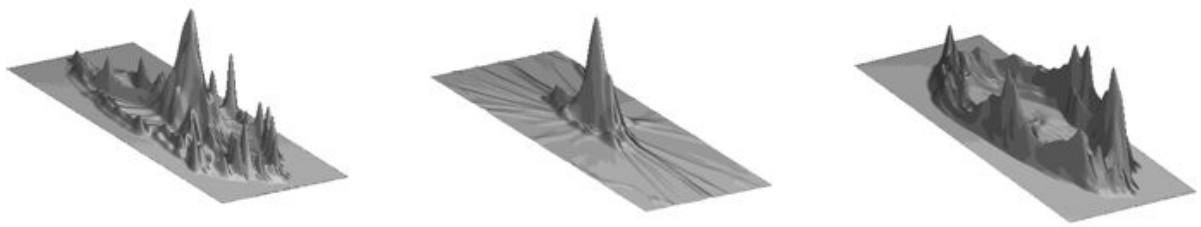

Figure 5.32: 3-D shaded surfaces of the PSF focal series for an extra-focus position (left), in the best focus position (centre), and for an intra-focus position (right).

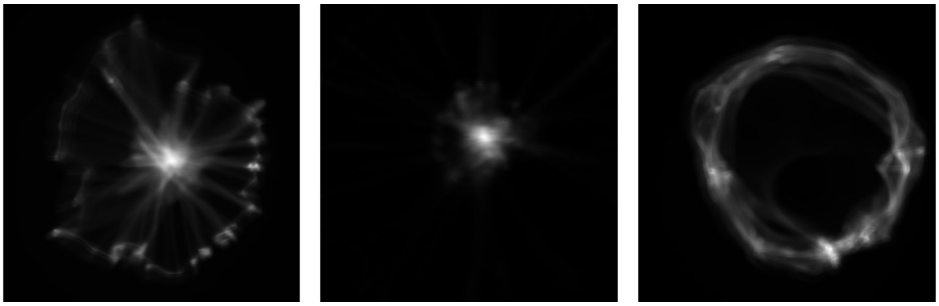

Figure 5.33: Images of the Teil2 PSFs referring to the same focal series of Figure 5.32.

This shape peculiarity causes the failure of the algorithm of the centroid automatic search. When this happens the user must provide a manual input of the approximate centroid coordinates estimated on the symmetry of the spot analyzed with the Ds9 software tools. Once the light barycentre of the PSF light is estimated, the software computes the photometry of the light spot through a series of progressively larger circular apertures centered on the centroid. Ideally, the larger aperture should enclose all the light from the PSF, but it could happen that the CCD sensor is not large enough to enclose the outer regions of the PSF. The analysis is meaningful if most of the PSF light is collected by the CCD, as in the current case of study. A reliable check to estimate whether the photometry of the PSF is reliable consists in looking to the profile of the encircled energy, contained in the photometric apertures traced around the spot. As shown in Figure 5.34, in this case the curve of the EE shows a stable plateau at large photometric apertures and it confirms that all the light from the PSF has been collected.

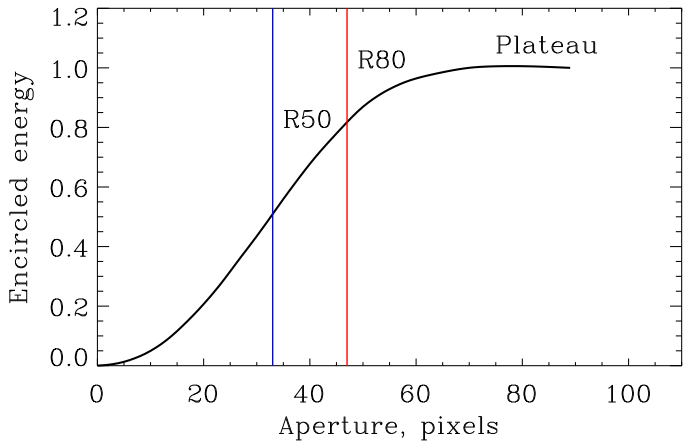


Figure 5.34: Normalized encircled energy for a PSF retrieved during Teil2 measurements. The photometry is performed inside progressively larger apertures that collect different energy percentage (blue 50 %, red 80 %) until all the light is gathered and the profile of the curve becomes flat. Usually R80 is assumed as reference value for the PSF size.

### Test result

As discussed in section 2.3.4 the sag profile of M2 is aspherical. The aspherical sag shows important deviations from the paraxial spherical profile (1-1.2 mm) in the outer part of the mirror. This sag profile results in a mirror having multiple foci. The PSFs from the entire mirror surface show a lot of diffuse light in the surroundings of the central core of the spot. The origin of this light is twofold: part of it originates from scattering processes on the glass surface and part is due to the fact that the mirror has different foci moving from the centre to the edge of

the sag. For this reason the study of the PSFs from the overall surface could be confusing as shown in Figures 5.35 and 5.36. It is preferred to subdivide the mirror surface in a series of rings by a set of spatial masks that obstruct all the surface but one ring. This technique and related results are discussed in the next section.

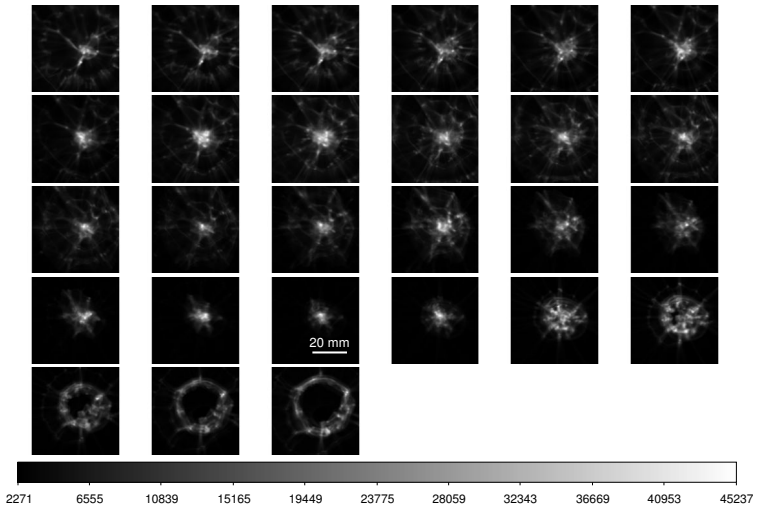


Figure 5.35: Images of the PSFs from Teil2 during the test campaign of June 2014. Images are taken moving the platform with the CCD camera and the illuminator at steps of 5 mm towards the mirror.

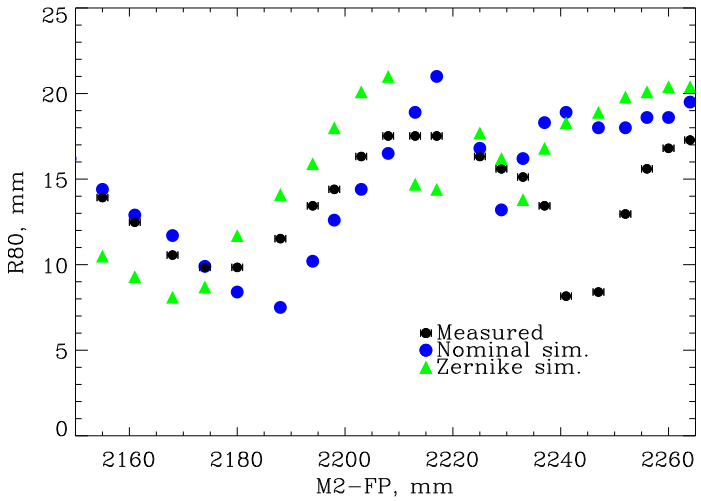


Figure 5.36: Photometry expressed in terms of R80 of the PSFs shown in Figure 5.35 (black points). Blue points, photometric simulated PSF radii for the nominal mirror and for the Teil2 profile retrieved by Zernike Polynomials analysis (green points). The mirror does not show a single minimum PSF i.e. a single focus.

The study of the PSF of the overall surface has pointed out that the focus depth of the mirror is about 2 mm.

## 5.8 M2 spatial masks and multiple foci recognition

More reliable information on the mirror PSFs can be obtained by subdividing the surface in different rings. This is achieved by the use of cardboard spatial masks which obstruct all the surface but one ring of interest. This technique allows a better examination of different radial regions of the surface that are inevitably convolved inside a single PSF when the overall mirror is considered. A series of eight spatial mask has been designed and fabricated for the testing of the M2 prototypes. Two spatial masks subdivide the surface roughly in two areas, the paraxial-spherical inner region and the outer, aspherical region; the other six masks isolate sharp rings at different radii over the surface as shown in Figure 5.37.

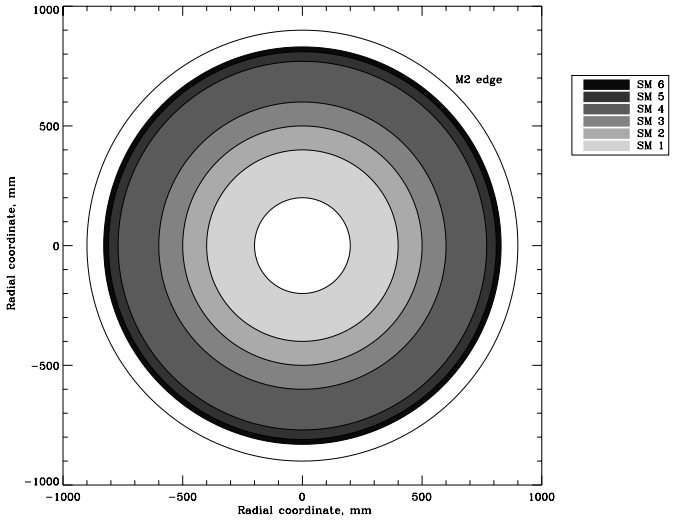


Figure 5.37: Schematics of the six sharp spatial masks and their footprint on M2 surface.

### Test procedure description

As for the test of the whole surface, the mirror is illuminated uniformly with a LED source positioned approximately at the mirror radius of curvature (2f configuration); as shown in Figures 5.38. Both the light source and the CCD camera are mounted on the same platform that can be moved to find the mirror best focus position. As in the former test the measurements begin in a position of extra-focus and the platform is progressively approached to the mirror surface. The uncertainty of platform positioning with respect to the mirror is ± 1mm. Subsequently the image frames are analyzed following the same procedure explained in section 5.7 to extract the PSFs photometry, R80 values and the best focus position. The goal of the this test, for each single mask, is to assess the likelihood of the measured PSFs with those simulated by the optical design.
The scan of the optical surface by means of this series of masks allows to check the correspondence between the measured and the simulated PSFs providing an excellent verification of the model built on the basis of the Zernike analysis and used for the simulations of the entire optical system.

### Test result

To get a term of comparison with the results a ray tracing simulation reproducing the same experimental setup is required. As discussed in section 5.4, the most complex part of the simulation is the representation of the mirror optical surface. The simulation has to take into account the

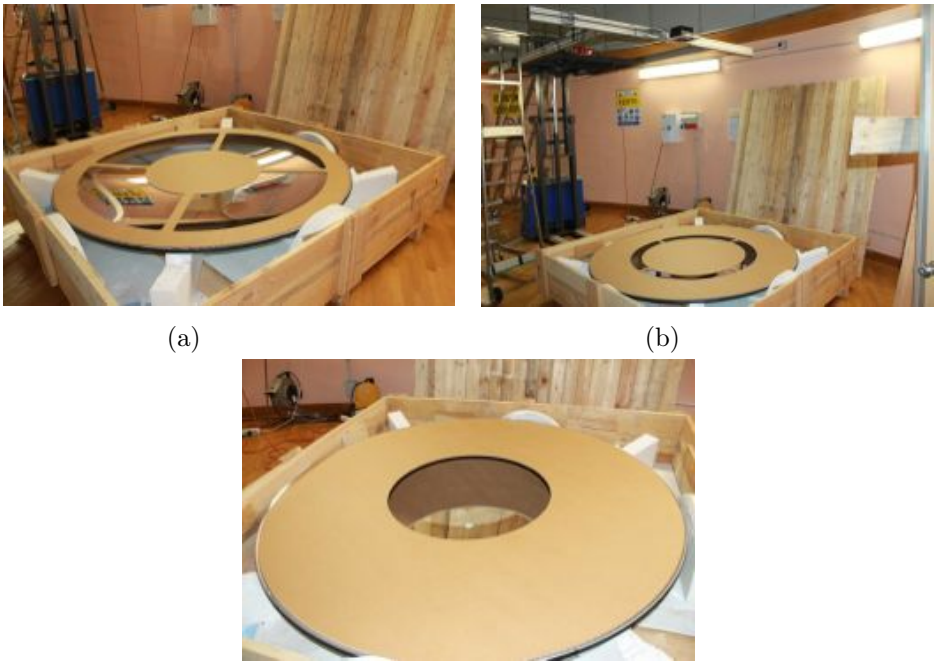

(a) (b)

(c)

Figure 5.38: Pictures from the tests campaign of Teil2. (a) large spatial mask to test the aspherical region of M2, (b) a sharp spatial mask in the 2f configuration with the CCD and the light source suspended on a platform above M2 and (c) large spatial mask to test the paraxial-spherical inner region.

manufacturing errors and imperfections while comparing the results with the experimental data. For each focal series with a certain spatial mask, a simulation with the same configuration, CCD and light source positions and the M2 Zernike representation is performed. Once the synthetic images are obtained, the same pipeline of data reduction presented in section 5.7 is applied. In the following paragraphs the results for each spatial mask are reported.

Despite the little deviations that occur in some configurations between simulations and data about the positions of the optimal focus, it is remarkable how closely the Zernike approach recreates even the smallest features of the measured PSFs.

### Spatial mask 1

We report here for the spatial mask 1 and in the following for the other masks, the photometric analyses of the PSFs acquired for a complete focal series, from an extra to an intra-focus position. In Figure 5.39 three focal series are plotted together: R80 from the experimental PSFs (black points), simulated R80 for the nominal sag of M2 (blue points) and simulated R80 for Teil1 and Teil2 represented through the Zernike Polynomials, labelled for convenience *Zernike-sag*. In addition, for each mask the real and simulated PSFs referring to the same focal series are given.

Although there is an off-set of about 5 mm between the position of the minima of the measured focal series and the nominal one, the agreement of the data with the Zernike-sag is satisfactory. As in most of the other focal series, the measured R80 are in average larger than the simulated values as a results of scattering processes from surface roughness that cause diffuse light and broadening of the spots. The focus depth of this first ring is about 15 mm.

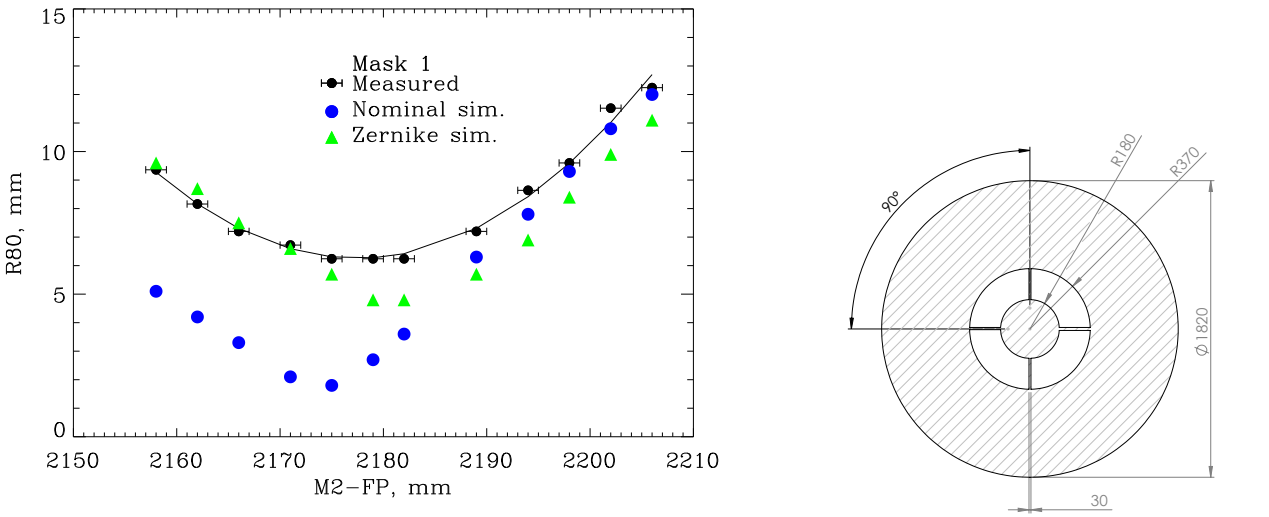


(a) (b)

Figure 5.39: (a) Focal series for the spatial mask 1, M2-FP is the separation between M2 and the focal plane i.e. $q$. (b) Construction design of mask 1.

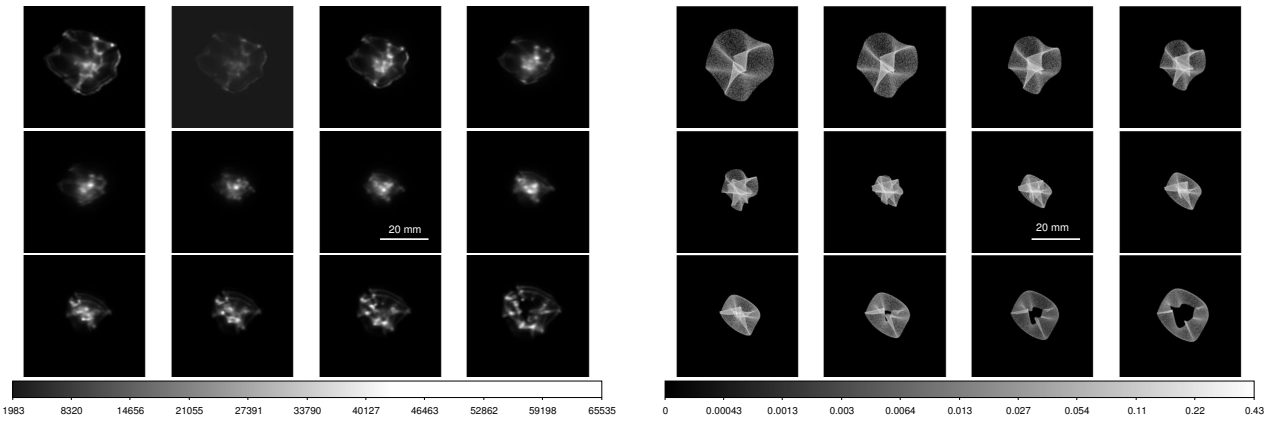


(a) (b)

Figure 5.40: (a) Focal series of the measured PSFs for the spatial mask 1. (b) Focal series of the simulated PSFs by Zernike analysis for the spatial mask 1.

### Spatial mask 2

The focal series produced by mask 2 is in excellent agreement with both the simulations. The focus depth of this first ring is about 10 mm. As the reader can observe, the ability of the simulations in reproducing even the smallest features of the measured PSFs is very satisfactory. With reference to images 5.42 the Zernike representation of the M2 surface is so likely that the rim of the extra-focus and intra-focus PSFs show the same ripples between the measured and simulated spots.

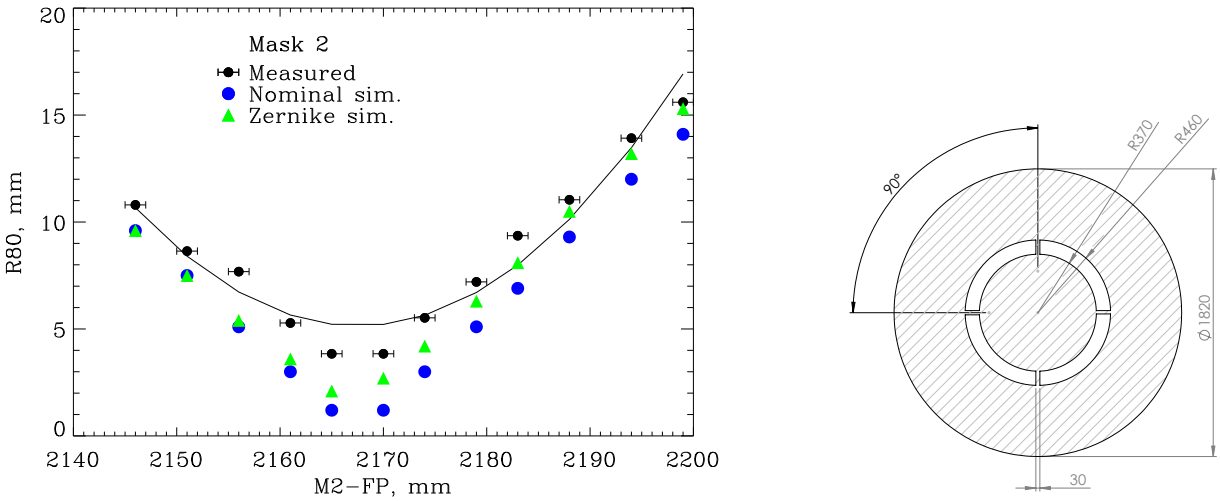


(a) (b)

Figure 5.41: (a) Focal series for the spatial mask 2, M2-FP is the separation between M2 and the focal plane i.e. $q$. (b) Construction design of mask 2.

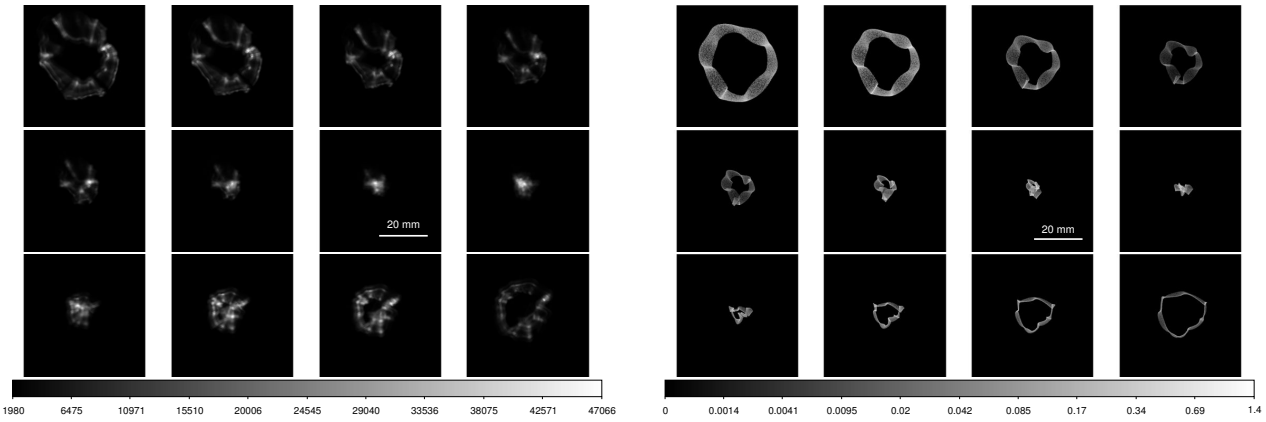


(a) (b)

Figure 5.42: (a) Focal series of the measured PSFs for the spatial mask 2. (b) Focal series of the simulated PSFs by Zernike analysis for the spatial mask 2.

### Spatial mask 3

As for the spatial mask 2, the spatial mask 3 shows a good agreement between the measured and the simulated focal series. This mask marks the boundary between the spherical portion of the mirror and the aspherical, outer part.

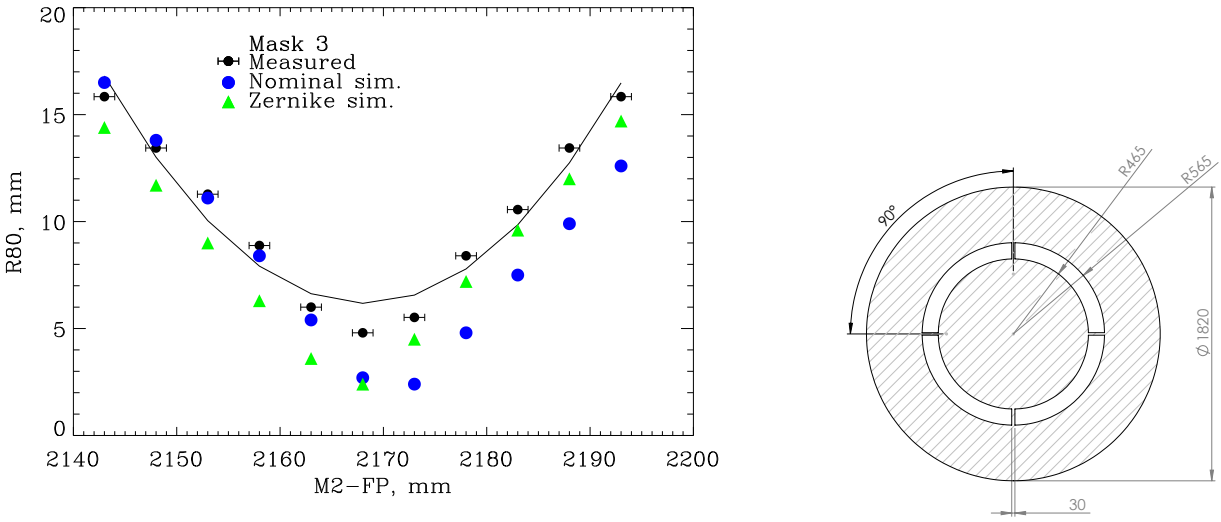


(a) (b)

Figure 5.43: (a) Focal series for the spatial mask 3, M2-FP is the separation between M2 and the focal plane i.e. $q$. (b) Construction design of mask 3.

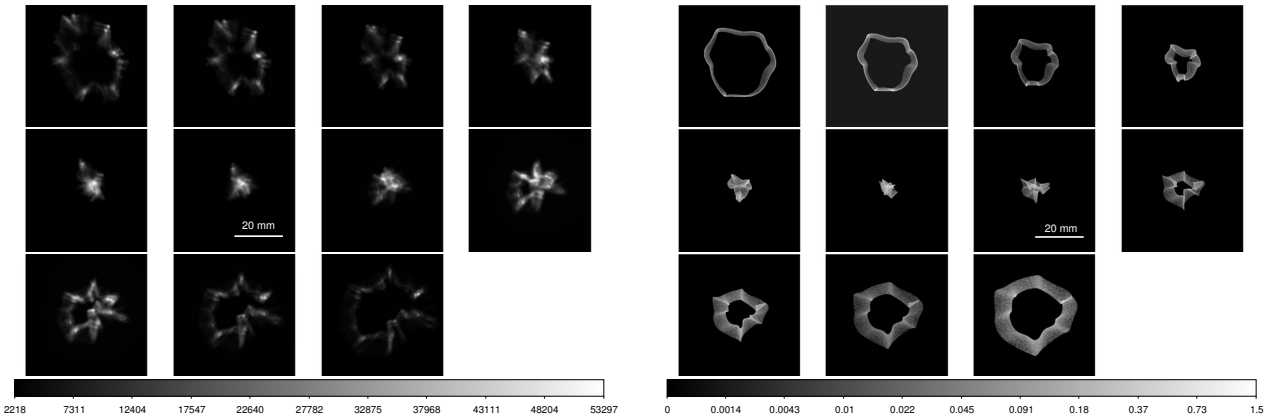


(a) (b)

Figure 5.44: (a) Focal series of the measured PSFs for the spatial mask 3. (b) Focal series of the simulated PSFs by Zernike analysis for the spatial mask 3.

### Spatial mask 4

The spatial mask 4 isolates a portion of the mirror that is highly aspherical. The PSFs are irregular and the focus depth of the ring is minimum. However the agreement shown between the measured and the simulated PSF is completely verified. An interesting behavior to note is the asymmetry of the focal series rings with respect to the best focus. The intra-focus segment of the focal series has less steeper profile in comparison to the extra-focus portion.

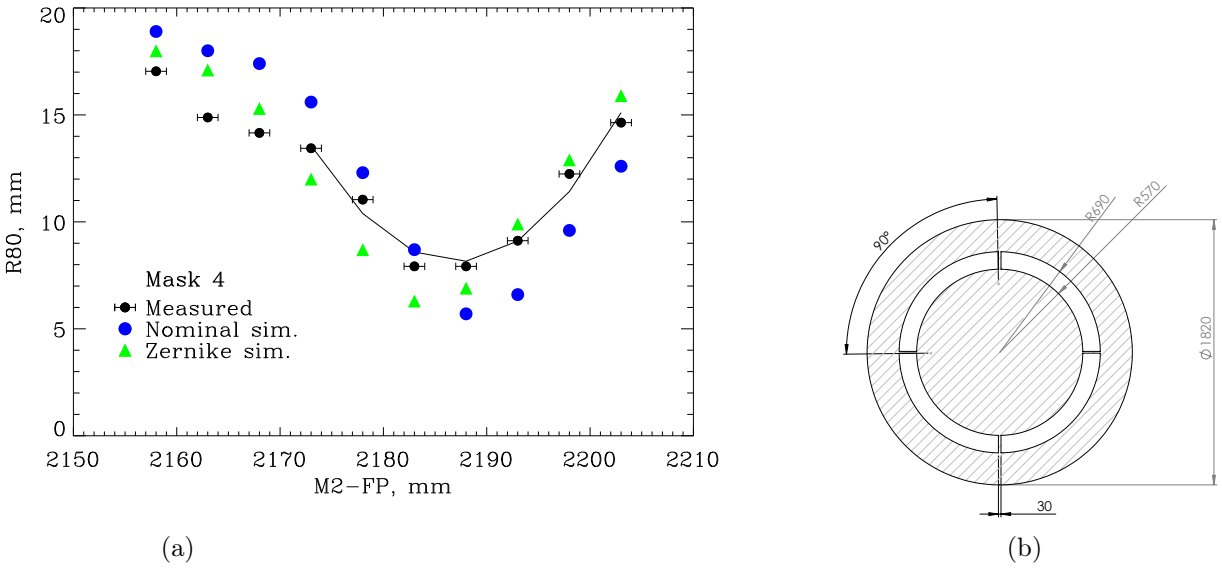


(a) (b)

Figure 5.45: (a) Focal series for the spatial mask 4, M2-FP is the separation between M2 and the focal plane i.e. $q$. (b) Construction design of mask 4.

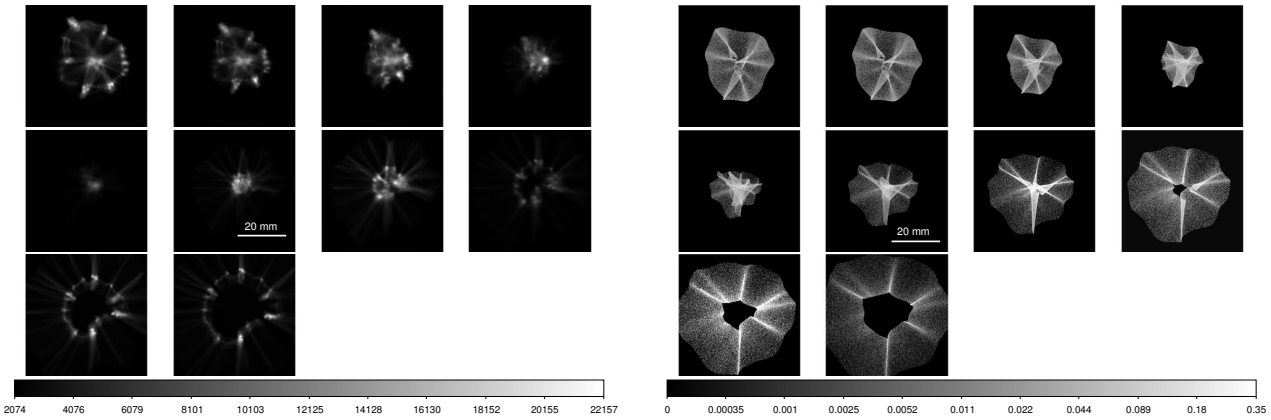


(a) (b)

Figure 5.46: (a) Focal series of the measured PSFs for the spatial mask 4. (b) Focal series of the simulated PSFs by Zernike analysis for the spatial mask 4.

### Spatial mask 5

As discussed for the spatial mask 4, mask 5 can be described by the same considerations of mask 4. The asymmetry of the focal series wings with respect to the best focus is even more pronounced showing a steeper extra-focus segment.

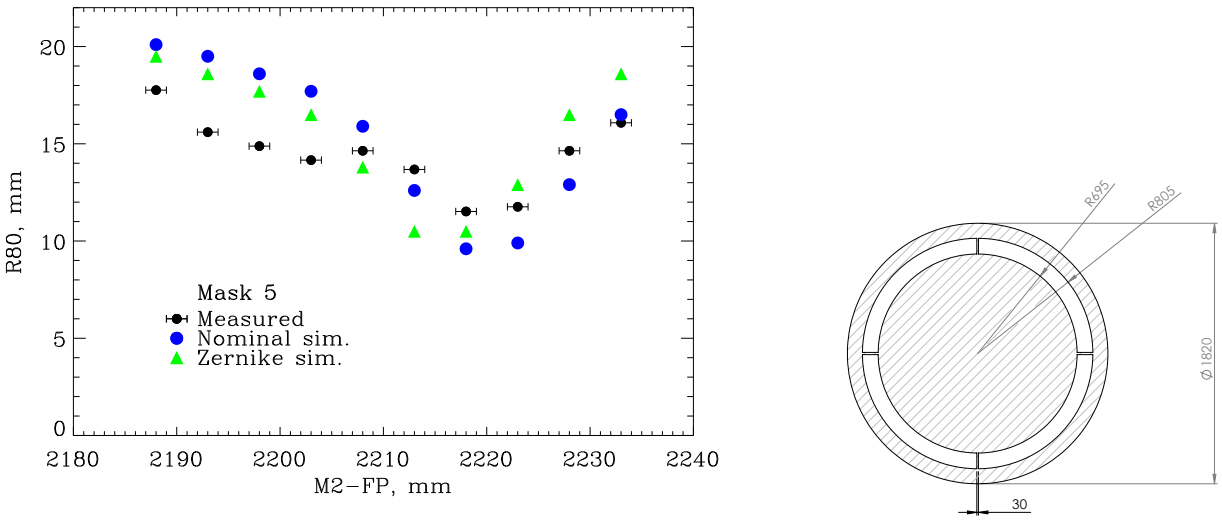


(a) (b)

Figure 5.47: (a) Focal series for the spatial mask 5, M2-FP is the separation between M2 and the focal plane i.e. $q$. (b) Construction design of mask 5.

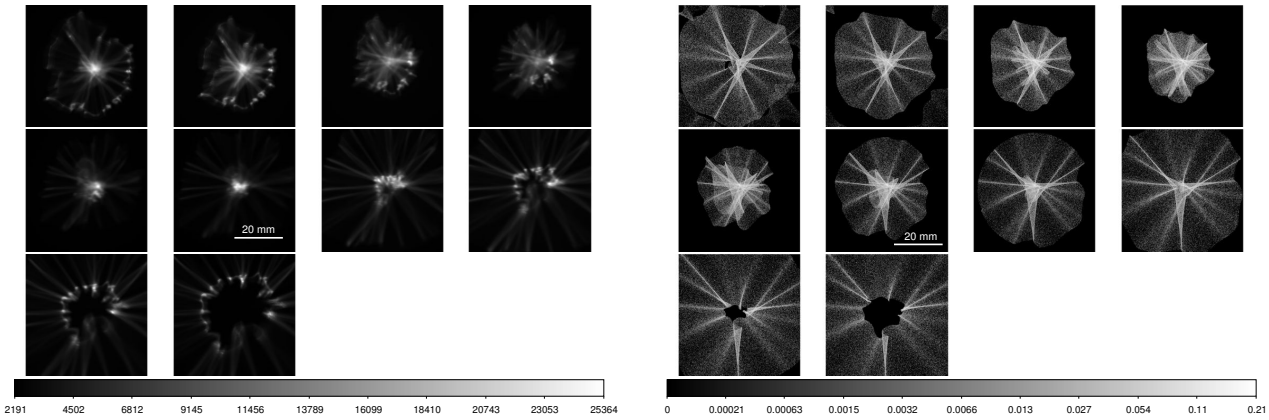


(a) (b)

Figure 5.48: (a) Focal series of the measured PSFs for the spatial mask 5. (b) Focal series of the simulated PSFs by Zernike analysis for the spatial mask 5.

### Spatial mask 6

The spatial mask 6 project the sharper profile, just 3 cm in radius. The region exposed to light is very limited and the asymmetry of the wings disappears leading to a regular profile in agreement with the simulations as shown in Figure 5.49.

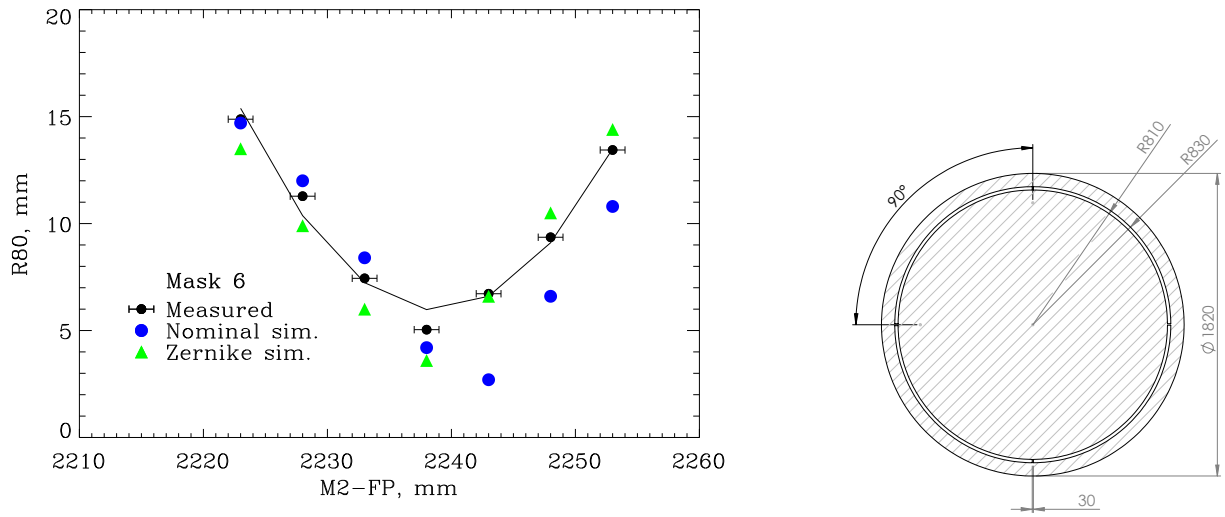


(a) (b)

Figure 5.49: (a) Focal series for the spatial mask 6, M2-FP is the separation between M2 and the focal plane i.e. $q$. (b) Construction design of mask 6.

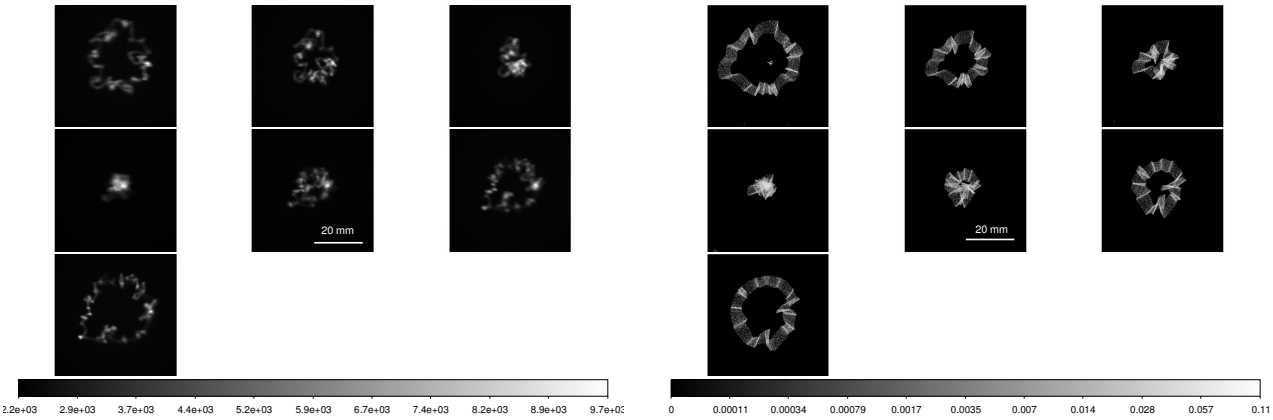


(a) (b)

Figure 5.50: (a) Focal series of the measured PSFs for the spatial mask 6. (b) Focal series of the simulated PSFs by Zernike analysis for the spatial mask 6.

### Spatial mask 7

The spatial mask 7 conversely to the previously presented masks leaves unobstructed the whole paraxial-spherical region of the mirror (see Figure 5.51 (b)). The profile of the focal series shows a well defined parabolic shape as expected from spherical surfaces; the focus depth of the measured profile is larger than the nominal and in average the spots size is greater than that foreseen by the nominal design. The position of the best focus of the measured focal series allows to measure the paraxial radius of curvature and focal length, respectively $R = 2184$ mm $\pm$ 1 mm and $f = 1092$ mm $\pm$ 1 mm. These measurements prove that the mirror prototype is compliant with the requirements reported in Table 2.6. A visual inspection of the PSFs confirms that the Zernike representation finely reproduces most of the features visible in the real images (Figure 5.52 (a)), confirming the reliability of the model based on the FLABEG dataset (Figure 5.52 (b)).

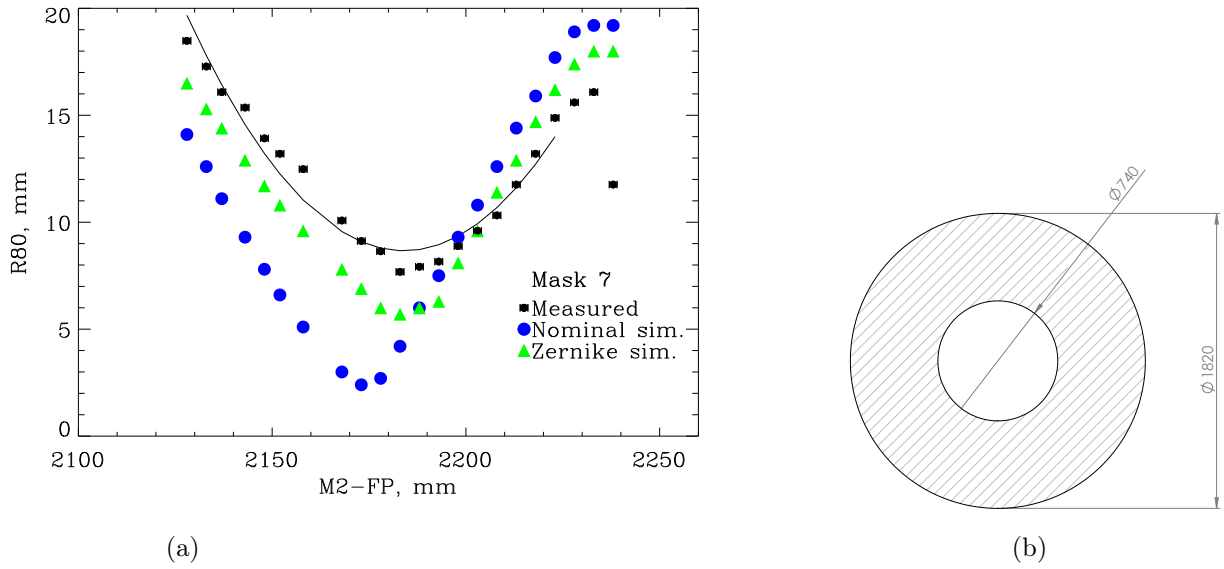


(a) (b)

Figure 5.51: (a) Focal series for the spatial mask 7, M2-FP is the separation between M2 and the focal plane i.e. $q$. (b) Construction design of mask 7.

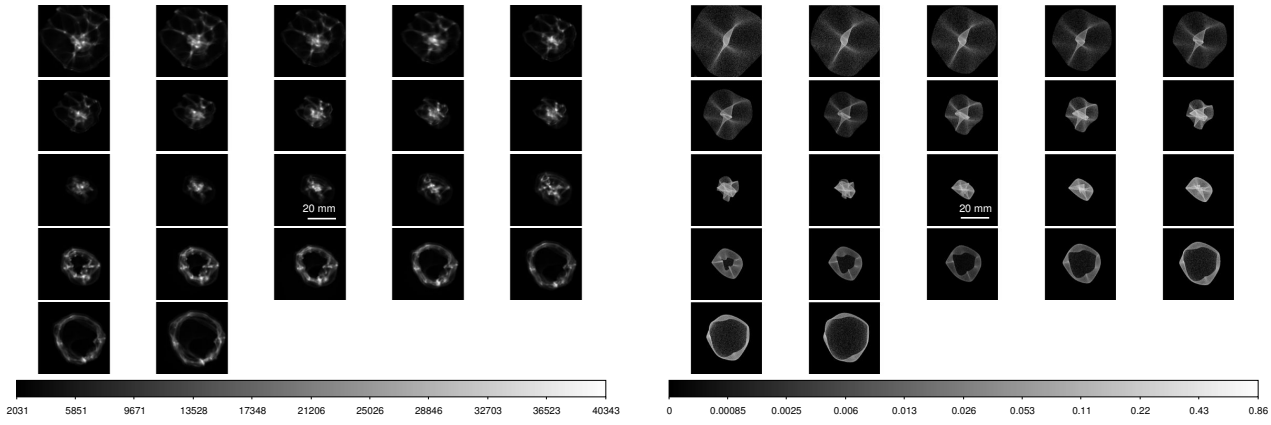


(a) (b)

Figure 5.52: (a) Focal series of the measured PSFs for the spatial mask 7. (b) Focal series of the simulated PSFs by Zernike analysis for the spatial mask 7.

### Spatial mask 8

Mask 8 obstructs the paraxial-spherical region and illuminates the outer aspherical regions (Figure 5.53 (b)). The profile of the focal series shows a good agreement with the simulations of the extra-focus segment while it deviates significantly in the intra-focus segment. A possible, partial explanation of this difference could come from Figure 5.10; the presence of a large depressed area at mid radii (blue region in Figure 5.10) introduces a net dishomogeneity in the azimuthal sag profile. Also the position of the best focus of the measured focal series shows a significant off-set from the nominal value.

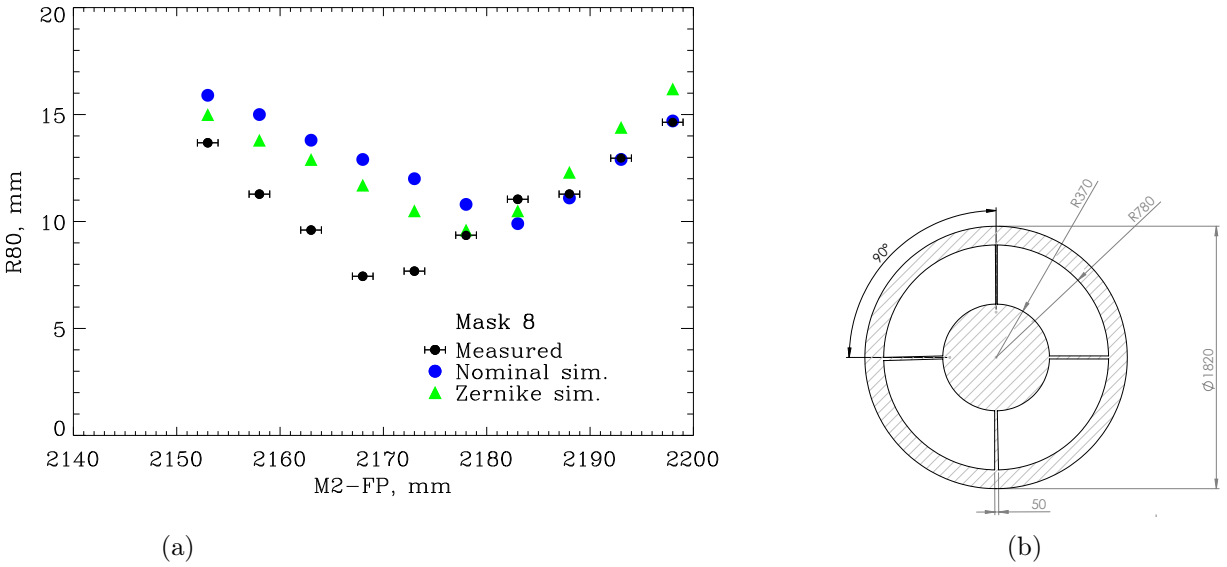


(a) (b)

Figure 5.53: (a) Focal series for the spatial mask 8, M2-FP is the separation between M2 and the focal plane i.e. $q$. (b) Construction design of mask 8.

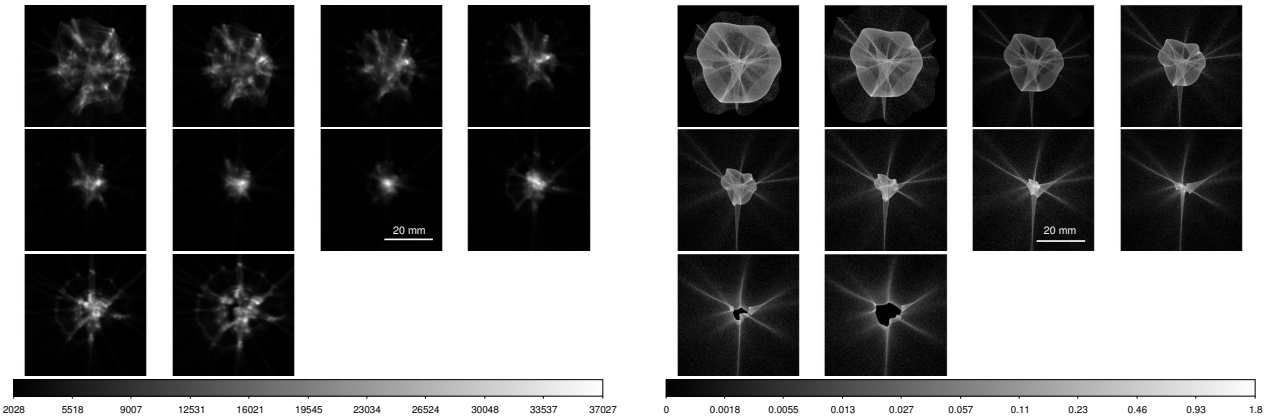


(a) (b)

Figure 5.54: (a) Focal series of the measured PSFs for the spatial mask 8. (b) Focal series of the simulated PSFs by Zernike analysis for the spatial mask 8. The last two PSFs patterns show deviations between simulation and measurements.

## 5.9 M2 PSF morphology

A detailed photometric study of the M2 PSFs has been presented in sections 5.7 and 5.8. The CCD camera used in those tests has a sensitive array 50 x 50 mm that is suitable for the R80 measurement, but not sufficient to study the overall PSF that has faint features extending beyond the size of the sensor. Here we study the images taken with a digital camera of the overall PSFs of M2 to trace their morphology until the outer regions. To compare the measured PSFs with the simulated we make use of the image correlation technique. Digital image correlation is an optical method that employs tracking and image registration techniques for accurate measurements of changes in images; it is often used to measure deformation, displacement and strain between couple of images.

### Test procedure description

The mirror is illuminated uniformly with a light source positioned at a distance approximately equal to the mirror radius of curvature. The light source, a LED working at $\lambda = 640$ nm, is kept off-axis with respect to the mirror and a large black screen is used to project the mirror PSF specularly with respect to the mirror optical axis ( see Figure 5.55). A neutral filter in front of the LED attenuates the light intensity of three orders of magnitude. $p$ is the separation between the light source and the mirror while $q$ the separation between the screen and the mirror. The light source is mounted on a platform that can be moved to find the mirror best focus position and explore the surrounding regions. In the centre of the mirror a digital camera controlled remotely by a pc takes pictures of the PSFs at different positions $\Delta p$.

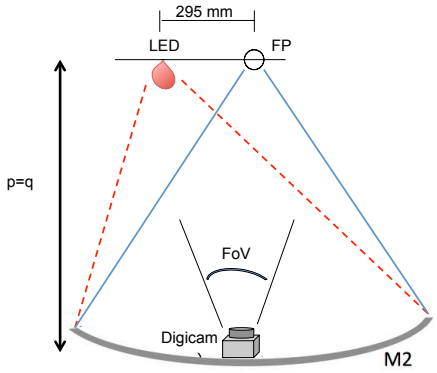


Figure 5.55: 2f-setup with a large screen to project the mirror PSFs that are acquired by a digital camera positioned in the centre of the mirror and remotely controlled by a PC.

### Test result

The pictures of the measured PSFs are collected in Figure 5.56a with the corresponding simulated patterns in Figure 5.56b. The focal series probed in Figures 5.56a and 5.56b extends for ∼150 mm and shows the overall PSFs size for extreme focal positions. As pointed out in section 5.7 the focal depth of M2 is about 2 mm and as discussed in section 5.8, the focal series explored for different spatial masks extends at maximum 60 mm around the focus position. The size of the overall PSFs (R80 value) is shown in Figure 5.58 and the size of the CCD camera used for the photometric studies of the previous sections is shown for comparison. Figure 5.58 proves that the CCD camera is suitable for studying the PSFs of M2 for focal shifts ± 30 mm around the best focus position as in the case of the spatial masks measurements. In addition the use of the spatial masks leads also to smaller PSFs than in the current measurement with a bare mirror.

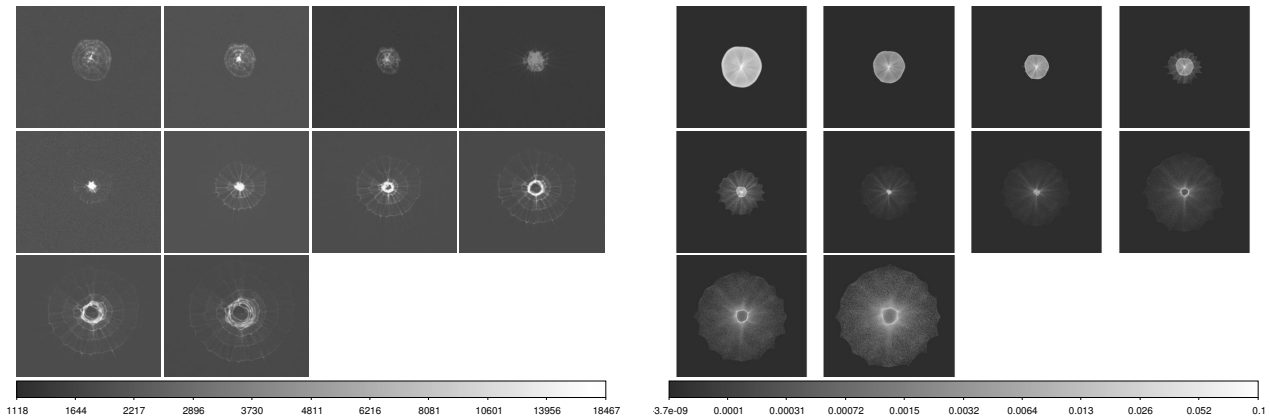


(a) (b)

Figure 5.56: (a) Focal series of the measured overall PSFs with the setup shown in Figure 5.55 (b) Simulated focal series of the PSFs shown in Figure 5.56a. In the simulation the Zernike representation of M2 discussed in section 5.4.1 has been used. The size of each image frame is 400 x 400 mm.

Comparing Figure 5.56a with 5.56b some morphological differences are visible especially in the intra-focus segment. A more quantitative analysis is done by a correlation between measured and simulated PSFs. Image correlation techniques track accurately the changes in images quantifying the deformation, displacement and strain between two patterns. Figure 5.57 collects the correlation patterns for the PSFs of Figures 5.56a and 5.56b: level 1 in the colorbar marks maximum correlation and similarity between the PSFs, while lower values down to zero, denote differences and changes of one image with respect to the other.

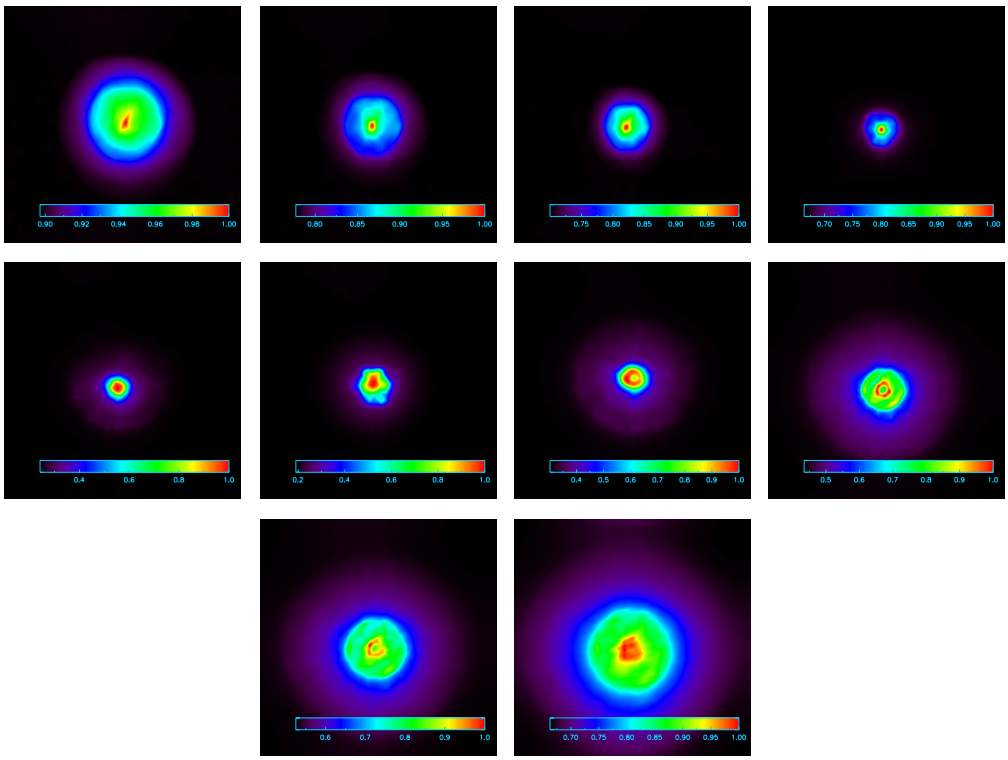

Figure 5.57: Image correlation of the measured and simulated PSFs of Figure 5.56a and 5.56b; the colorbar indicates the level of correlation/similarity between the patterns in a scale from 0, minimum correlation, to 1, maximum correlation.

As mentioned above, the decorrelation effects are more pronounced in the intra-focus segment of the focal series (last images). This result somewhat confirms the deviations already detected with spatial mask 8 in section 5.8 in the outer, aspherical region of the mirror. The reader should also bear in mind that, image correlation works efficiently for point-like sources or well shaped patterns. In the present case the general broadening of all the PSFs limits the precision of this technique.

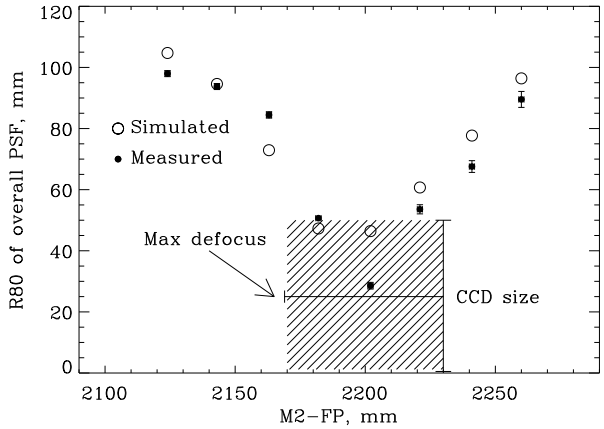


Figure 5.58: Extended focal series of the overall PSFs obtained with the setup shown in Figure 5.55. The photometric properties of the measured and simulated overall PSFs (R80) are shown in comparison to the size of the CCD camera and the maximum out-of-focus shift explored during the M2 measurements with the spatial masks. The sensitive frame of the CCD camera (50 x 50 mm) is suitable to study the photometric properties of the M2 PSFs with the spatial masks and/or the overall PSFs from a bare mirror for a maximum out-of-focus position of $\sim \pm 30$ mm.

This analysis gives the important confirmation on the reliability of using the 50 x 50 mm CCD camera for the photometric study of the M2 PSFs. The sensor is adequate to image the PSFs of M2 with a maximum extra-focus of $\pm$ 30 mm from the best focus position.

## 5.10 M2 Hartmann mask test

Another optical method for the metrology of a reflecting surface is the Hartmann test. The tool consists of an opaque mask with a pattern of holes through which the light can pass projecting a light spot pattern on the optical surface to be tested. The mask selects thin pencils of rays which are used for measuring the transverse aberration of rays reflected on different regions of the surface under test [92]. The holes of the Hartmann masks, HM, can have different shapes and size provided that they are large enough to avoid diffraction phenomena. A commonly used Hartmann mask in optics (Figure 5.59) consists of a matrix of holes producing a regular pattern of spots.

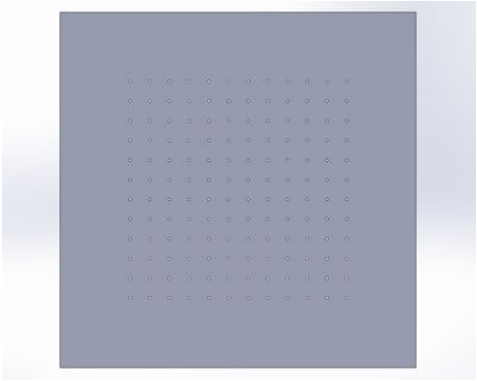

Figure 5.59: Example of Hartmann mask with 12 x 12 holes designed by SolidWorks [166].

Before applying the HM test to real mirrors some assessment analyses have been done using the Zemax software. The aim of such simulations is the determination of the sensitivity of the HM test in detecting image aberration by the use of the Zernike polynomials. Instead of performing the HM test directly on the optical design of ASTRI M2 it is preferred to begin with a perfect spherical mirror design. For a perfect spherical mirror, the observer retrieves on the conjugate plane of the HM, the same spot pattern. This configuration however, allows to introduce in the Zemax design a single Zernike coefficient per time. By varying the Zernike coefficient or by progressively adding other terms the mirror can be virtually aberrated of a known quantity. Once the spots pattern is reproduced with Zemax the interpolation of the data is performed by IDL to estimate the Zernike coefficient that produced that particular pattern and compare it with the input coefficient.

In general the HM test as the Shack-Hartmann test measures the derivative $\vec{\nabla}W$ of the wavefront rather than the wavefront itself $W$. The Shack-Hartmann test relies on a more elaborated device which consists of an array of lenses of the same focal length. Each lens is focused onto a photon sensor and the local tilt of the wavefront across each lens can then be calculated from the position of the focal spot on the sensor [101]. Coming back to the HM test, the spot pattern created is the result of the sampling of the wavefront derivative at precise points corresponding to the holes of the mask. Following R. Ragazzoni [111] the wavefront derivatives are expressed in linear coordinates:

$$\vec{\nabla}W = \vec{x}\frac{\partial W}{\partial x} + \vec{y}\frac{\partial W}{\partial y}$$

and collected in the vector B:

$$B = \left[\frac{\partial W}{\partial x}|_{x1,y1}; ...; \frac{\partial W}{\partial x}|_{xn,yn}; ...; \frac{\partial W}{\partial y}|_{x1,y1}; ...; \frac{\partial W}{\partial y}|_{xn,yn}\right]$$

To perform a data interpolation with the Zernike polynomials that are parametrized in polar a conversion of them is required:

$$\frac{\partial Z}{\partial x} = \frac{\partial Z}{\partial \rho}\frac{\partial \rho}{\partial x} + \frac{\partial Z}{\partial \theta}\frac{\partial \theta}{\partial x}$$

with the derivatives from polar to cartesian given by the transformation:

$$\frac{\partial \rho}{\partial x} = \frac{x}{\rho} \qquad \frac{\partial \rho}{\partial y} = \frac{y}{\rho} \qquad \frac{\partial \theta}{\partial x} = -\frac{y}{\rho^2} \qquad \frac{\partial \theta}{\partial y} = \frac{x}{\rho^2}$$

The same is performed for the $y$ coordinate. The analytical derivative of the Zernike polynomials to be compared with the experimental data are collected in the matrix $A$:

$$A = \begin{bmatrix} \frac{\partial Z_1}{\partial x}|_{x1,y1} & ;\cdot\cdot; & \frac{\partial Z_1}{\partial x}|_{xn,yn} & ;\cdot\cdot; & \frac{\partial Z_1}{\partial y}|_{x1,y1} & ;\cdot\cdot; & \frac{\partial Z_1}{\partial y}|_{xn,yn} \\ \cdot & \cdot & \cdot & \cdot & \cdot & \cdot & \cdot \\ \cdot & \cdot & \cdot & \cdot & \cdot & \cdot & \cdot \\ \frac{\partial Z_m}{\partial x}|_{x1,y1} & ;\cdot\cdot; & \frac{\partial Z_m}{\partial x}|_{xn,yn} & ;\cdot\cdot; & \frac{\partial Z_m}{\partial y}|_{x1,y1} & ;\cdot\cdot; & \frac{\partial Z_m}{\partial y}|_{xn,yn} \end{bmatrix}$$

By inverting the relation:

$$Az = B$$

one can extract the Zernike coefficients $z$ getting a description of the pattern aberrations.

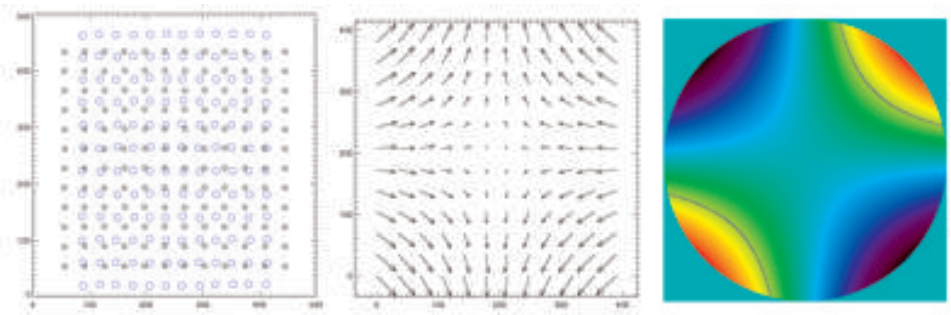

Figure 5.60: From left to right: spots pattern for a perfect (black circles) and an astigmatic mirror (blue circles) are compared, the map of the wavefront derivatives is calculated (centre), and the aberrated surface is reconstructed using the retrieved Zernike coefficient (right).

This data processing is shown in Figure 5.60: the spots pattern for a perfect spherical mirror and an astigmatic spherical mirror are compared, the wavefront derivatives are computed and the distortion pattern is reconstructed. The sensitivity of the HM test can be assessed by progressively decreasing the aberration terms. Smaller aberration terms lead to smaller spatial derivatives $\vec{\nabla}W$, until the test reaches a confusion limit where the Zernike polynomials fit does not retrieve an efficient image reconstruction. An example of loss of sensitivity in the HM test is reported in Figure 5.61 in which the astigmatic term is progressively reduced until the algorithm is not able to map the spatial derivative associated with the corresponding Zernike polynomial.

The situation becomes more complicated when this procedure is applied to the aspherical ASTRI M2. The deviations of the surface from the spherical profile are large as shown in Figure 2.9, and they increase with the radial coordinate. The most pronounced deviations from the spherical profile occur between $R = 550 - 900\,mm$. The most important issue pointed out by the simulations on the HM test applied to ASTRI M2 is the effect of surface asphericity on the HM spots pattern. The aspherical shape of the mirror twists heavily the spots distribution and

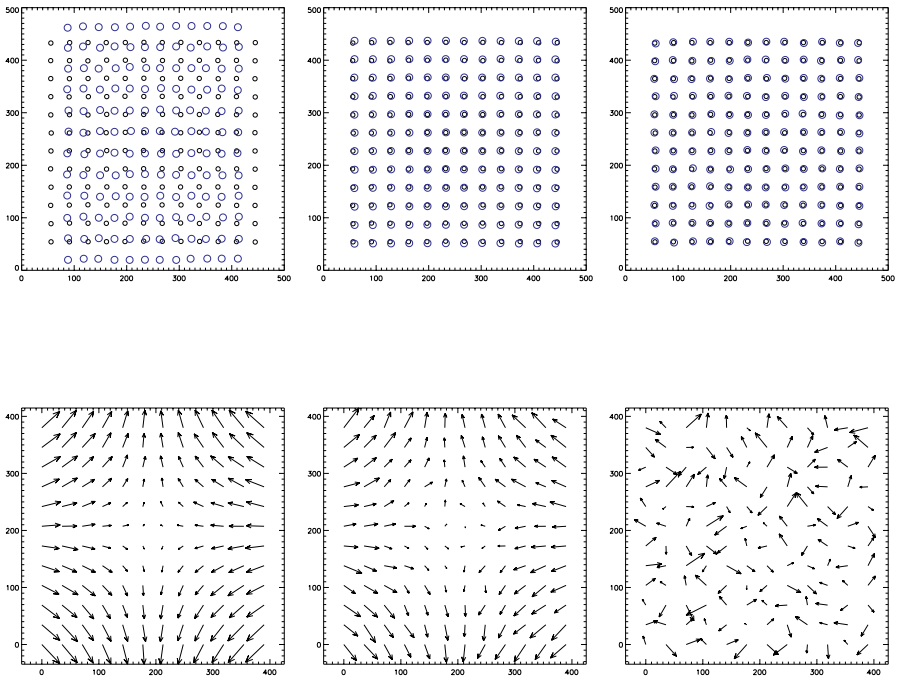

Figure 5.61: The sensitivity of the HM test decreases as the aberration term is diminished. From left to right, the astigmatic term is equal to $10^{-1}$, $10^{-2}$ and $10^{-3}$ mm.

shifts away many spots from their original positions. As mentioned above, the spot displacement must not exceed the mean spot separation otherwise the algorithm of image analysis can't keep track of the spatial derivates. In this case, as shown in Figure 5.63, the spots displacement introduced by the reflection on M2 changes the regular spot pattern that impinges on the mirror (see Figure 5.62).In addition also the shape of the spots changes all over the surface as a result of the aspherical profile, becoming more elongated as the distance of the spots from the centre of the mirror increases. To overcome this problem a series of different and custom HMs has been designed with the aim of sampling specific rings of the mirror surface. Rather than working with standard square matrix spots array, a series of HMs with a circular symmetry were adopted, characterized by a single ring of spots projecting their pattern on a specific annulus of the mirror surface.

### Test procedure and setup description

The experimental set up for a typical Hartmann test is reported in Figures 5.64 and 5.65: a light source (purple cone) is positioned in the proximity of the surface radius of curvature, the light is intercepted by the HM and a certain spots pattern is projected on the mirror that reflects back the spots pattern (green cone) on a detector. For a perfect spherical mirror the light spots pattern has the same distribution of the holes on the HM. For a non-spherical or aberrated surface the light spots pattern is distorted and the centroids of the light spots change. By mapping and measuring the centroid displacement precious information can be retrieved about the surface shape imperfections and aberrations.

The separation between two consecutive holes determines the spatial sampling of the optics: the smaller the separation the greater and more accurate is the surface sampling. The choice of the best sampling method is related to the desired sensitivity and the expected error budget of the optics manufacturing. In the presence of important surface imperfections or heavy aberrations a high spatial sampling could be counterproductive. The method works correctly only if the

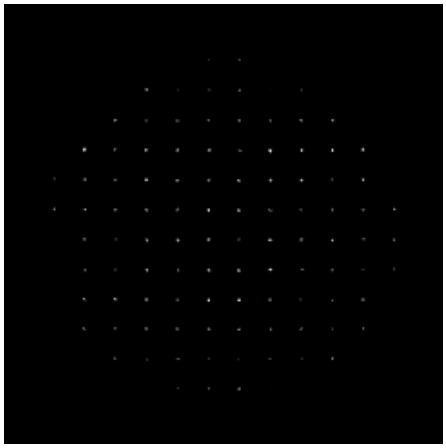

Figure 5.62: Input spots pattern projection on M2 as produced by an HM with 12 x 12 holes.

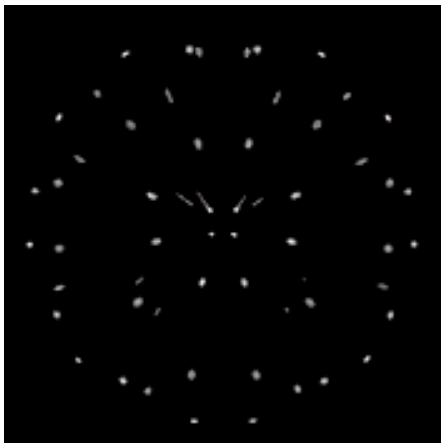

Figure 5.63: Output spots pattern of the same HM after the reflection on M2.

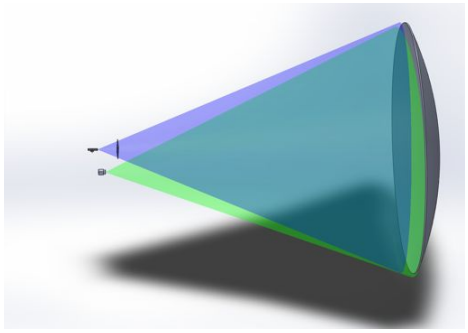

Figure 5.64: HM test set up for an optical mirror, the light source is slightly off-axis to allow the spots pattern detection.

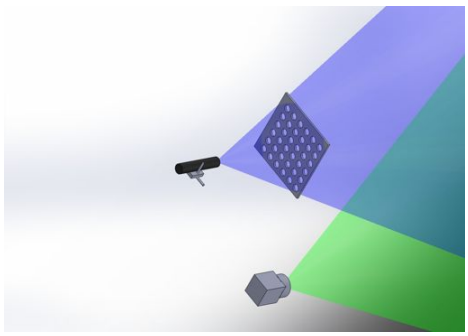

Figure 5.65: The light from a source passes through the HM, is reflected by the mirror and detected by a camera.

centroids displacement is smaller than the hole separation, otherwise the algorithm is not able to trace the spots displacement anymore and to derive the gradients affecting the pattern.

Figure 5.66 reports a scheme of the 8 rings of spots that are used to measure the surface profile of M2. The radial distribution of the spots varies from a ring to another. The inner rings of the mirror are characterized by a low asphericity and they can be measured by means of spot rings of circular shape as in Figure 5.68; the rings sampling the aspherical outer annuli produce highly elongated spots that can overlap to the spots of the other adjacent rings. To prevent this problem, the holes of the outer rings are rectangular as designed in Figure 5.69, with a narrow edge in the radial direction, to counterbalance the elongation of the spot due to the aspherical profile. Using the set up shown in Figure 5.64 it is possible to simulate by Zemax the expected spots patterns for the different 8 rings (Figure 5.66).

The change in the mirror curvature that occurs around R = 550 mm, is clearly visible as a flip (up-to-down) between the spots patterns originated by the inner rings and those retrieved from the outer rings. In each subplot of Figure 5.67 we report the spots patterns of ASTRI M2 are (green marks) compared with those originated by a spherical mirror (blue marks). The displacement between the two distributions (M2 and the spherical mirror) increases moving toward wider rings i.e. sampling outer regions of the mirror. Once the most suitable design for the HM masks is recognized by the optical simulations, the executive designs (examples in Figures 5.68 and 5.69) are set by the DXF standard to an automatic cutter for the manufacturing. All the HMs were manufactured by the TNG Foundation [168] by means of the TNG punching

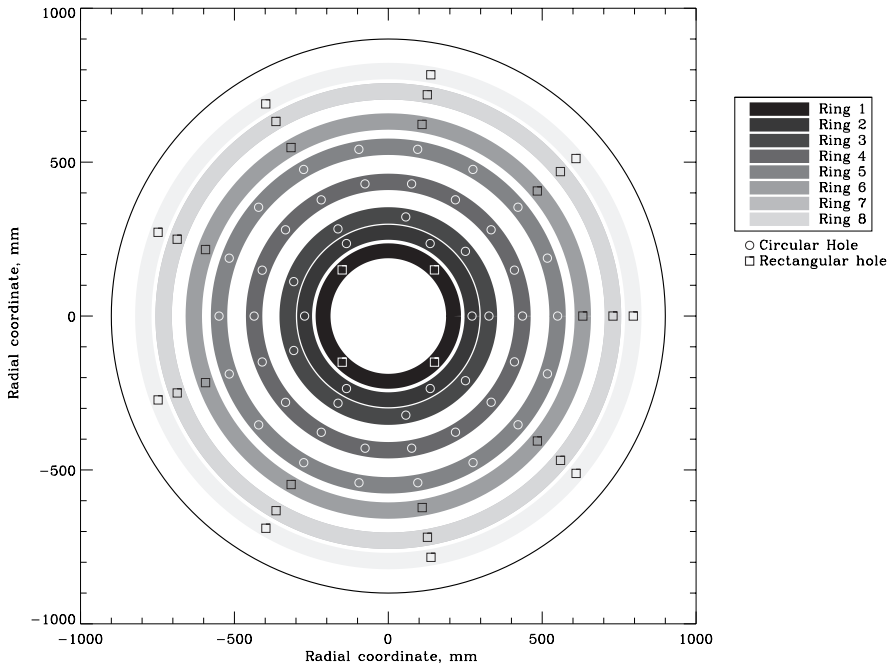


Figure 5.66: The surface of ASTRI M2 is measured by 8 different HMs that project on the mirror 8 spot rings. The inner rings have mainly circular holes while the outer rings have rectangular holes that squeeze the light spots in the radial direction.

machine [62]. A picture of group of the HM masks is shown in Figure 5.70. All the HM masks have a central hole for the optical alignment with the mirror under test.

To project the spot pattern on the mirror as shown in Figure 5.66 an ad hoc objective lens group has been realized. The objective is made of two diverging, commercial lenses and a laser beam. The first lens is plano concave while the second is double concave, these optics are put before the HMs and expands the collimated light from the laser that subsequently passes through the mask to create the specific pattern. The lens objective does not create any additional aberration because it intercepts the light beam before the Hartmann mask.

The large size of the CCD camera mechanics 157 x 157 mm requires a modification of the 2f-setup shown in Figure 5.64. To avoid vignetting of the diverging light cone from the objective, the optical path is modified by a large semi-reflective glass. As shown in Figure 5.74a the light coming out the objective passes through the semi-reflective glass (Figure 5.74b) and encounters the M2 surface being reflected towards the same glass that tilts the beam in the direction of the CCD camera. This configuration removes any vignetting problem even if it introduces a series of multiple images of the same spot pattern. To assess possible distortions of the wavefront induced by the semi-reflective glass, the surface is analyzed by a Zygo interferometer[1]. The glass shows a good optical quality and the deviations introduced are in the order of fractions of wavelength (Figure 5.75) that are completely negligible in comparison to the optical quality of the mirrors to be tested.

[1]A particular acknowledgment to the team of Prof. R. Ragazzoni that helped in the test operations.

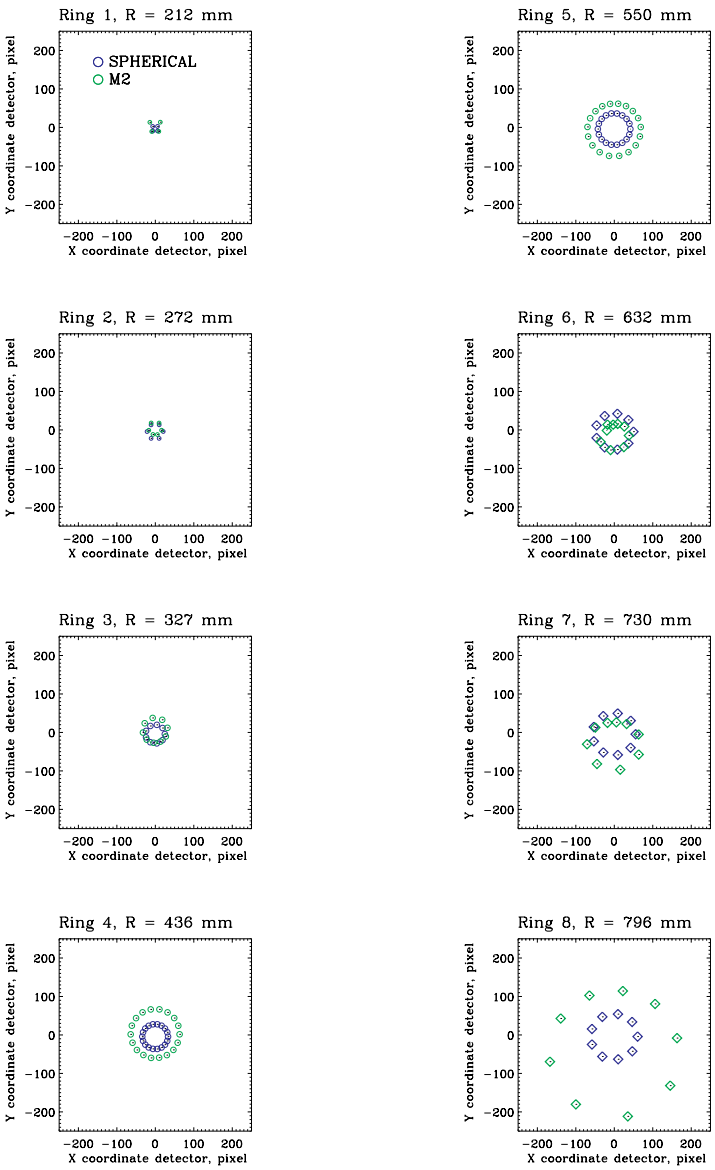


Figure 5.67: Spots patterns as seen by a detector 6 x 6 cm positioned in a conjugated plane with the HM. It is worthwhile to note the changing in the curvature of the surface that is encountered sampling the outer regions of the mirror: the spot pattern flip marks the change in the surface curvature.

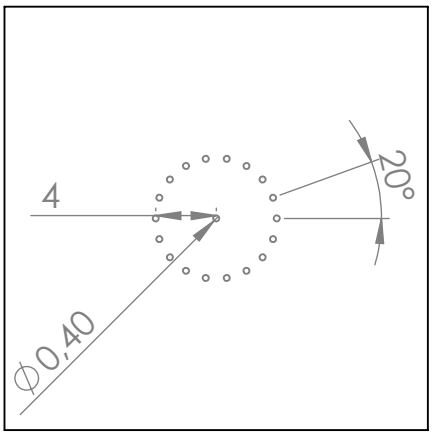


Figure 5.68: SolidWorks design of HM4 sampling a scarcely aspherical annulus of M2.

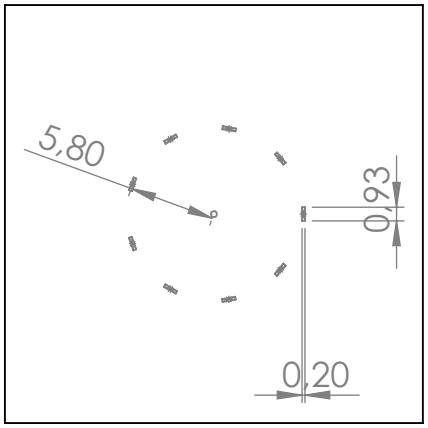


Figure 5.69: SolidWorks design of HM6 projecting its rectangular light spots on an highly aspherical annulus of M2.

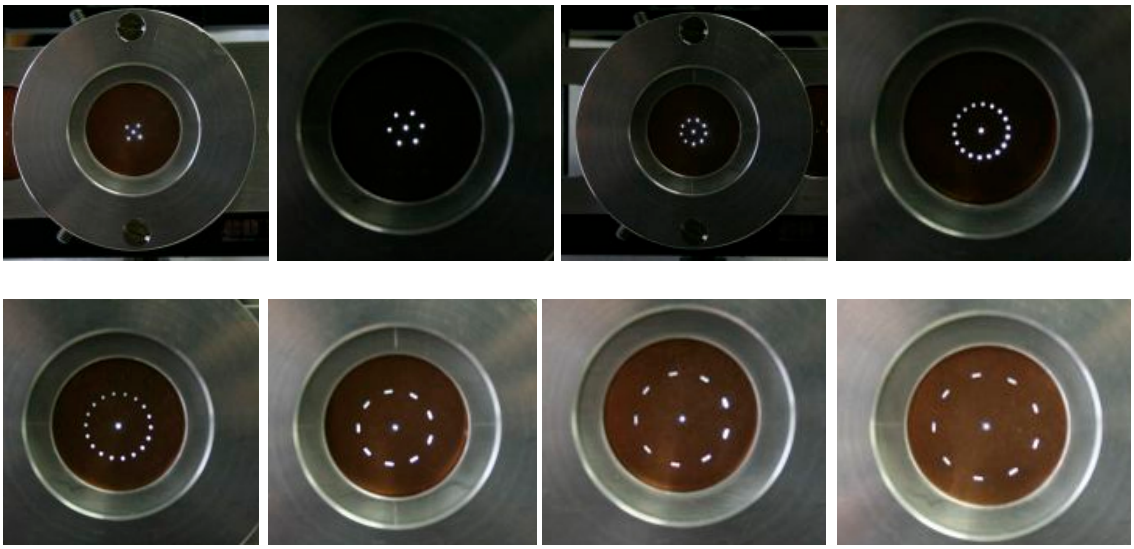

Figure 5.70: Photos of the eight HMs masks used during the test campaign. The HMs designed for the outer aspherical regions of the mirror are those having the rectangular holes. All the HM masks have a central hole for the optical alignment with the mirror under test.

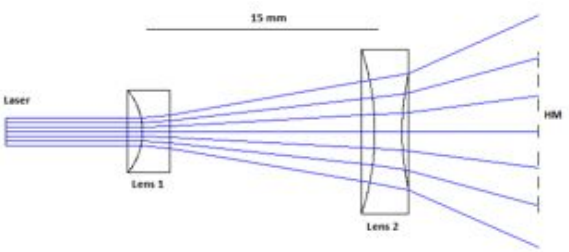


(a)

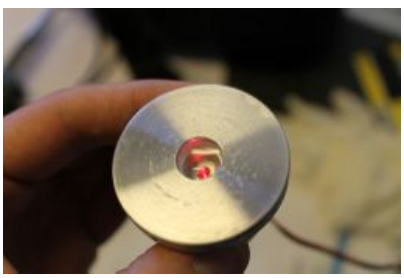

(b)

Figure 5.71: (a) Optical scheme of the expanding objective. (b) Mechanical assembly for the housing of the lenses and the light source: a view of the frontal lens and the light from the laser.

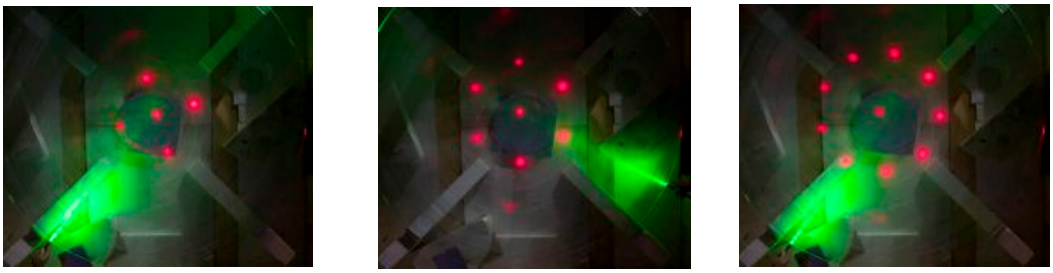

(a) (b) (c)

Figure 5.72: In the order HM1 (a), HM2 (b) and HM3 (c). The light spots projected on the uncoated mirror surface. The green laser diffuses the light to help surface visualization.

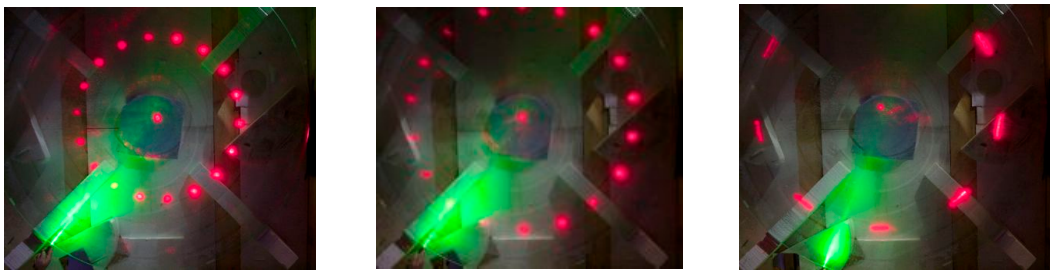

(a) (b) (c)

Figure 5.73: In the order HM4 (a), HM5 (b) and HM6 (c). The light spots projected on the uncoated mirror surface hit M2 at different rings.

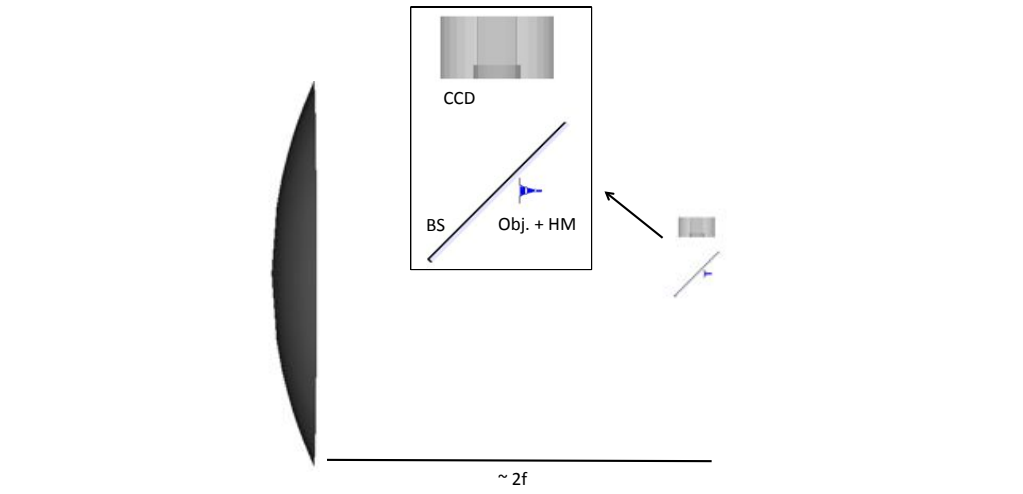


(a)


(b)

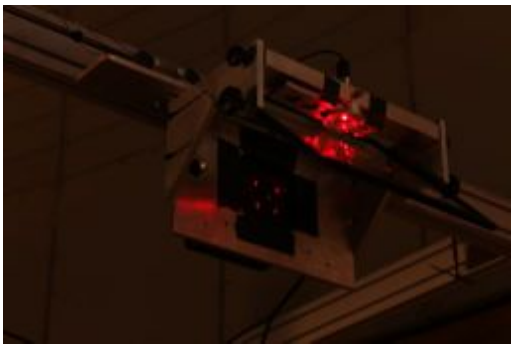

(c)

Figure 5.74: (a) Optical setup for the Hartmann test comprehensive of CCD camera, semi-reflective glass (BS), lens objective and Hartmann mask (obj. + HM). (b) View of the semi-reflective plate that intercepts the light reflected back from the mirror redirecting it towards the CCD camera. (c) Light spots projected on the CCD shutter by the semi-reflective glass after the reflection on M2.

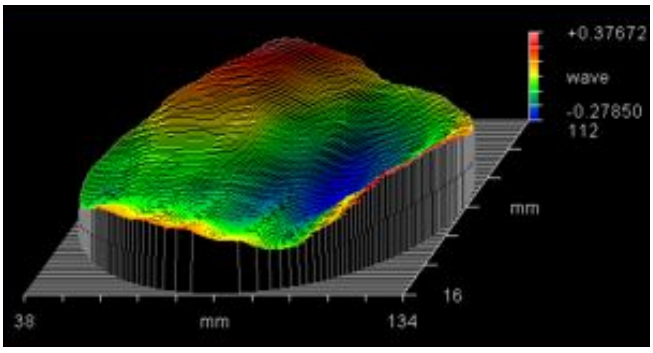


Figure 5.75: Wavefront map analysis by the Zygo interferometer on the semi-reflective glass (central region) used for the test. The deviations are fractions of optical wavelength.

**Test result**

The practical realization of the Hartmann test in the case of ASTRI M2 is rather complex. In particular, the large size of the mirror prevents an adequate calibration that would require a spherical mirror of the same diameter with a surface manufactured at optical precision. Having proved the reliability of the Zemax M2 representation with the Zernike polynomials, the measured spots pattern have been compared with those simulated recreating the same experimental setup (see Figure 5.74a). The first operation to do on the pristine images is the centroids recognition but, as shown in Figure 5.76, there are multiple, ghost images of the same spot. In Figure 5.76b the reader can recognize three different images of the same spot (indicated by red, green, blue arrows); the choice of the right spot is done comparing the height of the peaks in a 3-D map of the image (Figure 5.76a).

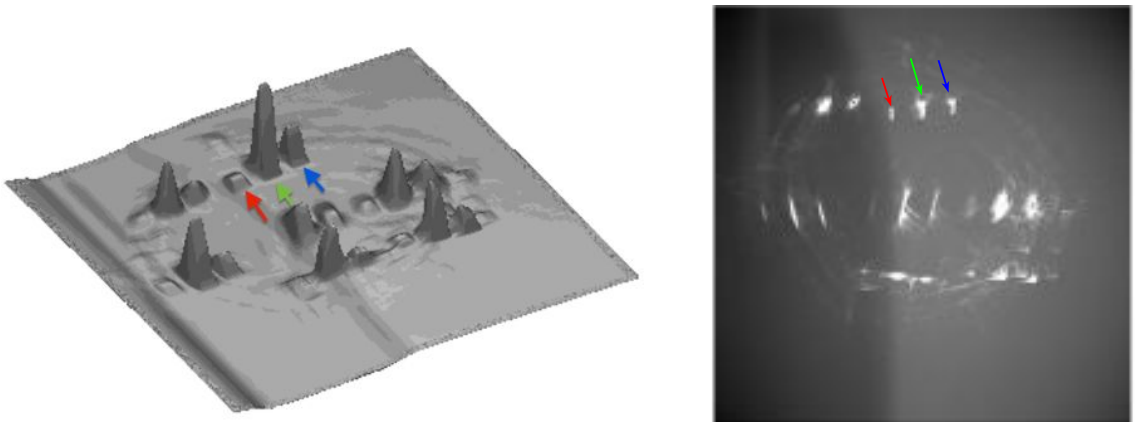

(a) (b)

Figure 5.76: (a) 3-D map of the smoothed image obtained with HM2, three peaks are visible for each spot (red, green, blue arrow). (b) Pristine image obtained with HM2.

Although the HMs are designed specifically for different rings on M2, the outer masks undergo severe problems due to a combination of sag asphericity, presence of ripples in the mirror surface and crowding of multiple spots as shown in Figures 5.77e and 5.77f; for these latter masks the precise estimate of the light spots centroids are prevented and it is preferred to exclude them from the analysis.
After the centroids are found in the measured and simulated frames the derivates $\partial W/\partial x$, $\partial W/\partial y$ of the spots coordinates are computed by an IDL routine. Following the mathematical derivation described in the previous section, the derivates are used to estimate the Zernike polynomials associated to each HM. This operation should give indications about the deviations of the different M2 rings from the nominal specifications. In the following for each of the analyzed HM are reported:

- Simulated spot pattern for a nominal sag
- Simulated spot pattern for a Zernike representation based on the FLABEG dataset
- Measured spot pattern

The deviations from the nominal sag in terms of optical wavelengths are large as discussed in section 5.3, moreover also the number of spots is limited to avoid spots intersections due to the steep optics profile (see Figure 5.63). The combination of these factors affects the precision of the surface reconstruction and limits the convergence of the Zernike analysis. In Figures 5.78, 5.79, 5.80 and 5.81 panel (b), the Zernike representation is limited to the $12^{th}$ term because beyond

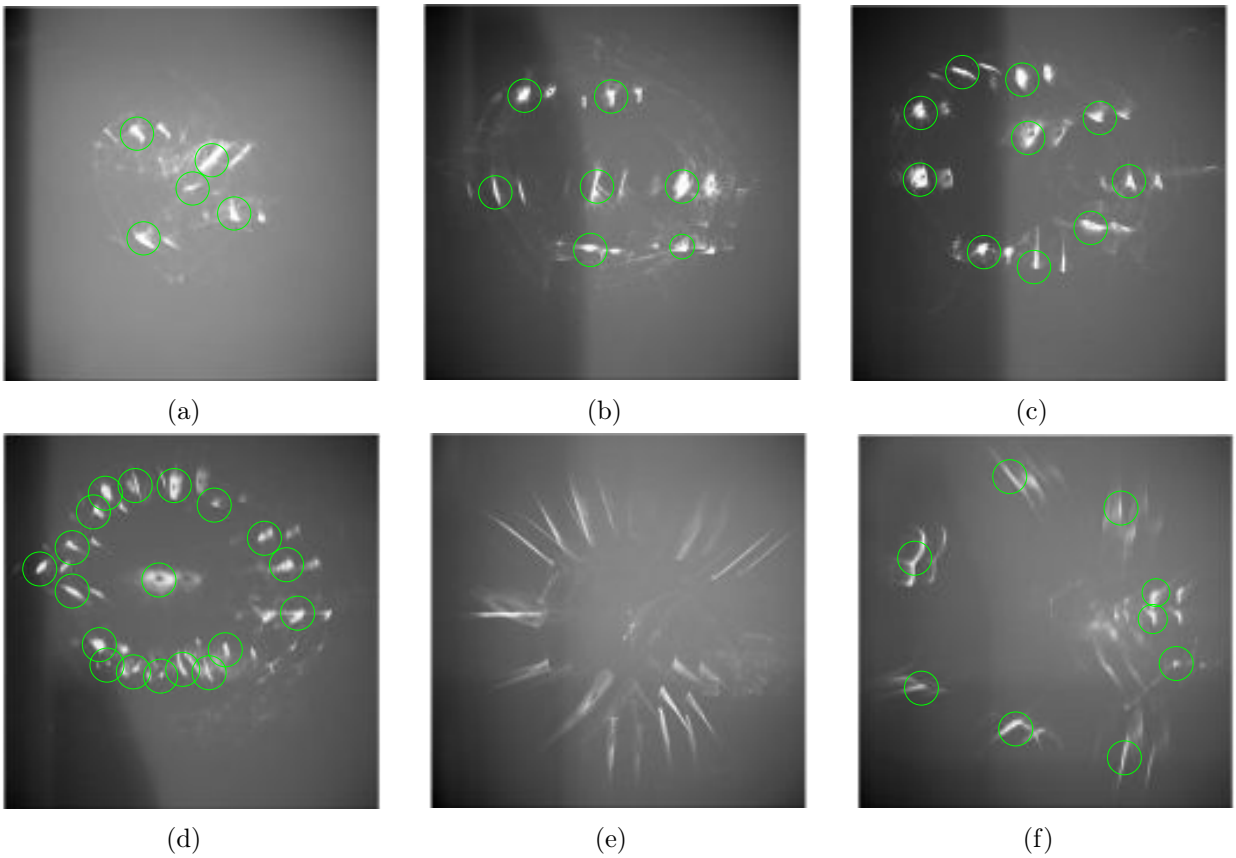

Figure 5.77: (a) Centroids from HM1, (b) HM2, (c) HM3, (d) HM4 , (e) The centroids for HM5 are not recognizable with sufficient precision due to the high asphericity of the sag and the surface ripples. The same considerations are applied to HM6 pattern which could also be affected by possible decentering with respect to M2 optical axis.

convergence problems arise. Being limited to low spatial frequencies, it is not possible to retrive a surface map of each ring to be compared with the residuals map from the FLABEG dataset (Figure 5.4). As alternative approach, for each HM, we compare the surface map reconstructed from the derivatives between the nominal sag and Zernike sag by FLABEG, and between the nominal sag and Zernike sag built with measured spot pattern. At a low Zernike order these two surface maps should give indications of good agreement and the residuals map between the two should be flat (Figures 5.78, 5.79, 5.80 and 5.81, panel (b)). This condition is verified satisfactory for the first two HMs (Figures 5.78, 5.79) while some deviations are presented for HM3 and HM4. As discussed above HM5 and HM6 show extremely complex spot patterns to recognize the centroids and perform this analysis, the spot patterns simulated and measured are shown in Figure 5.82. This test has fixed an upper limit to the precision of such technique applied to the Cherenkov aspherical mirrors. The method probably could perform better results if applied to spherical Cherenkov mirrors where the sag profile are less steep and for mirrors characterized by longer focal lengths with respect to M2 (f = 1090 mm). An interesting and significant modification of the test setup would require the use of a liquid crystals, computer generated hologram (CGH) that working as a spatial light modulator allows real time adjustment of the spot pattern projected on the mirror [98], [53].

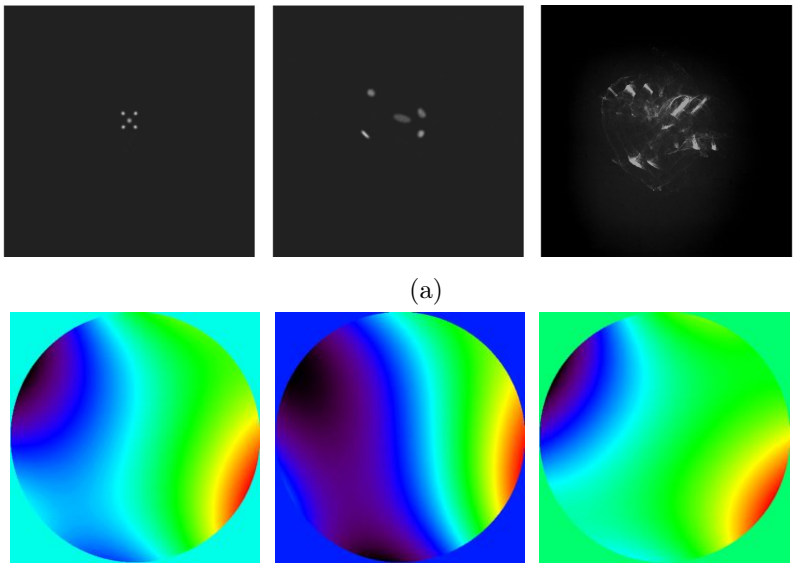

(a)

(b)

Figure 5.78: (a) Comparison among simulated and measured spots pattern from HM1. **Left** Simulated pattern for nominal M2 sag **Centre** Simulated pattern for Zernike representation of the FLABEG dataset. **Right** Measured pattern by HM. To help visualization, the multiple images visible in the measured frame and created by the semi-reflective glass have been suppressed by an anti-reflection coating in the simulated pattern. (b) Surface map reconstructed by the first 12 Zernike polynomials, from left to right: map from derivatives Nominal - FLABEG, Nominal - Measured by HM, difference between the maps.

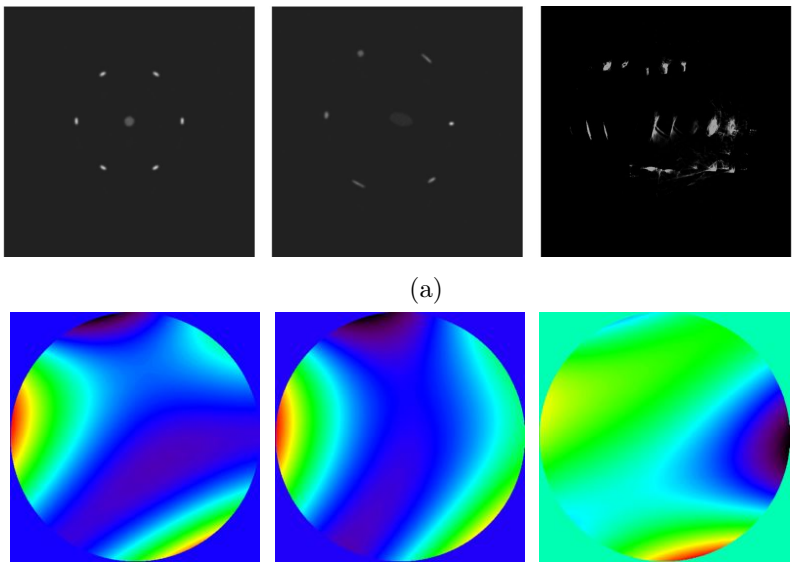

(a)

(b)

Figure 5.79: (a) Comparison among simulated and measured spots pattern from HM2. **Left** Simulated pattern for nominal M2 sag **Centre** Simulated pattern for Zernike representation of the FLABEG dataset. **Right** Measured pattern by HM. To help visualization, the multiple images visible in the measured frame and created by the semi-reflective glass have been suppressed by an anti-reflection coating in the simulated pattern. (b) Surface map reconstructed by the first 12 Zernike polynomials, from left to right: map from derivatives Nominal - FLABEG, Nominal - Measured by HM, difference between the maps.

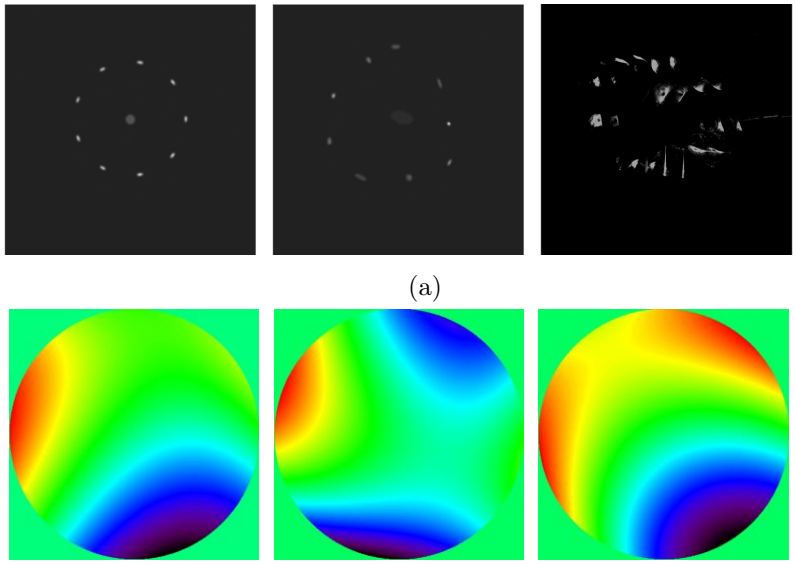

(a)

(b)

Figure 5.80: (a) Comparison among simulated and measured spots pattern from HM3. **Left** Simulated pattern for nominal M2 sag **Centre** Simulated pattern for Zernike representation of the FLABEG dataset. **Right** Measured pattern by HM. To help visualization, the multiple images visible in the measured frame and created by the semi-reflective glass have been suppressed by an anti-reflection coating in the simulated pattern. (b) Surface map reconstructed by the first 12 Zernike polynomials, from left to right: map from derivatives Nominal - FLABEG, Nominal - Measured by HM, difference between the maps. Some deviations between the two reconstructed maps are visible in the residuals pattern.

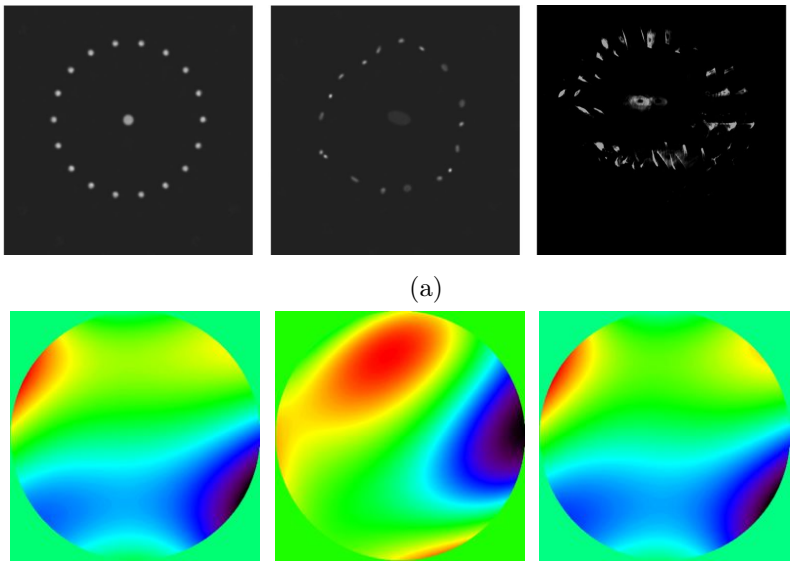

(a)

(b)

Figure 5.81: (a) Comparison among simulated and measured spots pattern from HM4. **Left** Simulated pattern for nominal M2 sag **Centre** Simulated pattern for Zernike representation of the FLABEG dataset. **Right** Measured pattern by HM. To help visualization, the multiple images visible in the measured frame and created by the semi-reflective glass have been suppressed by an anti-reflection coating in the simulated pattern. (b) Surface map reconstructed by the first 12 Zernike polynomials, from left to right: map from derivatives Nominal - FLABEG, Nominal - Measured by HM, difference between the maps. Some deviations between the two reconstructed maps are visible in the residuals pattern.

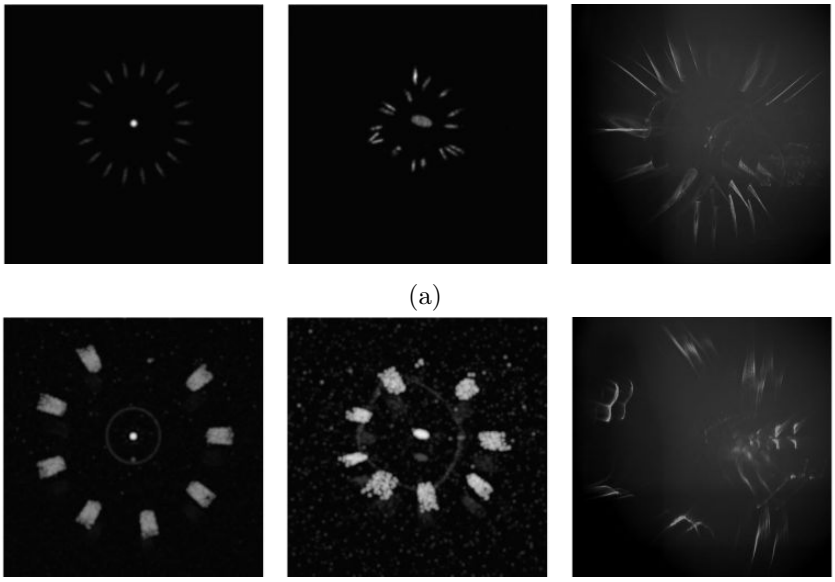

Figure 5.82: Comparison among simulated and measured spots pattern from HM5 (a) and HM6 (b). **Left** Simulated pattern for nominal M2 sag **Centre** Simulated pattern for Zernike representation of measured M2 **Right** Measured pattern. To help visualization, the multiple images visible in the measured frame and created by the semi-reflective glass have been suppressed by an anti-reflection coating in the simulated pattern.

## 5.11 M2 coating reflectivity

The coating of ASTRI M2 is composed of a 200 nm Aluminum layer covered by a protective layer of $SiO_2$ 150 nm thick. To check the compliance with the CTA requirements on the mirror reflectivity the local reflectance and the homogeneity of M2 coating have to be measured.

### Test procedure description

The measurement of the local reflectance is done at different positions along the radial coordinate of the mirror spaced by about 10 cm. The instrument used for the measurements is a Shimadzu ISR-2600 operating in the wavelength range 220 to 850 nm.

### Test result

The most critical aspect of coating deposition for highly curved surfaces is the homogeneity. In the case of M2 the extreme sag (192 mm) the problem is particularly important. As shown in Figure 5.83a, however, the local reflectance of M2 shows a very good uniformity along the entire sag profile. In the spectral region 0.45 - 0.7 $\mu m$ the simulated profile shows a slightly higher reflectance with respect to the measured profile.

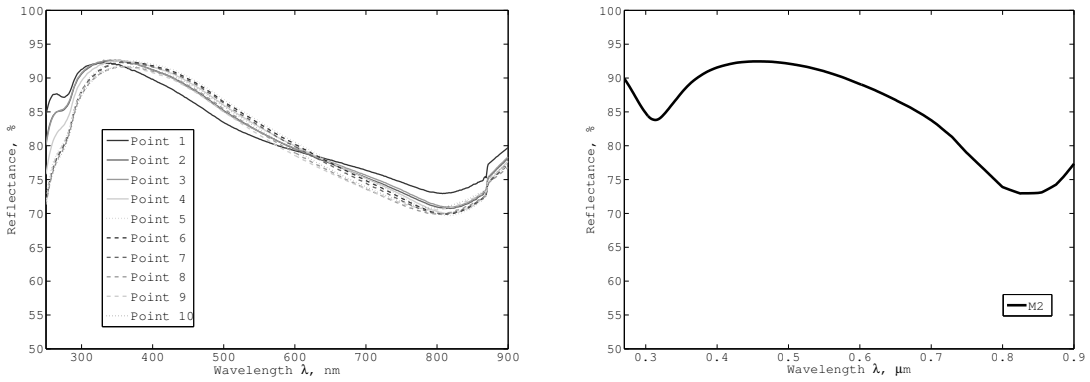


(a) (b)

Figure 5.83: Comparison among measured (a) and simulated (b) reflectance profile of the M2 coating. The local reflectance has been measured in ten different points along the radial profile of M2.

## 5.12 M2 Fourier analysis

A possible improvement of the quality and performances of M2 is here discussed in relation to its manufacturing process. The Fourier analysis is applied to the M2 residuals map provided by FLABEG and discussed in section 5.4. The goal of this analysis is estimating how different levels of residuals influence the size and the photometric properties of the PSFs for different angles in the FoV.

### Test procedure description

The power spectral density, PSD, of the residuals map from FLABEG is firstly computed, then the residuals map is filtered with a Butterworth low-pass filter that removes the highest spatial frequencies while smoothing the mid and low spatial frequencies. The filtered residuals map is interpolated by a series of Zernike polynomials and inserted in the optical design to simulate the telescope PSFs.

### Test result

The PSD of the residuals map from FLABEG interpolated with 231 Zernike terms (Figure 5.84b) is shown in Figure 5.84a. The residuals map after a first filtering cycle with a Butterworth low-pass filter is shown in Figure 5.84d; the high spatial frequencies in the corresponding PSD have been removed efficiently (see Figure 5.84c).

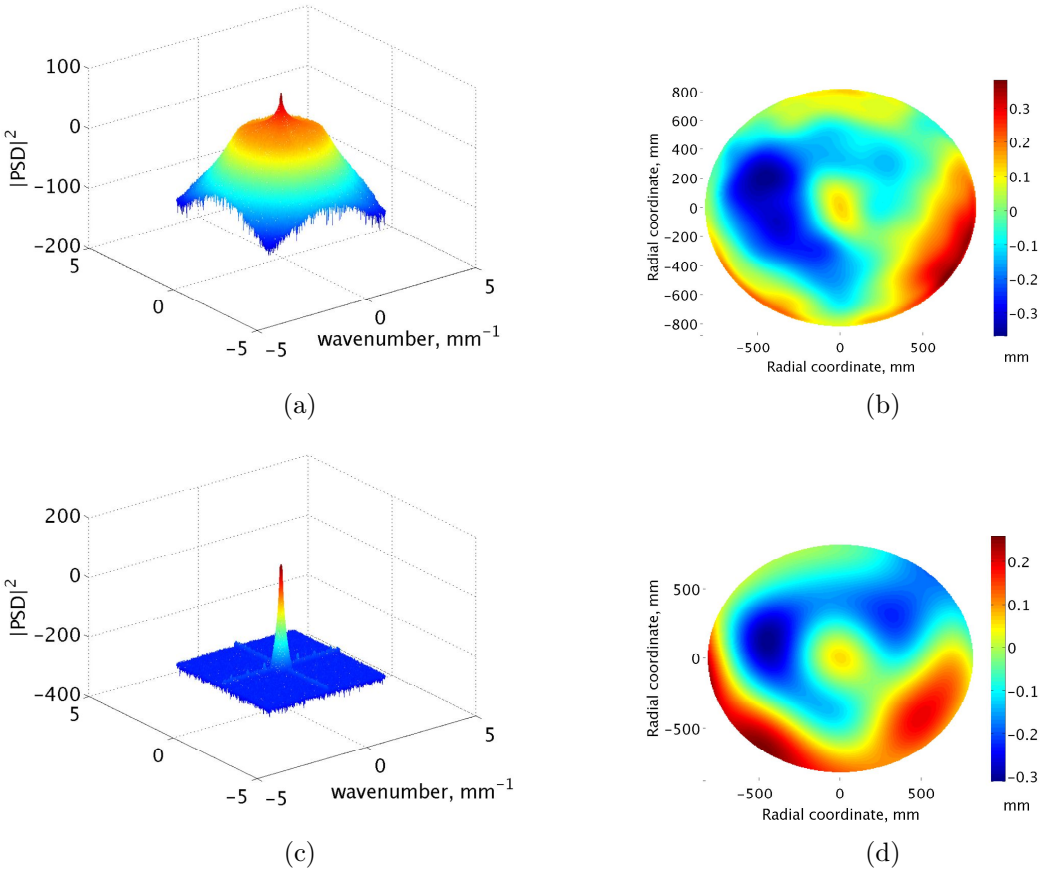


Figure 5.84: (a) PSD of the Zernike fit of the original residuals map from FLABEG, low spatial frequencies are predominant, but higher frequencies are present. (b) Zernike representation of the original residuals map from FLABEG. (c) PSD of the filtered residuals map cleaned by the highest spatial frequencies. (d) Filtered Zernike residuals map.

Once a second, additional filtering cycle is applied, the PSD is cleaned by all the high and mid spatial frequencies (Figure 5.85a) and the corresponding residuals map results in a smooth and flat distribution with maximum deviations from the nominal sag in the order of $\sim 0.02$ mm (PV), as shown in Figure 5.85b.

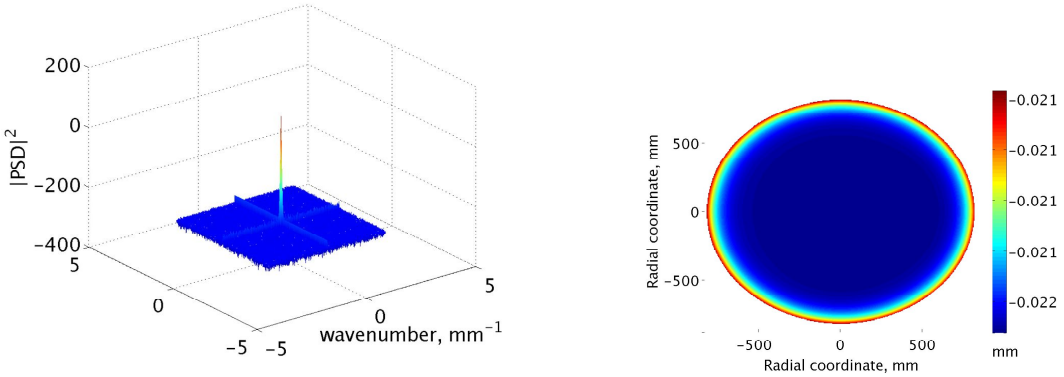


(a) (b)

Figure 5.85: (a) PSD of the double filtered residuals map, the entire high and mid spatial frequencies content has been removed. (b) The residuals map is flat and has an average residual from the nominal sag of $\sim 0.02$ mm.

If one analyzes only the $z$ component of the residuals map, the single spatial frequencies affecting the mirror can be put in evidence by a mono-dimensional Fourier analysis. Figure 5.86 refers to the PSD of the $z$ component of the FLABEG residuals map: two main peaks, $l_1$ and $l_2$ represent the predominant contribution to the deviations from the nominal sag. It is interesting to note how the first peak $l_1$ is associated to a spatial length of $\sim 200$ mm that is roughly the size of the large blue depression of the residuals map of M2 shown in Figure 5.84b.

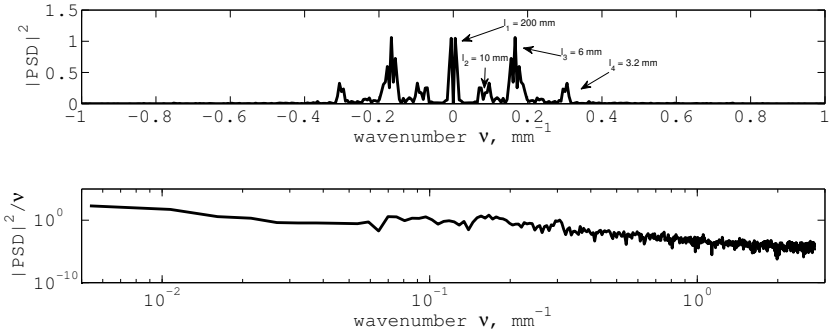


Figure 5.86: (Top) Mono-dimensional PSD of the FLABEG residuals z component, about four main peaks are visible; the highest frequency contribution is associated to a spatial length of $\sim 200$ mm that could originate from the large depression in the residuals map of Figure 5.84b. (Bottom) PSD in spatial frequency units as a function of the wavenumber: the major contributions come from long spatial scales.

If the same calculation is applied to the filtered residuals map shown in Figure 5.85b, the PSD is cleaned from all the spatial frequencies present in Figure 5.86. The highest peak refers to a spatial length of about 2000 mm that roughly corresponds to the size of M2 while the second peak is probably an artifact of the filtering process or of the Zernike fitting.

As discussed above, the filtering process leads to an average residual from the nominal sag of $\sim 0.02$ mm, that corresponds to about one-tenth the original value from the residuals map requested to the manufacturer (see section 5.3).

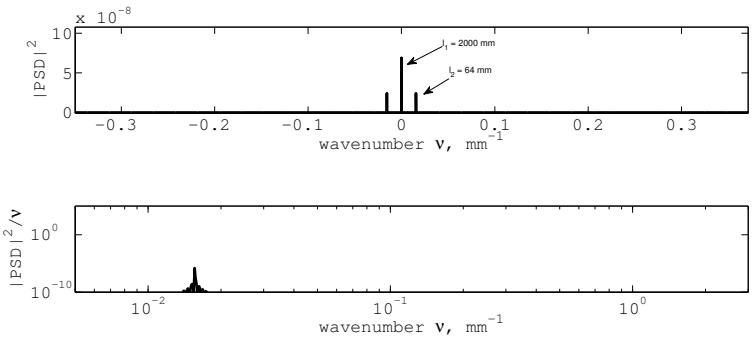


Figure 5.87: (Top) Mono-dimensional PSD of the residuals z component from the double filtered map: the spatial frequencies visible in Figure 5.86 disappear and only a long spatial frequencies associated to the size of the whole mirror remains. (Bottom) PSD in spatial frequency units as a function of the wavenumber.

Once the filtered residuals map are interpolated with a series of 231 Zernike polynomials (Figures 5.84b, 5.84d and 5.85b), they are loaded into the optical design of the telescope to evaluate the properties of the PSFs at different levels of residuals from the nominal sag. In Figure 5.88a, the size of the telescope PSFs (R80 value) from the Zernike representation of the different residuals maps, the original FLABEG data, the first filtered map and the second filtered map, are compared with the PSFs from the nominal sag of M2. The deviations in the R80 values for the different residuals level of M2 are plotted in Figure 5.88b. For increasing filtering the photometric radii of the PSFs get closer to the nominal values (black line Figure 5.88a). The double filtered map (red line) overlaps, at least completely, to the curve from the nominal sag proving that residuals in the order of 0.02 mm have no impact on the M2 performances.

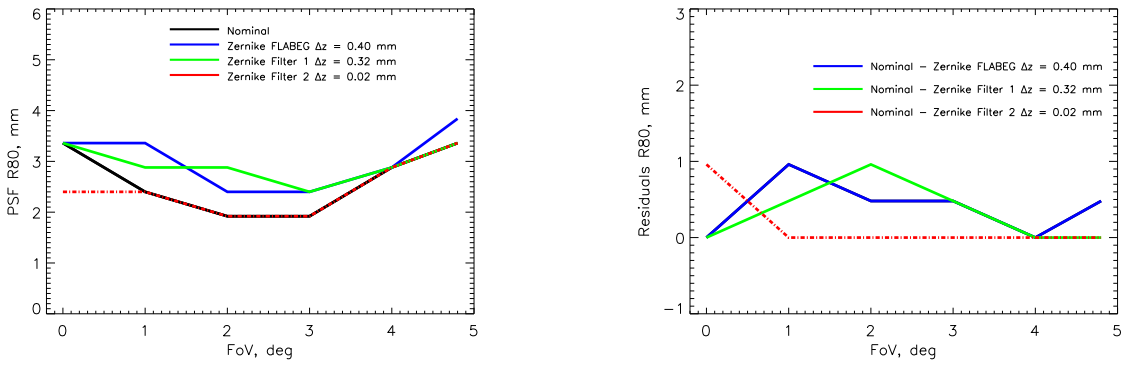


(a) (b)

Figure 5.88: (a) R80 values of the telescope PSFs at different angles in the FoV for the nominal M2 sag, the Zernike fit of the FLABEG profile and the Zernike fit of the filtered maps. (b) Difference between R80 values of the nominal configuration and the studied residuals maps. Both the plots report the average residuals from the nominal sag in the legend.

Manufacturing a mirror with a PV error of $\sim 0.02$ mm, i.e. with a surface quality of $40\lambda$ @ optical wavelengths, is fully in the capabilities of the standard grinding and lapping techniques used to produce optical mirrors. Grinding can easily reach an RMS $\sim 5$ $\mu$m [33], that is an order of magnitude better than the value required for M2. These simulations indicate that a two-stage manufacturing process based on a first hot slumping cycle of the glass, followed by a basic grinding and polishing process would lead to a sag for M2 fully compliant with the profile from its nominal optical design.

# Chapter 6

# New intensity interferometry perspectives with future large telescopes

The new generation of extremely large telescopes and arrays opens new perspectives for the future of the experimental astronomy. The 30-metres class of optical telescopes as the European-Extremely Large Telescope (E-ELT), the Giant Magellan Telescope, (GMT), the Thirty Meter Telescope, (TMT) and kilometer-scale arrays at radio, millimeter and optical bands like the Square Kilometer Array, (SKA), the Atacama Large Millimeter Array, (ALMA) and CTA have been in part already deployed or will be soon constructed. This golden age for the ground-based astronomy will provide research infrastructures that will overcome by orders of magnitude the capabilities of the current facilities. The common denominator of these projects will be the boosted sensitivity that will lead to new experimental scenarios in many astronomy fields.
Concerning CTA, there is an active and growing discussion about possible non-gamma ray uses of the Observatory among the scientific community. The huge collecting power of the array of telescopes is well-suited for intensity interferometry studies, rapid photometry of bright sources, searching for exoplanets transits [169], observing stellar occultations by small bodies (Transjovian and Kuiper Belt Objects) in the outer Solar System (Lacki 2014, [86]) and the implementation of free-space optical communications for future deep-space links (Carrasco-Casado et al., [21]).
Of particular interest is the revival of the intensity interferometry (II) technique (LeBohec et al. (2008), [88]) in relation to the advent of CTA. This Observatory indeed, will provide the first kilometer-scale optical array suitable to perform II investigations and to realize a modern version of the stellar intensity interferometer originally built by Hanbury Brown & Twiss. An intensity interferometry with kilometer-scale baselines working at optical wavelengths ($\lambda$ ∼350 nm) in principle can provide an angular resolution of about 30 $\mu$as ($\mu$as = $10^{-6}$ arcsec) (Dravins et al., 2014, [37]), competing with the Very Long Baseline Interferometry (VLBI) performances at radio frequencies. High-resolution observations by means of the II technique to resolve the surface of bright stars in our galaxy are among the goals of CTA [170]. Simulations on the performances of such technique applied to CTA carried out by many authors as Dravins et al. (2012) [35] and Nuñez et al. (2012) [104], point out that this technique will enable imaging of stellar surfaces and their surrounding environments, stellar winds and gas flows in binary stars. Moreover another application, called *Interferometric Parallax*, based on the II technique has been proposed by Jain and Ralston [70]. The technique aims to estimate the direct distance of the celestial bodies. In this chapter after an introductory section about high-resolution observations and intensity interferometry problematics and capabilities, we describe this latter experimental method that makes use of large incoming observatories as CTA.

## 6.1 High-resolution in astronomy

The quest for high-resolution imaging in astronomy has always been one of the most compelling science drivers for the construction of progressively larger telescopes. Parallel to the realization of large radio, infrared and optical telescopes, the angular resolving power has been pushed to extreme values by the use of interferometry. Facilities operating today as the Very Large Telescope Interferometer (VLTI) and the Center for High Angular Resolution Astronomy (CHARA) constitute the major optical-NIR interferometers. The VLTI at Paranal (Chile) consists in the coherent combination of the four VLT Unit Telescopes (8 m class) and of the four moveable 1.8 m Auxiliary Telescopes. Once fully operational, the VLTI will provide both a high sensitivity as well as milli-arcsec angular resolution using baselines of up to 200 m length [171]. The CHARA Array is a six, 1m-telescopes optical/infrared interferometric array on Mount Wilson, California that provides 15 baselines from 31 to 331 m with a limiting resolution of 0.15 mas (milli-arcsec) between 470 - 800 nm and 0.6 mas between 2.0 - 2.5 $\mu$m [172]. The optical-NIR facilities above mentioned have demonstrated great potentials in the imaging of bright, nearby stars as shown by some case studies in Figure 6.1.

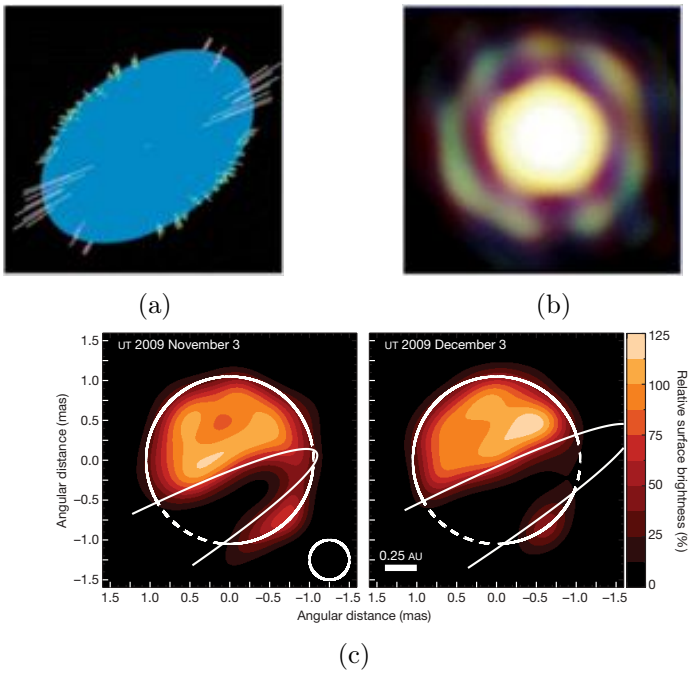


Figure 6.1: (a) The VLTI measured the shape of the star Achernar; rapid rotators can modify the stellar shapes and surfaces, causing an increased polar surface brightness [132]. (b) VLTI image of the molecular shell surrounding the star T Leporis [89]. (c) The image of the star Epsilon Aurigae obtained with CHARA, whit a transiting, obscuring circumstellar disk [76].

At radio wavelengths the Very Long Baseline Interferometry (VLBI) network connects radio telescopes across the Planet (baselines $\sim 10^4$ km) and the U.S. Very Long Baseline Array (VLBA), which consists of 10 identical antennas on transcontinental baselines up to 8000 km is operated as a unique array synchronized with atomic clocks capable of reaching $\sim$ 10 $\mu$as angular resolution. At millimeter/submillimeter scale a new array, namely ALMA has been just constructed by the European Southern Observatory (ESO), the National Radio Astronomy Observatory (NRAO) and the National Astronomical Observatory of Japan (NAOJ) and it comprises sixty-five 7-m and 12-m antennas, which can be configured to achieve baselines up to 16 km, reaching an angular resolution of 0.7 arcsec at $\lambda$ =1 mm. Such facilities can produce images at milli-arcsec scale as shown in Figure 6.2.

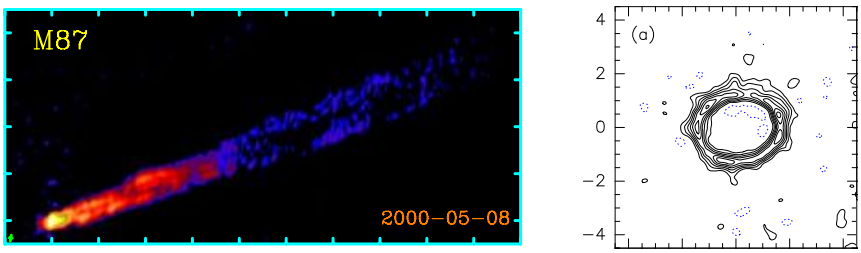


Figure 6.2: (a) VLBA ($\lambda = 2$ cm) image of the M87 jet. The tick marks are spaced 10 mas apart, and the resolution is about 1 mas = 0.08 parsec. This high dynamic range image which traces the jet out to nearly 0.1 arcsec was obtained from a full sky track using the VLBA along with one VLA antenna to increase the effective FoV [74]. (b) Continuum emission at 0.45 mm from a planetary ring in a double star system detected by ALMA [39].

Despite the excellent results already achieved by amplitude interferometry, this technique, especially at optical wavelengths, is strongly limited by the atmospheric perturbations and the thermal and mechanical stability of the observing instruments. Current optical interferometers have baselines in the order of ∼100 m and the next jump to km-scale baselines seems to be too challenging for the current technology both for ground and space observatories. This important limitation motivates the development of alternative techniques to perform high-resolution observations over km-scale baselines at optical wavelengths. Differently from an amplitude interferometer, an intensity interferometer measures the second-order coherence of the light by observing the correlation in the time of arrival of photons at different telescopes in space. The telescopes are not optically linked and the photons are detected by ultra-fast photometers that convert the light into a digital signal that is correlated among the interferometer units. All these operations are done by software and electronics that provide a time resolution of a few nanoseconds. For this reason the optical paths of the photons can tolerate phase shifts in the order of $\tau_{electronics} \times c \sim 0.3$ m ($c = 3 \cdot 10^8$ m/s) leading this technique to be cleaned from the atmospheric perturbations and from the optics misalignments that severely limit the amplitude optical interferometry beyond hundreds meters-scale baselines. Although this technique suffers some limitations with respect to amplitude interferometry, the next generation of large optical telescopes will provide a huge light collecting power and attractive perspectives for high-resolution researches.

## 6.2 Intensity interferometry technique

In the classical Michelson interferometer, the light collected by two telescopes separated by a baseline $d$ is combined coherently on the focal plane to form an interference pattern as shown in Figure 6.3a. If the interferometer observes a point-like source of angular diameter $\delta\theta < 1.22\lambda/d$, a series of fringes from the interference pattern will be observed; increasing the telescope separation, the resolution of the interferometer increases. However as discussed in the previous section, Michelson interferometers suffer limitations due to atmospheric perturbations, vibrations and thermal gradients: keeping sub-wavelength coherence for baselines above ∼0.1 km is extremely challenging on the ground and still unfeasible and too expensive from space. The intensity interferometer conversely, measures the correlations between the photocurrents generated by the starlight in photomultipliers at the foci of a pair of separate telescopes (Figure 6.3b). The intensity of the photocurrent $i$ is proportional to the intensity of the starlight $I$. The latter is defined as the product of the electric field amplitude $E$ and its complex conjugate averaged over a certain time, $\langle I(t)\rangle = \langle E(t)E^*(t)\rangle$. The correlation is a multiplication process between the photocurrents $i_1(t), i_2(t)$ averaged over a time equal to the bandwidth of the system. If the

interferometer baseline is small the two telescopes collect the light from the same area of the source and $i_1(t) = i_2(t)$. Increasing the baseline $d$, the correlation between the photocurrents progressively decreases and this provides a method for the estimation of the angular diameter $\delta\theta$ of the source.

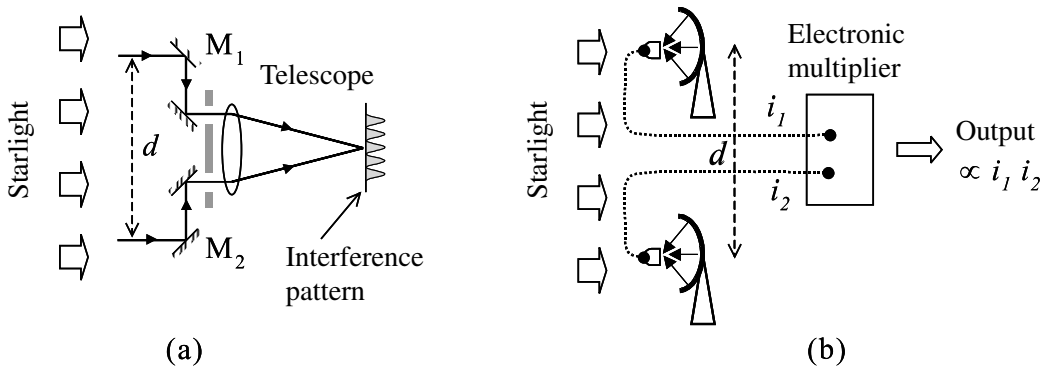


Figure 6.3: (a) Michelson interferometer built on Mount Wilson in 1920s, the light is collected coherently by two mirrors and driven to the focal plane where the interference pattern in created. The intensity interferometer converts the starlight collected by separate receivers into photocurrents that are multiplied over time to study the intensity fluctuations of the light at different apertures in space. Image taken from [43].

It is shown by a quantum-mechanical treatment that the emission times of photoelectrons at different points illuminated by a plane wave of light are partially correlated (Hanbury Brown & Twiss 1957, [56]). The intensity correlations are expressed in terms of the second order correlation function:

$$g^{(2)} = \frac{\langle \Delta I_1(t) \Delta I_2(t) \rangle}{\langle \Delta I_1 \rangle \langle \Delta I_2 \rangle} \tag{6.1}$$

where $\Delta I_1(t) = I_1(t) - \langle I_1 \rangle$ is the intensity fluctuation at the single telescope (the symbol $\langle\ \rangle$ denotes average over time). The phenomenon can be explained both as a correlation between intensity fluctuations at different points which arises from the interference of different frequencies components in the light beam assuming a wave behavior of the light, or considering a corpuscular nature of the light and the correlation as a result of the photons bunching. The working principle of the intensity interferometer is based on the assumption that the light under study is *chaotic*.

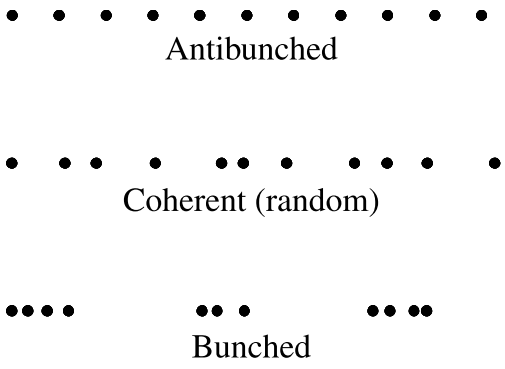


Figure 6.4: (Top) antibunched light is a purely quantum phenomenon, (Middle) coherent light is the result of a Poissonian statistics and (Bottom) bunched, thermal light as delivered from a black body. Image taken from [43].

Figure 6.4 shows the possible statistics of the light originated from different phenomena. The classification can be done on the basis of the value of the second order coherence function at null time:

- **bunched light**, $g^{(2)}(0) > 1$, classical light, blackbody, Gaussian or Lorentzian broadened
- **coherent light**, $g^{(2)}(0) = 1$, laser light
- **antibunched light**, $g^{(2)}(0) < 1$, light from single atoms

Thermal starlight is a classical chaotic light that can originate from three main processes: black body radiation, Gaussian-Doppler and Lorentzian emission. This chaotic light is described by a Super-Poissonian statistics. Laser and maser light sources produce coherent (random) light that obeys to a Poissonian statistics, while antibunched light is the result of a quantum effect produced in the emission of photons by a single atom and it follows a Sub-Poissonian statistics.

The intensity interferometry technique was pioneered in astronomy thanks to the work of Hanbury-Brown & Twiss at the Narrabri Observatory (Australia) in the decades of sixties and seventies. The story of the early developments that led to the subsequent successful estimation of about 32 apparent angular diameters of bright stars is collected in a series of four main publications that are briefly envisaged below.

To prove the theory of the intensity fluctuations in light, Hanbury Brown & Twiss prepared a laboratory test in which two photomultipliers were illuminated with partially coherent light and the correlation between the fluctuations in their outputs measured as a function of the degree of coherence (Hanbury-Brown & Twiss 1958, [57]). A scheme of the setup is given in Figure 6.5a: a quasi-monochromatic light source was splitted in two beams directed towards the two photomultipliers; one of the two detectors ($P_2$) could be translated along a linear stage to explore the spatial coherence of the light beam. It was observed that the correlation degree decreased as the $P_2$ detector was shifted off-axis with respect to the incident light beam (Figure 6.5b).

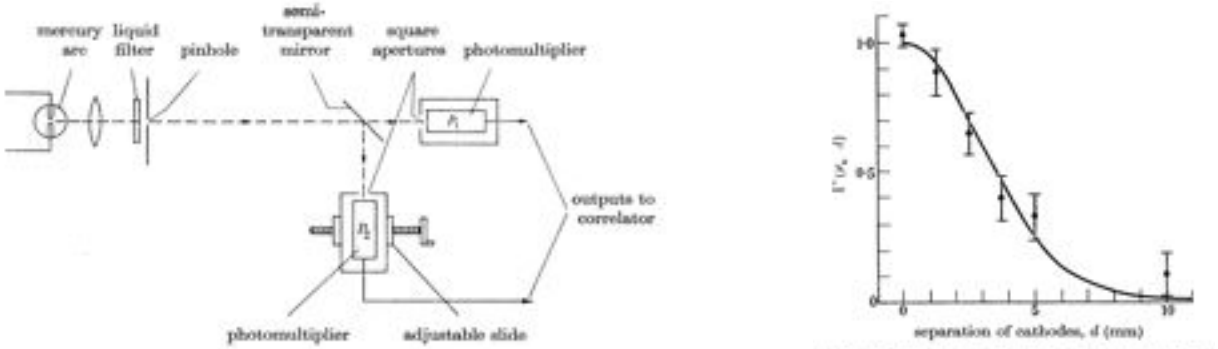


(a) (b)

Figure 6.5: (a) Schematics of the experimental setup to explore the spatial coherence of a light beam. (b) Experimental measurements and theoretical profile of the normalized correlation factor $\Gamma^2$ for different translational off-set of the photomultipliers. Images from [57].

This successful experiment proved how the intensity correlations could be used to measure the apparent angular distribution of intensity over the source light. A theoretical study on the concept of a stellar intensity interferometer concept then followed. The aim of such interferometer was that of estimating the apparent angular diameter of stars by studying the spatial coherence of their light. The intensity fluctuations were recorded by a pair of telescopes separated by a variable baseline. An adjustable time delay was inserted in the appropriate channel to compensate for any difference in the times of arrival of the light from the star at the two mirrors (Hanbury-Brown &

Twiss 1958, [58]) as shown in Figure 6.6a. The telescope separation was varied to sample different areas of coherence of the source and determining the apparent angular size of the source. The mathematical expression of the correlation factor for the starlight coherence area:

$$\Gamma^2_\lambda(d) = \left[\frac{2J_1(\pi\theta d/\lambda_0)}{\pi\theta d/\lambda_0}\right]^2 \tag{6.2}$$

is described by a Bessellian function $J_1$ that is function of the apparent angular diameter $\theta$, the wavelength of observation $\lambda_0$ and the telescopes separation $d$. In a intensity interferometer that measures the spatial correlation factor $\Gamma^2_\lambda(d)$, the apparent angular diameter of the source is derived by measuring the radius $r_0$ of the coherence area in correspondence of the first zero of the Bessellian function $\theta \sim \lambda/(\pi r_0)$.

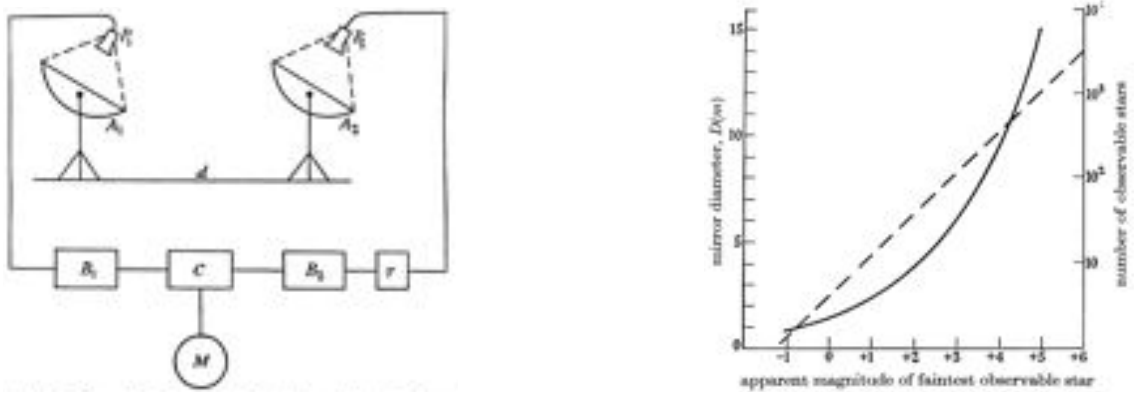


(a) (b)

Figure 6.6: (a) Schematic diagram of an intensity interferometer. A, mirrors; B, amplifiers; C, multiplier; M, integrator; P, phototubes; $\tau$, adjustable time delay. (b) Mirror diameter necessary to achieve a SNR = 3 in a period of 1 h as a function of the apparent magnitude at $\lambda$= 430 nm. The broken line shows the total number of stars in the two hemispheres. Images from [58].

An overall budget of the sensitivity of the observation was assessed (Figure 6.6b) as a function of the telescope diameter. For a signal to noise ratio (SNR) of 3, only the brightest stars ($m_B < 6$) are observable with ∼10 m apertures. The maximum resolving power of the intensity interferometer was however remarkable if compared with the Mount Wilson Michelson interferometer, respectively $\delta\theta \sim 2 \times 10^{-9}$ rad and $\delta\theta \sim 10^{-7}$ rad.

A first interferometer prototype, was operated by Hanbury-Brown & Twiss to observe Sirius and measuring its apparent angular diameter. With a couple of searchlight reflectors (1.65 m in diameter) they observed the correlation profile reported in Figure 6.7b, and they derived an apparent angular diameter of the star $\delta\theta \sim 0.007$ arcsec (Hanbury Brown & Twiss 1958, [59]).

The significant improvement in the angular resolution and the success in the Sirius measurement motivated the construction of the first, large intensity interferometer at the Narrabri Observatory in Australia (Figure 6.7a). The interferometer was composed by two 6.7 m telescopes equipped with a photomultiplier that could be moved along a circular railway (188 m in diameter) to follow the star in azimuth and to probe different regions of the starlight spatial coherence. The high frequency fluctuations (10-100 MHz) from the photomultipliers were conveyed to a central correlation unit with an adequate time delay and multiplied over time. By varying the telescopes separation the spatial coherence of the source was traced and the apparent angular diameter retrieved. With this procedure the apparent angular diameter of the 32 brightest stars in the spectral range O5 to F8 of the Southern hemisphere was measured (Hanbury-Brown et al. 1973, [60]). After this extraordinary achievement, the Observatory was dismantled with the project of constructing a larger and more sensitive interferometer that however was never

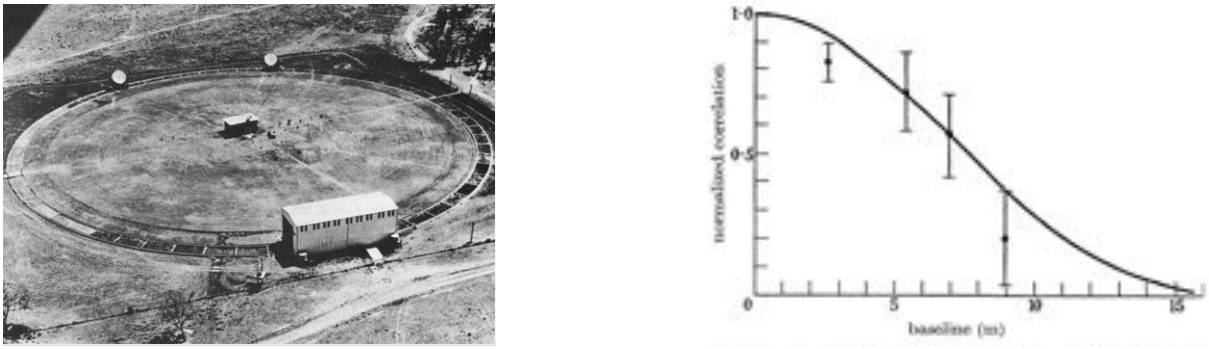


(a) (b)

Figure 6.7: (a) Narrabri Observatory: two 6.7 m telescopes could move along a circular railway with a diameter 188 m to explore the spatial coherence of bright stars. The correlation unit was placed in the centre of the rail. (b) Correlation dependence on the telescopes separation while observing intensity fluctuations from Sirius, measured points and theoretical curve (solid line). Image from [59].

realized.

## 6.3 The potentialities of IACTs

The parameters of imaging air Cherenkov telescopes are remarkably similar to the requirements for intensity interferometry (Dravins et al. 2012 [36]). The IACTs in fact fulfill many requirements of the II technique:

- Huge collecting flux
- Fast detectors and electronics
- Blue-optimized reflecting surfaces
- Sparse apertures, multiple baselines

IACTs provide unprecedented collecting area making possible the observation of thousands of stars by means of a dedicated detection unit working at nanosecond scale and a fast electronics architecture (MHz-GHz) that handles the signals from different telescopes to a common correlation unit. A radical difference lays in the acquisition system that requires to integrate over time for hours the intensity fluctuations instead of triggering a faint Cherenkov shower. Cherenkov telescopes are designed to observe in the UV-blue range that is also the preferred spectral window for the observation of hot stars with II. The incoming CTA Observatory will be composed of tens of telescopes spread over an area of about 3 $km^2$ thus providing a multi-element array and a high coverage of the u-v plane. These capabilities will make CTA the first kilometer-scale intensity interferometer capable to reach sub-milliarcsecond angular resolution. The u-v plane is filled exploiting the Earth rotation that causes a change in the projected baselines between the telescopes and a dedicated series of electronics delay lines that keep the phasing of the array. Since the number of independent baselines scales with the number of the telescopes as N(N-1)/2, even if the signal phase is lost in this technique, it is possible to reconstruct an image on the basis of some methods of phase recovery (e.g. Cauchy-Riemann, Nuñez et al. [104]). The SNR is independent of the optical passband, but it is preferred to work with a narrow band to increase the temporal coherence of the signal and this is achieved by means of a narrow-band filter positioned in front the detector. The sensitivity in terms of SNR of the II technique is derived from the following expression:

$$SNR = n(\lambda, T, m_v) A \alpha \gamma^2 \sqrt{\Delta f t / 2} \tag{6.3}$$

with $\gamma$ degree of correlation, $A$ telescope effective area, $n$ spectral density n($m^{-2}$ $s^{-1}$ Hz), $\alpha$ detector quantum efficiency, $\Delta f$ electronic bandwidth and $t$ observation time. An estimation of the limiting magnitude observable as a function of the telescope diameter is shown in Figure 6.8.

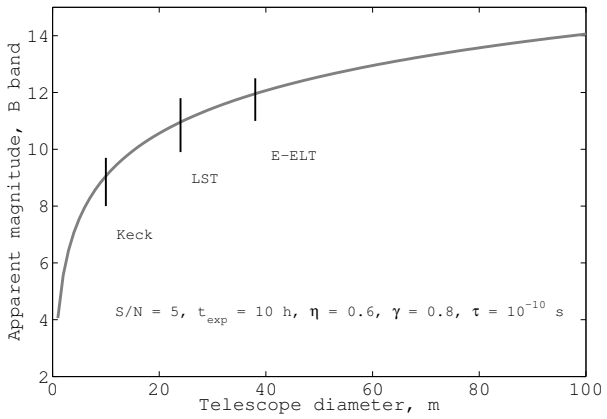


Figure 6.8: Limiting apparent magnitude for an electrical bandwidth of $10^{10}$ Hz in B band. The vertical black lines indicate the theoretical sensitivity (for the parameters of the SNR reported into the plot) of a 10-m telescope (Keck), an LST telescope (24 m) of CTA and the E-ELT telescope (39 m). Plot obtained with Matlab.

The exact SNR behavior depends also on the properties of the source; for progressively increasing telescope diameters one will reach a size where the source is spatially resolved already by a baseline equal to the telescope diameter and the SNR cannot further increase. At that point the signal one measures is then the spatial coherence pattern averaged over the telescope aperture. However, better S/N values could be obtained for stars of equal apparent magnitudes, but with higher temperatures, being several times smaller in diameter and permitting correspondingly larger telescope diameters before their spatial coherence pattern become resolved over a single telescope aperture. Outside this caveat, the SNR can be further increased involving more telescopes into the array and/or adding multiple electromagnetic channels. As discussed by Horch et al. 2013 [69], the gain in SNR from these two parameters is given by:

$$SNR_{Array} = \left[ \begin{pmatrix} N_{Array} \\ 2 \end{pmatrix} \; M_{Channels} \right]^{1/2} SNR_{Baseline} \tag{6.4}$$

where $SNR_{Array}$ is the overall SNR of an array composed of $N_{Array}$ telescopes, each with $M$ channels, as compared to the $SNR_{Baseline}$ of two telescopes. Increasing the number of telescopes or channels will make the curve of Figure 6.8 moving up towards fainter limiting magnitudes.

Figure 6.8 shows a significant improvement of the sensitivity of CTA with respect to the Narrabri Observatory that should allow the robust observation of stars down to an apparent magnitude $m_B \sim 7 - 9$. With this threshold thousands of stars would be detectable with CTA as assessed by many authors (e.g. Dravins et al. 2012 [36] and Nuñez et al. 2012 [104]). As shown in Figure 6.9, the population of bright ($m_B < 7$) stars from the Hipparcos Catalogue is numerous in both the sky hemispheres. Moreover, as discussed above, with multiple baselines in addition to the measurement of the apparent angular diameter of these stars, it will be possible to retrieve a resolved image of their surfaces. Simulations performed by different authors (e.g. Dravins et al. 2012 [36], Nuñez et al. 2012 [104], and Dravins & Lagadec 2014 [37]) indicate promising results

for sub-milliarcsecond imaging of the brightest stars and the observation of stellar surfaces, winds and surrounding disks. As shown in Figure 6.11, obscuring structures and/or transiting objects such as exoplanets could also be detectable for the brightest and nearby stars.

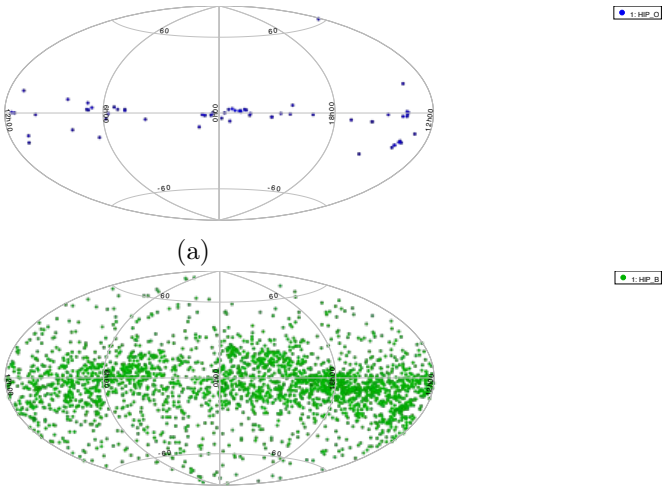

(a)

(b)

Figure 6.9: All sky distribution from the Hipparcos Catalogue of the (a) O stars and (b) B stars with $m_B < 7$. Image obtained with Topcat.

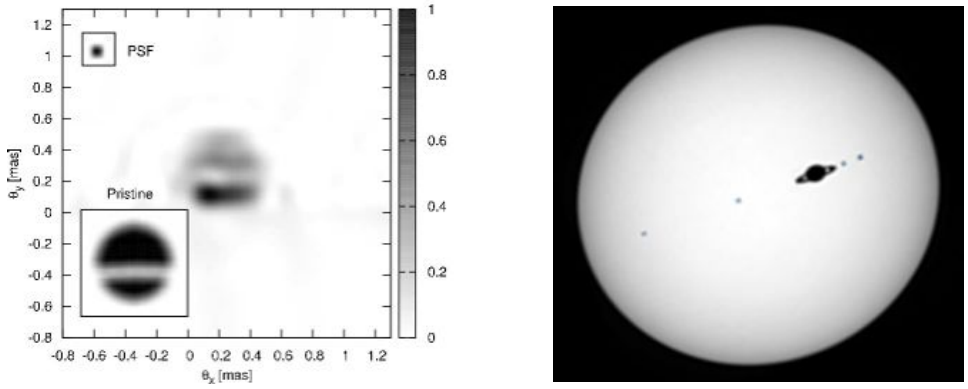


(a) (b)

Figure 6.10: (a) Star with obscuring disk (raw reconstruction). This corresponds to 4th magnitude and 10 hrs of observation time. The correlation between the real and reconstructed image is c = 0.947 ± 0.001. An inverted grey scale is used, image and label from Nuñez et al. 2012 [104]. (b) A vision of microarcsecond optical imaging: expected resolution for an assumed transit of a hypothetical exoplanet across the disk of Sirius, using II on CTA. Stellar diameter = 1.7 solar, Distance = 2.6 pc, Angular diameter = 6 mas; assumed planet of Jupiter size and oblateness; Saturn-type rings; four Earth-size moons; equatorial diameter = 350 $\mu$as. With the CTA array spanning 2 km, a 50 $\mu$as resolution provides more than 100 pixels across the stellar diameter. Image and label from Dravins & Lagadec [37].

The ASTRI mini-array (section 2.7), that is an array of presumably seven ASTRI telescopes replicated, provides an attractive pathfinder experiment for II with CTA. Seven telescopes spaced by about 300 m provide twenty-one independent and simultaneous baselines up to about 700 m. The layout used for some assessment simulations [47] is shown in Figure 6.11a and an example of reconstruction of the correlation function for the star $\lambda Eri$ ($m_V = 4.27$) in 5 hours of integration time is reported in Figure 6.11b. For this specific simulation the estimated apparent angular diameter is $\delta\theta = 0.209 \pm 0.001$ mas (Hanbury-Brown & Twiss found $\delta\theta = 0.21$ mas). Actually a pathfinder experiment to develop a technology demonstrator is under realization with the goal of assessing possible problematics and the technology readiness of the detection scheme on the

single ASTRI prototype [38].

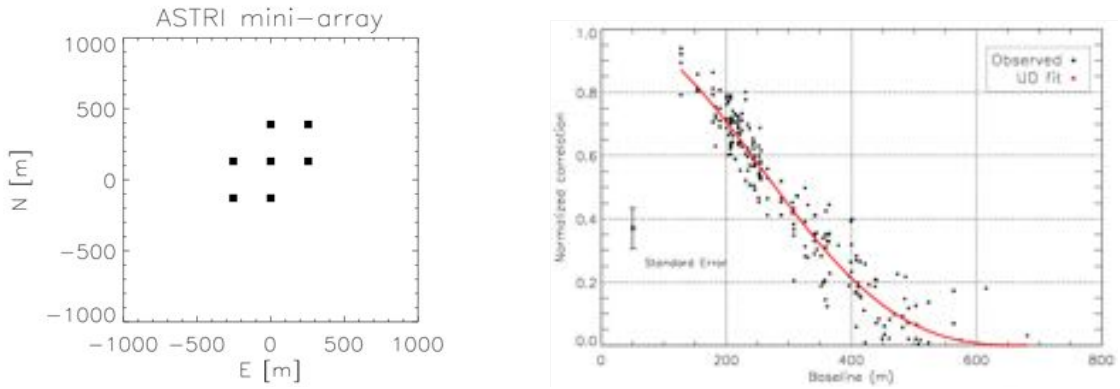


(a) (b)

Figure 6.11: (a) Simulated layout for the ASTRI mini-array of seven telescopes separated by ground baselines of about 300 m. (b) Simulated correlation function for the star $\lambda Eri$ in 5 hours of observation with the ASTRI mini-array: sampling time 1 ns, detector quantum efficiency 0.7 and mirror reflectivity 72 %. [47].

In addition to this exciting scenario that could bring to measure the apparent angular diameter and possibly resolving the surperficial features of the nearby stars, there are other possible applications for II with CTA. In the next sections one of the them is discussed in detail.

## 6.4 A new application for II: interferometric parallax

In the following sections a new application of the intensity interferometry for the measurement of the astronomical objects distance is discussed in detail. The method is called interferometric parallax (IP) and it can be performed both at amplitude (phase) and intensity interferometry. The mathematical derivation of the method and the differences between other methods as for instance the trigonometric parallax are first described (section 6.4.2). Then some simulations on the method performances and the technical aspects of the observation are discussed. Possible applications to the observation of some astrophysical sources, the estimate of some orders of magnitude that could be achieved and the perspectives with the next generation of ground-based large telescopes are presented in section 6.5. Finally we describe a pathfinder experiment at radio frequencies with current facilities for the assessment of the technical reliability (section 6.6).

### 6.4.1 Interferometric parallax science case

The direct estimate of distances in Astronomy has always been one of the most difficult measurements to perform. Although many indirect methods based on photometric and spectroscopic observations already exist, the methods providing direct, geometric distance of the celestial bodies, independent of any additional parameter, is limited to our own Galaxy. At optical wavelengths, the method of the trigonometric parallax (TP) probed distances to the order of kpc with the Hipparcos satellite for more than 100,000 stars in the solar neighborhood (Perryman et al., 1997 [109]) and the GAIA mission aims to extend this measurement to ∼1 billion stars (de Bruijne 2012 [30]). At radio frequencies, examples of TP measurement are provided by Hachisuka et al. 2006 [54], Reid et al. 2009 [112] and van Langevelde 1999 [133] that estimated the distances and proper motions of galactic masers by means of the VLBA and Japanese VLBI, exploring the nearby interstellar medium until ∼ 10 kpc. However the TP technique requires extreme instrumental stability to produce images of the quality to obtain precise astrometric analyses.

A new method to estimate distances and proper motions called *interferometric parallax* (IP), that differs substantially from TP has been proposed by Jain & Ralston [70], hereafter JR08. This method does not require a precise measurement of the object's angular position, neither by making an image nor resolving the object under study. The IP method entirely bypasses the step of image production/acquisition, while concentrating on the raw signals collected by pairs of receivers. An observation carried out by IP in principle could probe distances up to the Mpc scale (JR08). The measurements can be performed either with the amplitude interferometry at radio frequencies or by using the optical intensity interferometry, thanks to the upcoming CTA. While interferometers work in the Fraunhofer far field hypothesis, IP relies on an extension of the Van Cittert-Zernike ($VCZ$) theorem that assumes a plane wave approximation. The extension includes effects from the curvature of the wavefronts from a source at finite distance, which contributes an observable phase difference. The basic use of IP assumes the observation of a foreground object (target) and one background object (reference) that are angularly close and preferably point-like sources; by cross-correlating the signals retrieved from a pair of separate receivers at different epochs, the distance of the foreground object can be estimated.

A direct cosmic distance ladder could be established by comparing objects at progressively greater distances: the amplitude correlations between wavefronts from a galactic maser or a pulsar and those of a radio galaxy could be used to probe galaxy-size distance scales. Also the distance of nearby extragalactic radio sources angularly close to powerful radio sources at cosmological distances could be potentially measured. In the case of the intensity interferometry, the signal intensities from many galactic stars could be observed against Large or Small Magellanic Clouds stars or some nearby extragalactic object to probe many galactic distances. The existence of wave curvature corrections has been recognized in precise VLBI time delays calculation within the Solar System (Kopeikin & Scäfen 1999 [80]). The novelty of the proposed approach consists in detecting this corrective term by interferometry, and then using it as a tool for distance and proper motion estimation.

### 6.4.2 Interferometric parallax scenario

Consider an array of two receivers, labeled 1 and 2, with vector coordinates $\mathbf{x}_1$ and $\mathbf{x}_2$ relative to a given origin. It will be convenient to represent the coordinates in terms of their separation $\mathbf{\Delta x}_{12} = \mathbf{x}_2 - \mathbf{x}_1$ and a center of mass vector $\mathbf{X}_{12} = (\mathbf{x}_1 + \mathbf{x}_2)/2$. Each receiver observes the signal from two unresolved objects located at a very small angular distance, but at very different distances to the Earth: the close object is the spacecraft, while the distant one is the radio source. The location of these two sources in the reference frame of the array receivers is parametrized by $\mathbf{r}$ and $\mathbf{r}'$ that represent the observer-source vector. If the pair is unresolved from the antenna, or a dipole antenna is used, each receiver responds to the total field $E = E_{spacecraft} + E_{radiosource}$. The correlation of a given frequency and polarization of electric fields measured in the receivers is denoted $< E(x_1)E^*(x_2) >$, and given by:

$$< E_1 E_2^* >= e^{-ik\psi}\left[\frac{I_S}{\mathbf{r}^2} + \frac{I'_S}{\mathbf{r}'^2}e^{-i\phi_{12}^{tot}}\right] \tag{6.5}$$

here $I_S$ and $I_{S'}$ parameterize emitted source intensities. The relative phase $\phi_{12}^{tot}$ between the two receivers contains information on the separation of the two sources. Let $\phi_{12}^0$ represents the *plane wave approximation* to the total phase caused by receivers-sources orientation. It is given by $\phi_{12}^0 = k\mathbf{\Delta x}_{12} \cdot (\hat{\mathbf{r}} - \hat{\mathbf{r}}')$, where $\hat{\mathbf{r}}, \hat{\mathbf{r}}'$ are the unit vectors pointing to the sources, located at vectors $\mathbf{r}$ and $\mathbf{r}'$, and $k$ is the wavenumber. This is the prediction of the standard VCZ theorem, and $\phi_{12}^0$ can be called the zeroth-order, or VCZ phase. Note that $\phi_{12}^0$ represents the geometric phase contribution between two elements of an array with the addition of the term $(\hat{\mathbf{r}} - \hat{\mathbf{r}}')$. This

last term parametrizes the angular separation of the pair and it does not appear in standard treatment usually referring to a single object observation. The difference with the standard phase usually assumed in radio astronomy is shown in Figure 6.12.

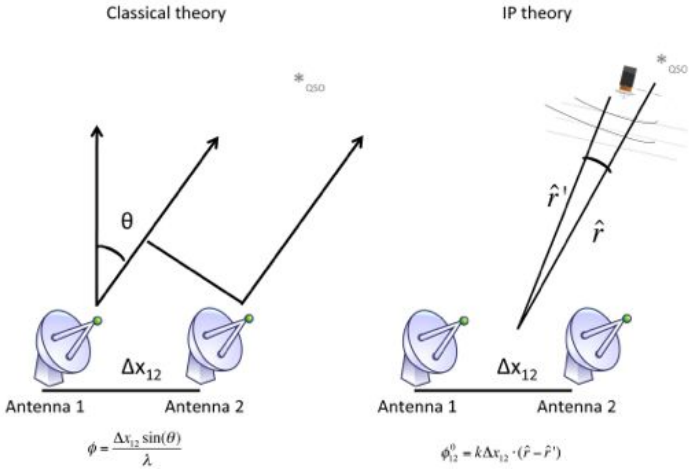


Figure 6.12: In the plane wave approximation the relative phase between two receivers depends on their separation in space (left). IP theory modifies the classical geometric phase $\phi$ to $\phi^0_{12}$ for including the angular separation of the sources pair. The plane wave approximation and the textbook $VCZ$ theorem do not take into account another phase, $\phi^{parallax}$, that depends on the positions of the receivers relative to the source over time.

The plane wave approximation treats sources as being at infinity. When the source is at finite distance, its wavefronts are curved. The curvature produces an additional phase shift, $\phi^{parallax}_{12}$, called *parallax phase*, from which $\phi^{tot}_{12} = \phi^0_{12} + \phi^{parallax}_{12}$, where:

$$\phi^{parallax}_{12} = -k\left(\frac{1}{r} - \frac{1}{r'}\right)\Delta\mathbf{x}_{12} \cdot \delta_T \cdot \mathbf{X}_{12} \tag{6.6}$$

Symbol $\delta_T \rightarrow \delta(r)^{ij}_T = \delta^{ij} - \hat{r}^i\hat{r}^j$ is a projector that removes the vector components parallel to $\hat{r}$, retaining components in the plane of the sky unchanged. The formula comes from the expansion of the phase differences to the next order of approximation, and re-computing the amplitude correlations of the electric field $E_i$ by means of the mathematical steps reported hereafter.

When dealing with a curved geometry of the wavefronts, the distance from the $J$th detector to the foreground source, which is the vector from the observer to the source, is expanded by equation 6.7 as shown in Figure 6.13:

$$r_J = r - \hat{\mathbf{r}} \cdot \mathbf{x_J} + \frac{1}{2r}x^i_J\delta^{ij}_T(r)x^i_J + O(1/r^2) \tag{6.7}$$

The second, non-null term is of the order $\sim 1/r$, i.e. the further away is the object the smaller is its curvature wavefront.

Let's consider the Green function for light propagation from source to detectors:

$$G_{x_J,r} = \frac{1}{4\pi}\frac{e^{ik|\mathbf{r}-\mathbf{x_J}|}}{|\mathbf{r}-\mathbf{x_J}|}e^{-ik\hat{\mathbf{r}}\cdot\mathbf{x_J}}exp(\frac{ik}{2r}\sum_{i,j=1}^{3}x^i_J\delta^{ij}_T x^i_J) \tag{6.8}$$

computing the the two-points amplitude correlations of the sum of the electric fields at the two receivers we get:

$$< (E+E')_1 \cdot (E+E')^*_2 >= E_1E^*_2 + E_1E'^*_2 + E'_1E^*_2 + E'_1E'^*_2 \tag{6.9}$$

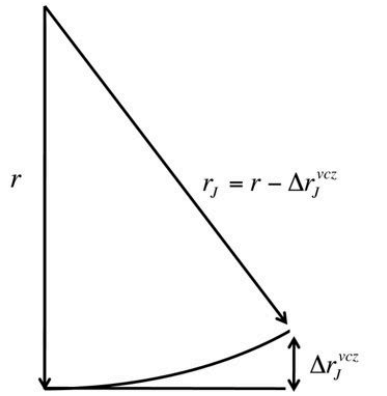


$$r_J = r - \hat{r}\cdot x_J + \underline{\frac{1}{2r}\sum_{i,j=1}^{3} x_J^i \delta_T^{ij}(r) x_J^j + O(1/r^2)}$$

Figure 6.13: The first term of the Taylor expansion accounts for curvature of the wavefront. The term underlined corresponds to $\Delta r_J^{VCZ}$.

the mixed terms $E_1 E_2'^*$ and $E_1' E_2^*$ are null because the two sources are completely uncorrelated one respect to the other and the pre-factors $\frac{e^{ikr}}{r}$, $\frac{e^{ikr'}}{r'}$ are dropped off because they cancel out in calculations. Using the Green function (eq. 6.8) to express the electric fields the correlation is:

$$\begin{aligned} < (E+E')_1 \cdot (E+E')_2^* > = & \frac{1}{16\pi^2 r^2} e^{-ik\hat{\mathbf{r}}(\mathbf{x_1}-\mathbf{x_2})} \cdot e^{\frac{ik}{2r}\delta_T^{ij}(x_1^i x_1^j - x_2^i x_2^j)} \\ & + \frac{1}{16\pi^2 r'^2} e^{-ik\hat{\mathbf{r}'}(\mathbf{x_1}-\mathbf{x_2})} \cdot e^{\frac{ik}{2r'}\delta_T^{ij}(x_1^i x_1^j - x_2^i x_2^j)} \end{aligned} \tag{6.10}$$

$$< (E+E')_1 \cdot (E+E')_2^* >= e^{-ik\psi}\left[\frac{I_S}{r^2} + \frac{I_S'}{r'^2} e^{-i\phi_{12}^0 - i\phi_{12}^{parallax}}\right] \tag{6.11}$$

which is exactly equation 6.5. The explicit mathematical expressions of the three phases engaged are:

$$\phi_{12}^0 = -k(\mathbf{x_1} - \mathbf{x_2}) \cdot (\hat{\mathbf{r}} - \hat{\mathbf{r}}')$$

$$\phi_{12}^{parallax} = k\left(x_1^i x_1^j - x_2^i x_2^j\right)\left(\frac{\delta_T(r)^{ij}}{2r} - \frac{\delta_T(r')^{ij}}{2r'}\right)$$

$$\psi = \hat{\mathbf{r}} \cdot (\mathbf{x}_1 - \mathbf{x}_2) - \sum_{i,j=1}^{3} (x_1^i x_1^j - x_2^i x_2^j)\delta_T^{ij}(\mathbf{r})/2r \tag{6.12}$$

This overall phase $\psi$ has not practical utility in the estimation of the source distance and it cancels when dealing with intensity correlations as depicted by equation 6.13:

$$< I_1 I_2 >= |E(\mathbf{x}_1)|^2 |E(\mathbf{x}_2)|^2 = \left(\frac{I_S}{r^2} + \frac{I_S'^2}{r'^2}\right)^2 + \frac{I_S^2}{r^4} + \frac{I_S'^2}{r'^4} + 2\frac{I_S}{r^2}\frac{I_S'}{r'^2}\cos\phi_{12}^{tot} \tag{6.13}$$

The approach of the IP method concentrates on the phase *changes* observable over the course of an experiment. For illustration the experiment baselines are pictured in Figure 6.14.

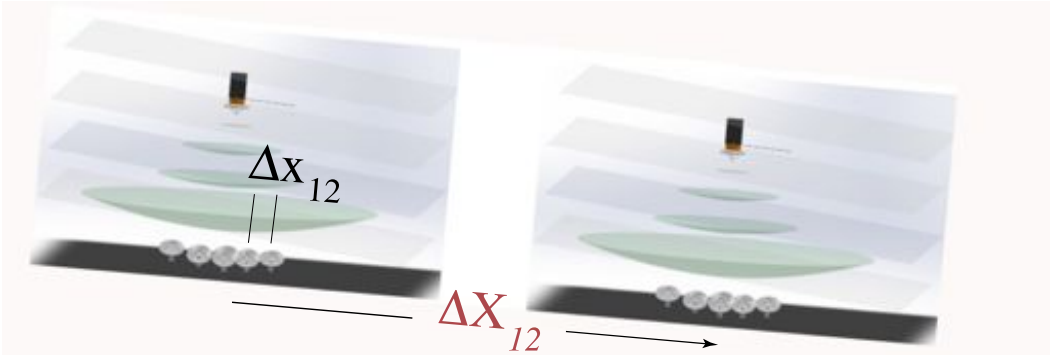


Figure 6.14: Interferometric parallax exploits two different baselines: a ground baseline $\Delta\mathbf{x}_{12}$ (that can be multiple) whose projection in the u-v plane is $\Delta x$, and an orbital baseline $\Delta\mathbf{X}_{12}$ (projection $\Delta X$) that originates from Earth revolution around the Sun.

### Translational Dependence

The dependence of the interference pattern on the array centre of mass position $\mathbf{X}_{12}$ is absent in the plane wave approximation: plane waves are unchanged by translations of the observer parallel to the wave plane. However, when the foreground source is at finite distance, its wavefronts are curved and the correlations depend on relative motion of array and source.

Following JR08, let's consider the case where the sources are fixed in space and the detectors are translating. The receivers are translated across wavefronts of the "fixed in space" distant sources with slightly different curvature. The translation vector $\mathbf{X}_{12}$ originates from the Earth revolution motion around the Sun, while the vector distance between the two receivers $\Delta\mathbf{x}_{12}$ changes its direction and modulus due to the Earth's rotation. After a net translation $\Delta\mathbf{X}_{12}$, (neglecting the Earth's rotation for this discussion), the relative phase between the two receivers will be:

$$\mathbf{X}_{12} \rightarrow \mathbf{X}_{12} + \Delta\mathbf{X}_{12}$$
$$\phi^0_{12} \rightarrow \phi^0_{12}$$
$$\phi^{parallax}_{12} \rightarrow \phi^{parallax}_{12} + \Delta\phi^{parallax}_{12}$$

The phase of the signal will contain a constant term namely $\phi^0_{12}$ and a linearly growing term proportional to the translation vector $\Delta\mathbf{X}_{12}$:

$$\Delta\phi^{parallax}_{12} = -k\left(\frac{1}{r} - \frac{1}{r'}\right)\Delta\mathbf{x}_{12}\cdot\delta_T\cdot\Delta\mathbf{X}_{12} \tag{6.14}$$

The greater the array baseline $\Delta\mathbf{x}_{12}$ and the translation vector $\Delta\mathbf{X}_{12}$, the larger the parallax phase, up to the point where series approximations used in the formula break down. [1] $\Delta\mathbf{X}_{12}$ can be regarded as a sort of *orbital baseline*. Assuming the distant source is effectively at infinity ($1/r' \rightarrow 0$), a measurement of the relative parallax phase leads to a direct determination of the distance of the closer object:

$$r \sim \frac{\Delta X \Delta x}{\Delta\phi^{parallax}_{12}\lambda} \tag{6.15}$$

The quantities $\Delta x$ and $\Delta X$ are the projection in the $u-v$ plane of the ground and orbital baselines $\Delta\mathbf{x}_{12}$ and $\Delta\mathbf{X}_{12}$ respectively. The latter are computed using planetary ephemerides and array geometry, the former by accurate simulations of the projected components. The phase difference $\Delta\phi^{parallax}_{12}$ is the observable to be retrieved by the experiment.

[1] The series expansions are always consistent whenever the parallax phase is small compared to the VCZ phase.

The $1/r$ dependence of the *parallax phase* is the same of the $1/d$ dependence of image offsets in classical trigonometric parallax measurements for which the parallactic angle $\pi$ is derived as:

$$\pi = \frac{1}{d} \tag{6.16}$$

with $d$ distance of the object under study. No image needs to be made in the case of IP, instead the method entirely relies on the direct measurement of the parallax phase using interferometry. There is however an important and conceptual difference between trigonometric parallax (TP) and IP. With TP an object is observed at two points $(x, t)$ (January), $(x', t)$ (July) on the opposite sides of the Earth orbit. At point $(x, t)$, assuming waves are plane, the wave normal is constructed. The source is assigned to be at infinity along the line of the normal. At point $(x', t)$, with the same assumptions, the source is along a different line. Where these lines intersect is the point TP assigns to the source location (see Figure 6.15). Thus TP is based on resolving a contradiction of its own assumptions. Its logic needs to backtrack and to assert waves from the source are spherical, hence oriented with different normals at $(x, t)$, $(x', t)$.

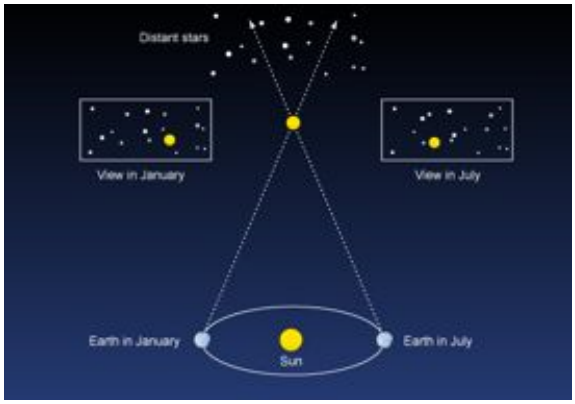


Figure 6.15: Classical trigonometric parallax depends on the apparent motion of nearby stars compared to more distant stars, using observations made six months apart. No explicit effects of wavefronts curvature are considered.

To measure the parallactic angle $\pi$ high-quality images must be available and the centroid shift of the target source between the two or multiple images has to be accurately measured. For this reason TP is inherently limited by the image resolution and quality i.e. by the angular resolution from the optics. Using the ground-based highest resolving system, i.e. VLBI, with terrestrial baselines ($\sim 10^4$ km) at the highest frequency achievable (∼22.2 GHz), the smallest parallactic angle that can be measured is about $\pi \sim 0.3$ mas that corresponds to a distance of about 3 kilo-parsec (kpc). As mentioned above GAIA is expected to reach the ∼10-100 kpc scale [30]. These rough estimates show how TP is limited to the nearby galactic neighborhood. Although TP performs the same measurement with a six-months interval to maximize the source apparent motion, the observation is limited at each epoch by the system angular resolution $\sim \frac{\lambda}{B}$, with $B$ corresponding to the VLBI or space baseline (in the case of a space telescope). In the process of imaging, the information on the wavefront curvature is completely lost. IP conversely exploits directly the translational motion of the Earth to detect a phase signal related to the wavefront curvature. As shown in equation 6.15 the dependence of the parallax phase on the orbital translation $\Delta X$ is explicit. Taking into account the translation dependence of the array even far away objects can accumulate a detectable phase because $\Delta X \sim 15\,000 \Delta x$, assuming $\Delta x$ = 1e4 km. If the instruments actually measure the curvature phase by changes in correlations at $(x, t)$ and $(x', t')$, then more information is achieved by including IP.

Pictures 6.16 help the reader understanding: consider random fluctuations from two sources A and B passing the receivers (Figure 6.16a). The timing of fluctuations from A depends on the

orientation of the source, and the detector separation and orientation. The timing is different for flat versus curved wavefronts (dashed orange wavefront vs solid orange one). Meanwhile the source at infinity B effectively provides a phase standard described with flat wavefronts. The observable phase difference in the correlation with $1/r$ dependence is isolated in $\phi^{parallax}$. As the graphics indicates, $\phi^{parallax}$ depends not only on the separation $\Delta\mathbf{x}_{12}$ at the single epoch but on how the whole array is embedded and then translated in the wave field, parameterized by $x - x'$ which corresponds to $\Delta\mathbf{X}_{12}$. The plane wave approximation ($\phi_{12}^{parallax} = 0$) conversely gives an expression for the fields correlation, which is the time domain representation of $\phi_{12}^{0}$:

$$c(t - t') \sim |x - x'| sin(\theta) \tag{6.17}$$

as can be observed from the geometry reported in Figure 6.16b. Equation 6.17 is identical to the Bragg's law which gives the angles for coherent and incoherent scattering of X ray from a crystal lattice. When curvature effects are considered, the correlations observed are slightly modified.

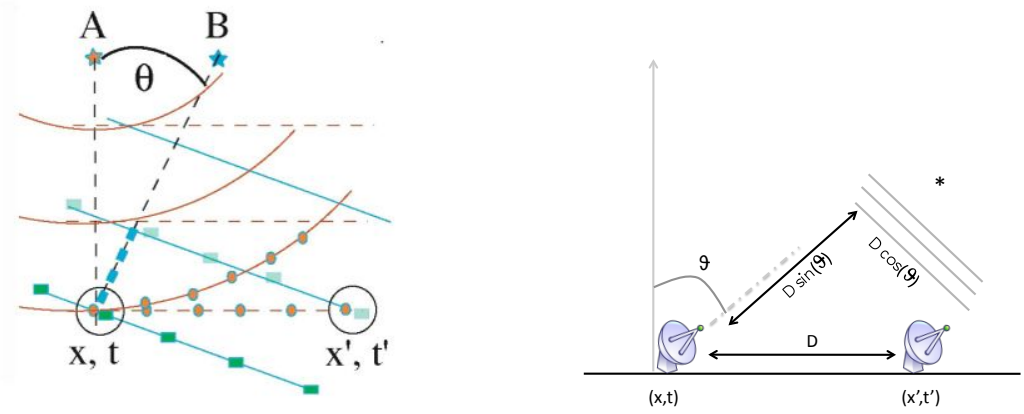


(a) (b)

Figure 6.16: (a) Independent fluctuations (beads or boxes) from sources A and B are observed at (x ,t) and (x',t'). The plane wave approximation (dashed wavefronts) predicts slightly different correlations compared to including the effects of wave curvature. Phase effects from curvature are described by $\phi_{12}^{parallax}(\Delta\mathbf{X}_{12})$ which depends on the translated vector $\Delta\mathbf{X}_{12}$. Image from JR08. (b) Assuming a plane wave approximation the geometry in Figure 6.16a degenerates to the time domain representation of $\phi_{12}^{0}$.

### Advantages and requirements of the interferometric parallax

To summarize, the interferometric parallax method requires i) measuring the correlations from two angularly close sources with two or more receivers, then ii) repeating the measurement after the array is translated, and finally iii) extracting a relative phase by cross-correlating the two observations from different epochs. The relative magnitude of the parallax effect is very small in most cosmological circumstances, but measurable at least to 100 kpc as shown in the following. The main complication comes from the size of the VCZ phase $\phi_{12}^{0}$ compared to parallax phase $\phi_{12}^{parallax}$. From Eqs. 6.18 and 6.19 the order of magnitudes are

$$\phi_{12}^{0} \sim 10^{4}\text{rad} \left(\frac{\Delta\theta}{\text{arcsec}}\right) \left(\frac{1\text{cm}}{\lambda}\right) \left(\frac{\Delta x_{12}}{10^{4}\text{km}}\right) \tag{6.18}$$

$$\phi_{12}^{parallax} \sim 10^{-1}\text{rad} \left(\frac{\Delta X_{12}}{\text{AU}}\right) \left(\frac{100\text{kpc}}{r}\right) \left(\frac{1\text{cm}}{\lambda}\right) \left(\frac{\Delta x_{12}}{10^{4}\text{km}}\right) \tag{6.19}$$

The second equation shows that $\phi_{12}^{parallax}$ is not itself intrinsically small for the parameters used: it is simply small compared to the other phase. At radio frequencies (e.g. $\lambda = 1$ cm) and using $\Delta X_{12} \sim$ AU the ratio of the two phase terms is about $10^{-5}$ for sources separated by arc-second values at distances $r \sim 100$ kpc. The fact that, at 1 cm wavelength, $\phi_{12}^{parallax} \sim 1$ rad (Fig. 6.17a) indicates that measurements out to that distance and even beyond are at least in principle possible with existing technology. The relative size of the parallax term is maximized by pushing the translated vector $\Delta\mathbf{X}_{12}$ toward $\sim 1$ AU (Fig. 6.17b) and by selecting a very close pair of objects (minimizing $\Delta\theta$).

The above considerations point to some cons and pros of IP compared to TP and other methods:

- IP does not require high pointing accuracy.
- IP does require high precision of array baseline alignments and coordinates positioning of the baselines in space.
- When using IP the signal phases are measured by interferometry. The amplitude correlations, however, are sensitive to the atmospheric/ionospheric disturbances that may be a limiting factor for observations with km-scale arrays. Another approach considers observing *intensity correlations* that are much less sensitive to atmospheric perturbations and cancel also the overall phase $\psi$.
- $\phi_{12}^{0} >> \phi_{12}^{parallax}$; consecutive observations must be carried out under the same ground baseline $\Delta x$ to limit the error on the distance measurement. There is in addition a technique using multiple baseline correlations with two or more different baselines to completely cancel the $\phi_{ij}^{0}$ term as discussed in JR08.
- IP is not limited by the aperture theorems that limit image resolution. Conversely image-making is relatively inefficient for getting distances. The TP method, neglecting the curvature effects, is limited by the image resolution at each observation $\sim \lambda/\Delta x$, conversely IP can get a better resolution $\sim \lambda/(\Delta x \Delta X)$ exploiting two epochs observation and accounting for curvature effects. While it's impossible to measure the TP of an unresolved pair (foreground + background object), the IP method does not require to resolve the pair for measuring the distance of the target.
- IP suffers the same limitation of the trigonometric parallax of having distance and proper motion *entangled* inside the same phase.
- IP is different from the *differential VLBI* that was used to accurately tie the lunar and spacecraft orbit to the nearly inertial quasar reference frame (Ichikawa 2003 [64] and Slade et al. 1977 [120]), which requires that single antennas at each end of the baseline move back and forth simultaneously between the two celestial sources to determine a differential phase. IP observes the sum of the fields from reference and target at each receiver, because by working with an overall signal, IP does not require to resolve the pair under study.
- IP bears some similarities with the technique of the radio pulsar timing, where the curvature of the wavefront as it reaches the Solar System causes measurable displacements in the pulse timing, along different positions of the Earth in its orbit around the Sun (Kuz'min & Kuz'min 1988 [85]). This *timing parallax* has being discussed in various pulsar timing schemes, e.g. by Smits et al. 2011 [121], including also error estimates for various types of observations. The pulsar timing technique relies on the pulsar objects family and exploit the periodicity of their signals features, while IP makes use of a background reference object and its applicability is generalized to any class of objects.

The considerations presented in these sections lead to establish a new method for estimating the geometric distances of the celestial bodies. One important aspect of IP is that the distance derived is *geometric*. Most of the methods commonly used in the definition of the cosmic distance ladder are indirect and based on intrinsic properties and some assumptions (luminosity, periodicity, etc.) of certain sources. These methods are subjected to uncertainties coming mainly from absorption effects (e.g. the Supernovae method) and the cosmology model assumed, as in the case of the distance luminosity and distance angular diameter. In a heuristic view the IP method resembles a sort of *multi-epoch interferometer*: while the VLBI system makes interfering simultaneous signals observed at different locations of the Earth to create large, high-resolving array, IP correlates signals at different epochs observed under a the same ground baseline $\Delta x$. A single observation carried out with a baseline $\Delta x$ at the epoch $t_1$ provides a first virtual telescope of resolution $\sim \lambda/\Delta x$, then the second observation at $t_2$ provides an analogue condition, and finally the correlation signals from the first epoch are cross-correlated with those from the second epoch leading to a resolution $\sim \lambda/(\Delta x \Delta X)$. It is important to note that the phases involved in the IP measurement, geometric $\phi_{12}^0$ and parallax $\phi_{12}^{parallax}$, refer always to the receivers and never to the sources; sources can undergo phases stochastic oscillations over time, what matters is the phase of one receiver with respect to the other.
Since ground-based observatories are bounded to a rotating reference frame (the Earth) the condition of equality of the projected ground baselines at the two epochs of observation $\Delta x(t_1) = \Delta x(t_2)$ is non-trivial to obtain. The vector baselines will be aligned after a sidereal day and will have different orientations but the same modulus for points specularly symmetric with respect to the culmination of a source in sky. Requiring the equality of the projected ground-baselines in fact, is equivalent to impose that the optical path difference $\phi = \Delta x_{12} \sin\theta/\lambda$ (left of Figure 6.12) is the same at the two epochs.
This requirement, being satisfied only for a small time-interval, would limit the method applicability only to the brightest sources that can be observed over short time-scales. The problem is overcome by adding to our primitive array of two receivers an adjustable time delay unit that compensates the optical path differences among the antennas like is routinely done in the modern radio telescopes arrays. The correlator treats all the source as being at infinity and it removes the geometric phase $\phi_{12}^0$ while completely ignoring the parallax phase $\phi_{12}^{parallax}$ induced by the curvature of the wavefront. Any contingent, relative phase shift induced by the electronics of the correlator or by an atmospheric perturbation leads to a systematic or stochastic error in the parallax phase estimation that is an intrinsically tiny effect. This is however the same limit suffered by standard radio observations that are corrected by the observation of a point-like calibrator with zero intrinsic phase. The antennas observe this calibrator simultaneously and derive a relative phase to be subtracted before the correlation. IP should follow this scheme when performed at radio wavelengths.

## 6.5 Towards new distance scales with the future large telescopes

As discussed in the previous paragraph, in the standard radio observations the atmosphere introduces phase variations among different antennas of the array and the problem is particularly important with VLBI system where the antennas observe through completely different layers of atmosphere. Although calibration techniques actually exist, when dealing with large distances ($\geq 100$ kpc) the parallax phase becomes progressively smaller and the atmosphere phase perturbations can prevail on IP effect. Two plots in Figure 6.17 provide to the reader some orders of magnitude of the problem for a VLBI ground baseline ($\Delta \sim 10^4$ km) and a pair separation $\Delta\theta =$ 30 arcsec. If target distances in the order of 100 kpc are not prohibited in principle, Mpc scales are likely prevented from the atmospheric disturbances.

This distance limit could be overcome by moving from amplitude to *intensity interferome-*

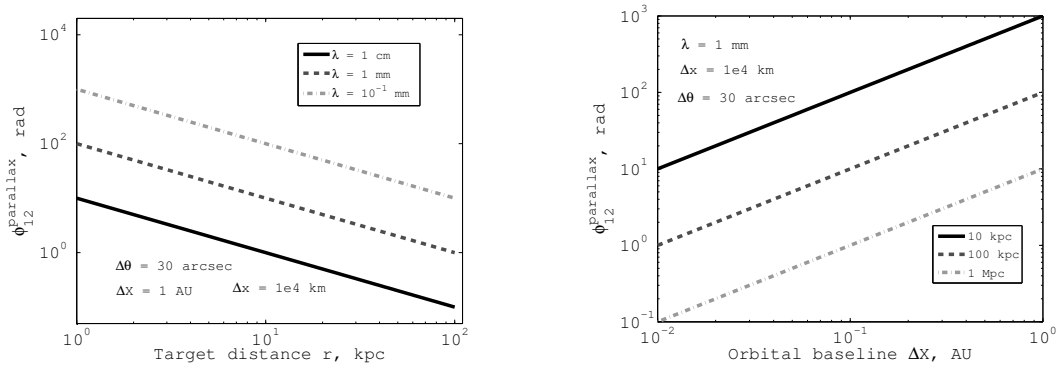


(a) (b)

Figure 6.17: (a) The interferometric parallax phase $\phi_{12}^{parallax}$ is inversely proportional to the target distance. Both $\phi_{12}^{parallax}$ and $\phi_{12}^{0}$ increase for progressively smaller wavelengths. (Logarithmic scale). (b) Interferometric parallax phase $\phi_{12}^{parallax}$ estimation for different target objet distances for a wavelength $\lambda = 1$ mm. The parameter space below the 10 kpc line has never been probed through direct distance estimation methods. (Logarithmic scale). Both the plot have been obtained assuming a pair separation $\Delta\theta = 30$ arcsec and a ground baseline $\Delta x =$ 1e4 km.

*try*. Intensity interferometry (II) is almost completely insensitive to atmospheric turbulence and scintillation [36]. As discussed in section 6.3, the next generation of IACTs will provide huge collecting areas that will make competitive II with respect to amplitude interferometry. The robustness of II technique with respect to optics defects and misalignments opens also the perspective to kilometer-scale interferometry at optical wavelengths that is extremely challenging with amplitude interferometers. Cherenkov telescope have large PSFs, between 5-10 arcmin, and an array of Cherenkov telescopes connected as an intensity interferometer behaves similarly to a radio telescopes array. The large PSF size, comparable to radio telescopes, fulfills the requirement of observing an unresolved pair of objects for considering the overall electric field from it (section 6.4.2). The tolerable phasing errors of II ($\sim$0.3 m for time resolution of $\sim$ 1 ns) make feasible the realization of a km-scale array at optical wavelengths that has comparable angular resolution with the VLBI system at radio frequencies. As shown in Figure 6.18, working with a ground baseline $\Delta x = 1$ km at $\lambda = 0.4$-$0.5$ $\mu$m is equivalent of working with a VLBI baseline $\Delta x$ = 1e4 km at $\lambda = 1$ cm. The advantage of moving to the II domain is the absence of atmospheric perturbations and the relaxed requirements on telescopes phasing that make the 100 kpc scale fully achievable and the Mpc-scale less challenging to reach.

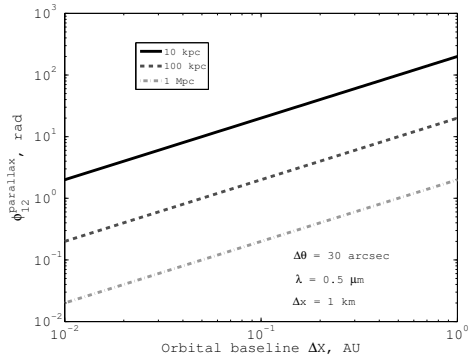


Figure 6.18: Interferometric parallax phase $\phi_{12}^{parallax}$ estimation for different target objet distances for a wavelength $\lambda = 0.5$ $\mu$m. The ground baseline assumed for intensity interferometry is $\Delta x = 1$ km and a pair separation $\Delta\theta = 30$ arcsec (Logarithmic scale). Changing the wavelength from radio to optical $\lambda_{radio}/\lambda_{optical} \sim 10^4$ balances the change in the ground baselines $\Delta x_{VLBI}/\Delta x_{II} \sim 10^4$, leading to achieve about the same target distance.

An important limitation of II is the SNR that disfavors this technique with respect to amplitude interferometry: comparing equations 6.5 and 6.13, one realizes that the sources intensity is reduced by a factor $1/r^2$ for amplitude correlations and a factor $1/r^4$ for intensity correlations. As shown in Figure 6.19a, a pair Large Sized Telescopes (LST) of CTA should reach a limiting magnitude in B band $m_B \sim$ 10-11 for 10 hours of observation under optimal observing conditions. This limit could be lowered by adding more telescopes to the interferometer or more channels per telescope as discussed in section 6.3. Assuming $m_B \sim$ 10-11 as likely limiting magnitude for the faintest detectable sources (SNR $\sim$ 5) many objects could be the target for IP measurements. Inside the Milky Way, at optical wavelengths, the distance of many galactic stars could be estimated against a background of Magellanic Cloud stars or outer extragalactic objects. Exiting the Local Group the optical emission from the unresolved Narrow Line Region (NLR) and accretion disks of a bright Seyfert I or other peculiar galaxies should be detectable out to Mpc scale (see Figure 6.19a) providing a good background source for a class of foreground objects of interest. Also the supernovae, even if transient events, could be interesting point-like sources to be investigated thanks to their high luminosity. As shown in Figure 6.19b, assuming a median absolute magnitude during the first month around the maximum $M_B \sim$ -17, these objects should be readily detectable out to the Mpc-scale (see Figure 6.19c). At radio wavelengths, the distance of pulsars and masers could be measured against a background of extragalactic objects, or a nearby extragalactic radio source could be measured against a powerful radio source at cosmological distances.

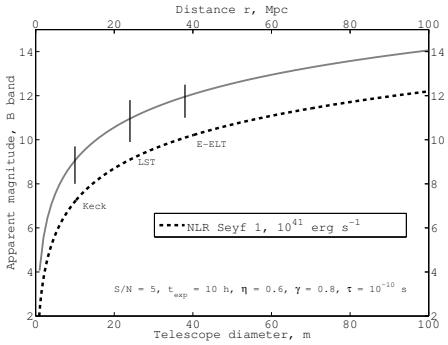


(a)

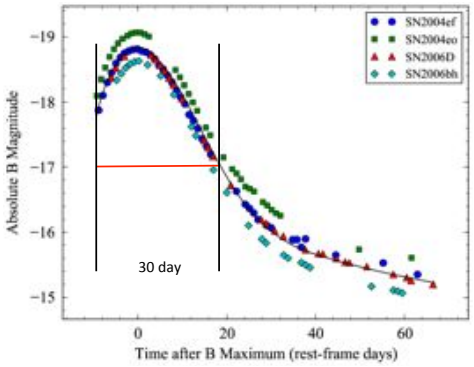


(b)

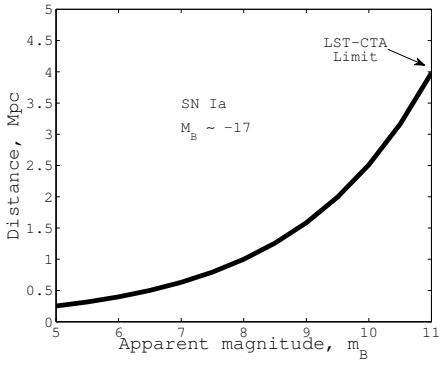


(c)

Figure 6.19: (a) Simulation of the expected apparent magnitude (around $H_\beta$ line) from the core of NLR Seyfert I galaxies at different distances; bright objects of this type should be observable with CTA II out to distances of tens of Mpc. (b) Light curve for a sample of Supernovae Ia (SN Ia), the peak of luminosity 10 days before and 20 days after the explosion represents a suitable interval of observation. Image from Burns et al. 2011 [20]. (c) Expected apparent magnitude in B band for a SN Ia for increasing distances, these objects should be detectable with CTA II until about 4 Mpc is an average absolute magnitude $M_B \sim$-17 is assumed.

Independently on the wavelength, an intriguing scenario derives from possibility to measure the distance of some bright sources outside the Local Group. Exiting this ensemble of galaxies to which the Milky Way belongs, objects motion are mainly driven by the Hubble flow and the relative velocity is usually expressed with respect to a cosmic reference frame given by the CMB radiation field. Observations of the CMB dipole by Planck has confirmed that the Earth is moving at about 369±0.9 km/s toward a point between the constellations of Crater and Leo [119]. The velocity with respect to the CMB reference frame originates an *extra* orbital baseline is about ten times larger than the orbital motion of the Earth around the Sun, $v_{CMB} \sim 10 \times v_{\odot\oplus}$ and it provides an important boosting of the orbital baseline (eq. 6.20).

$$r \sim \frac{10 \cdot \Delta X \Delta x}{\Delta \phi_{12}^{parallax} \lambda} \tag{6.20}$$

As shown in Figure 6.20a the CMB dipole map divides the sky roughly in two portions: the regions aligned with the direction of the CMB dipole ($\vec{\beta}_{\parallel}$), for which the extra orbital baseline projection is minimum and the regions orthogonal to the dipole ($\vec{\beta}_{\perp}$) that 'see' the maximum baseline projection. Figure 6.20b shows the relative transverse velocity in km/s due to the motion with respect to the CMB reference frame: the two regions aligned with the CMB dipole have null velocity i.e. no extra orbital baseline is produced in this direction by Earth motion with respect to the cosmic reference frame and the unique contribution comes from the motion around the Sun.

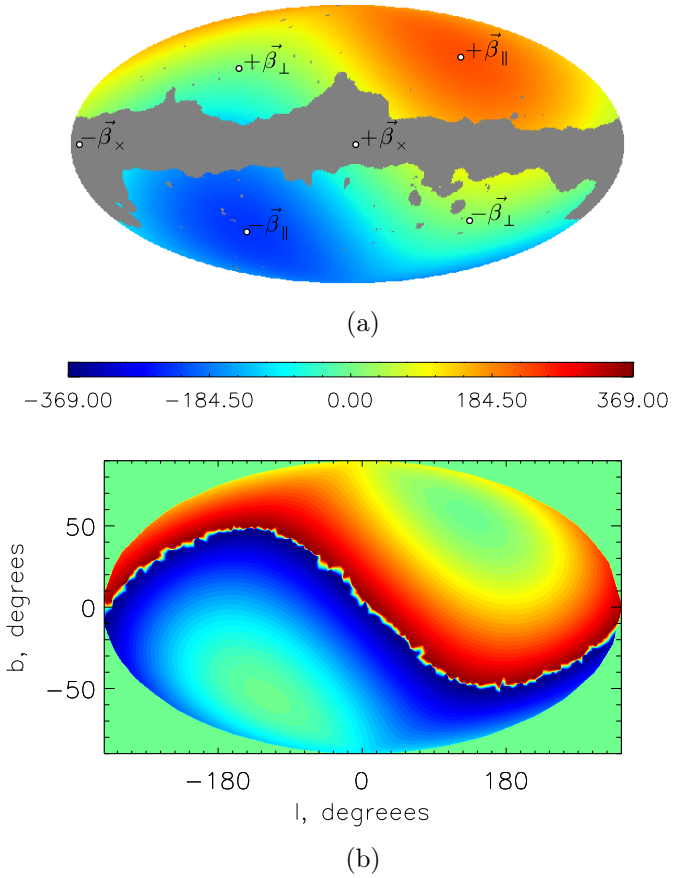


Figure 6.20: (a) CMB dipole map measured by Planck [119]; the grey area is the shaded region of galactic emission. The map put on evidence two different regions, one roughly aligned with the CMB dipole $\vec{\beta}_{\parallel}$, and the other orthogonal to it, $\vec{\beta}_{\perp}$. (b) Relative transverse velocity in km/s of the observer due to its motion with respect to the CMB reference frame: the regions perpendicular to the CMB dipole maximize the extra orbital baseline.

The orthogonal regions ($\vec{\beta_\perp}$), conversely see an increasing transverse velocity that is the composition of the orbiting around the Sun and the motion with respect to the CMB dipole that enlarges significantly the orbital baseline until a maximum level of about $10\Delta X$. For the sources belonging to these latter regions the rate of accumulation of the parallax phase for a given distance is higher and the probe of the wavefront curvature is maximized. Supernovae phenomenology could be too short to be observed at large distances by means of a six-months interval, but they could produce fairly detectable parallax phases if they would belong to such CMB orthogonal sky regions ($\vec{\beta_\perp}$).

A possible pathfinder experiment to assess the reliability and the limits of the IP method is described in the next paragraphs.

## 6.6 A pathfinder experiment for IP verification

As a pathfinder experiment for IP verification we seek to measure the distance of an object orbiting the Solar System and producing a fairly detectable IP effect over a short time period. Given the fact that II with CTA is not yet available, an IP experiment can be carried out only at radio wavelengths using the current radio telescopes array. The test case described here exploits amplitude correlations of signals from deep space interplanetary spacecraft in conjunction with distant galactic and extragalactic radio sources (Fig. 6.21). The target bodies envisaged for this pilot experiment are Cassini, Juno, Dawn and New Horizons spacecraft. VLBA astrometric observations of the Cassini spacecraft were carried out by Jones et al. 2011 [73] to improve the Saturn planetary ephemerides. The Cassini spacecraft was used as a bright artificial radio source and its precise astrometry was retrieved. The spacecraft should be observed during signal emission with a similar approach that includes significant new features, to estimate the average distance and proper motion coordinates of the spacecraft at some suitable times when we can conveniently extract the parallax phase.

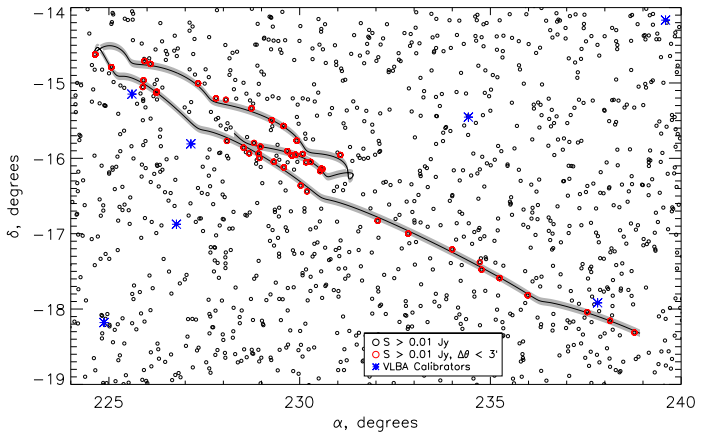


Figure 6.21: The Cassini epicyclic trajectory over the second semester of 2014 calculated by the NASA Horizons System powered by JPL as seen from a mid latitude Earth site. The field of view in X band of a 25m antenna ($\sim 6'$) is represented by the shaded area around the Cassini orbit. The NVSS sources above an $F = 0.01Jy$ are represented by the grey circles. NVSS sources angularly close to Cassini and well-suited for the interferometric parallax measurement are represented by red crosses. The blue asterisks represent the calibrators (F > 200 mJy) from the VLBA Calibrators List provided by NRAO for phase referencing available in the field.

The method requires a source in the near space (the spacecraft) and a very distant astronomical source (the background radio source). Figure 6.21 shows the orbit of Cassini projected on the sky plane along with a number of background radio sources for the second semester of 2014. The simulation can be easily extended to any epoch of interest. There are many near conjunctions of Cassini with the radio sources in the NRAO VLA Sky Survey [26]. These radio sources are our target sources for reference objects in the interferometric parallax measurement. As we will show, each radio source provides an independent opportunity for direct determination of distance from the receiving system to the spacecraft. The Cassini spacecraft is assumed as example candidate, but the method is applicable to all the other spacecraft mentioned above.

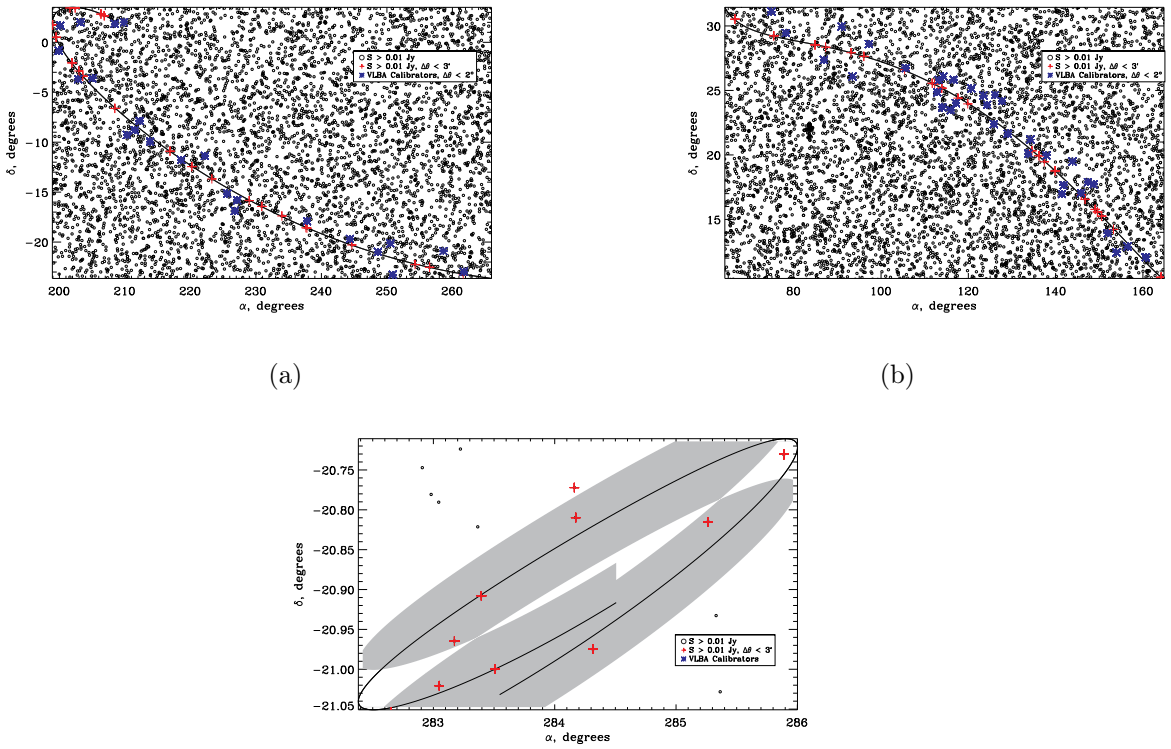


Figure 6.22: (a) Dawn, (b) Juno and (c) New Horizons spacecraft orbits as seen from a mid-latitude terrestrial site over the year 2014. he NVSS sources above $F = 0.01Jy$ are represented by the grey circles. NVSS sources angularly close to Cassini and well-suited for the interferometric parallax measurement are represented by red circles. The blue asterisks represent the calibrators (F > 200 mJy) from the VLBA Calibrators List provided by NRAO for phase referencing available in the field.

### 6.6.1 Why a spacecraft is ideal

An ideal test-system for observing the IP effect should have the following basic requirements:

- A system with a high signal to noise ratio (SNR);
- A system where the distance to the source is well known;
- A system with a clearly detectable parallax phase;
- A system that behaves like a point-like source;

- An angularly close pair of objects.

The observation of a spacecraft in conjunction with a distant radio source is an ideal test bench for a verification of the IP capabilities. The distance of the spacecraft can indeed be determined with a high level of precision using precise ephemerides and light travel time between the spacecraft and Earth stations, providing an accurate term of comparison for the assessment of the IP output. In addition, observing an object inside the Solar System maximizes the relative size of the parallax phase: the median rate of accumulation with time of the parallax phase (based on Eq. 6.19) during the conjunctions of interest is $d\phi^{parallax}/dt \sim 0.15$, 0.05, 0.67 and 0.06°/min for Cassini, Juno, Dawn and New Horizons respectively. Both the background source and the target should be point-like sources to the interferometer to guarantee a reliable phase estimation of both the components avoiding additional phases coming from resolved objects. Moreover as discussed in section 6.2, the sources project a coherence area, as illustrated in Figure 6.23b, which depends on their apparent angular diameter; the smaller the apparent angular diameter of the source the larger is the projected area.

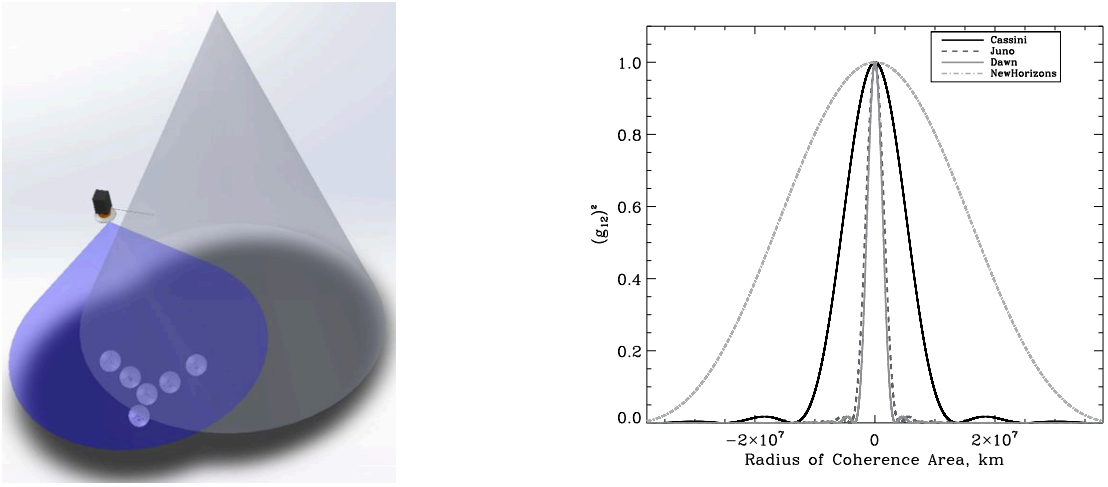


(a) (b)

Figure 6.23: (a) Graphical representation of the coherence zones projected from the spacecraft and the background radio source. (b) The spacecraft antenna produces a zone of coherence approximately determined by a first order Bessel function. An analogous pattern is associated with the background radio source. Symbol $(g_{12})^2$ is the square of the spatial degree of coherence.

The amplitude correlations between two detectors are significant only if both are inside the area of coherence. The 4 meters Cassini antenna seen by an Earth observer at about 10 AU subtends an angle $\theta \sim 5.5 \cdot 10^{-7}$ arcsec. Using the transmitted wavelength $\lambda = 0.036$ m (X-band) the coherence area of Cassini has a mean diameter of about $D \sim 2.6 \times 10^7$ km. Given a quasar for the background radio source with a core physical size of order 1 AU, implies an angular extent $\theta_q \sim 10^{-9}$ arcsec. That translates to an area of coherence of comparable size $D_q \sim 2 \times 10^6$ km. An attractive possibility of IP detection comes from the modern, kilometer–scale array of radio telescope. For the current scenario, a compact configuration with km-scale baseline $\Delta x_{12}$ is blind to the effects of curvature of the spacecraft wavefront within a single measurement (Fig. 6.24a). This could be no longer true for large baselines of VLBI over which the effects of wavefronts curvature are expected to manifest with decorrelation effects already in a single observation (Fig. 6.24b).

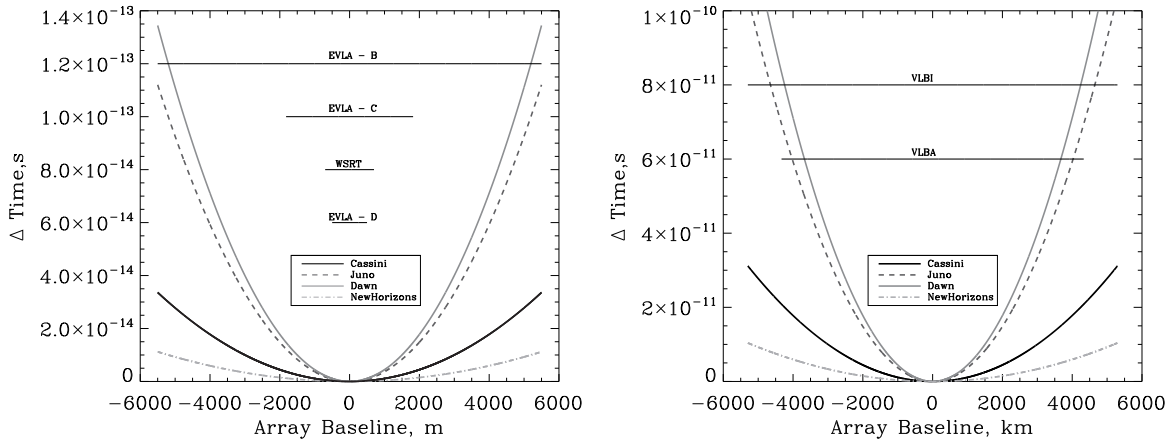


(a) (b)

Figure 6.24: (a) Expanded very large array (EVLA) configurations and the Westerbork array (WSRT) at $\lambda = 3.6$ cm cannot resolve the curvature of the wavefront emitted by the spacecraft with a single measurement assuming a receiver clock of $10^{-12}$s. (b) With VLBA and VLBI observations at the largest baselines at $\lambda = 3.6$ cm, the effects of wavefront curvature arise already within a single measurement. Observations with these large facilities are preferred for extra Solar System objects.

### 6.6.2 Simulations and estimates

In the following we present the results of the simulations we implemented to determine the possible outcome of the experiment. The average values of the parameters of the simulated observation are summarized in Table 6.1.

| **Parameter** | **Symbol** | **Value** |
|---|---|---|
| **Array Baseline** | $\Delta x_{12}$ | 1 km |
| **Orbital Baseline** | $\Delta X_{12}$ | $\sim 10^5$ km |
| **Cassini distance** | $r$ | $\sim$10 AU |
| **Wavelength** | $\lambda$ (X band) | 3.6 cm |

Table 6.1: Average parameters over the course of the simulation with the Cassini spacecraft.

The simulation uses a reference frame with the Sun at origin, the z-axis perpendicular to ecliptic plane and the x-axis along the perihelion point of the Earth. The calculation takes into account spacecraft proper motion. $\phi_{12}^{parallax}$ and $\phi_{12}^{0}$ have different behaviour and dependence on the pair angular separation and the orbital baseline as shown in Figures 6.25a and 6.25b.
$\phi_{12}^{0}$ *increases* with angular separation while remains *constant* with the baseline $\Delta X_{12}$, $\phi^{parallax}$ has exactly the opposite behaviour. The orientation effects of the unit vector $\hat{\Delta} x_{12}$ relative to the sources and the unit vector $\hat{X}_{12}$ are not shown. Generally $\Delta\phi^0 >> \Delta\phi^{parallax}$. Yet $\Delta\phi^0$ will go to zero when the receiver pair separation rotates through the plane perpendicular to the sources, while $\Delta\phi^{parallax}$ reaches a maximum, all other things fixed.

### 6.6.3 Ideal vs real receivers

A basic and simple signature of the interferometric parallax comes from the time dependence of 2-point correlations. In general we expect a time sequence characterized by a small contribution due to the parallax phase (which grows relatively slowly with $\Delta X_{12}$), and a dominant contribution coming from faster varying overall and VCZ phases. The equation:

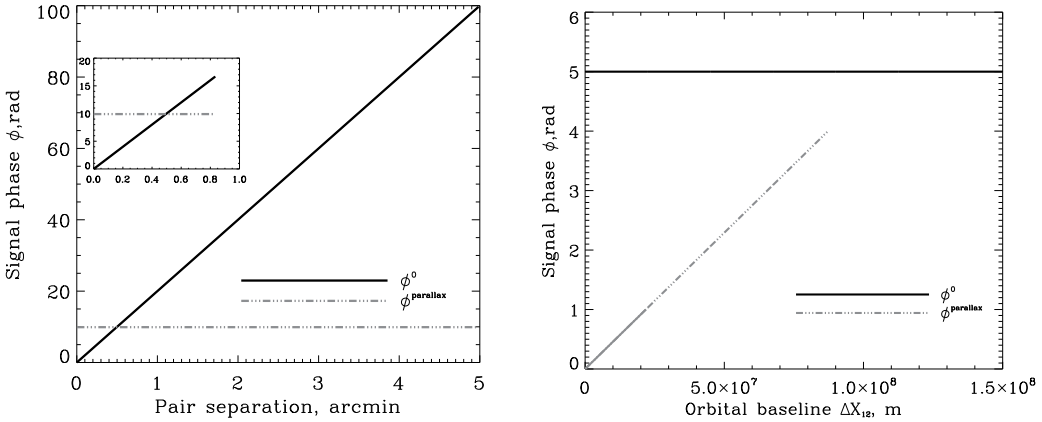


(a) (b)

Figure 6.25: (a) $\phi_{12}^0$ is linearly proportional to the pair angular separation, hence smaller for pairs that are closer. $\phi_{12}^{parallax}$ does not depend on the angular separation. Calculation based on Table 6.1. (b) $\phi_{12}^{parallax}$ (grey) is linearly proportional to the orbital baseline $\Delta X_{12}$. $\phi_{12}^0$ does not depend on the orbital baseline. The solid part of the grey line represents the linear behavior of $\phi_{12}^{parallax}$ and the dashed extension is a linear extrapolation for purposes of illustration. Calculation based on Table 6.1.

$$< E_1 E_2^* >= I_s \Lambda_s cos(\psi) + I'_s \Lambda'_s cos(\psi + \phi_{12}^{tot}) \tag{6.21}$$

represents the cross-correlation of the signals from two receiving systems at a single epoch. This quantity is the cross-correlation output from two *ideal* receivers, noiseless and with null integration time. We assume that the intensity of the spacecraft signal is $I_s\Lambda_s = 10$ and the background radio source is $I'_s\Lambda'_s = 1$. Two techniques can lead to detect IP phase signature in the signal pattern: cross-correlation of the signals and matched-filter correlations. In the direct cross-correlation the signal from the first receiver is retrieved and cross-correlated with that coming from the second one; the observation is repeated after a given time. The signal pattern from the two epochs is cross-correlated and a relative phase inversely proportional to the object distance is extracted. Other indications of IP in the signal could be retrieved by using the matched filters that find the correlations between a given function (the template function described by Eq 6.21) and the measured signal pattern. Matched filter techniques have known dependence on additive stochastic noise. However, when dealing with real receivers all the signals are convolved, filtered and averaged in time. The output of a correlator of a radio interferometer is called *fringe function*. In a two-element interferometer, the fringe function varies proportionally to $\nu\tau_g$, where $\tau_g = (\Delta x_{12}/c)\sin(\theta)$, is the geometric time delay between the two antennae depending on the zenith angle $\theta$ of the pair. As the Earth rotates the most rapid rate of variation of $\theta$ is equal to the Earth's rotational velocity $\omega_\oplus \sim 10^{-4}$ rad/ s$^{-1}$. The rate of variation of $\nu\tau_g$ is about $10^6$ smaller than $\nu t$, and the most rapid varying terms are filtered out by the correlator. For this reason the fast time-varying overall phase $\psi$ cannot be tracked by the correlator. The slow time-varying phases $\Delta\phi_{12}$ and $\Delta\phi_{12}^{parallax}$ conversely contribute to the fringe function. The ordinary fringe function, standard output of an interferometer multiplier:

$$F = 2\sin(2\pi\nu t)\cdot\sin 2\pi\nu(t-\tau_g)$$

can be modified to include the parallax term as follows:

$$F = 2\sin(2\pi\nu t)\cdot\sin 2\pi\nu(t-\tau_g-\tau_{parallax}) \sim \cos 2\pi\nu(\tau_g+\tau_{parallax}) \tag{6.22}$$

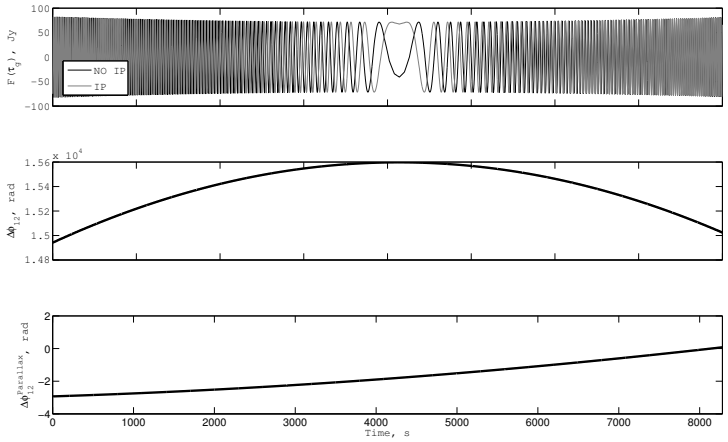


Figure 6.26: Phases simulation for Cassini spacecraft culmination 28 Aug 2014. **Top**: Fringe washing function $F(\tau_g)$ with (grey line) and without (black line) parallax term for an overall input signal $S = 10$ Jy and a bandwidth $\Delta\nu = 1$ MHz. **Middle**: geometric phase $\Delta\phi_{12}$ due to $\tau_g$. **Bottom**: parallax phase $\Delta\phi_{12}^{parallax}$. $\Delta\phi_{12}$ grows and decreases symmetrically with time in absence of object proper motion, while the parallax phase increases due to the orbital baseline. Over longer time intervals the modulation on $\Delta\phi_{12}^{parallax}$ by the ground baseline is also observable. Evident signals of IP phase are detectable over an interval of about 2 hours (bottom panel).

with the terms $2\pi\nu \cdot \tau_{parallax} = \Delta\phi_{12}^{parallax}$ and $2\pi\nu \cdot \tau_g = \Delta\phi_{12}$ corresponding to:

$$\Delta\phi_{12}^{parallax} \sim \frac{\Delta x_{12} \cdot \Delta X_{12}}{r\lambda} \qquad \Delta\phi_{12} \sim \frac{\Delta x_{12} \cdot \sin\theta}{\lambda}$$

taking into account the effect of the bandwidth we get the so called *fringe washing function*:

$$F(\tau_g) = \exp\left[-2\left(\frac{\pi\Delta x_{12}\Delta\nu\sin\theta}{c}\right)^2\right]\cos 2\pi\nu(\tau_g + \tau_{parallax})(V_{array})^2 \tag{6.23}$$

with $\Delta\nu$ bandwidth of observation and $V_{array}$ overall signal intensity in input to the radio receiver. The effect of the parallax phase on the fringe pattern can be observed in Figure 6.26 where also the time dependence of the phases is shown.

By observing the pair at two different epochs at the opposite sides of its culmination path we look for two time windows in which the array projected baselines ($\Delta x$) are the same in modulus and the relative geometric phases $\Delta\phi_{12}(t_1)$ and $\Delta\phi_{12}(t_2)$ give the same delay contribution. In this condition the relative shift in the fringe patterns at the two epochs is addressed almost entirely to the parallax phase term as shown in Figure 6.27. With this geometry possible inequalities of $\Delta\phi_{12}$ between the epochs could originate from the object proper motion. We numerically cross-correlate the amplitude signals patterns between two epochs of observation, six minutes each, separated by a six-hour time interval (Figure 6.27) for a given date (28 Aug 2014). We retrieve a best distance estimation for Cassini $r \sim 9.6$ AU that is only 5% different from the real value foreseen by the ephemerides.

This important result has to be weighted with possible errors from different sources of noise. High frequency Gaussian noise related to the receivers electronics does not affect the overall phase shift created by the parallax phase because high time variable terms are already removed by the correlator and filters. Conversely a slow time-varying phase lag induced

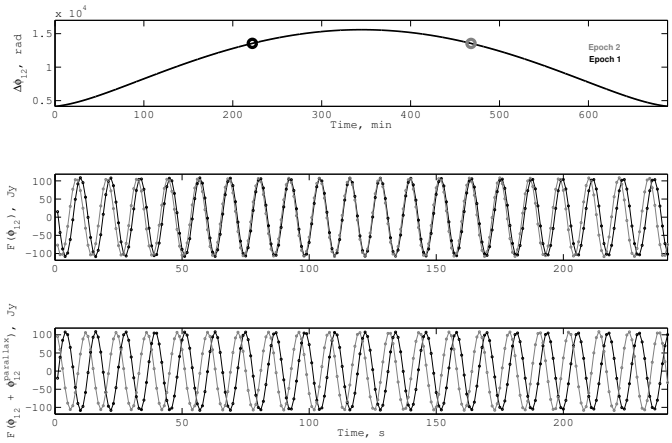


Figure 6.27: **Top:** Two observations are performed at two different epochs (1 (black) and 2 (grey)) separated by ∼6 hours. $\phi_{12}^0$ is continuously varying with time, increasing during first epoch and decreasing during the second epoch. **Middle:** fringe function signal stream for six minutes of observation; an optimal window of observation exists in which the contribution from the geometric phases $\phi_{12}(t_1)$ and $\phi_{12}(t_2)$ is the same and the relative shift among the fringe patterns is minimum. **Bottom:** taking into account $\phi_{12}^{parallax}$ in the same time frame, a substantial relative shift (related to target object distance) between the fringe patterns originates. The measurement of this relative phase shift leads to an estimation of the target object distance (eq. 6.15).

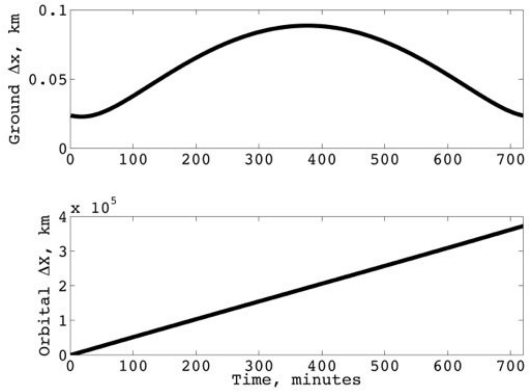


Figure 6.28: Ground and orbital projected baselines during the 28 Aug 2014 for a two–elements array separated by a ground baseline $|\Delta x_{12}| \sim 144$ m. The projected ground baseline changes under the effect of the Earth rotation; the orbital baseline grows linearly with time as the Earth orbits the Sun.

by the atmosphere creates a bias in the distance estimation because it behaves indistinguishably from the geometrical time delay $\tau_g$ and the parallax term (fringe function is modified to $F \sim \cos 2\pi\nu(\tau_g + \tau_{parallax} + \tau_{atmosphere})$). Frequent pointing switches on a phase calibrator are for this reason mandatory. In the specific case of Cassini, for the simulation scenario assessed, a gross error of 5° in the removal of the atmospherical contribution would lead to an error of about 1 AU in the distance estimation that corresponds to a 10% uncertainty in the measurement.

Even if some practical issues are beyond the scope of this work, a practical scenario of experiment involving the interplanetary spacecraft has been assessed and simulated showing promising results. In the application to an astrophysical context, the limit seems not finding a suitable pair

of objects with an adequate angular separation and flux intensities. The experiment involves new issues coming from non-standard observations that may present new problems to be solved, but the exciting perspective to bring into existence a new methodology of observational Astronomy gives good reasons to pursue the experiment.

# Conclusions

*From concept to reality*

In my PhD work I had the rare and priceless experience of participating in a project from the early design and concept to its final realization. Besides the large number of things I have learnt, the most important conclusion is probably the ASTRI prototype mounted at the Serra La Nave site ready to investigate the sky in a new and unexplored window.

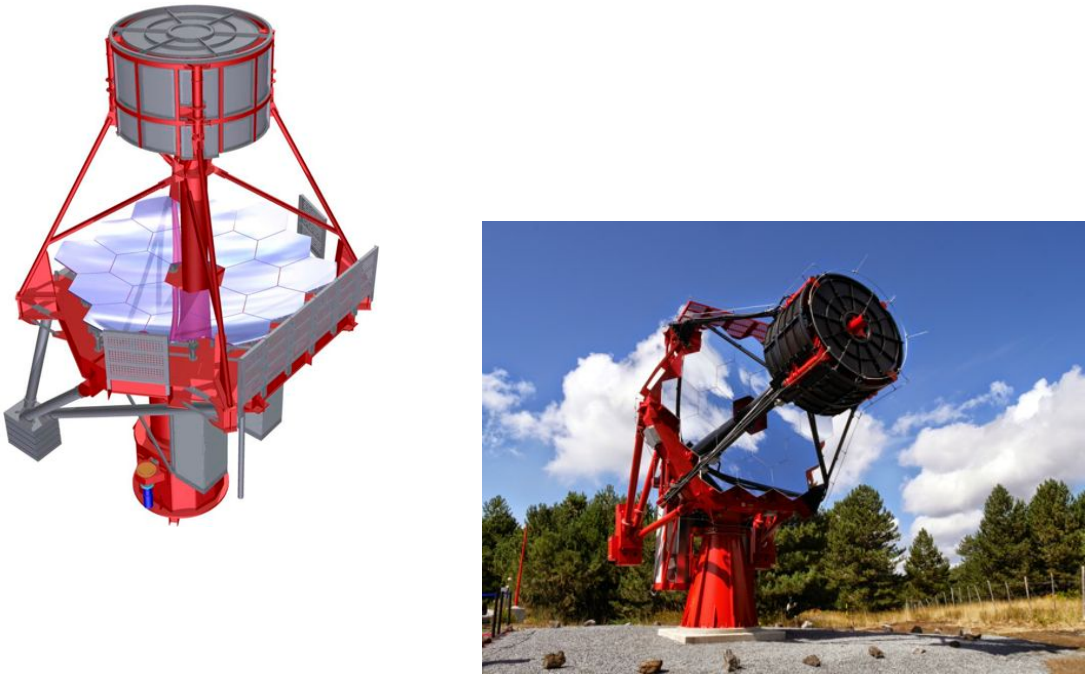

(a) (b)

(a) Design concept of the ASTRI telescope. (b) ASTRI SST-2M prototype at Serra La Nave site on Mount Etna (1800 m a.s.l.) the $24^{th}$ Septemeber 2014.

# Acknowledgments

I desire to acknowledge Dr. P. Conconi for having introduced me with deep humility, patience and wisdom to the art of the optical design, teaching me the smart tricks of this complex, but fascinating discipline. A dear thanks to Prof. C. Barbieri for making me discover the CTA experiment that has been the core of my PhD work. I'm very grateful to Dr. E. Giro, C. Pernechele and A. Franceschini for the continuous and precious support provided in these three years experience, their absolute intellectual honesty and for the wide knowledge they have transmitted to me. A special thanks is addressed to Prof. R. Mirzoyan for his profound and detailed review of the entire thesis and to Dr. G. Bonnoli, S. Blake and Prof. D. Dravins for having reviewed important parts of the manuscript. I want to sincerely acknowledge Prof. J.P. Ralston and P. Jain for having driven me towards a fascinating experience of a new both theoretical and observational scenario in Astronomy. Their absolute commitment and didactics will be always dear to me. I thank the IP team, F. Gini, N. Marchili, A. Possenti, D. Dallacasa, G. Naletto for the venture in radio interferometry. I want to acknowledge the tireless technicians of the Asiago Ekar Observatory for the extended support they gave to me during the entire tests campaign: A. Frigo, L. Traverso, L. Lessio, V. Chiomento, G. Martorana, M. Rebeschini and Vanni G.S.C.E.-S.L.T. $\sqrt{D.C.}^3$ I'm grateful to the whole ASTRI team for these three years of work together and in the specific, O. Catalano, D. Gardiol, G. Pareschi, R. Canestrari, G. Sironi, M.C. Maccarone. A particular thank is addressed to Prof. R. Ragazzoni and P. Benvenuti for their review and supervision during final exam acceptance review. A sincere thanks to my family and grandparents for all the support and encouragement they gave to me during all these years of education and work. A special thanks to the friends of always: the SCRAT Team, Ivano, Andrea, Maurizio, Weierstrass, Alberto, Davide, Enrico, Giacomo, Valentina (Gnagna), Rosy, Laura, Boss, for the beers, the labs, dinners and mountain trips. A final acknowledgement to Valentina for her precious company and support during these nice years together.

*Alles garibet*

# Appendix

Nuclear Instruments and Methods in Physics Research A 764 (2014) 176–185

Contents lists available at ScienceDirect

Nuclear Instruments and Methods in Physics Research A

journal homepage: www.elsevier.com/locate/nima

# Illumination technique for the relative calibration of the ASTRI SST-2M camera

Gabriele Rodeghiero [a,*], Osvaldo Catalano [b], Alberto Segreto [b], Vincenzo De Caprio [c], Enrico Giro [d], Luigi Lessio [d], Paolo Conconi [e], Rodolfo Canestrari [e]

[a] Department of Physics and Astronomy, University of Padova, Vicolo dell'Osservatorio 5, 35100 PD, Italy
[b] INAF IASF Palermo, Via Ugo La Malfa 153, 90146 PA, Italy
[c] INAF OACN, Salita Moiariello, 16, 80131 Napoli, NA, Italy
[d] INAF OAPD, Vicolo dell'Osservatorio 5, 35100 PD, Italy
[e] INAF OAB, Via E. Bianchi 46, 23807 Merate, LC, Italy

ARTICLE INFO

*Article history:*
Received 22 November 2013
Received in revised form
15 July 2014
Accepted 19 July 2014
Available online 27 July 2014

*Keywords:*
Illumination
ASTRI SST-2M
Optical fiber
PMMA
MPPC

ABSTRACT

We present a new illumination technique for the camera relative gain calibration of the ASTRI SST-2M Cherenkov telescope. The camera illumination is achieved by means of an optical fiber that diffuses the light inside a protective PMMA window above the focal plane. We report the encouraging results of the development tests carried out on two PMMA window prototypes illuminated by a standard optical fiber. We checked also the reliability of the method by a series of ray tracing simulations for different scattering models and PMMA window shapes finding good agreement with experimental results.



## 1. Introduction

For the relative gain calibration of the pixels in the detector camera of an optical telescope it is necessary to illuminate the camera with a reasonably uniform light level, a procedure generally achieved by dome illumination [1]. The situation is rather different when we deal with Cherenkov telescopes which have no enclosure, so the dome illumination technique is not available. This is the case of the ASTRI SST-2M, a prototype of the Small Size class Telescope (SST) with dual mirror (2M) optics configuration for the Cherenkov Telescope Array, CTA [2]. The ASTRI SST-2M secondary mirror is monolithic, so it is not possible to illuminate directly the camera with a source positioned between two adjacent mirror segments. A workaround solution was then adopted to this problem based on a new illumination technique for the relative gain calibration of the ASTRI SST-2M camera at the focal plane which is protected by a Poly-Methyl-Metha-Acrylate (PMMA) window. The technique exploits the light emitted by an optical fiber to indirectly illuminate the focal plane of the camera by scattering processes inside the protective PMMA window. Based on the first results of the development tests on two prototypes PMMA windows this innovative and cost-effective approach successfully addresses the problem of the camera illumination of the ASTRI SST-2M Cherenkov telescope. The reliability of the achieved illumination pattern is supported also by dedicated ray tracing simulations. After an overview of ASTRI SST-2M telescope prototype and of its camera, in this paper we will detail the camera illumination technique and the first results of the development tests coupled with ray-tracing simulations.

## 2. The ASTRI SST-2M telescope

ASTRI (Astrofisica con Specchi a Tecnologia Replicante Italiana) is a flagship project of the Italian Ministry of Education, University and Research led by INAF within the framework of the CTA International Observatory [2]. The ASTRI project [3] foresees the full development, realization, operation and calibration of a 4-m class, Small Size Telescope prototype, named ASTRI SST-2M compliant with the requirements of the Very High Energy, VHE, array of CTA. The ASTRI SST-2M prototype adopts an aplanatic, wide field, double reflection optical layout in a Schwarzschild-Couder configuration as shown in Fig. 1, and it will explore the sky in the $\sim 1$ TeV–$10^2$ TeV domain. Investigations in this spectral window constitute a young and rapidly developing discipline of the

* Corresponding author. Tel +39 049 827 8250.
*E-mail addresses:* gabriele.rodeghiero@studenti.unipd.it, gabriele.rodeghiero@gmail.com (G. Rodeghiero).

http://dx.doi.org/10.1016/j.nima.2014.07.038
0168-9002/

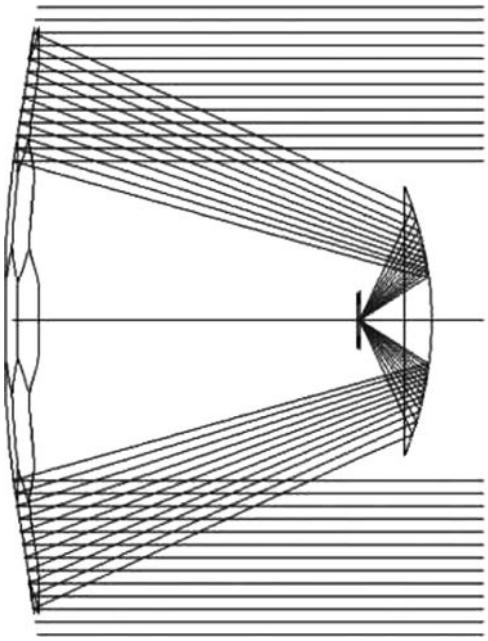

**Fig. 1.** The ASTRI SST-2M Schwarzschild-Couder telescope is based on a two mirror configuration, both the surfaces are aspherical. The blue rays indicate the optical path for the photons coming from an on-axis source at the focal point (10 km). Cherenkov telescopes in fact observe events that originate at the boundary of the troposphere.

ground-based γ-ray astronomy [4]. ASTRI SST-2M focal plane camera explores a new design based on monolithic Multi-Pixel-Photon Counter, MPPC, array sensors. This is a novelty in the Cherenkov astronomy which historically has always relied on photo tubes with Winston cones [5].

## 3. The ASTRI SST-2M camera

The Schwarzschild-Couder configuration (Fig. 1) produces a curved focal plane and consequently the camera surface is convex with a radius of curvature $R_{FP} = 1060$ mm, a diameter $D = 500$ mm and a field of view FoV$=9.6^{\circ}$.

To cover the focal plane the pixels are arranged in a modular configuration: the physical pixels (MPPCs, 3 mm × 3 mm) of each sensor unit are grouped in a $2 \times 2$ logical pixel (6.2 mm × 6.2 mm) having a sky-projected angular size of $0.17^{\circ}$. The MPPCs are Avalanche Photo Diodes working in Geiger mode (G-APD) by setting a bias voltage greater than the Breakdown Voltage. An MPPC array is composed of 3600 SPADs of 50 × 50 μm, and it is produced by Hamamatsu, model $S11828-3344M$, further information can be found in the work of Sottile et al. [7]. A picture of an MPPC array by Hamamatsu is given in Fig. 2. There are many advantages in using MPPCs, such as excellent single photon resolution, high quantum efficiency, low operating voltage, and no damage when exposed to ambient light. There are however also some drawbacks like the very high dark counts, afterpulses, optical crosstalk and gain strongly dependent on temperature.

The aggregation of $4 \times 4$ sensor units ($8 \times 8$ logical pixels) forms the Photon Detection Module (PDM) [6]. The PDM module is the mechanical unit containing MPPCs, Front End Electronics, FEE, and PDM-FPGA Printed Circuit Boards (PCBs). The focal plane is covered by a mosaic of 37 PDMs, 57 × 57 mm each, that fits the curved surface of the camera. The PDMs in the outermost regions of the focal plane are not entirely populated by physical pixels because they are vignetted by the mechanical structure of the camera as shown in Fig. 3. A view of the focal plane tessellated by the PDMs is given in Fig. 4 and a picture of a single PDM is shown in Fig. 5.

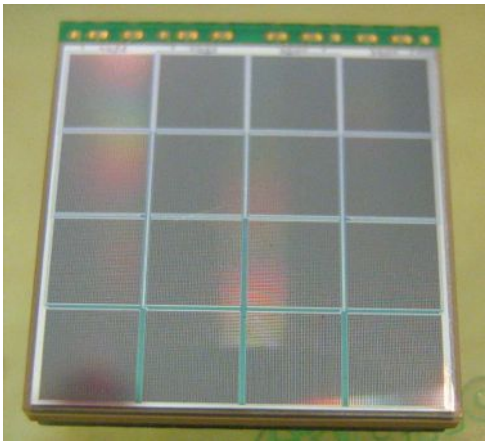

**Fig. 2.** The $S11828-3344M$ detector by Hamamatsu constitutes the unit module of the ASTRI SST-2M camera. The pixels are connected together in $2 \times 2$ groups to form a logical pixel, corresponding to a channel.

A detailed model of the ASTRI SST-2M camera is reported in Fig. 6: the focal plane is covered by a PMMA window and a light-tight lid. The PMMA window prevents sand, dust, water and all the other environmental agents from depositing over the PDMs and keeps a thermalized environment around the focal plane avoiding breakdown voltage variation and then gain variations of the MPPCs. The lid is composed of two petals that are opened during the observation runs, but are closed during camera relative calibration procedures and when the telescope is not observing. For further details on the camera design the reader should refer to the work of V. De Caprio and collaborators [8].

## 4. Camera illumination technique

The basic idea to obtain a reasonably uniform illumination of the ASTRI SST-2M camera by the relative calibration system, consists in using the PMMA window as a means of uniform transmission of light diffused by an optical fiber. Similar techniques of light framing from visible to UV and IR are common in a wide range of applications in the fields of security surveillance, emergency lighting, fiber-optical sensing, dosimetry and medical phototherapy [10]. The optical fiber is positioned in a groove along the inner side of the lateral baffle in proximity of the bottom PMMA window profile, as reported in Fig. 7 (left side). The light enters the PMMA and undergoes a series of total internal reflections and scattering processes, before exiting the window on the front side, skyward, or on the back side, toward the focal plane, illuminating the PDMs units. Careful design of the later baffle prevents direct light to reach the focal plane while allows only indirect, scattered component. By tuning the intensity of the light emitted by an optical fiber it is possible to achieve a suitable illumination level to calibrate the PDMs and eventually for establishing a single photon counting regime.

The emissivity of the optical fiber decreases along its length by an exponential relation:

$$I = \frac{I_0}{4\pi}\exp(-k\Delta x) \tag{1}$$

with $I_0$ input radiation intensity, $k$ side-scattering efficiency coefficient, $\Delta x$ fiber length and $I$ output radiation intensity. In the analyzed case, with a total fiber length of 1.5 m, this variation is detectable but limited. The optical fiber that will be used for the camera illumination in the final configuration is a graded-index polymer optical fiber, model GIPOF-120, with a core diameter of 120 μm, from Chromis Fiberoptics [9].

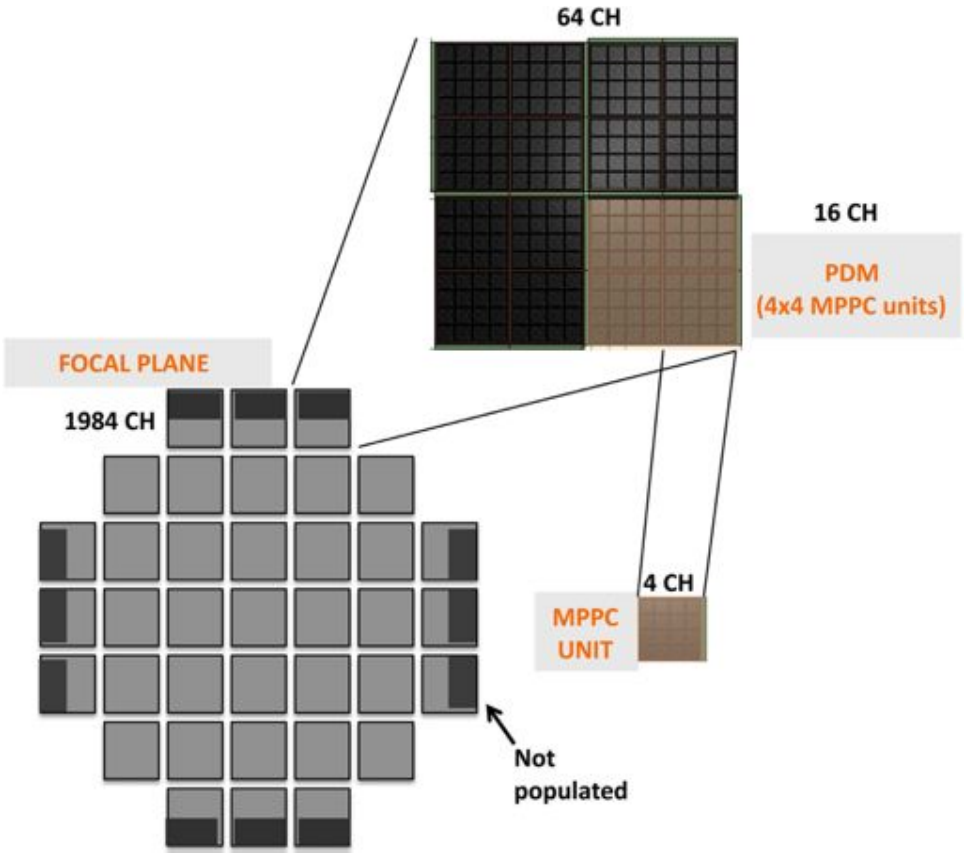


**Fig. 3.** The pixels arrangement scheme is constituted by a hierarchical assembly of MPPCs units to create the PDMs. The focal plane is a curved mosaic of 37 plane PDMs (light gray blocks), 64 channels each. Nevertheless, the PDMs allocated at the borders of the focal plane have only half of their area populated by MPPCs (dark gray); this consequently diminishes to 1984 the total number of channels.

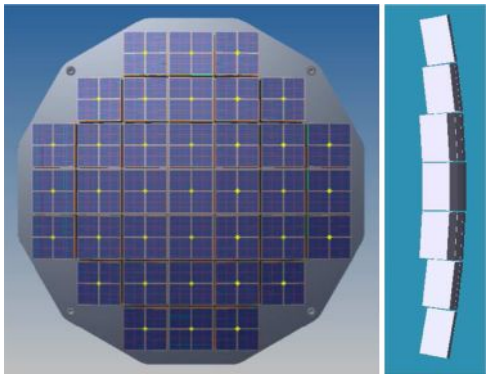

**Fig. 4.** Front and side view of the ASTRI SST-2M focal plane. In the front view the PDMs arranged to cover the focal plane; the side view shows the curved profile of the focal plane composed of a mosaic of PDM modules (white blocks).

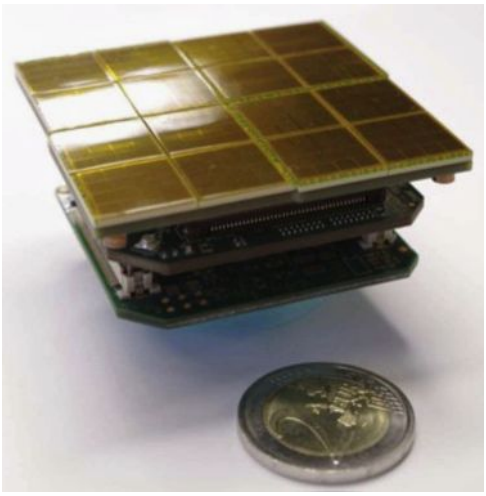

**Fig. 5.** A prototype of Photo Detection Module, PDM, Front End and FPGA PCBs. The volume of a PDM is 57 × 57 × 30 mm (two euro coin for reference scale).

## 5. Development tests

To validate this new technique a dedicated experimental setup to estimate the scattered light by two prototypes PMMA windows has been built at IASF Palermo workshop. The description of the detector and the set up used are presented in the following sections.

### 5.1. UVscope detector

UVscope is a portable multi-pixels photon detector developed at IASF-Pa to support experimental activities in the high-energy astrophysics and cosmic rays field [11]. UVscope instrument is a light detector working in Single Photon Counting mode and it was originally designed for the study of the night sky background in the range 300–650 nm. The UVscope light sensor is a Multi Anode Photo Multiplier Tube (MAPMT) manufactured by Hamamatsu, series R7600-03-M64 [12]; the sensor is composed of 64 anodes arranged in matrix of 8 × 8 pixels (18.1 mm × 18.1 mm) [11] (Fig. 8).

### 5.2. Measurement set up description

The experimental set up is rather simple and it comprises a commercial optical fiber, 1.05 mm in diameter, two prototypes PMMA windows, a plane window 5 mm thick and a curved one,

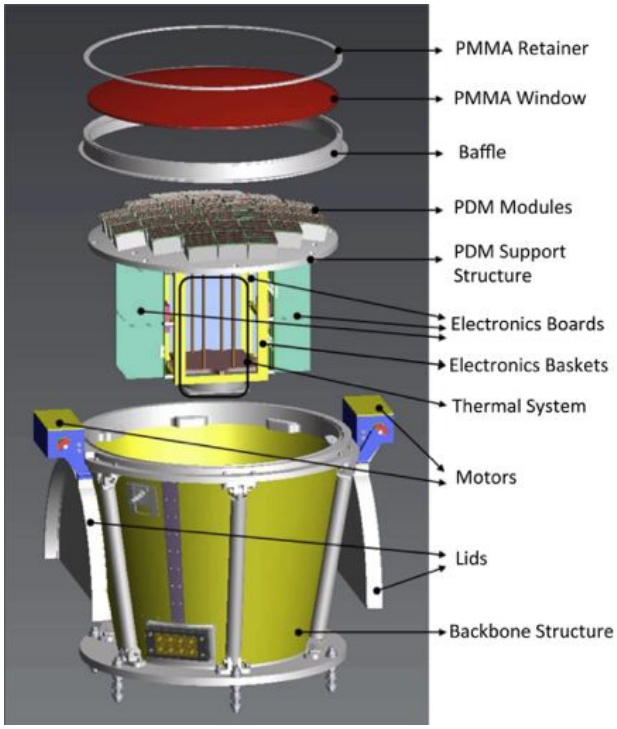


**Fig. 6.** The ASTRI SST-2M camera subsystem with the main units (top to bottom): the PMMA window (red) above the PDMs mosaic and the lateral baffle (gray). Below the PDMs, there is the electronics assembly to process the analog signals from MPPCs, the thermal enclosure for thermal control of the camera, the backbone structure, the mechanical interface with the telescope and camera lids (open). (For interpretation of the references to color in this figure caption, the reader is referred to the web version of this paper.)

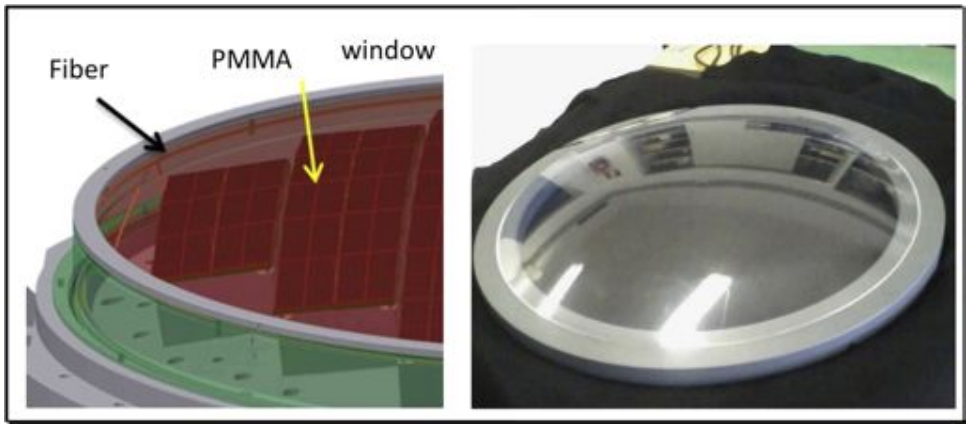


**Fig. 7.** Left: the PMMA window (red) is mounted above a mechanical lateral baffle (green) to protect the focal plane. A optical fiber is integrated along the inner side of the lateral baffle (red ring) in contact with the bottom profile of the PMMA window. Right: prototype PMMA window (used for tests campaign) mounted on a mechanical support ring that hosts the optical fiber. (For interpretation of the references to color in this figure caption, the reader is referred to the web version of this paper.)

3 mm thick. The plane window has a larger thickness to avoid flexures of the glass in the central region. The complete set up is enclosed in a dark box sufficiently large to include the UVscope detector. The radius of curvature of the curved prototype PMMA window is $R_w = 746$ mm and the diameter $D_w = 476$ mm.[1] A pulsed laser ($f_{pulse} = 50$ Hz) injects a green light (0.53 μm) with a power $I = 2$ mW into the optical fiber that diffuses light towards the PMMA window. The UVscope measures the level of scattered light in different position along the window diameter. Some images of the experimental set up are shown in Fig. 9.

[1] The radius of curvature of the window is different from the nominal configuration (1060 mm), the differences introduced are evaluated in Section 6.1.

### 5.3. Test operations and results

During the tests campaign UVscope was operated at a high voltage, HV = 850 V and with a discriminator threshold $Thrd_{mV} = 4$ mV. A series of dark frames were acquired by UVscope together with a calibration frame with a uniform light source. The illumination pattern created by the scattered light was sampled by UVscope which was moved radially along two different orthogonal window chords by steps of 30 mm, from −150 mm to +150 mm with respect to the window center, as shown in Fig. 9 (top right). For each UVscope position, 100 frames with $T_{frame} = 1$ s, were acquired by the detector at a sampling frequency $f_{Samp} = 100$ MHz. A complete dataset for each window prototype, plane and curved, was saved for analysis. In Figs. 10 and 11 the median (over 100 frames) normalized counts measured by

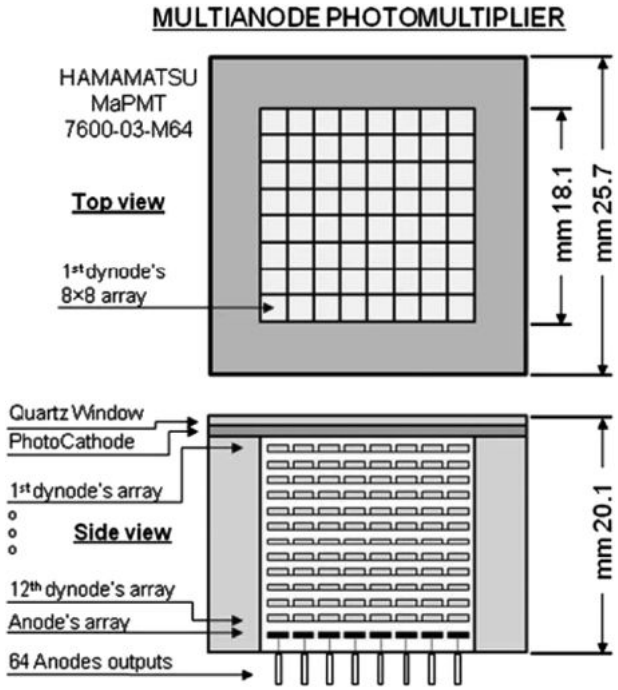


**Fig. 8.** Layout of the MAPMT light sensor used for the tests campaign, image taken from M.C. Maccarone et al. [11].

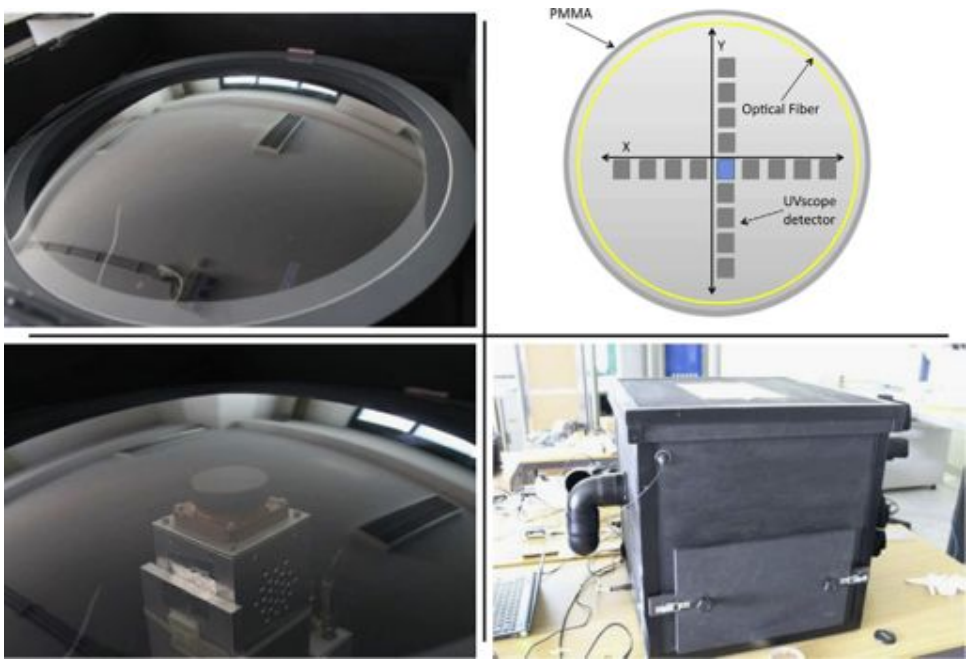


**Fig. 9.** Bench set up for the development test carried out at IASF facility in Palermo. Top left: the optical fiber is put in contact with the bottom PMMA window profile; bottom left: UVscope device below the PMMA window to measure the scattered light; bottom right: closed dark box hosting the measurement set up; top right: schematic view of the PMMA window, optical fiber and UVscope sampling points along two orthogonal directions (blue and gray squares) performed during the tests campaign. (For interpretation of the references to color in this figure caption, the reader is referred to the web version of this paper.)

UVscope for the curved PMMA windows are plotted for the two orthogonal chords (X,Y). Only the X chord dataset is available for the plane window (Fig. 12). The median as statistical estimator has been chosen in substitution to the arithmetic average, to ensure a better reliability of the statistics representation and a greater robustness against possible outliers or intrinsic noise. The central decrease of the illumination pattern is associated to two different causes: the progressively increasing distance from the optical fiber and (for the curved window) the growing distance between the light sensor and the scattering window. An extended, comparative analysis and discussion of the UVscope data and the simulated illumination profile are discussed in Section 6.

## 6. Zemax assessment and development simulations

Using the software for optical design Zemax [13], the same measurement set up described in Section 5.2 has been reproduced

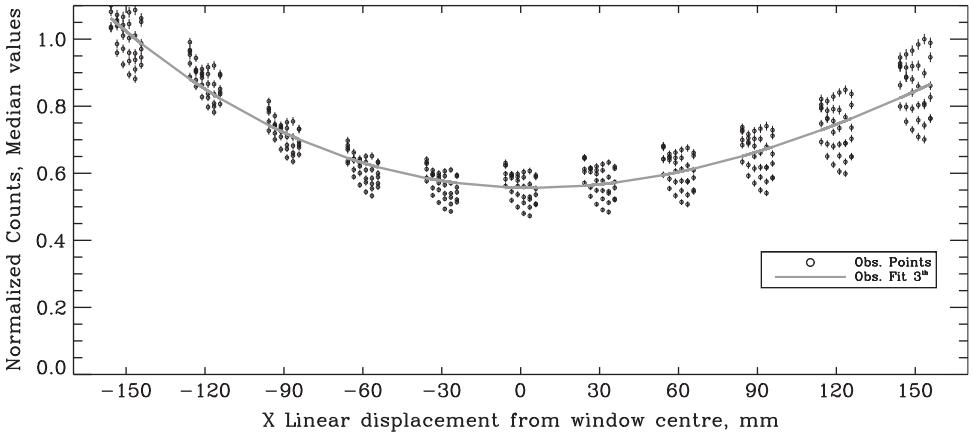


**Fig. 10.** Normalized received counts of the laser light scattered off by the curved PMMA window prototype. The separation between consecutive measurement points is 30 mm. The retrieved points are well interpolated by a 3rd order fitting polynomial. The *X* axis coincides with one chord of the window explored with UVscope.

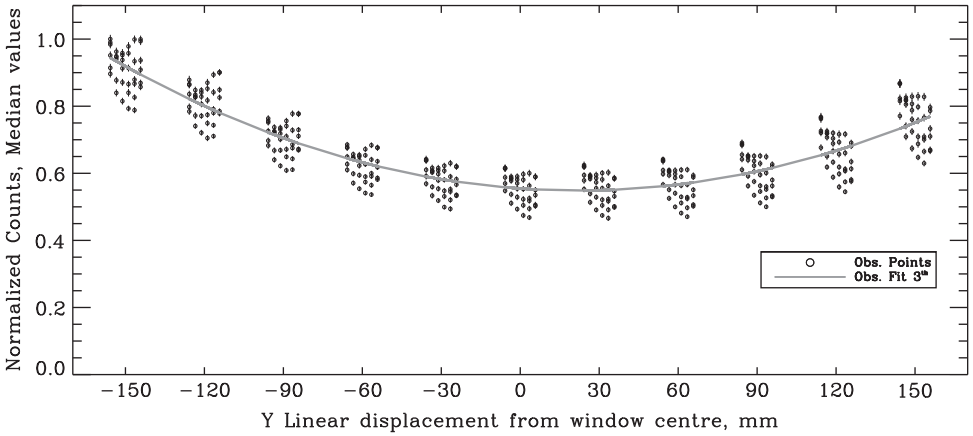


**Fig. 11.** Normalized received counts and 3rd order fitting polynomial for sampling points along the Y chord of the window explored with UVscope. The different illumination level of the two outer points ( − 150,150) is due to the optical fiber light leakages.

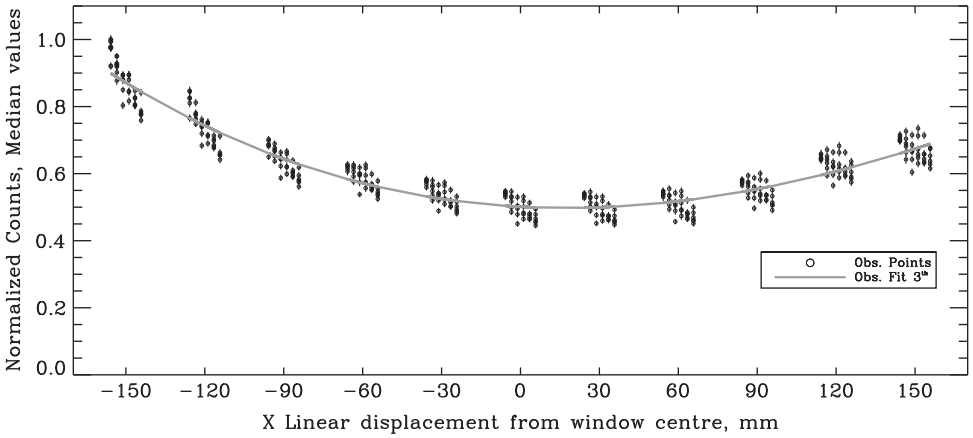


**Fig. 12.** Normalized received counts and 3rd order fitting polynomial for sampling points along the X chord of the plane prototype window explored with UVscope. The radial decrease in light flux clearly visible for the curved window (Figs. 10 and 11) is less pronounced for the plane window prototype because the UVscope detector keeps a constant separation from the window.

to make a comparative analysis with the experimental results gathered by UVscope. The optical fiber is modeled by a filament source of the same section ($D = 1.05$ mm) and length ($l_{FB} \sim 1500$ mm) of the real optical fiber. The ray tracing detector has no intrinsic noise and the analysis is performed for a green light ($\lambda = 0.53$ μm). The dependence on the wavelength radiation and dispersion effects seems not relevant as can be observed in Fig. 13, where the flux retrieved by each MPPC is plotted for three different wavelengths $\lambda_1 = 0.37$ μm, $\lambda_2 = 0.45$ μm and $\lambda_3 = 0.6$ μm. The changes in the PMMA refractive index is less than 1% over the wavelength range $\lambda_1 - \lambda_3$. This slowly

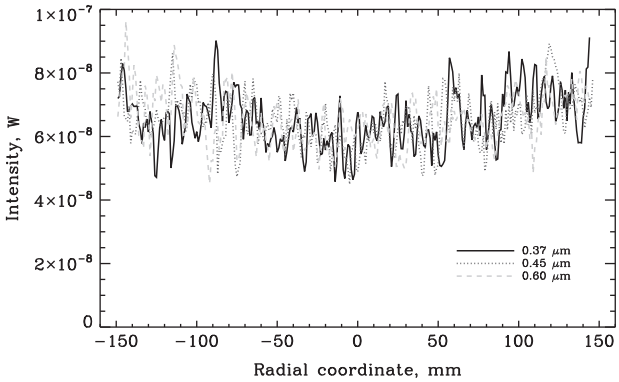


**Fig. 13.** Illumination pattern for three different wavelengths and the curved PMMA window. The dependence of light propagation from wavelength is small and the dispersion effects can be neglected.

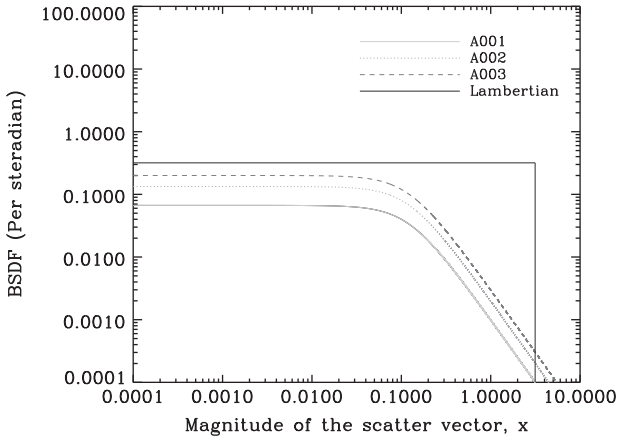


**Fig. 14.** Three different scattering models A0001, A0002, A0003, are used in Zemax to model the scattering due to random isotropic surface, these models work properly when the roughness is small or comparable to the wavelength of light being scattered. For comparison the scattering profile for a lambertian surface whose BSDF is constantly equal to $1/\pi$ is reported.

varying dispersion response of the window is of particular interest for a possible multi-wavelength calibration of the MPPCs.

An essential parameter that allows light diffusion inside the PMMA window is the scattering of the medium itself. In the simulations two different sources of scattering are assumed: the scattering due to the roughness of the optical surface and the bulk scattering caused by the polymer structure. The former contribution is expected to be very small because the surfaces of the window are mirror polished. For the scattering due to the surface roughness three different models provided by Zemax are explored; the scattering is parametrized with a Bi-Directional Scatter Distribution Function, BSDF. The BSDF represents the scattered radiance per unit incident irradiance, and a projected vector that represents the magnitude of the scattered ray. The three models give similar results and describe most of the optical surfaces when the scattering is mainly due to random isotropic surface roughness, and the scale of the roughness is small compared to wavelength of light being scattered [14]. The BSDF for these models is shown in Fig. 14.

To model the bulk scattering Zemax simply requires the mean free path of the photons in the medium between two consecutive scattering processes and the aperture of the angle of exit for the scattered ray. We set the parameters based on the measurements of B. Christ et al. [15] assuming a range among $4\times10^{-4}$–$4\times10^{-3}$ mm for mean free path and the angles of exit equal to 45° and 90°.

### 6.1. Simulations and observations results

Two prototypes of PMMA windows for the final camera prototype are simulated: curved and plane. The propagation of the light inside this element is expected to depend on the refractive index of the material and its scattering properties as discussed in Section 6. As shown in Fig. 13, the dispersion effects inside the PMMA window are negligible and thus the simulations have been carried out selecting a wavelength $\lambda = 0.53$ μm. The interpolated radial profiles extracted from the 2-D map of illumination retrieved by Zemax are shown in Figs. 15 and 16 superimposed to the measured curves by UVscope. Both experimental and simulated results confirm the reliability of the technique envisaged for the ASTRI SST-2M camera relative calibration. The plane window shows a slightly better uniformity in the illumination pattern with respect to the curved window. However the reader should bear in mind that the dataset on curved window was acquired moving UVscope along the window profile in a horizontal configuration. Conversely the final camera focal plane will have the same radius of curvature of the PMMA window resulting in a better uniformity of the illumination pattern. Moreover the plane window has a thickness of 5 mm and provides a greater volume of scattering for the photons with respect to the thinner curved window (3 mm), but the former solution causes also a greater absorption of astronomical Cherenkov light of interest than the latter. Nevertheless the most important aspect of this technique is reliability and

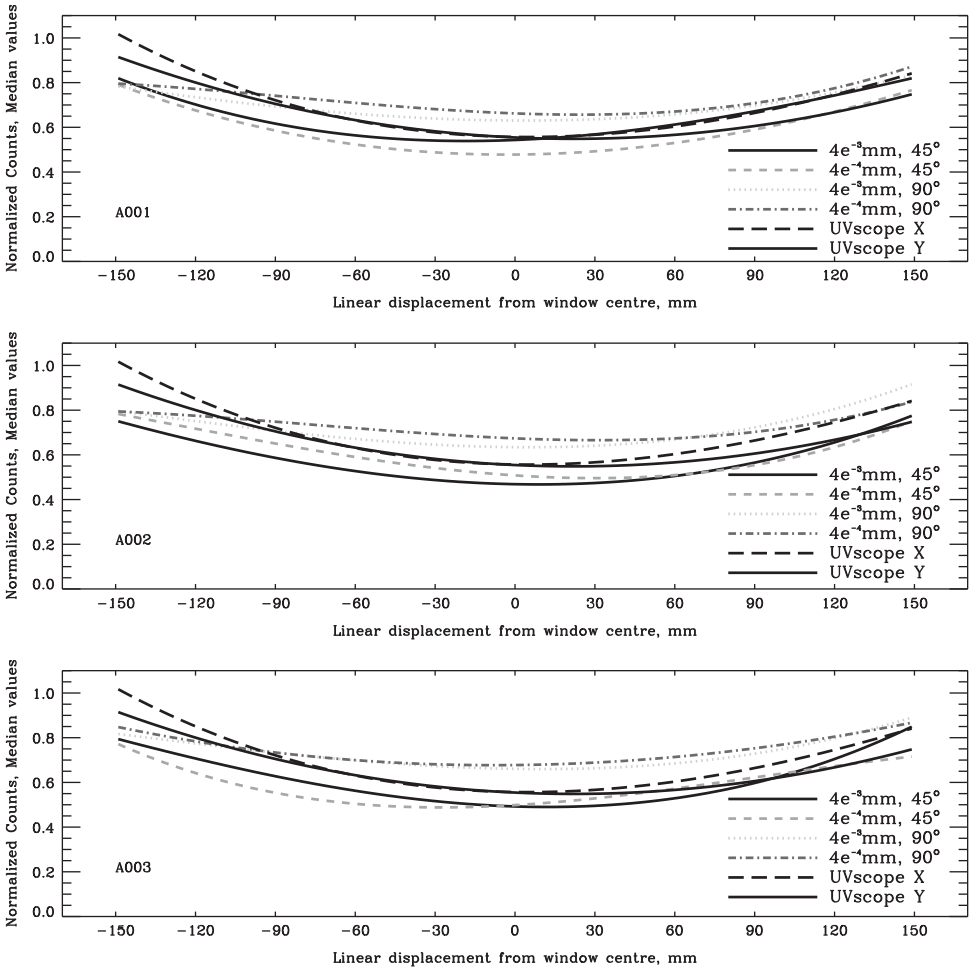


**Fig. 15.** Interpolated radial profile of the simulated points for the propagation of photons with different optical mean free paths and exit angles into the curved prototype PMMA window used for the tests campaign for the three scatter models plotted in Fig. 14. The simulations embrace the interval of values measured by Christ et al. [15] reported in Section 6 and the measured profiles are compatible with the three scattering models. The variations in the scattering angles and the photons mean free path provide upper and lower limits for the measured profiles along the two chords (solid and long dashed black line).

repeatability. In fact, being a relative gain calibration technique, it is not really important to guarantee a uniform illumination pattern all over the focal plane, rather to keep a constant level of illumination in a given region of the camera with time. In this perspective both the solutions address successfully the problem.

To conclude the discussion on this method we assessed the reliability of the technique when applied to the nominal design of the ASTRI SST-2M camera that foresees a curved PMMA window with a radius of curvature $R_{curv} = 1060$ mm. A series of ray tracing simulations have been performed by Zemax and the preliminary results show a good and even better uniformity (with respect to prototype used in tests campaign) of the illumination pattern as shown in Fig. 17.

## 7. Conclusions

We have presented a new illumination technique for the relative calibrations of the ASTRI SST-2M camera. The method exploits the light emitted by an optical fiber in the proximity of the PMMA window covering the camera focal plane. The window diffuses a small fraction of the light by bulk and surface scattering processes towards the camera focal plane. The results retrieved during the test campaign on two PMMA window prototypes, curved and plane, show a good reliability of the technique. The ray tracing simulations carried out in parallel to the tests campaign explore different scattering models describing most of the optical surfaces. These simulated profiles are representative of a lower and an upper limit in terms of the photons scattering angles and the mean free path. The measured light distributions are expected to be inside these intervals as verified by the current explorative test campaign. The measurements indicate a good repeatability and reliability of the proposed method: one important conclusion of this work is the constant stability of the technique over a wide range of scattering angles, photons mean free path and surface scattering models confirmed both by the test campaigns and the simulations. As discussed in Section 6.1, local variations induced by the factors above mentioned do not represent an issue for the camera illumination provided that these are constant with time. Also the final configuration of the ASTRI SST-2M camera (with a slightly different radius of curvature) was simulated and showed encouraging results. Based on the experimental and simulation results the proposed technique successfully addresses the problem of the relative gain calibration for both a curved and a plane PMMA window.

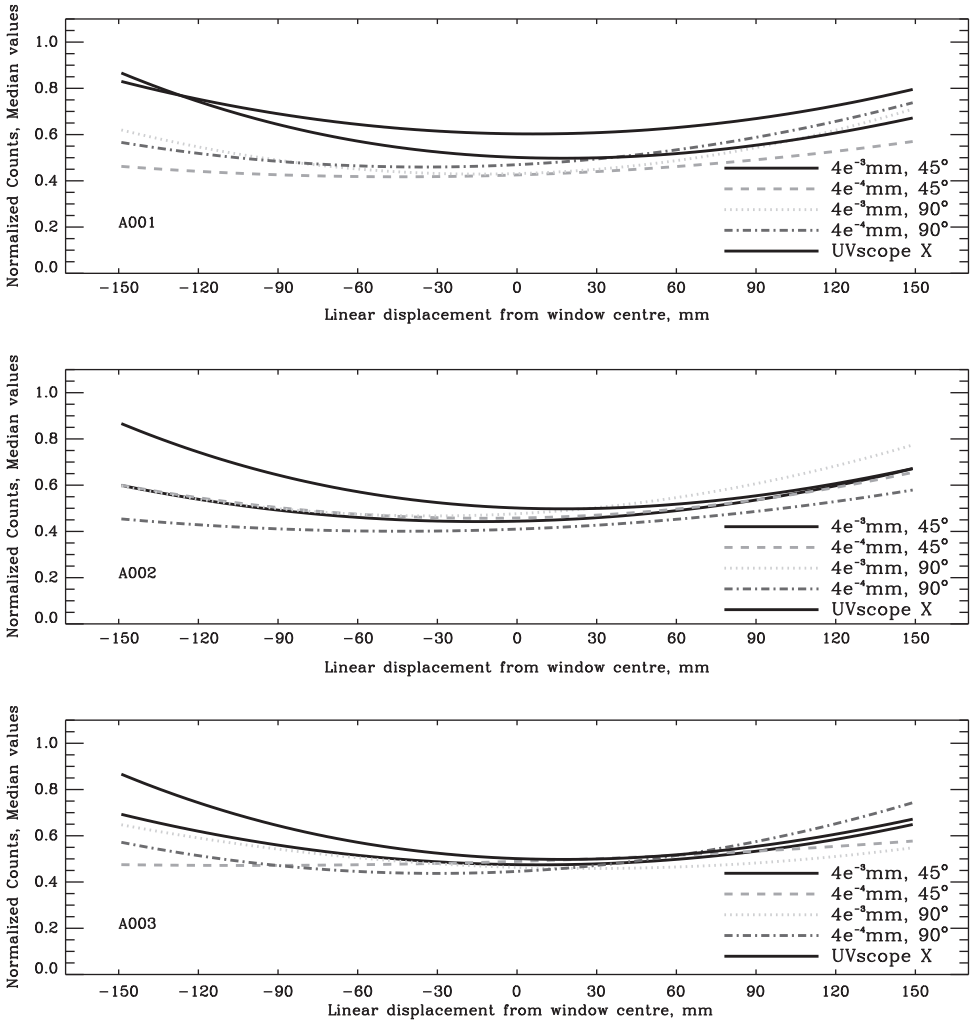


**Fig. 16.** Interpolated radial profile of the simulated points for the propagation of photons with different optical mean free paths and exit angles into the plane prototype PMMA window used for the tests campaign for the three scatter models plotted in Fig. 14. Only the measured profile along X chord was retrieved during the tests campaign, but the three models are compatible with the experimental values (solid black line). The higher level of illumination in the measured profile at $x=-150$ mm coincides with the initial point of fiber connection to the window, while the point at $x=+150$ mm shows a lower level of illumination due to optical fiber light leakages.

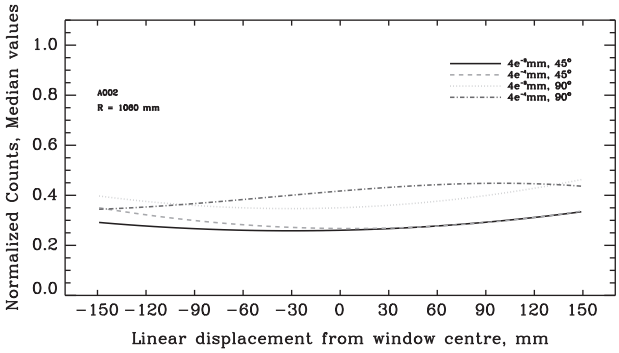


**Fig. 17.** Simulated illumination patterns for the nominal configuration of the ASTRI SST-2M PMMA window ($R_{curv}=1060$ mm). The intermediate A002 scatter model used for the evaluation of the tests campaign results is considered (see Fig. 14).

## Acknowledgments

This work was partially supported by the ASTRI "Flagship Project" financed by the Italian Ministry of Education, University, and Research (MIUR) and led by the Italian National Institute of Astrophysics (INAF). We also acknowledge partial support by the MIUR Bando PRIN 2009. Authors are grateful to Dott.ssa M. C. Maccarone, Dott. L. Stringhetti, Dott. G. Bonanno and Dott.ssa

Valentina Calvi for the discussions and the suggestions on this work. Authors are thankful to anonymous referees and to Alma Fibre Ottiche Sas for the provided optical fibers.

## References

[1] ⟨http://www.ctio.noao.edu/ tmca/CCD/docs/cookbook/top.html⟩.
[2] ⟨http://www.cta-observatory.org/⟩.
[3] ⟨http://www.brera.inaf.it/astri/⟩.
[4] J.A. Hinton, W. Hofmann, Annual Review of Astronomy and Astrophysics 47 (1) (2010) 523.
[5] R. Winston, Journal of the Optical Society of America 60 (1970) 245.
[6] O. Catalano, et al., in: Proceedings of Thirty-third ICRC2013, 2–9 July 2013, Rio de Janeiro, Brazil - arXiv:1307.5142.
[7] G. Sottile, et al., arXiv:1305.2699.
[8] V. De Caprio, et al., in: Proceedings of SPIE Optics+Photonics, 25–29 August 2013, San Diego, CA, paper no. 8836-2.
[9] Thorlabs, graded-index polymer optical fiber (GI-POF) from Chromis Fiberoptics ⟨http://www.thorlabs.de/thorproduct.cfm?partnumber=GIPOF120-P⟩.
[10] J. Spigulis, et al., in: A. Krumins, et al. (Eds.), Proceedings of SPIE, vol. 2967, Bellingham, WA, 1997, pp. 226–231.
[11] M.C. Maccarone, et al., Nuclear Instruments and Methods in Physics Research Section A 659 (2011) 569.
[12] Hamamatsu, R7600-03-M64 Photo Multiplier Tube Multi Anode and its Assembly H7546B-03 ⟨http://www.sales.hamamatsu.com/en/products/electron-tube-division/detectors/photomultiplier-tubes/part-r7600-03-m64.phpS⟩.
[13] ⟨http://www.radiantzemax.com/en/zemax/⟩.
[14] Zemax User's Guide, ⟨http://www.radiantzemax.com/support/downloads/zemax⟩.
[15] B. Christ, et al., SPIE, vol. 297, Emerging Optical Materials, 1981, p. 169.

# Bibliography


[1] Abdo, A., et al. 2009, Phys. Rev. Lett. 103, 251101.

[2] Acciari, V. A., et al., The Astrophysical Journal Letters, 715:L49-L55, 2010 May 20.

[3] Ackermann, M., et al. 2012 ApJ 750 3.

[4] Aharonian, F.A., et al., H.E.S.S. letter of intent, Tech. rep. (1997).

[5] Aharonian, F.A., et al., ApJ 614, 897 (2004).

[6] Aharonian, F.A., et al., 2008, reports on Progress in Physics, 71, 9.

[7] Aharonian, F. A. et al., A&A, 508, 2, 2009, p.561-564.

[8] Aharonian, F. A. et al, <http://arxiv.org/abs/astro-ph/0603021>

[9] Albert, J., et al., 2007, ApJ, 667, 358-366.

[10] Aleksić, J. et al 2013, <http://arxiv.org/pdf/1311.3637v1.pdf>

[11] Aliu, E., et al., 2008, Science, 322, 1221.

[12] Baffes, Mast and Nelson, SPIE 7018-29.

[13] Bastieri, D., et al. 2005, 29th International Cosmic Ray Conference Pune (2005) 00, 101-106.

[14] Bahcall, J. N., Neutrino Astrophysics, Cambridge University Press, 1989.

[15] Bely, P.Y., The design and construction of large optical telescopes, A&A library Springer, 2002.

[16] Bigongiari, C., et al., 33rd ICRC, 2013.

[17] Biland, A., et al., arXiv:1403.5747v2.

[18] Bradt, H., Astrophysics processes, Cambridge University Press, 2008.

[19] Brunthaler, A., et al., Astron. Nachr. / AN 999, No. 88, 789–794 (2010).

[20] Burns, C.R., et al. Astron.J. 141 (2011) 19.

[21] Carrasco-Casado, A., 10 April 2013 / Vol. 52, No. 11 / APPLIED OPTICS.

[22] Carrigan, S., et al., ICRC 2013, <http://arxiv.org/pdf/1307.4690v3.pdf>

[23] Chandrasekhar, S. 1950, Radiative Transfer (Oxford: Oxford University Press).

[24] Catalano, O., et al., 2014, Proc. of SPIE Vol. 9147 91470D-1.

[25] Cherenkov, P.A., Phys. Rev. 52, 378, 1937.

[26] Condon, J. J., Cotton, W.D., Greisen, E.W., et al., 1998, ApJ, 115, 1693-1716.

[27] Contreras, J.L. et al., A study of the polarization of Cherenkov Radiation in Extensive Air Shower of energy around 1 TeV.

[28] Davies, J.M., Cotton, E.S., Design of the quartermaster solar furnace, J. Solar Energy Sci. Eng. 1 (1957) 16-21.

[29] De Angelis, A., Mansutti, O. and Persic, M., Nuovo Cim., Vol. 31, N. 4, 2008.

[30] de Bruijne, J.H.J., Astrophys. Space Sci (2012) 341:31-41.

[31] Delaunay, B., Bulletin de l'Académie des Sciences de l'URSS, Classe des sciences mathématiques et naturelles, No. 6: 793-800, 1934.

[32] Dermer, C. D., 1986, A&A 157, 223.

[33] Dierickx, P., Enard, D., Geyl, R., Paseri, J., Cayrel, M., Béraud, P., Tech. Rep. for VLT M1, <http://www.eso.org/sci/facilities/paranal/telescopes/ut/m1unit.html>

[34] Döring, M. et al., Proceedings of ICRC 2001.

[35] Dravins, D., et al., New Astron. Rev. (2012), http://dx.doi.org/10.1016/j.newar.2012.06.001.

[36] Dravins, D., LeBohec, S., Jensen H., Nunẽz, P.D., 2012, Astroparticle Physics, 56, 143-167.

[37] Dravins, D. & Lagadec, T., arXiv:1407.5993.

[38] Dravins, D., Intensity Interferometry & Optical Astronomy ASTRI, Tech. rep. 2014.

[39] Dutrey, A., et al., doi:10.1038/nature13822.

[40] Fairbairn, M., et al, JCAP06(2014)005.

[41] Fazio, G., et al., 1972, Ap. J. (Letters), 175, L117.

[42] Fomalont, E. & Reid, B., 2004, New Astronomy Reviews, 48, 1473-1482.

[43] Fox, M., Quantum Optics, an introduction, Oxford University Press, 2005.

[44] Franceschini, A., AIP Conf. Proc. 1112, 101 (2009).

[45] Galbraith, W. & Jelley, J.V., Nature 171 (1953) 349.

[46] Gaidos, J.A., et al., Nature 383, 319-320, 1996.

[47] Gardiol, D., Rodeghiero, G., et al., Workshop on Hanbury-Brown & Twiss Interferometry, Nice 2014.

[48] Ghigo, M., et al., 2009, Proc. SPIE 7439, Astronomical and Space Optical Systems, 74390M (September 17, 2009).

[49] Ghigo, M., et al., 2009, Proc. of SPIE Vol. 7437 74370P-1 (2009).

[50] Giacconi, R., et al., 1962, Phys. Rev. Lett. 9, 439.

[51] Giro, E., et al., Proc. SPIE 4843, Polarimetry in Astronomy, 456 (February 1, 2003).

[52] Goldwurm, A., <http://arxiv.org/abs/1007.4174>

[53] Guo, C.S., et al., Appl. Opt. 42, 413-418 (2007).

[54] Hachisuka, K., et al. 2006, ApJ, 645, 337.

[55] Halzen, F., Astron. Nachr. / AN 335, No. 5, 507 - 516 (2014).

[56] Hanbury Brown, R. & Twiss R.Q., Proceedings of the Royal Society of London, Vol. 242, No. 1230 (Nov. 5, 1957), 300-342.

[57] Hanbury Brown, R. & Twiss R.Q., Proceedings of the Royal Society of London, Vol. 243, No. 1234 (Jan. 14, 1958), 291-319.

[58] Hanbury Brown, R. & Twiss R.Q., Proceedings of the Royal Society of London, Vol. 248, No. 1253 (Nov. 11, 1958), 199-221.

[59] Hanbury Brown, R. & Twiss R.Q., Proceedings of the Royal Society of London, Vol. 248, No. 1253 (Nov. 11, 1958), 222-237.

[60] Hanbury Brown, et al., Mon. Not. R. Astron. Soc., Vol. 167, pp 121-136 1974.

[61] Heck, D. et al., CORSIKA: A Monte Carlo code to simulate extensive air showers, Tech. Rep. FZKA 6019, Forschungszentrum Karlsruhe 1998.

[62] Held, E.V., Ciattaglia, S.C., Giro E., Zitelli V., G. Sedmak ed., 12-1 May 1999 S.Agata (NA), Mem.S.A.It.

[63] Hess, V., Phys. Z., 13 (1913) 1084.

[64] Ichikawa, T., 2003, SICE Annual Conference in Fukui, August 4-6.

[65] Hillas, M., <http://cdsads.u-strasbg.fr/abs/1985ICRC....3..445H>

[66] Hinshaw, G., et al., 2013, <http://arxiv.org/pdf/1212.5226v3.pdf>

[67] Hirata, K., et al., Phys. Rev. Lett., Vol. 58, N. 14, 1987.

[68] Hofmann, W., Cherenkov Telescopes for Gamma-Ray Astrophysics, <http://www.cppm.in2p3.fr/Houches/Proceedings/MainCourse/Haufmann1.pdf>

[69] Horch, E.P., et al. 2013, Journal of Astronomical Instrumentation, Vol.2, No.2, 1340009.

[70] Jain, P. & Ralston, J.P., A&A 484, 887–895 (2008).

[71] Jelley, J.V. & Porter, N.A., J.R. Quart, Astron. Soc. 4 (1963) 275.

[72] Jones, R. C., Journal of the Optical Society of America 31 (7): 488-493, 1941.

[73] Jones, D.L., et al 2011, ApJ, 141:29.

[74] Kellermann, K.I., et al., Astrophys Space Sci (2007) 311: 231-239.

[75] Klebesadel, R.W., et al. 1973, Ap. J. 182:L85-L88.

[76] Kloppenborg, B., et al., Nature 464 (2010) 870.

[77] Kneiske, T. M. & Dole, H., A&A 515, A19 (2010).

[78] Kolhörster, W. (1913). Messungen der Durchdringenden Strahlung im Freiballon in Grösseren Höhen, Physikalische Zeitschrift, 14, 1153-1156.

[79] Komin, N., et al. 2011, 32ND ICRC.

[80] Kopeikin, S., & Schafer, G. 1999, Phys. Rev. D, 60, 124002.

[81] Koshut, T.M., et al., American Astronomical Society, 186th AAS Meeting, #53.01; Bulletin of the American Astronomical Society, Vol. 27, p.886.

[82] Koul, R., et al., $32^{nd}$ International Cosmic Ray Conference, Beijing 2001.

[83] Kraushaar, W., et al. 1965, Ap. J. 141:845-863.

[84] Kraushaar,W., et al. 1972, Ap. J. 177:341-363.

[85] Kuzmin & Kuzmin, Sov.Astron.Lett. 14, 180, 1988.

[86] Lacki, C.B., MNRAS, Volume 445, Issue 2, p.1858-1877.

[87] Lamanna, G., Rencontres de Moriond - Very High Energy Phenomena in the Universe, La Thuile : Italy (2013).

[88] LeBohec, S., et al., Proc. of SPIE Vol. 7013, 70132E, (2008).

[89] Le Bouquin, J.B., Millour, F., Merand, A., VLTI Science Operations Team, The Messenger 137 (2009) 25.

[90] Longair, M.S. (1988). The new astrophysics, in The New Physics, ed. Davies, P., pp. 94-208. Cambridge: Cambridge University Press.

[91] Longair, M.S., High Energy Astrophysics, Cambridge University Press, 2011.

[92] Malacara-Doblado, D., Optical Shop Testing, Third Edition, John Wiley and Sons, 2007.

[93] MAN-PO/121004, <https://www.cta-observatory.org/indico/>

[94] Meyer, M., Zechlin, H. S., Horns, D., Fermi Symposium, Washington, D.C., 2009 Nov. 2-5.

[95] Mirabel, I. F. & Rodriguez, L. F., Annual Review of Astronomy and Astrophysics, Vol. 37, pp. 409-443.

[96] Mirzoyan, R. & Andersen, M. I., Astroparticle Physics 31 (2009) 1-5.

[97] Mirzoyan, R., Astroparticle Physics, Volume 53, p. 91-99.

[98] Mok, F., et al., Optics Letters / Vol. 11, No. 11 / November 1986.

[99] Mukanov, J. B. 1983, Izv Krimsk. Astrofiz. Obs., 67, 55.

[100] Muno, M. P. et al., ApJ, 181:110-128, 2009.

[101] Neal, D. R., Copland, J. Neal, D., Proceedings of SPIE Vol. 4779 (2002).

[102] Nikishov, A. I. 1962, Sov. Phys. J. Exp. Theor Phys., 14, 393.

[103] Noll, R. J., JOSA, Vol. 66, Issue 3, pp. 207-211 (1976).

[104] Nuñez, P., et al., Mon. Not. R. Astron. Soc. 419, 172 (2012).

[105] Pacini, D., Nuovo Cim., 3 (1912) 93.

[106] Pacini, F., Nature, Vol. 216, November 11, 1967.

[107] Pareschi, G., et al. 2008, Proc. of SPIE Vol. 7018 70180W-1.

[108] Parodi, G., Internal report, BCV Progetti S.R.L., ASTRI Project SST prototype telescope structure design report, January 2013, 31.

[109] Perryman, M., et al. 1997, A&A 323, L49-L52.

[110] Ptuskin, V. & Zirakashvili, N., 2003, A&A 403, 1.

[111] Ragazzoni, R., TNG technical report N°10, Feb. 1992.

[112] Reid, B., et al. 2009,ApJ, 700:137-148.

[113] Ressell, M.T. & Turner, M.S., Comm. on Astrophys., 14 (1990) 323.

[114] Sandoval, A., Recent results from the HAWC high energy $\gamma$ ray observatory, $7^{th}$ SST Meeting, CERN.

[115] Schliesser, A., Mirzoyan, R., Astroparticle Physics 24 (2005) 382-390.

[116] Schneermann, M., Cui, X., Enard, D., Noethe, L., and Postema, H., ESO VLT III: the support system of primary mirrors, SPIE Proc., Vol. 1236, p. 920, 1990.

[117] Schneider, D. P., Hall, P.B., Richards, G.T., et al., 2007, ApJ, 134, 102-117.

[118] Schultz, C., PhD thesis, <https://magic.mpp.mpg.de/backend/publications/thesis>

[119] Scott, D., et al. for the Planck Collaboration, A&A, Nov 2014.

[120] Slade, M. A., et al., 1977, The moon, October 1977, Volume 17, Issue 2, pp 133-147.

[121] Smits, R., et al. A&A 528, A108, (2011).

[122] Sottile, G., et al., (arXiv:1305.2699).

[123] Sperello di Serego Alighieri, Polarimetry with large telescopes, Cambridge University Press, 2010.

[124] Stamerra, A., MAPS school, Perugia, 2009.

[125] Stecker, F. W., 1971, NASA Special Publication 249.

[126] Stetson, P. B., Astronomical Society of the Pacific, Publications, (ISSN 0004-6280), vol. 99, March 1987, p. 191-222.

[127] The MAGIC Collaboration, Science 320, 1752 (2008).

[128] The MAGIC Collaboration, Science DOI: 10.1126/science.1256183.

[129] Tavani, M., The Gamma-400 Project, $9^{th}$ AGILE Workshop, 17 April, 2012.

[130] Tinberger, J., Astronomical Polarimetry, Cambridge University Press, 1996.

[131] Tomelleri, R. & P. Rossettini, Internal report, OAB.010.004 CTA-SST-DM, 2013-02-08.

[132] Townsend, R.H.D., Owocki, S.P., Howarth, I.D., Mon. Not. Roy. Astron. Soc. 350 (2004) 189.

[133] van Langevelde, H. J., Diamond, P. J., Vlemmings, W., et al., 1999, New Astron. Rev., 43, 575.

[134] Vassiliev, V., et al., Astroparticle Physics, 2007, 28.

[135] Vercellone S. and the ASTRI Collaboration for the CTA Consortium, SPIE Newsroom, 2014, 10.1117/2.1201405.005488.

[136] Vernetto, S., INAF-INFN Torino, What Next, Dec 2014, Padova.

[137] Wagner, R.M., Ph.D. thesis, 2006, Technische Universität München, MPP-2006-245.

[138] Weekes, T.C., Cawley, M.F., Fegan, D.J., et al., Astrophys. J. 342 (1989) 379.

[139] Weekes, T.C., et al. 2002, Astroparticle Physics 17 (2002) 221-243.

[140] Wilson, R.N., Karl Schwarzschild and telescope optics, D-85296 Rohrbach, FRG, NASA ADS.

[141] Wilson, R.N., Reflecting Telescope Optics I, A&A Library.

[142] Winter, A., Vongehr, M. & Friedrich, P., Proc. of SPIE Vol. 7732, (2010).

[143] Wood, M. & Meyer, M. <http://www.pa.ucla.edu/sites/default/files/webform/ucla_dm_cta_dmnp_v2_1.pdf>

[144] Woosley, S.E. & Bloom, J.S., 2006, ARA&A, 44, 507-556.

[145] <http://fermi.gsfc.nasa.gov/science/mtgs/symposia/2014/abstracts/185>

[146] <http://www.hawc-observatory.org>

[147] CGRO Science Support Center Image Gallery, <http://cossc.gsfc.nasa.gov/docs/cgro/images/epo/gallery/glast/>

[148] <http://www-ucjf.troja.mff.cuni.cz/ hess/experimental.php>

[149] <http://imagine.gsfc.nasa.gov/docs/sats_n_data/gamma_missions.html>

[150] <http://www.astro.wisc.edu/ bank/>

[151] <http://www.cv.nrao.edu/course/astr534/Pulsars.html>

[152] <http://heasarc.gsfc.nasa.gov/docs/cgro/cgro/comptel_al26.html>

[153] <http://www.nist.gov/pml/data/xcom/index.cfm>

[154] <http://large.stanford.edu/courses/2014/ph241/alaeian2/>

[155] <http://english.ihep.cas.cn/ic/ip/LHAASO/>

[156] CTA SCI-LINK/130226, <https://www.cta-observatory.org/indico/>

[157] <https://www.cta-observatory.ac.uk>

[158] <https://www.zemax.com>

[159] ASTRI-SPEC-OAB-3100-002, 04/11/2011.

[160] <https://www.cta-observatory.org/indico/>

[161] <https://portal.cta-observatory.org/Pages/Home.aspx>

[162] Perf_Req_Lvl_A_MAN-TPC20120315, <http://www.cta-observatory.org/>

[163] Internal report, ASTRI Project CTA Cherenkov Telescope Prototypes, Prototype FEM report, GEC Group.

[164] <http://www.tpsoft.demon.co.uk>

[165] Internal report, ASTRI-ES-TOM-3110-024.

[166] <http://www.solidworks.com/>

[167] <http://www.flicamera.com/>

[168] <http://www.tng.iac.es>

[169] <http://hep.ph.liv.ac.uk/ mkdaniel/Presentations/Exoplanets.pdf>

[170] CTA SCI-LINK/121120, <https://www.cta-observatory.org/indico/>

[171] <http://www.eso.org/sci/facilities/paranal/telescopes/vlti.html>

[172] <http://www.chara.gsu.edu>